



ISSN 1343-2230

CNS-REP-95
March, 2017

Annual Report 2015

Center for Nuclear Study,
Graduate School of Science, the University of Tokyo

Editors

Taku Gunji

Yukino Kishi

Center for Nuclear Study

CNS Reports are available from:

Wako-Branch at RIKEN

Center for Nuclear Study,

Graduate School of Science, the University of Tokyo

2-1 Hirosawa, Wako

351-0198, Japan

Tel: +81-48-464-4191

Fax: +81-48-464-4554

Annual Report 2015

Center for Nuclear Study,
Graduate School of Science, the University of Tokyo

Preface

This is the annual report of the Center for Nuclear Study (CNS), Graduate School of Science, the University of Tokyo, for the fiscal year 2015 (April 2015 through March 2016). During this period, a lot of research activities in various fields of nuclear physics have been carried out and a wide variety of fruitful results have been obtained at CNS. This report summarizes research such activities. I hereby mention some highlights of the report.

The Center for Nuclear Study (CNS) aims to elucidate the nature of nuclear system by producing the characteristic states where the Isospin, Spin and Quark degrees of freedom play central roles. These researches in CNS lead to the understanding of the matter based on common natures of many-body systems in various phases. We also aim at elucidating the explosion phenomena and the evolution of the universe by the direct measurements simulating nuclear reactions in the universe. In order to advance the nuclear science with heavy-ion reactions, we develop AVF upgrade, CRIB and SHARAQ facilities in the large-scale accelerators laboratories RIBF. We started a new project OEDO for a new energy-degrading scheme, where a RF deflector system is introduced to obtain a good quality of low-energy beam. We promote collaboration programs at RIBF as well as RHIC-PHENIX and ALICE-LHC with scientists in the world, and host international meetings and conferences. We also provide educational opportunities to young scientists in the heavy-ion science through the graduate course as a member of the department of physics in the University of Tokyo and through hosting the international summer school.

The NUSPEQ (NUclear SPectroscopy for Extreme Quantum system) group studies exotic structures in high-isospin and/or high-spin states in nuclei. The CNS GRAPE (Gamma-Ray detector Array with Position and Energy sensitivity) is a major apparatus for high-resolution in-beam gamma-ray spectroscopy. Missing mass spectroscopy using the SHARAQ is used for another approach on exotic nuclei. In 2015, the following progress has been made. Experimental data taken in 2013 under the EURICA collaboration has been analyzed for studying octupole deformation in neutron-rich Ba isotopes and preparing publication. Exochemic charge exchange reaction (${}^8\text{He}, {}^8\text{Li}^*(1+)$) on ${}^4\text{He}$ has been analyzed for studying spin-dipole response of few-body system on the photon line. The tetra-neutron studied by the ${}^4\text{He}({}^8\text{He}, {}^8\text{Be})4n$ reaction, showing a candidate of the ground state of the tetra neutrons just above the $4n$ threshold as well as continuum at higher excitation energy, has been published. We plan to measure the reaction with better statistics and more accuracy in missing mass. The readout system of 14 detectors of the CNS GRAPE was upgraded, where digital pulse data taken by sampling ADCs are analyzed by FPGAs on boards.

The nuclear astrophysics group in CNS is working for experimental researches using the low-energy RI beam separator CRIB. In 2015, experiments on the alpha-cluster structure in ${}^{14}\text{C}$ and ${}^{19}\text{Ne}$ nuclei, ${}^{18}\text{F}(p, \alpha)$ astrophysical reaction using the Trojan Horse method with a improved precision, and the ${}^{17}\text{F}+\text{Ni}$ scattering near the Coulomb barrier were performed at CRIB under international collaborations including Korean, Italian, and Chinese groups. The call for CRIB proposals at the NP-PAC has been resumed in 2014, and 3 new proposals were approved in 2015.

Main goal of the quark physics group is to understand the properties of hot and dense nuclear matter created by colliding heavy nuclei at relativistic energies. The group has been involved in the PHENIX experiment at Relativistic Heavy Ion Collider (RHIC) at Brookhaven National Laboratory, and the ALICE experiment at Large Hadron Collider (LHC) at CERN. As for PHENIX, the group has been concentrating on the physics analysis involving dielectron measurement in Au+Au collisions. As for ALICE, the group has involved in the data analyses, which include the measurement of low-mass lepton pairs in Pb-Pb and p-Pb collisions, heavy flavor baryon measurements in pp and p-Pb collisions, particle correlations with large rapidity gap in p-Pb collisions, and searches for dibaryons in Pb-Pb collisions. The group has involved in the ALICE-TPC upgrade using a Gas Electron Multiplier (GEM). Performance evaluation of the MicroMegas + GEM systems for the upgrade has been

performed. R&D of GEM and related techniques has been continuing. Development of Teflon GEM has been progressing in collaboration with the Tamagawa group of RIKEN.

The Exotic Nuclear Reaction group studies various exotic reactions induced by beams of unstable nuclei. In 2015, analyses of experiments performed in 2014 showed progress: (1) parity transfer probe of the (^{16}O , $^{16}\text{F}(\text{g.s.})$) reaction on ^{12}C gave an enhancement on 0^- states in ^{12}B near zero degrees demonstrating the effectiveness of this reaction, (2) the spectrum of two-neutron relative momentum in knockout reactions from Borromean nucleus ^{11}Li was successfully decomposed into each angular momentum and a candidate of a d-wave resonance was found.

The OEDO/SHARAQ group promotes high-resolution experimental studies of RI beams by using the high-resolution beamline and SHARAQ spectrometer. A mass measurement by TOF-Br technique was performed for very neutron-rich calcium isotopes around $N=34$. For the experiment, we introduced new detector devices. A set of diamond detectors, developed as timing counters with excellent resolution, were installed as time-of-flight counters at the first and final foci of the beam line. Clover-type Ge detectors were installed at the final focal plane of the SHARAQ spectrometer for the first time, enabling particle identification of RI beams by probing delayed gamma rays from known isomeric states of specific nuclei. The OEDO project, which is a major upgrade of the high-resolution beamline for high-quality RI beams with energies lower than 100 MeV/u, is ongoing. The basic magnet arrangement and ion optics was fixed. We will finish the construction of the new beamline before March, 2017.

Two types of gaseous active target TPCs called GEM-MSTPC and CAT are developed and used for the missing mass spectroscopy in inverse kinematics. The common remarkable features of these detectors are the capabilities of the high intensity beam injection and the low energy recoil measurement. The astrophysical reactions of (α, p) on ^{18}Ne , ^{22}Mg and ^{30}S were measured by using the GEM-MSTPC. The alpha emission following the beta decay of ^{16}N was measured with the GEM-MSTPC in combination with the gating grid. The present topic of the CAT is the monopole transition strength distribution in nuclei extracted via deuteron inelastic scattering. We measured the deuteron scattering off ^{132}Xe and ^{16}O to study the equation of state of nuclear matter and the cluster structure, respectively, at the HIMAC in Chiba. The measurement of deuteron inelastic scattering off ^{132}Sn will be performed in RIBF soon.

We measured the proton resonance elastic scattering with the energy degraded ^{34}Si beam at RIPS facility. This experiment aims to get the excitation function with higher statistics and better energy resolution than the previous experiment. Though the beam intensity was less than expected, we successfully observed the excitation function. We are also developing two types of the exotic targets, Ti-3H and high-spin isomeric state of $^{178m2}\text{Hf}$. For the first target, we tested vulnerability with Ti-D which has an atomic ratio of 1:0.2 as the first step. We are going to test the uniformity and impurity in the target with ^{20}Ne beam of 8.2 MeV/u. For the second target, we measured the production cross section of $\text{natYb}(a,2n)$ reaction and conducted the chemical separation. Although the activities of other short-lived isotopes are around 10MBq, we successfully identified the cascade decay from $^{178m2}\text{Hf}$ of about 100 Bq by employing EURICA. We obtained the condition for mass production of $^{178m2}\text{Hf}$ at RIBF.

One of the major tasks of the accelerator group is the AVF upgrade project that includes development of ion sources, upgrading the AVF cyclotron of RIKEN and the beam line to CRIB. Development of ECR heavy ion sources is to provide new HI beams, higher and stable beams of metallic ions, and to improve the control system. The Hyper ECR and the Super ECR sources provide all the beams for the AVF cyclotron and support not only CRIB experiments but also a large number of RIBF experiments. Injection beam monitoring and control are being developed and studied. Detailed study of the optics from the ion sources are expected to improve transmission and qualities of beams for the RIBF facility.

The nuclear theory group has been promoting the CNS-RIKEN collaboration project on large-scale nuclear structure calculations and performed shell-model calculations under various collabora-

tions with many experimentalists for investigating the exotic structure of neutron-rich nuclei, such as $^{37,38}\text{Si}$, ^{50}Ar and $^{80,82}\text{Zn}$. We also participated in activities of HPCI Strategic Programs, which was finished at the end of FY2015. Since FY2015, we joined a new project “Priority Issue 9 to be tackled by using the Post-K Computer” and promotes computational nuclear physics utilizing supercomputers.

The 14th CNS-EFES International Summer School (CNS-EFES15) has been organized in August 2015 with many invited lecturers including four foreign distinguished physicists.

Finally, I thank Mr. Yoshimura, Mr. Oki and other administrative staff members for their heartfelt contributions throughout the year.

Susumu Shimoura
Director of CNS

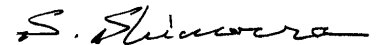


Table of Contents

1a. Experimental Nuclear Physics: Low and Intermediate Energies

Separated flow operation of the SHARAQ spectrometer for in-flight proton-decay experiments	3
<i>M. Dozono, T. Uesaka, S. Michimasa, M. Takaki, M. Kobayashi, M. Matsushita, S. Ota, H. Tokieda, and S. Shimoura</i>	
Feasibility study for the ${}^7\text{Be}+n$ reaction measurement by Trojan horse method at CRIB	5
<i>K. Abe, S. Hayakawa, H. Yamaguchi, and L. Lamia</i>	
Study on the Reaction Mechanism of ${}^{17}\text{F}+{}^{58}\text{Ni}$ around the Coulomb Barrier	7
<i>L. Yang, C. J. Lin, H. M. Jia, N. R. Ma, H. Yamaguchi, M. Mazzocco, L. J. Sun, D. X. Wang, S. Hayakawa, D. Kahl, S. M. Cha, G. X. Zhang, F. Yang, Y. Y. Yang, C. Signorini, Y. Sakaguchi, K. Abe, A. Kim, K. Y. Chae, M. S. Kwag, D. Pierrousakou, C. Parascandolo, M. La Commara, and E. Strano</i>	
Isomer gamma-ray spectroscopy of neutron-rich nuclei near $N = 40$	9
<i>Y. Kiyokawa, S. Michimasa, M. Kobayashi, R. Yokoyama, D. Nishimura, A. Mizukami, H. Oikawa, K. Kobayashi, H. Baba, G.P.A. Berg, M. Dozono, N. Fukuda, T. Furuno, E. Ideguchi, N. Inabe, T. Kawabata, S. Kawase, K. Kisamori, T. Kubo, Y. Kubota, C.S. Lee, M. Matsushita, H. Miya, H. Nagakura, S. Ota, H. Sakai, S. Shimoura, A. Stolz, H. Suzuki, M. Takaki, H. Takeda, S. Takeuchi, H. Tokieda, T. Uesaka, K. Yako, Y. Yamaguchi, Y. Yanagisawa, and Y. Yoshida</i>	
New measurement of proton resonant elastic scattering from ${}^{34}\text{Si}$	11
<i>N. Kitamura, N. Imai, O. Beliuskina, Y. Kiyokawa, S. Masuoka, S. Michimasa, M. Kobayashi, S. Ota, P. Schrock, N. Shimizu, S. Shimoura, Y. Yamaguchi, K. Wimmer, Y. Ichikawa, H. Ueno, K. Yoneda, T. Teranishi, and Y. Utsuno</i>	
Role of hexadecapole deformation in the shape evolution of neutron-rich Nd isotopes	13
<i>R. Yokoyama, E. Ideguchi, G. Simpson, Mn. Tanaka, S. Nishimura, P. Doornenbal, P.-A. Söderström, G. Lorusso, Z.Y. Xu, J. Wu, T. Sumikama, N. Aoi, H. Baba, F. Bello, F. Browne, R. Daido, Y. Fang, N. Fukuda, G. Gey, S. Go, S. Inabe, T. Isobe, D. Kameda, K. Kobayashi, M. Kobayashi, T. Komatsubara, T. Kubo, I. Kuti, Z. Li, M. Matsushita, S. Michimasa, C.B. Moon, H. Nishibata, I. Nishizuka, A. Odahara, Z. Patel, S. Rice, E. Sahin, L. Sinclair, H. Suzuki, H. Takeda, J. Taprogge, Zs. Vajta, H. Watanabe, and A. Yagi</i>	
Search for a double Gamow-Teller giant resonance in ${}^{48}\text{Ti}$ via heavy-ion double charge exchange (${}^{12}\text{C}, {}^{12}\text{Be}$) reaction	15
<i>M. Takaki, T. Uesaka, S. Shimoura, N. Aoi, M. Dozono, T. Furuno, C. Iwamoto, T. Kawabata, M. Kobayashi, Y. Matsuda, M. Matsushita, S. Michimasa, S. Ota, M. Sasano, L. Stuhl, A. Tamii, M. Tsumura, R. Yokoyama, and J. Zenihiro</i>	
Measurement of Deuteron Inelastic Scattering on ${}^{15,16}\text{O}$ in inverse kinematics using CNS Active Target	17
<i>H. Tokieda, S. Ota, M. Dozono, M. Itoh, C. S. Lee, S. Michimasa, M. Kobayashi, N. Imai, T. Uesaka, Y. Kiyokawa, Y. Nasu, K. Yako, J. Zenihiro, and E. Takada</i>	
First Determination of the ${}^{30}\text{S}(\alpha, p)$ Thermonuclear Reaction Rate from Experimental Level Structure of ${}^{34}\text{Ar}$	19
<i>D. Kahl, A. A. Chen, S. Kubono, H. Yamaguchi, D. N. Binh, J. Chen, S. Cherubini, N. N. Duy, T. Hashimoto, S. Hayakawa, N. Iwasa, H. S. Jung, S. Kato, Y. K. Kwon, S. Michimasa, S. Nishimura, S. Ota, K. Setoodehnia, T. Teranishi, H. Tokieda, T. Yamada, C. C. Yun, and L. Y. Zhang</i>	
Time-of-flight mass measurements of neutron-rich Ca isotopes beyond $N = 34$	21
<i>M. Kobayashi, S. Michimasa, Y. Kiyokawa, H. Baba, G.P.A. Berg, M. Dozono, N. Fukuda, T. Furuno, E. Ideguchi, N. Inabe, T. Kawabata, S. Kawase, K. Kisamori, K. Kobayashi, T. Kubo, Y. Kubota, C.S. Lee, M. Matsushita, H. Miya, A. Mizukami, H. Nagakura, D. Nishimura, H. Oikawa, S. Ota, H. Sakai, S. Shimoura, A. Stolz, H. Suzuki, M. Takaki, H. Takeda, S. Takeuchi, H. Tokieda, T. Uesaka, K. Yako, Y. Yamaguchi, Y. Yanagisawa, R. Yokoyama, and K. Yoshida</i>	
Feasibility study of mass production of ${}^{178m2}\text{Hf}$	23

N. Kitamura, N. Imai, Y. Yamaguchi, S. Mishimasa, and H. Haba

Development of a TiD_x target as the test of a Ti^3H_x target	25
<i>N. Imai, K. Wimmer, N. Kitamura, S. Michimasa, and Y. Hatano</i>	
The ($^{16}O, ^{16}F(0^-)$) reaction to study spin-dipole 0^- states	27
<i>M. Dozono, T. Uesaka, K. Fujita, N. Fukuda, M. Ichimura, N. Inabe, S. Kawase, K. Kisamori, Y. Kiyokawa, K. Kobayashi, M. Kobayashi, T. Kubo, Y. Kubota, C. S. Lee, M. Matsushita, S. Michimasa, H. Miya, A. Ohkura, S. Ota, H. Sagawa, S. Sakaguchi, H. Sakai, M. Sasano, S. Shimoura, Y. Shindo, L. Stuhl, H. Suzuki, H. Tabata, M. Takaki, H. Takeda, H. Tokieda, T. Wakasa, K. Yako, M. Yamagami, Y. Yanagisawa, J. Yasuda, R. Yokoyama, K. Yoshida, and J. Zenihiro</i>	
Development of recoil-proton detector for identification multi-neutrons	29
<i>S. Masuoka, S. Shimoura, R. Yokoyama, S. Michimasa, M. Matsushita, M. Takaki, M. Kobayashi, S. Ota, N. Kitamura, Y. Yamaguchi, and Y. Kunimoto</i>	

1b. Experimental Nuclear Physics: PHENIX Experiment at BNL-RHIC and ALICE Experiment at CERN-LHC

Overview of ALICE Results in 2015 and Activities of CNS	33
<i>T. Gunji, H. Hamagaki, Y. Watanabe, S. Hayashi, Y. Sekiguchi, K. Terasaki, H. Murakami</i>	
Charmed baryon measurements with ALICE at the LHC	35
<i>Y.S. Watanabe for the ALICE collaboration</i>	
Long range two-particle correlations in p -Pb collisions with the ALICE detector	37
<i>Y. Sekiguchi, H. Hamagaki, and T. Gunji for the ALICE Collaboration</i>	
π^0 and η measurement of direct photons via external conversions in high multiplicity pp collisions at 13 TeV	39
<i>H. Murakami for ALICE collaboration</i>	
Measurement of dielectrons from charm and bottom quark decays in p-Pb collisions with the ALICE detector	41
<i>S. Hayashi, H. Hamagaki, and T. Gunji on behalf of ALICE Collaboration</i>	

2. Accelerator and Instrumentation

Development of polycrystalline CVD diamond detectors	45
<i>S. Michimasa, M. Kobayashi, A. Stolz, M. Takaki, M. Dozono, H. Baba, S. Ota, K. Kisamori, H. Miya, H. Tokieda, K. Yako, H. Sakai, S. Shimoura, T. Uesaka, R.G.T. Zegers</i>	
Development of particle identification method using fast response detectors	47
<i>S. Ota, J. Zenihiro, H. Takeda, S. Michimasa, M. Dozono, M. Matsushita, K. Kisamori, M. Kobayashi, Y.N. Watanabe, Y. Kiyokawa, Y. Yamaguchi, S. Masuoka, S. Shimoura, K. Yako, N. Imai, H. Baba, T. Kubo, K. Yoshida, N. Inabe, N. Fukuda, H. Suzuki, D.S. Ahn, D. Murai, H. Sato, Y. Sato, H. Otsu, and T. Uesaka</i>	
Development of the gamma-ray interaction point calculation algorithm using the GRAPE Ge detector	49
<i>Y. Yamamoto, N. Aoi, Y. Fang, E. Ideguchi, S. Noji, and T. Yamamoto</i>	
Performance Evaluation of CAT in $^{132}Xe(d, d')$ Measurement	51
<i>C. S. Lee, S. Ota, H. Tokieda, T. Uesaka</i>	
Development of Data Acquisition System for Ge Detectors Array for Multi Gamma-Ray with DSP	53
<i>Y. Yamaguchi, S. Shimoura, K. Wimmer, N. Imai, N. Kitamura</i>	
Pulse-height defect in single crystal CVD diamond detectors	55

O. Beliuskina, A.O. Strelakovsky, A.A. Aleksandrov, I.A. Aleksandrova, H.M. Devaraja, C. Heinz, S. Heinz, S. Hofmann, S. Ilich, N. Imai, D.V. Kamanin, M. Kis, G.N. Knyazheva, C. Kozhuharov, E.A. Kuznetsova, J. Maurer, G.V. Mishinsky, M. Pomorski, Yu.V. Pyatkov, O.V. Strelakovsky M. Träger, and V.E. Zhuchko

Beam transport analysis of RIKEN AVF Cyclotron injection line using pepper-pot emittance monitor 57
Y. Kotaka, Y. Ohshiro, H. Yamaguchi, N. Imai, T. Nagatomo, M. Kase, K. Hatanaka, H. Mutoh and S. Shimoura

Beam emittance of fixed plasma boundary in Hyper ECR ion source 59
Y. Ohshiro, Y. Kotaka, S. Watanabe, H. Muto, H. Yamaguchi, N. Imai and S. Shimoura

3. Theoretical Nuclear Physics

Stochastic estimation of nuclear level density in large-scale shell-model calculations 63
N. Shimizu, Y. Utsuno, Y. Futamura, T. Sakurai, T. Mizusaki, and T. Otsuka

New aspect of island of inversion shed by microscopic theory and large-scale calculation 65
N. Tsunoda, T. Otsuka, N. Shimizu

E1 strength function in Monte Carlo shell model 67
T. Togashi, T. Otsuka, N. Shimizu, and Y. Utsuno

Structure of Be isotopes 69
T. Yoshida, N. Shimizu, T. Abe, and T. Otsuka

Monte Carlo shell model calculations for structure of nuclei around Z=28 71
Y. Tsunoda, T. Otsuka, N. Shimizu, M. Honma, and Y. Utsuno

4. Other Activities

The 14th CNS International Summer School (CNSSS15) 75
K. Yako, S. Shimoura, T. Gunji, H. Hamagaki, E. Hiyama, N. Imai, Y. Iwata, S. Michimasa, T. Nakatsukasa, S. Ota, T. Otsuka, H. Sakai, H. Sakurai, N. Shimizu, T. Uesaka, Y. Utsuno, and H. Utsunomiya

Laboratory exercise for undergraduate students 77
S. Ota, M. Niikura, N. Kitamura, T. Saito, K. Yako, H. Sakurai and S. Shimoura

Appendices

Symposium, Workshop, Seminar, PAC and External Review 81

CNS Reports 82

Publication List 83

Talks and Presentations 94

Personnel 102

Experimental Nuclear Physics: Low and Intermediate Energies

Separated flow operation of the SHARAQ spectrometer for in-flight proton-decay experiments

M. Dozono, T. Uesaka^a, S. Michimasa, M. Takaki, M. Kobayashi, M. Matsushita, S. Ota, H. Tokieda, and S. Shimoura

Center for Nuclear Study, Graduate School of Science, University of Tokyo
^aRIKEN Nishina Center

The SHARAQ spectrometer [1] is a high resolution magnetic spectrometer designed for radioactive isotope (RI) beam experiments at the RI Beam Factory (RIBF). The spectrometer has been used in various precise measurements in combination with the high-resolution beam line [2]. Among physics programs performed, the most characteristic one is a new missing mass spectroscopy with an RI beam used as a “probe”. With the SHARAQ, investigations of spin-isospin properties in nuclei have been strongly promoted by RI-induced charge-exchange reactions such as ($t, ^3\text{He}$), ($^{12}\text{N}, ^{12}\text{C}$), ($^{10}\text{C}, ^{10}\text{B}$), and ($^8\text{He}, ^8\text{Be}$).

In this report, we present a recent development of the ion-optical mode of SHARAQ operation for the coincident measurement of a proton and a heavy-ion fragment. The new mode, called the “*separated flow mode*” enables the invariant-mass spectroscopy of proton-unbound states with the SHARAQ, and thus extends the research field in the nuclear chart toward proton-rich nuclei. In addition, proton-unbound nuclei can be used as probe particles. One interesting example is the parity-transfer reaction ($^{16}\text{O}, ^{16}\text{F}(0^-, \text{g.s.})$) [3]. This reaction has a unique sensitivity to unnatural parity states, and can be used as a powerful tool to probe 0^- states in a target nucleus.

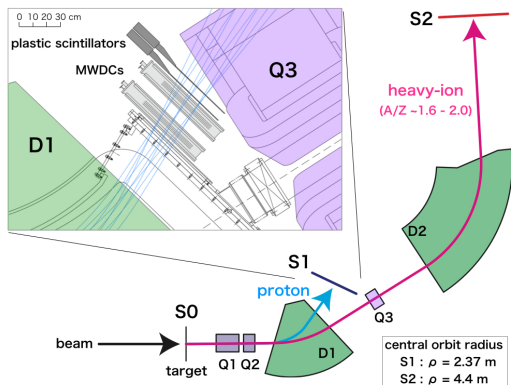


Figure 1: Schematic layout of the SHARAQ spectrometer. The SHARAQ spectrometer consists of three quadrupole magnets (Q1, Q2, and Q3), and two dipole magnets (D1 and D2) in a “QQDQD” configuration. The inset shows the tracking detector system at S1, which consists of two MWDCs and two plastic scintillators.

In the separated flow mode, the SHARAQ spectrometer is used as two spectrometers with different magnet configurations of “QQD” and “QQDQD” at the same time (see Fig. 1). The reaction products from the target (S0) are sepa-

rated and analyzed in either of these two configurations depending on their mass-to-charge ratios (A/Z). The particles with $A/Z \sim 1$, such as protons, are analyzed in the “Q1-Q2-D1” configuration and detected in the S1 focal plane, which is located on the low-momentum side downstream of the D1 magnet. On the other hand, the heavy-ion products are analyzed in the “Q1-Q2-D1-Q3-D2” configuration to increase the resolving power and detected at the S2 final focal plane. Therefore, this new technique enables us to perform coincidence measurements of the proton and heavy-ion pairs produced in the decays of proton-unbound states in nuclei. Details of the ion-optical designs can be found in Ref. [4].

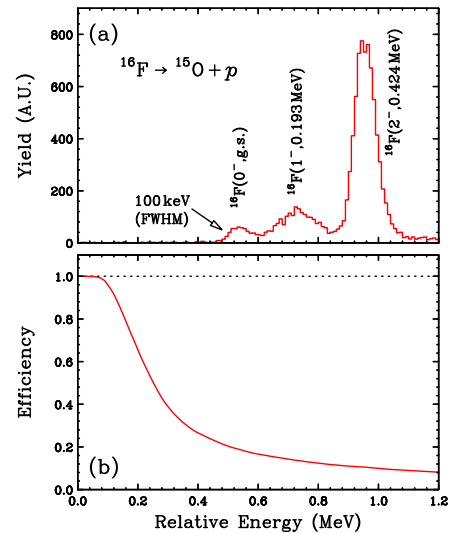


Figure 2: (a) Yields and (b) detection efficiency, for the $^{15}\text{O} + p$ coincidence events, as a function of relative energy.

The performance of the separated flow mode is studied with the ($^{16}\text{O}, ^{16}\text{F}$) reaction. A primary ^{16}O beam at 247 MeV/u and 10^7 pps is transported to the S0 target position. The beam line is set to be dispersion-matched to the SHARAQ. A plastic scintillator with a thickness of 1 mm is used as a reaction target. The outgoing $^{15}\text{O} + p$ produced in the decay of ^{16}F are measured in coincidence. The momenta of the particles are analyzed using the SHARAQ spectrometer. The ^{15}O particles are detected with two low-pressure MWDCs in the S2 focal plane, while the protons are detected with two MWDCs in the S1 focal plane.

Figure 2(a) shows the relative energy (E_{rel}) spectrum for the $^{15}\text{O} + p$ coincidence events. The obtained E_{rel} resolution is 100 keV (FWHM), and the 0^- g.s. of ^{16}F ($E_{\text{rel}} = 0.535$ MeV) is clearly separated from the excited states, the 1^- state at 0.193 MeV ($E_{\text{rel}} = 0.728$ MeV) and the 2^- state at 0.424 MeV ($E_{\text{rel}} = 0.959$ MeV).

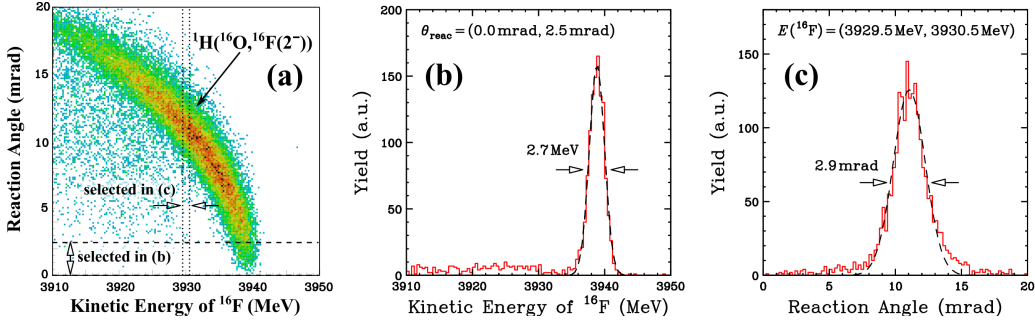


Figure 3: (a) Kinematic correlation for the ${}^1\text{H}({}^{16}\text{O}, {}^{16}\text{F}(2^-), 0.424 \text{ MeV})$ reaction. The horizontal and vertical axes represent the kinetic energy of ${}^{16}\text{F}$ ($E({}^{16}\text{F})$) and the reaction angle (θ_{reac}), respectively. (b) The projection of the events in the region between the dashed lines in (a) onto the $E({}^{16}\text{F})$ axis. (c) The projection of the events in the region between the dotted lines in (a) onto the θ_{reac} axis.

We also evaluate the detection efficiency for the ${}^{15}\text{O} + p$ coincidence events from the Monte Carlo simulation, where the acceptance and the finite resolution in angles and momenta are taken into account. The result is shown in Fig. 2(b) as a function of E_{rel} . The obtained efficiency is 0.189 at $E_{\text{rel}} = 0.535 \text{ MeV}$, which is mainly determined by the angular acceptance for the proton.

We evaluate resolutions of the ${}^{16}\text{F}$ kinetic energy $E({}^{16}\text{F})$ and the reaction angle θ_{reac} using the $({}^{16}\text{O}, {}^{16}\text{F}(2^-, 0.424 \text{ MeV}))$ reaction on hydrogens in the plastic scintillator. Figure 3(a) shows the kinematic correlation between $E({}^{16}\text{F})$ and θ_{reac} . For the identification of ${}^{16}\text{F}(2^-)$, the events in the relative energy region of $E_{\text{rel}} = 0.88\text{--}1.04 \text{ MeV}$ are selected in the analysis. We make two projections from Fig. 3(a). One is gated by $\theta_{\text{reac}} = 0.0\text{--}2.5 \text{ mrad}$ and projected onto the $E({}^{16}\text{F})$ axis [Fig. 3(b)]. The other distribution is gated by $E({}^{16}\text{F}) = 3929.5\text{--}3930.5 \text{ MeV}$ and projected onto the θ_{reac} axis [Fig. 3(c)]. The width of the $E({}^{16}\text{F})$ distribution in Fig. 3(b) is 2.7 MeV FWHM. The intrinsic energy resolution is evaluated to be about 2.0 MeV FWHM by considering the energy straggling of the particles in the target ($\sim 1.8 \text{ MeV}$). We also determine the θ_{reac} resolution to be 2.9 mrad FWHM from the width of the distribution in Fig. 3(c). This value is comparable to the angular spread of the beam of about 3 mrad, and thus the intrinsic angular resolution of the spectrometer seems to be much better.

Table 1 summarizes performances of our system. For the invariant-mass measurement, we compare our performances with those of the magnetic analysis system with the large-acceptance spectrometer KaoS at GSI; with this system, Iwasa *et al.* [5] measured the Coulomb dissociation of ${}^8\text{B}$ into ${}^7\text{Be}$ and a proton at 254 MeV/nucleon. As can be seen from Table 1, our resolution is better by a factor of about 3, while the efficiency is smaller by a factor of about 4. This is because momentum and angular acceptances in the SHARAQ spectrometer are smaller at the cost of higher resolutions.

For the missing-mass measurement, high energy and angular resolutions of 2.7 MeV and 2.9 mrad are achieved at a beam energy of 247 MeV/u. Such an accurate missing-mass measurement combined with an invariant-mass method

	This work	Iwasa <i>et al.</i> [5]
Spectrometer	SHARAQ	KaoS
Beam energy	247 MeV/u	254 MeV/ nucleon
Measured products	${}^{16}\text{F} \rightarrow {}^{15}\text{O} + p$	${}^8\text{B} \rightarrow {}^7\text{Be} + p$
Relative energy resolution	0.10 MeV at $E_{\text{rel}} = 0.535 \text{ MeV}$	0.26 MeV at $E_{\text{rel}} = 0.6 \text{ MeV}$
Efficiency	0.189 at $E_{\text{rel}} = 0.535 \text{ MeV}$	~ 0.8 at $E_{\text{rel}} = 0.6 \text{ MeV}$
Kinetic energy resolution	2.7 MeV at $\sim 3940 \text{ MeV}$	—
Reaction angle resolution	2.9 mrad	—

Table 1: Performances of separated flow mode of the SHARAQ spectrometer. Performances of the magnetic analysis system with the KaoS spectrometer are also shown for comparison.

gives unique opportunities to explore little-studied excitation modes in nuclei using new types of reaction probes with particle-decay channels.

References

- [1] T. Uesaka, S. Shimoura, H. Sakai, Prog. Theor. Exp. Phys. **2012** (2012) 03C007.
- [2] T. Kawabata *et al.*, Nucl. Instrum. Methods Phys. Res. B **266** (2008) 4201.
- [3] M. Dozono *et al.*, RIKEN Accel. Prog. Rep. **45**, (2012) 10.
- [4] M. Dozono *et al.*, arXiv:1602.00726.
- [5] N. Iwasa *et al.*, Phys. Rev. Lett. **83** (1999) 2910.

Feasibility study for the ${}^7\text{Be}+n$ reaction measurement by Trojan horse method at CRIB

K. Abe, S. Hayakawa, H. Yamaguchi, and L. Lamia^a

Center for Nuclear Study, Graduate School of Science, University of Tokyo

^aDepartment of Physics and Astronomy, University of Catania, Italy

The cosmological theory of Big Bang is the greatest achievement of the modern science, which is supported by three fundamental observational evidences: the cosmic microwave background, Hubble's law of the galaxies, and the abundance ratio of the primordial light elements. The respective observation and theoretical calculation are consistent with high accuracies. However, for the ${}^7\text{Li}$ abundance, there is a discrepancy that the observation is about 3 times smaller than the calculation, called as “ ${}^7\text{Li}$ problem” which has been investigated from various approaches. The ${}^7\text{Li}$ abundance depends on that of ${}^7\text{Be}$ at the end of Big Bang Nucleosynthesis (BBN) rather than the ${}^7\text{Li}$ production during BBN because surviving ${}^7\text{Be}$ decay into ${}^7\text{Li}$ by electron capture after BBN, whereas ${}^7\text{Li}$ can be easily destroyed by the ${}^7\text{Be}(n, \alpha){}^4\text{He}$ reaction. The only parameter of BBN calculation is the baryon density which is accurately determined, and this simulation is called out numerically by taking many possible paths of nuclear reaction network into account. Therefore, for more precise BBN calculation, informations of nuclear reaction cross section is necessary.

We aim to reduce the uncertainty of calculation for BBN by measuring reaction cross sections of the ${}^7\text{Be}(n, p){}^7\text{Li}$ and ${}^7\text{Be}(n, \alpha){}^4\text{He}$ reactions which are related to the ${}^7\text{Be}$ abundance during BBN. The first reaction has been considered as the main process to destroy ${}^7\text{Be}$ during BBN. There are some studies by direct measurement [1] up to 13.5 keV and by time-reversal measurement [3–6] above that energy. However, the transition to the first excited state of ${}^7\text{Li}$ has never been considered at all. Figure.1 shows a possible contribution evaluated by R-matrix simulation. According to a

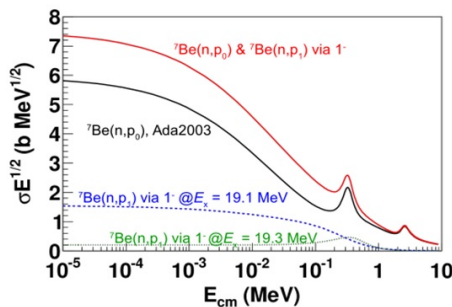


Figure 1: R-matrix simulation for possible contributions from the ${}^7\text{Be}(n, p){}^7\text{Li}$ channel going to the 1^- state resonance around $E_x=19.3$ MeV

recent study [2], the sensitivity of the ${}^7\text{Li}$ abundance to this reaction is expressed by

$$\frac{\partial \log Y_{7\text{Li}}}{\partial \log \langle \sigma v \rangle_{7\text{Be}}} = -0.71, \quad (1)$$

where $Y_{7\text{Li}}$ is the yield of ${}^7\text{Li}$ and $\langle \sigma v \rangle_{7\text{Be}}$ is the reaction

rate of ${}^7\text{Be}(n, p){}^7\text{Li}$. This means that if the reaction rate is doubled, the yield becomes about half, and the ${}^7\text{Be}(n, p){}^7\text{Li}$ reaction rate could affect ${}^7\text{Li}$ abundance significantly. For the second reaction, this reaction has not been considered in the BBN reaction network until recently, and there are not sufficient experimental data near BBN energies. The reaction rate has only 1 significant digit based on published rate [8–10] in the BBN network calculation [7], which results in the uncertainty of ${}^7\text{Li}$ abundance about 40%, and a new measurement is desired.

We will apply the indirect method, the Trojan Horse method (THM) [11], because this method is useful for assessing neutron-induced reaction at low energies. If we use THM we can measure the half-off-energy-shell (HOES) cross section covering down to Gamow-peak energy region via three-body reaction. In THM approach, the two-body cross section for the process of interest, $a + x \rightarrow c + d$, is determined by selecting the quasi-free (QF) contribution of a three-body reaction, $a + b \rightarrow c + d + s$, the “TH nucleus” b consists of $x + s$. In the hypothesis of the QF process, the s nucleus will act as a *spectator* and virtually only x nucleus joins the reaction. The THM is expressed in the framework of the Plain Wave Impulse Approximation, where the three-body reaction cross section is proportional to the cross section of HOES binary reaction of our interest;

$$\frac{d^3 \sigma}{d\Omega_1 \Omega_2 dE_1} \propto (\text{KF}) |\phi(p_s)|^2 \frac{d\sigma(E)}{d\Omega^{\text{HOES}}}, \quad (2)$$

where (KF) is called as kinematic factor which depends on experimental setup and $|\phi(p_s)|$ is momentum distribution of TH nucleus including spectator. In our case, deuteron is the TH nucleus and proton will act as the spectator. Thus, the cross sections of the ${}^7\text{Be}(n, p){}^7\text{Li}$ and ${}^7\text{Be}(n, \alpha){}^4\text{He}$ reactions will be obtained via the ${}^7\text{Be}(d, {}^7\text{Li}p)p$ and ${}^7\text{Be}(d, \alpha\alpha)p$ reactions, respectively.

This experiment is going to be held at CRIB of CNS located at the RIBF of RIKEN Nishina Center. We already have a lot of experiences to produce almost pure ${}^7\text{Be}$ beam [12–14] near our demand (1×10^6 pps at 28 MeV). ${}^7\text{Be}$ beam can be produced by the ${}^7\text{Li}(p, n){}^7\text{Be}$ ($Q = -1.644$ MeV) reaction in inverse kinematics. We requested a ${}^7\text{Li}^{2+}$ primary beam at 5.0 MeV/u with 500 pμA. The expected secondary ${}^7\text{Be}$ beam energy is 3.4 MeV/u on CD_2 target.

We plan to detect the α - α and the ${}^7\text{Li}$ - p coincidence events and reconstruct three body kinematics from the beam bombarding energy, the beam trajectory, the energies of emitted two particles, the scattering angles and the reaction Q -value. Figure 2 indicates angular and energy correlations for each reactions by Monte Carlo calculation.

The whole allowed kinematic area is represented by

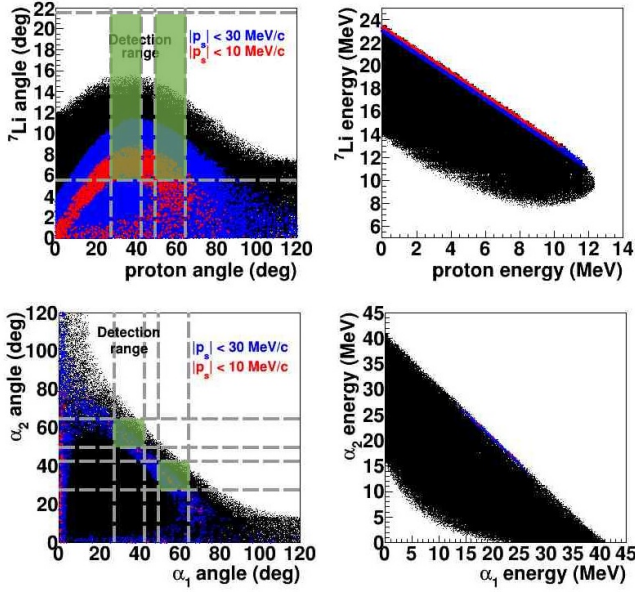


Figure 2: Correlations of energy and angle. Top two figures are for the ${}^7\text{Be}(d, {}^7\text{Li})p$ reaction and bottom two for the ${}^7\text{Be}(d, \alpha\alpha)p$ reaction.

black dots, the area for spectator momentum range $|p_s| < 30$ MeV/c by blue (or dark gray) and the area for $|p_s| < 10$ MeV/c by red (or light gray). We will put silicon-detectors at $\pm 13^\circ$, $\pm 35^\circ$ and $\pm 57^\circ$ to select the momentum range of spectator for QF mechanism, and identify coincidence events. We can measure cross sections around BBN energy illustrated in Figure 3 if we select momentum range of spectator as $|p_s| < 30$ MeV/c. The tentative design of the exper-

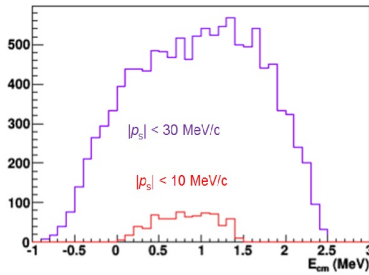


Figure 3: Coverage of $E_{c.m.}$ range with our measurement

imental setup for this experiment is shown in Figure 4. We will use a CD_2 target with a thickness of $50 \mu\text{g}/\text{cm}^2$ causing the energy straggling of about 100 keV, so we can separate the ground state and the 1st excited state (478 keV) by Q -value. First Micron-SSD ΔE_1 (Figure 4) will be put only at $\pm 13^\circ$ for the identification of ${}^7\text{Li}$. Considering above simulations, typical three-body cross section, total solid angle, beam intensity, number of deuteron in CD_2 target and QF process contribution, the expected yield is 1.5×10^{-4} cps/50-keV bin, that is, 150 count/50-keV bin in 12-days run. This experiment is going to be performed in November, 2016.

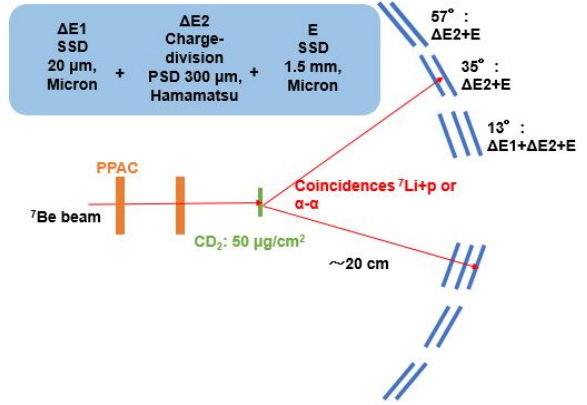


Figure 4: A schematic view of experimental setup

References

- [1] P. Koehler, C. Bowman, F. Steinkruger, D. Moddy, G. Hale, J. Starner, S. Wender, R. Haight, P. Lisowski, and W. Talbert, *Physical Review C* **37**, 917 (1988).
- [2] A. Coc and E. Vagioni, *Journal of Physics: Conference Series* **202**, 012001 (2001).
- [3] R. L. Macklin and J. H. Gibbons, *Physical Review* **109**, 105 (1958).
- [4] R. R. Borchers and C. H. Poppe, *Physical Review* **129**, 2679 (1963).
- [5] C. H. Poppe, J. D. Anderson, J. C. Davis, S. M. Grimes, and C. Wong, *Physical Review C* **14**, 438 (1976).
- [6] K. Sekharan, H. Laumer, B. Kern, and F. Gabbard, *Nuclear Instruments and Methods* **133**, 253 (1976).
- [7] P. D. Serpico, S. Esposito, F. Iocco, G. Mangano, G. Miele, and O. Pisanti, *Journal of Cosmology and Astroparticle Physics* **2004**, 010 (2004).
- [8] R. V. Wagoner, *Astrophysical Journal* **148**, 3 (1967).
- [9] R. V. Wagoner, *Astrophysical Journal Supplement Series* **18**, 247 (1967).
- [10] R. V. Wagoner et al., *Astrophysical Journal* **179**, 343 (1973).
- [11] C. Spitaleri, A. M. Mukhamedzhanov, L. D. Blokhintsev, M. La Cognata, R. G. Pizzone, and A. Tumino, *Physics of Atomic Nuclei* **74**, 1725 (2011).
- [12] H. Yamaguchi, Y. Wakabayashi, G. Amadio, S. Hayakawa, H. Fujikawa, S. Kubono, J. J. He, A. Kim, and D. N. Binh, *Nuclear Instruments and Method in Physics Research Section A: Accelerators, Spectrometers, Detectors and Associated Equipment* **589**, 150 (2008).
- [13] H. Yamaguchi, Y. Wakabayashi, S. Kubono, G. Amadio, H. Fujikawa, T. Teranishi, A. Saito, J. J. He, S. Nishimura, and Y. Togano, *Physics Letters B* **672**, 230 (2009).
- [14] H. Yamaguchi, D. Kahl, Y. Wakabayashi, S. Kubono, T. Hashimoto, S. Hayakawa, T. Kawabata, N. Iwasa, T. Teranishi, Y. K. Kwon, D. N. Binh, L. H. Khiem, and N. N. Duy, *Physical Review C* **87**, 034303 (2013).

Study on the Reaction Mechanism of $^{17}\text{F}+^{58}\text{Ni}$ around the Coulomb Barrier

L. Yang^{a,b}, C. J. Lin^a, H. M. Jia^a, N. R. Ma^a, H. Yamaguchi^b, M. Mazzocco^{c,d}, L. J. Sun^a,
 D. X. Wang^a, S. Hayakawa^b, D. Kahl^b, S. M. Cha^e, G. X. Zhang^f, F. Yang^a, Y. Y. Yang^g,
 C. Signorini^{c,d}, Y. Sakaguchi^b, K. Abe^b, A. Kim^e, K. Y. Chae^e, M. S. Kwag^e, D. Pierroutsakou^d,
 C. Parascandolo^d, M. La Commara^{d,h}, and E. Strano^{d,g}

^aDepartment of Nuclear Physics, China Institute of Atomic Energy

^bCenter for Nuclear Study, the University of Tokyo

^cthe University of Padova

^dIstituto Nazionale di Fisica Nucleare (INFN)

^eDepartment of Physics, the Sungkyunkwan University

^fDepartment of Physics, Beihang University

^gInstitute of Modern Physics, Chinese Academy of Sciences

^hUniversity of Naples

⁸the University of Catania

The special attention has been devoted to the reactions induced by the weakly bound nuclear systems [1, 2]. In the interaction process, the weakly bound projectile can easily break up into smaller fragments due to the small binding energy, leading to strong couplings of continuum states with discrete ones [3]. Moreover, the consequence of the breakup channel on the fusion process is still controversial, from not only theoretically, but also experimentally [4, 5]: the removal of the incident flux arising from the breakup reaction would lead to fusion suppression; on the other hand, the coupling to the breakup channel can change the barrier distribution which could result in fusion enhancement. Therefore, a detailed knowledge on the breakup process is important to understand the reaction induced by the weakly bound nucleus thoroughly.

Thus we undertook the investigation of the system $^{17}\text{F}+^{58}\text{Ni}$ with the energies around the Coulomb barrier. With low threshold of 0.6 MeV of ^{17}F , the breakup channel of $^{17}\text{F}\rightarrow^{16}\text{O}+p$ is expected to take place easily. However, ^{16}O could be produced both in breakup and transfer reactions, and the origin of ^{16}O can only be distinguished by means of complete-kinematics coincidence measurement. Recently, a new detector array has been built up [6], to perform a complete-kinematics measurement. The array, as shown in Fig. 1, consists of ten detector units, each of which contains one ion-chamber (IC), one double-side silicon detector (DSSD, 60 μm , with an active area of $50\times 50\text{ mm}^2$ and strip width of 3 mm), and two quartered silicon detectors (QSDs, the thicknesses are 300 μm and 1000 μm , respectively). With the telescope consisted of the IC and DSSD, the heavy ions, such as ^{17}F and ^{16}O , could be distinguished. While for the light particles produced in the reaction process, like proton and alpha, they could be identified by the two QSDs.

This array is a powerful tool for the study of reaction mechanism, especially for the breakup mechanism of weakly bound nuclei, for its outstanding advantages: 1) Multi-telescopes structure. The multi-layer structure of the detector unit makes it possible to identify heavy and light

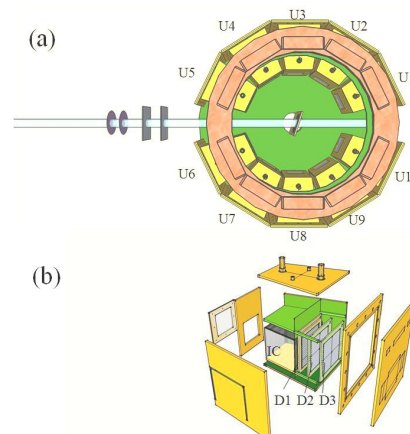


Figure 1: (a) The schematic diagram of the detector array. The symbols U1 to U10 demonstrate 10 detector units. (b) The de-construction diagram of one detector unit. The symbol IC represents the ion-chamber, D1 is the DSSD with the thickness of 60 μm , D2 and D3 are the QSDs with thickness of 300 μm and 1000 μm , respectively.

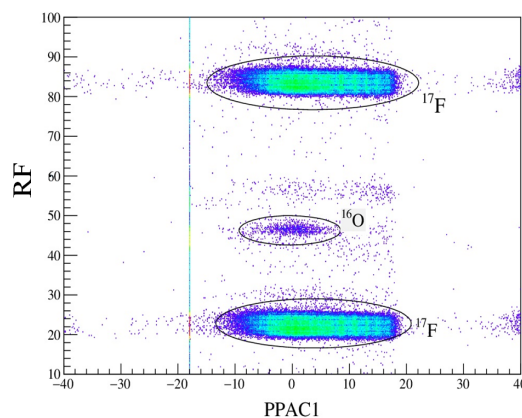


Figure 2: Discrimination of ^{17}F and ^{16}O with the time of RF versus PPAC.

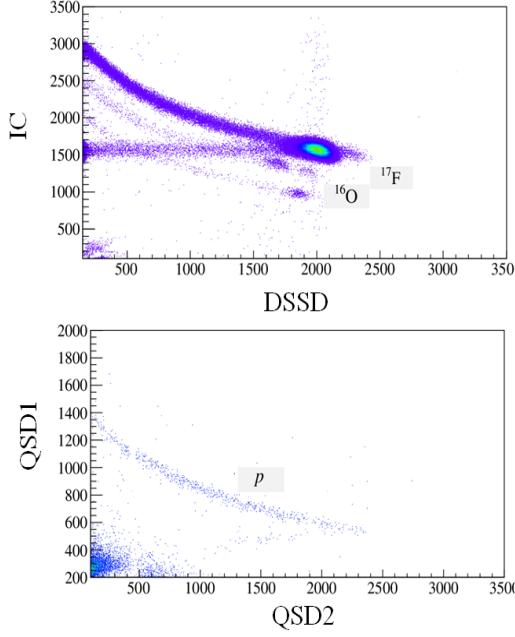


Figure 3: Identification of particles yielding from $^{17}\text{F}+^{58}\text{Ni}$ at $E_{\text{lab}}(^{17}\text{F})=59.7$ MeV. Symbols QSD1 and QSD2 represent the QSDs with the thickness of $300\ \mu\text{m}$ and $1000\ \mu\text{m}$, respectively.

ions simultaneously. 2) Large angle coverage. The angle range covered by the array is from 15.2° to 164.8° in the laboratory frame. Such a large angle coverage is beneficial to obtain the information of the angle correlation, and reconstruct the intermediate state before the breakup. 3) High detect efficiency. Take ^{17}F breaking up into ^{16}O and proton as an example, the detect efficiency is as high as 10% according to the simulation result.

Based on this detector array, the experiment on the $^{17}\text{F}+^{58}\text{Ni}$ system was performed at CNS Radio Isotope Beam (CRIB) separator from Dec. 10th to 19th, 2015. The radioactive ^{17}F was produced by the $^2\text{H}(^{16}\text{O},^{17}\text{F})$ reaction using a $6.6\ \text{MeV/u}$ ^{16}O primary beam impinging on a H_2 gas target. Four different ^{17}F secondary beam energies were obtained. The first one is $59.7\ \text{MeV}$, which was achieved with a gas pressure of $254\ \text{torr}$ and a Al degrader with a thickness of $5\ \mu\text{m}$. Then by increasing the gas pressure and Al degrader up to $262\ \text{torr}$ and $12\ \mu\text{m}$, as well as $316\ \text{torr}$ and $17\ \mu\text{m}$, the beam energies of $49.7\ \text{MeV}$ and $46\ \text{MeV}$ were obtained, respectively. The last energy, $65\ \text{MeV}$, was achieved with a gas pressure of $250\ \text{torr}$ and without a degrader. After selection by the WF and tracked by two PPACs, the secondary beam, with an intensity of $6\text{-}10 \times 10^5$ pps, was then impinged on the secondary target, ^{58}Ni , with a thickness of $1\ \text{mg/cm}^2$. The discrimination of ^{17}F by the time of RF versus PPAC is shown in Fig. 2. It can be seen that the secondary beam ^{17}F can be distinguished clearly, with the purity of about 82%. The particle identification by the first detector unit (θ_{lab} from 15.2° to 30.5°) is shown in Fig. 3. It can be seen that both the heavy (^{17}F and ^{16}O) and the light (proton) ions can be distinguished clearly.

The data analysis is in progress now.

References

- [1] L. F. Canto, P. R. S. Gomes, R. Donangelo, and M. S. Hussein, Phys. Rep. **424** (2006) 1.
- [2] N. Keeley, R. Raabe, N. Alamanos, and J. L. Sida, Prog. Part. Nucl. Phys. **59** (2007) 579.
- [3] N. Keeley, N. Alamanos, K. W. Kemper and K. Rusek, Prog. Part. Nucl. Phys. **63** (2009) 396.
- [4] J. F. Liang and C. Signorini, Int. J. Mod. Phys. E **14** (2005) 1121.
- [5] M. Mazzocco, Int. J. Mod. Phys. E **19** (2010) 977.
- [6] N. R. Ma, C. J. Lin, J. S. Wang *et al.*, accepted by Chin. Phys. C, to be published.

Isomer gamma-ray spectroscopy of neutron-rich nuclei near $N = 40$

Y. Kiyokawa, S. Michimasa, M. Kobayashi, R. Yokoyama, D. Nishimura^a, A. Mizukami^a, H. Oikawa^a, K. Kobayashi^b, H. Baba^c, G.P.A. Berg^d, M. Dozono, N. Fukuda^c, T. Furuno^e, E. Ideguchi^f, N. Inabe^c, T. Kawabata^e, S. Kawase, K. Kisamori^c, T. Kubo^c, Y. Kubota^c, C.S. Lee, M. Matsushita, H. Miya, H. Nagakura, S. Ota, H. Sakai^c, S. Shimoura, A. Stolz^g, H. Suzuki^c, M. Takaki, H. Takeda^c, S. Takeuchi^c, H. Tokieda, T. Uesaka^c, K. Yako, Y. Yamaguchi, Y. Yanagisawa^c and Y. Yoshida^c

Center for Nuclear Study, Graduate School of Science, University of Tokyo

^aTokyo University of Science

^bRikkyo University

^cRIKEN Nishina Center

^dUniversity of Notre Dame

^eKyoto University

^fRCNP, Osaka University

^gNSCL, Michigan State University

The neutron number $N = 40$ is one of the regions of interest to understand nuclear structure. For instance, the proton number $Z = 28$ is magic and an energy gap at $N = 40$ between the pf shell and $vg_{9/2}$ makes $^{68}\text{Ni}_{40}$ a doubly magic nucleus. Actually, the Coulomb excitation measurement of ^{68}Ni indicates $N = 40$ neutron subshell closure in the ^{68}Ni [1, 2]. However, according to recent mass measurements in the neutron-rich Ni isotopes, the $N = 40$ shell closure is not evident when inferred from changes in the two neutron separation energies [3, 4]. The experimental information of $vg_{9/2}$ near $N = 40$ is essential for understanding the nuclear structure.

We performed an isomeric γ -ray spectroscopy of the neutron-rich near $N = 40$ at the RI Beam Factory (RIBF) of RIKEN Nishina Center. Neutron-rich nuclear isomers were produced by using projectile fragmentation reaction of 345 MeV/u ^{70}Zn beam bombarding a Be production target. The typical intensity of the primary beam was 75 pnA. The fragments were separated and identified in the BigRIPS, the High Resolution Beam Line (HR Beam Line), and the SHARAQ spectrometer on an event-by-event basis by measurements of A/Q and Z . The A/Q value was obtained from the time-of-flight (TOF) and magnetic rigidity ($B\rho$) measured in the second stage of the BigRIPS separator, the HR Beam Line and the SHARAQ (between F3 to S2 focal planes). The Z value was obtained from the energy loss (ΔE) measured in a silicon strip detector (SSD) at the final focal plane S2. The schematic view of the beam line is shown in Fig. 1 (a). The TOF was obtained by diamond detectors [5] between F3 and S2 focal planes. The $B\rho$ value was determined by position measurement using a parallel plate avalanche counter (PPAC) located at the dispersive focus position of the SHARAQ (S0). A detailed explanation of experimental setup is presented in [6].

The detector setup for the delayed γ -rays measurement at the downstream of S2 (S2+) are shown in Fig. 1 (b). The RI beam was implanted into a 20-mm-thick plastic scintillator. The γ -rays from implanted beam were detected by a γ -ray detector array, consisting of 2 HPGe clovers and 16 NaI(Tl)

detectors. The γ -rays data were acquired with single triggers from the HPGe or NaI(Tl) detectors, without beam trigger from the beamline data acquisition (DAQ). The data of γ -rays were correlated with the data of particle identified using a common timestamp, and were recorded without any hardware time window. Delayed γ -rays within < 5 msec from beam implantation were regarded as valid events since that time window is much shorter than the beam rate which was 2 kcps on an average at the most. The experimental setup in detail is found in [7].

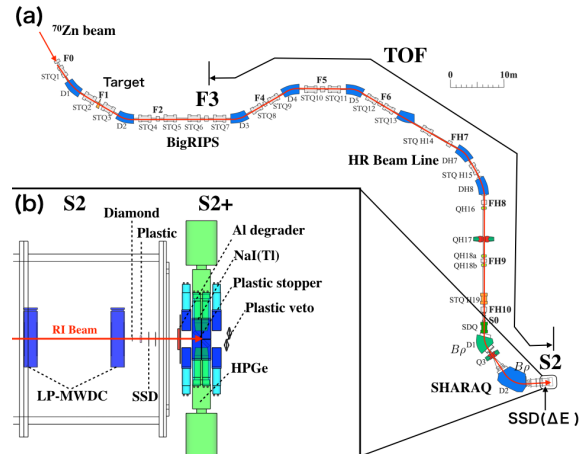


Figure 1: Schematic diagrams of the BigRIPS, the HR Beam line and the SHARAQ beam line (a), and the stopper and detector setups at S2+ (b).

Table 1 summarize six known nuclear isomers in the present experiment along with the γ -ray energies (E_γ) and the half-lives ($T_{1/2}$). The known isomers observed in the present work are consistent with the previous work.

We discovered two new isomers in very neutron-rich nuclei: $^{58}\text{Sc}_{37}$ and $^{61}\text{Ti}_{39}$ and obtained a wealth of spectroscopic information such as γ -ray energies, half-lives, and γ -ray relative intensities, and found a candidate of new isomer: $^{63}\text{Cr}_{39}$.

Figure 2 (a) and (c) show a delayed γ -ray energy spec-

Table 1: γ -ray energies and half-lives of previously known isomers observed in the present work.

Isomers	E_γ [keV]	$T_{1/2}$ [μ s]
$^{60}\text{V}^m$ [Ref. [8,9]]	99.6(1) $_{stat}$ (4) $_{sys}$ 103.7(2) $_{stat}$ (4) $_{sys}$	0.221(13)
$^{59}\text{Ti}^m$ [Ref. [9]]	108.9(4) $_{sys}$	0.572(19)
$^{56}\text{Sc}^m$ [Ref. [9,10]]	140.6(2) $_{stat}$ (4) $_{sys}$ 187.8(3) $_{stat}$ (4) $_{sys}$ 587.5(1) $_{stat}$ 728.0(4) $_{stat}$ (4) $_{sys}$	0.228(24)
$^{54}\text{Sc}^m$ [Ref. [9–11]]	110.6(4) $_{sys}$	2.82(9)
$^{50}\text{K}^m$ [Ref. [8,9]]	128.3(1) $_{stat}$ (4) $_{sys}$ 172.5(1) $_{stat}$ (4) $_{sys}$	0.132(9)
$^{43}\text{S}^m$ [Ref. [9,12]]	320.6(4) $_{sys}$	0.414(14)

Table 2: New isomers observed in the present work along with the γ -ray energies (E_γ), half-lives ($T_{1/2}$), and γ -ray relative intensities (I_γ).

Isomers	E_γ [keV]	$T_{1/2}$ [μ s]	I_γ (%)
$^{61}\text{Ti}^m$	576.1(3) $_{stat}$ (4) $_{sys}$ 125.2(4) $_{stat}$ (4) $_{sys}$	0.23(9) 0.32(13)	100 50(27)
$^{58}\text{Sc}^m$	580.9(2) $_{stat}$ (4) $_{sys}$ 412.3(5) $_{stat}$ (4) $_{sys}$ 247.0(20) $_{stat}$ (4) $_{sys}$ 180.5(4) $_{stat}$ (4) $_{sys}$	0.49(15) 0.86(50) 1.25(83) 0.58(20)	100 85(36) 26(19) 27(14)

trum obtained between 250 ns to 4000 ns after ^{58}Sc and ^{63}Cr beam implantation. Some peaks are present at energies of 180.5 keV, 247 keV, 412.3 keV and 580.9 keV in ^{58}Sc . Some candidates for peaks are present at energies of 121, 173, and 361 keV in ^{63}Cr , though the statistics are low.

Figure 2 (b) shows a delayed γ -ray energy spectrum obtained from ^{61}Ti beam. There are two peaks at 125.2 keV and 576.1 keV. Based on the systematics in neighboring nuclei, we propose that the observed isomer in $^{61}\text{Ti}_{39}$ is an $E2$ isomer and $M2$ isomer. The relative intensity suggests two isomeric γ -rays are mutually independent. The isomeric state of 125.2 keV is an $E2$ isomer with spherical structure, which is generated due to the small transition energy. The reduced $E2$ transition probability $B(E2)$ of the isomeric transition is 4.0 ± 1.6 W.u., consistent with spherical structure. The possibility of higher multiplicities is excluded, because the reduced transition probability significantly exceeds the recommended upper limits [13, 14]. The possibility of hindered $E1$ or $M1$ transition is also excluded, because such an isomeric state, which usually appears as a shape isomer, has not been observed in the neighboring isotopes. The isomeric state of 576.1 keV is an $M2$ isomer, which is generated due to the spin gap and transition energy. The reduced $M2$ transition probability $B(M2)$ of the isomeric transition is 0.14 ± 0.05 W.u.. It is suggested that a new isomeric γ -ray at 576.1 keV participate in $\nu g_{9/2}$ orbit.

The new isomers that we identified are summarized in Table 2.

In conclusion, two new isomers and a candidate of isomeric states in $^{58}_{21}\text{Sc}_{37}$, $^{61}_{22}\text{Ti}_{39}$, and $^{63}_{24}\text{Cr}_{39}$ were observed in very neutron-rich exotic nuclei near $N = 40$. The ex-

perimental results suggest ^{61}Ti isomeric state of 576.1 keV which is $M2$ isomer are caused by $\nu g_{9/2}$ orbit.

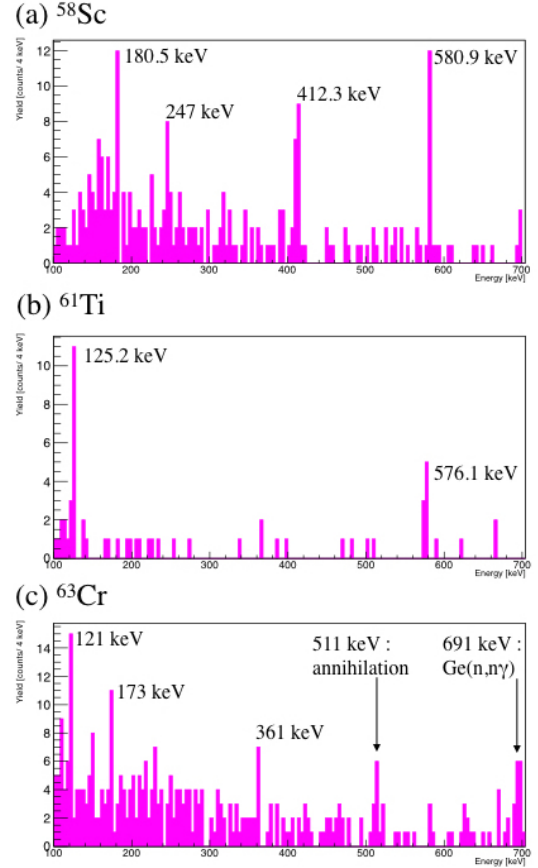


Figure 2: A delayed γ -ray energy spectrum obtained between 250 ns to 4000 ns after each beam implantation. (a) ^{58}Sc , (b) ^{61}Ti . (c) Some candidates for peaks are obtained between 250 ns to 4000 ns after ^{63}Cr beam implantation.

References

- [1] R. Broda *et al.*, Phys. Rev. Lett. **74**, 868 (1995).
- [2] M. Bernas, *et al.*, Phys. Lett. B **113**, 279 (1982).
- [3] C. Guenaut, *et al.*, Phys. Rev. C **75**, 044303 (2007).
- [4] S. Rahaman, *et al.*, Eur. Phys. J. A **34**, 5 (2007).
- [5] S. Michimasa *et al.*, Nucl. Instr. Meth. B **317**, 305 (2013).
- [6] M. Kobayashi *et al.*, CNS-REP-94 13 (2016).
- [7] Y. Kiyokawa *et al.*, CNS-REP-94 23 (2016).
- [8] J.M. Daugas *et al.*, Phys. Rev. C **81**, 034304 (2010).
- [9] D. Kameda *et al.*, Phys. Rev. C **86**, 054319 (2012).
- [10] H.L. Crawford *et al.*, Phys. Rev. C **82**, 014311 (2010).
- [11] R. Grzywacz *et al.*, Phys. Rev. Lett. **81**, 766 (1998).
- [12] F. Sarazin *et al.*, Phys. Rev. Lett. **84**, 5062 (2000).
- [13] P. M. Endt, At. Data Nucl. Data Tables **23**, 547 (1979).
- [14] P. M. Endt, At. Data Nucl. Data Tables **26**, 47 (1981).

New measurement of proton resonant elastic scattering from ^{34}Si

N. Kitamura, N. Imai, O. Beliuskina, Y. Kiyokawa, S. Masuoka, S. Michimasa, M. Kobayashi, S. Ota, P. Schrock, N. Shimizu, S. Shimoura, Y. Yamaguchi, K. Wimmer^a, Y. Ichikawa^b, H. Ueno^b, K. Yoneda^b, T. Teranishi^c, and Y. Utsuno^d

Center for Nuclear Study, Graduate School of Science, University of Tokyo

^aDepartment of Physics, University of Tokyo

^bRIKEN Nishina Center

^cDepartment of Physics, Kyushu University

^dAdvanced Science Research Center, Japan Atomic Energy Agency

In the framework of the shell model, the emergence of the so-called island of inversion can be attributed to the shell evolution caused by the monopole effect, which leads to shifts in the single-particle energies. However, the single-particle states around this region have not been well studied experimentally.

The most straightforward way to investigate the single-particle structure of unstable nuclei would be (d, p) one-neutron transfer reactions in inverse kinematics. The spectroscopic information is gained from the energies and angular distributions of the protons from the (d, p) reaction. In inverse kinematics, it should be noted that there are two conflicting requirements. On the one hand the thickness of the target needs to be limited to minimize the energy straggling, on the other hand thick targets increase the luminosity.

The same information can be obtained via isobaric analog resonances (IARs) observed by means of proton resonant elastic scattering since IARs have the same configuration as the parent states except for the isospin part [1]. The spectroscopic information, i.e., the resonance energies, spectroscopic factors, and orbital angular momenta, can be extracted by the R -matrix analysis. The thick target inverse kinematics method is applicable to obtain the excitation function.

We have already applied this method to the ^{35}Si nucleus located just outside the island of inversion. By measuring proton elastic scattering of ^{34}Si , eight resonances were observed in the highly excited states in ^{35}P . Six out of eight resonances are assigned as $T_{>}$ excitations, namely IARs of ^{35}Si , and the spectroscopic information was deduced by the R -matrix analysis [2]. Recently, a measurement of the single-particle states via the (d, p) reaction was reported by Burgunder *et al.* [3], and they presented different spectro-

Table 1: Excitation energies, J^π assignments and spectroscopic factors (SFs) of the observed single-particle states.

Imai <i>et al.</i> [2]			Burgunder <i>et al.</i> [3]		
E_x (keV)	J^π	SF	E_x (keV)	J^π	SF
0	$7/2^-$	0.63(16)	0	$7/2^-$	0.56(6)
803(18)	$3/2^+$	0.79(20)			
984(36)	$3/2^-$	1.37(32)	910(3)	$3/2^-$	0.69(10)
1444(44)	$1/2^+$	0.45(28)			
			2044(7)	$1/2^-$	0.73(10)
2093(12)	$5/2^+$	0.04(1)			
2194(15)	$3/2^-$	0.12(7)			

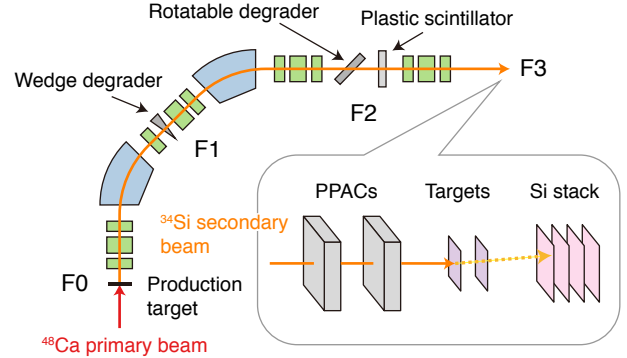


Figure 1: Schematic drawing of the experimental setup.

scopic factors from our values. Comparison of the spectroscopic factors is shown in Table 1. This disagreement motivated us to perform a new measurement with a modified experimental setup.

The experiment was performed at the RIKEN Projectile Fragment Separator (RIPS) facility. The experimental setup is shown in Figure 1. A primary ^{48}Ca beam was accelerated up to 63 MeV/u and impinged on a 1.25-mm thick beryllium production target. A secondary beam of ^{34}Si was produced with a typical purity of 30 % and an intensity of 40 kpps. The beam particles were identified event-by-event with the time difference between the radio-frequency signals provided by the accelerator and the timing measured by a thin plastic scintillator at the F2 focal plane (see Figure 2). The energy of the beam was tuned to 6 MeV/u using a carbon rotatable degrader placed at F2. The beam was tracked using two parallel plate avalanche counters (PPACs) at F3.

As reported in Reference [4], the reaction target was separated into two layers in order to discriminate between elastic scattering and possible contributions from inelastic scattering. This enables us to search for the inelastic channel $^{34}\text{Si}(p, p')^{34}\text{Si}(0_2^+)$. Two polyethylene targets were installed downstream of the PPACs. The thickness of each target was 90 μm . The protons emerging from the targets were detected downstream of the targets in a stack of silicon detectors, 0.1, 1.0, 1.5, and 1.5 mm thick. In order to increase the excitation energy window, the configuration was optimized with respect to the original experiment. The silicon detectors were tightly fixed to a water-cooled aluminium frame via heat-conductive insulators to improve the energy resolution.

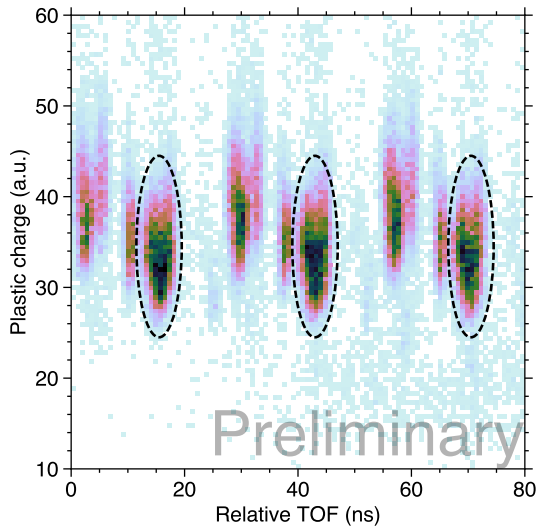


Figure 2: Particle identification of the ^{34}Si secondary beam. The vertical axis is proportional to the energy loss in the plastic scintillator.

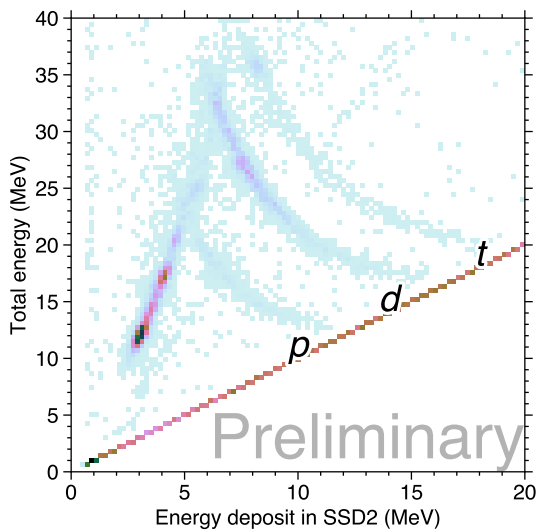


Figure 3: Correlation between the total energy and the energy deposit in the second layer of the silicon stack. Protons, deuterons and tritons are indicated beside the loci.

Though the intensity of the secondary beam was much lower than expected, the scattered protons were clearly identified (see Figure 3). Further analysis is in progress.

References

- [1] D. Robson, Phys. Rev. **137**, B535 (1965).
- [2] N. Imai *et al.*, Phys. Rev. C **85**, 034313 (2012).
- [3] G. Burgunder *et al.*, Phys. Rev. Lett. **112**, 042502 (2014).
- [4] N. Imai *et al.*, CNS Annual Report 2014, 3 (2016).

Role of hexadecapole deformation in the shape evolution of neutron-rich Nd isotopes

R. Yokoyama, E. Ideguchi^a, G. Simpson^b, Mn. Tanaka^a, S. Nishimura^c, P. Doornenbal^c, P.-A. Söderström^c, G. Lorusso^c, Z.Y. Xu^d, J. Wu^{c,e}, T. Sumikama^f, N. Aoi^a, H. Baba^c, F. Bello^g, F. Browne^{h,c}, R. Daidoⁱ, Y. Fangⁱ, N. Fukuda^c, G. Gey^{b,c,j}, S. Go, S. Inabe^c, T. Isobe^c, D. Kameda^c, K. Kobayashi^k, M. Kobayashi, T. Komatsubara^l, T. Kubo^c, I. Kuti^m, Z. Li^e, M. Matsushita, S. Michimasa, C.B. Moonⁿ, H. Nishibataⁱ, I. Nishizuka^f, A. Odaharaⁱ, Z. Patel^{c,o}, S. Rice^{c,o}, E. Sahin^g, L. Sinclair^{c,p}, H. Suzuki^c, H. Takeda^c, J. Taprogge^{q,r}, Zs. Vajta^m, H. Watanabe^s, and A. Yagiⁱ

Center for Nuclear Study, the University of Tokyo

^a*Research Center for Nuclear Physics, Osaka University*

^b*LPSC, UJF, INP Grenoble, CNRS/IN2P3*

^c*RIKEN Nishina Center*

^d*Department of Physics, the University of Tokyo*

^e*Department of Physics, Peking University*

^f*Department of Physics, Tohoku University*

^g*Department of Physics, University of Oslo*

^h*School of Computing Engineering and Mathematics, University of Brighton*

ⁱ*Department of Physics, Osaka University*

^j*JILL, Grenoble*

^k*Department of Physics, Rikkyo University*

^l*Department of Physics, University of Tsukuba*

^m*MTA Atomki*

ⁿ*Department of Display Engineering, Hoseo University*

^o*Department of Physics, University of Surrey*

^p*Department of Physics, University of York*

^q*Instituto de Estructura de la Materia, CSIC*

^r*Departamento de Física Teórica, Universidad Autónoma de Madrid*

^s*Department of Physics, Beihang University*

Atomic nuclei are finite quantum many-body systems consisting of two different kinds of nucleons, protons and neutrons. The existence of two degrees of freedom, proton and neutron numbers, is one of the features adding variety to the nuclear phenomena. The quantum effect in a many-body system yields shell structure. The shell effect is one another key feature driving wide variety of phenomena in atomic nuclei. Nuclear deformation is one of the phenomena driven mainly by shell effect. The nuclei at closed shell have spherical shape but as the number of particles in unfilled shell increase, nuclei break their symmetry spontaneously and get deformed even if they are in the space with spherical symmetry. Study of the nuclear deformation of unstable nuclei is important to understand how the shell effect drives macroscopic shape of nuclei to have different shapes at different proton or neutron numbers. Study of the shape evolution of unstable nuclei has often been focused on quadrupole deformation ($\lambda = 2$) and higher-order, such as hexadecapole ($\lambda = 4$) deformations have relatively little been studied. In certain regions of stable nuclei, however, large hexadecapole deformations have been observed. For example, $\beta_4 \sim 0.07$ was observed in ¹⁴⁸Nd [1]. If such higher-order deformation appears, it may change the nature

of single particle orbitals significantly. To date, there is little experimental data on hexadecapole deformation in unstable nuclei and it is largely unknown how the hexadecapole deformation of Nd evolves as neutron numbers increase.

In rare-earth nuclei around $Z = 60$, large prolate deformation is known to appear in $N \geq 90$ nuclei and many quasi-particle K isomers have been discovered. γ -ray spectroscopy of neutron-rich $Z \sim 60$ isotopes had been carried out by using thermal neutron induced fission of heavy nuclei [3]. The work revealed that there exists many K isomers in $Z = 60$ and 62 (Nd and Sm) isotopes. The existence of such K isomers indicates that those nuclei have a shape with stable axial symmetry so that the transitions with large ΔK are hindered to become isomers. More recently, K isomers are discovered in ¹⁶⁶Gd and ¹⁶⁴Sm [2] which is assumed to be neutron two quasi-particle excitation with the configuration of $v5/2[512] \otimes v7/2[633]$. According to their potential energy surface calculation, significantly non zero β_4 and β_6 values are required to reproduce the observed energy of the isomeric state. Theoretically, an FRDM [4] and an RMF [5] calculations predict even larger hexadecapole deformation in Nd than in Gd or Sm. It is expected that the large hexadecapole deformation in Nd changes the single

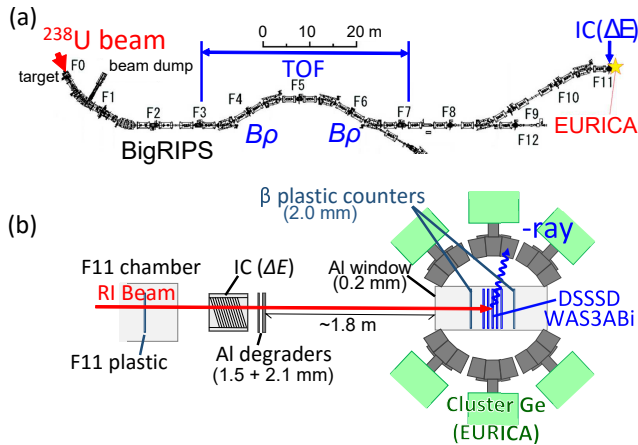


Figure 1: Schematic diagrams of the BigRIPS and ZeroDegree spectrometer beam line (a), and the stopper and detector setups at F11 (b). A passive stopper was installed in front of the WAS3ABi system only in the isomer runs.

particle orbitals significantly and it may be observed as the change of excitation energies of isomers.

We have performed isomer and β - γ spectroscopy on neutron-rich $Z \sim 60$ isotopes at the RI Beam Factory at RIKEN Nishina Center. By using in-flight fission of $345 \text{ MeV/u } ^{238}\text{U}$ beam at RIBF, it became possible for the first time, to produce such neutron-rich nuclei with high production rates. The primary ^{238}U beam bombarded 4-mm thick Be production target. The typical intensity of the primary beam was $\sim 7 \text{ pA}$. Fission fragments were separated and identified in the BigRIPS in-flight separator [6]. The particle identification was carried out by measuring the time-of-flight (TOF) and magnetic rigidity ($B\rho$) in the second stage of the BigRIPS and by measuring the energy loss (ΔE) in an ion chamber at the final focal plane, F11. The schematic view of the beam line is shown in Fig.1 (a). The TOF was obtained from the time difference between plastic scintillators at the F3 and F7 focal planes. The $B\rho$ value was obtained by the trajectory reconstruction from position and angular information measured by position-sensitive parallel plate avalanche counters (PPACs) at F3, F5 and F7. Detailed explanation of the particle identification at the BigRIPS is found in [7].

The measurement was conducted in two different stopper setups at F11. One was optimized for isomer spectroscopy by using a copper passive stopper in order to accept a wide range of nuclides with high implantation rates of $\sim 1 \text{ kHz}$. In the other setup, an active stopper WAS3ABi [8], which consists of five layers of Double-Sided-Silicon-Strip-Detectors (DSSSDs) with 40×60 strips, was used in order to measure β - γ events. In the latter setup, the total implantation rate of ions was limited up to $\sim 100 \text{ Hz}$.

The delayed γ rays from the implanted ions were detected by EURICA [9] array with 12-cluster Ge detectors. Each cluster consists of seven crystals that enable adding back Compton-scattered events in the neighboring crystals. The total detection efficiency of the array for photons of 1332 keV was 8.4%. The energies and timings of delayed γ rays were measured in a time window of $16 \mu\text{s}$ following the ion

implantation for isomer spectroscopy. The detector setup at the F11 focal plane is shown in Fig.1 (b).

Delayed γ -ray spectra of neutron-rich Nd isotopes, ^{158}Nd and ^{160}Nd were newly observed in this work. Preliminary spectra and γ -ray energies of those nuclei have already shown in [10]. From γ - γ coincidence analysis, all the observed γ rays are assigned in a single cascade from the isomer. The excitation energies of the isomers in ^{158}Nd and ^{160}Nd were assigned at 1648 and 1108 keV, respectively.

There are known $K^\pi = 4^-$ isomers above 1 MeV excitation in $N = 100$ rare-earth isotones [11–13]. The configurations of those isomers are generally assumed to be a neutron two quasi-particle excitation with $\nu 1/2[521] \otimes \nu 7/2[633]$. We expect that the isomer of ^{160}Nd has the same configuration. A Projected Shell Model calculation by Yang *et al.* predicts the $K^\pi = 4^-$ isomers at $\sim 1.2 \text{ MeV}$ in ^{160}Nd [14], which is very close to our result. They predict increase of the isomer energy by $\sim 100 \text{ keV}$ from ^{162}Sm to ^{160}Nd by employing larger hexadecapole deformation in neutron-rich Nd ($\beta_4 = 0.032$) than in Sm ($\beta_4 = 0.008$). Our result on ^{160}Nd , 1108 keV of the isomer energy, is also larger by $\sim 100 \text{ keV}$ than that of ^{162}Sm . This may indicate that the neutron-rich Nd isotope, ^{160}Nd , have large hexadecapole deformation. Details are under discussion for publication. The results of the new isomers by this work will give us further information on the higher-order deformation and single particle structures of neutron-rich rare-earth nuclei.

References

- [1] B. S. N. Singh *et al.*, J. Physics **61** (2003) 507.
- [2] Z. Patel *et al.*, Phys. Rev. Lett. **113** (2014) 262502.
- [3] G. S. Simpson *et al.*, Phys. Rev. C **80** (2009) 024304.
- [4] P. Möller *et al.*, At. Data Nucl. Data Tables **59** (1995) 185.
- [5] G. A. Lalazissis *et al.*, At. Data Nucl. Data Tables **71** (1999) 1.
- [6] T. Kubo *et al.*, NIM B **204** (2003) 97.
- [7] T. Ohnishi *et al.*, J. Phys. Soc. Jpn. **79** (2010) 073201.
- [8] S. Nishimura *et al.*, Nucl. Phys. News **22** (2012) No.3.
- [9] S. Nishimura *et al.*, RIKEN Accel. Prog. Rep. **46** (2013) 182.
- [10] Mn. Tanaka *et al.*, CNS Rep. **93** (2015) 27.
- [11] P. M. Walker *et al.*, Nucl. Phys. A **365** (1981) 61.
- [12] C. Y. Wu *et al.*, Phys. Rev. C **68** (2003) 044305.
- [13] S. Go *et al.*, RIKEN Accel. Prog. Rep. **46** (2013) 21.
- [14] Y. C. Yang *et al.*, J. Phys. G. Nucl. Part. Phys. **37** (2010) 085110.

Search for a double Gamow-Teller giant resonance in ^{48}Ti via heavy-ion double charge exchange (^{12}C , ^{12}Be) reaction

M. Takaki, T. Uesaka^a, S. Shimoura, N. Aoi^b, M. Dozono, T. Furuno^c, C. Iwamoto^b, T. Kawabata^c, M. Kobayashi, Y. Matsuda^d, M. Matsushita, S. Michimasa, S. Ota, M. Sasano^a, L. Stuhl^a, A. Tamii^b, M. Tsumura^c, R. Yokoyama, and J. Zenihiro^a

Center for Nuclear Study, Graduate School of Science, University of Tokyo

^a*RIKEN (The Institute of Physical and Chemical Research)*

^b*Research Center for Nuclear Physics, Osaka University*

^c*Department of Physics, Kyoto University*

^d*Department of Physics, Konan University*

A double Gamow-Teller resonance (DGTR) consists of two single Gamow-Teller resonances, which is induced by the spin-isospin operator $\sigma\tau\sigma\tau$. Our motivation of this study is to understand if the DGTRs are just superpositions of the single GTRs, or, the nuclear (spin-dependent) correlations cause further changes to the structure and responses of the DGT states. Another attractive topic of the DGT study is the relevance to $\beta\beta$ -decays [1]. The $2\nu\beta\beta$ -decay process is expressed by the spin-isospin operator, $\sigma\tau\sigma\tau$, which is equivalent to the DGT transition. In other words, the best studied DGT process is the $2\nu\beta\beta$ -decay. So far, 11 isotopes have been found to be the $2\nu\beta\beta$ -decay nuclei. The half-life of the decay is so long as 10^{19} - 10^{24} years [2]. This means that the DGT transition strength for $2\nu\beta\beta$ -decay is as small as 10^{-4} - 10^{-3} of the total DGT sum rule value [3]. The most of the DGT strength is considered to concentrate in the DGTR. Therefore, the observation of the missing DGT strength, especially its concentration states of DGTRs, will serve as another good calibrator of the nuclear structure calculation for $\beta\beta$ -decay processes.

The DGT study has a potential to open new research fields. However, the experimental access to the DGT states has been quite limited [4]. Partly because there is no suitable reaction probes for a DGTR search so far. Thus, a new probe of ($^{12}\text{C}, ^{12}\text{Be}(0_2^+)$) reaction was conceived on the basis of the result of our previous heavy-ion double charge exchange reaction $^{12}\text{C}(^{18}\text{O}, ^{18}\text{Ne})^{12}\text{Be}$ experiment [5]. In the experiment, the strong transition from the ground state of ^{12}C to the second 0^+ state of ^{12}Be was observed with a forward scattering angle peaking distribution of the cross section. The forward peaking distribution reflects the monopole ($\Delta L = 0$) transition. The reason is that all of the initial $^{12}\text{C}(0_{g.s.}^+)$, the intermediate $^{12}\text{B}(1_{g.s.}^+)$ and the final $^{12}\text{Be}(0_2^+)$ states are dominated by a $0h\omega$ configuration. Consequently, the strong DGT transition can occur. The reaction probe bears an additional advantage for the identification of the final state by detecting the delayed γ -rays emitted from the $^{12}\text{Be}(0_2^+)$ state. The $^{12}\text{Be}(0_2^+)$ state is the isomeric state which has the lifetime of 331 ns [6]. This long lifetime enables us to detect the delayed γ -rays downstream of a focal plane of a spectrometer. It eases experimental requirements because γ -rays backgrounds downstream of the spectrometer are considerably smaller than that at the target

position.

The experiment was performed at Research Center for Nuclear Physics, Osaka University. A 100 MeV/nucleon ^{12}C beam was directed to a enriched ^{48}Ca target with the areal density of 10.2 mg/cm^2 . The outgoing particles were momentum-analyzed using Grand Raiden (GR) spectrometer. The excitation energies of residual nuclei were measured utilizing a missing mass method. The outgoing ^{12}Be was implanted in a plastic scintillator stopper with a thickness of 8.4 mm placed 1-m downstream of the GR focal plane. For the event identification with the delayed γ -rays detection, the array consisted of 46 NaI(Tl) detectors surrounded the stopper scintillator.

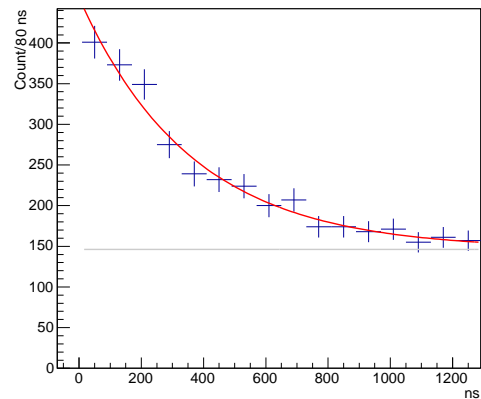


Figure 1: Detection timing spectrum of two 511-keV γ -rays in back-to-back geometry. The red curve shows the fitting result with a function of $A \exp(t/\tau) + B$. The gray line shows a continuous background level.

Figure 1 shows a timing spectrum of the NaI(Tl) detectors after the implantation of ^{12}Be into the plastic scintillator. The two 511 keV gamma rays which were detected within 10 ns in back-to-back geometry were selected. The red curve is the result of the fitting with a function of $A \exp(t/\tau) + B$, where τ and B denote the lifetime and a continuous background level, respectively. The measured lifetime is $\tau = 360 \pm 50.6 \text{ ns}$. This lifetime is consistent with the known lifetime of 331 ns within the error. The

continuous background level is shown with a gray line in the figure. The source of the continuous background was mainly due to an accidental coincidence with the β^+ decay of ^{11}C with the half-life of 20.4 minutes.

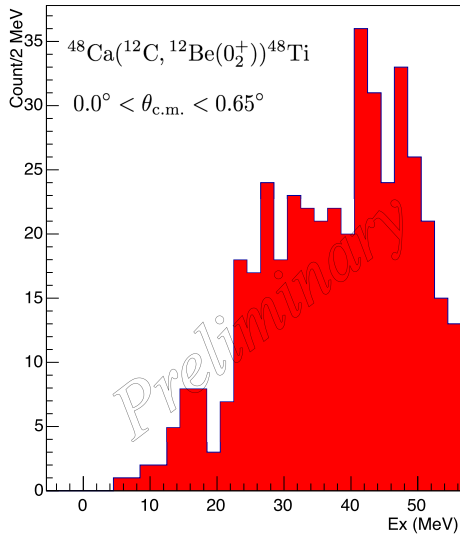


Figure 2: Preliminary result of the ^{48}Ti excitation energy spectrum at the most forward scattering angle of $\theta_{c.m.}$ smaller than 0.65° .

Figure 2 shows a preliminary result of a ^{48}Ti excitation energy spectrum at the scattering angle of $0.0^\circ < \theta_{c.m.} < 0.65^\circ$. In the spectrum, three bumps are found at the excitation energy of ~ 17 MeV, ~ 30 MeV and ~ 45 MeV. The peak at 17 MeV might be a double isobaric analog state, which was clearly observed at the excitation energy of 17.4 MeV in a pion-DCX experiment [7]. The other bumps are possibly DGTRs. In the energy region, no apparent structure found in the pion-DCX experiment. It should be noted that the spectrum contains accidental coincidences of ^{12}Be and the β^+ decay of ^{11}C , and continuum contributions. The further analysis is in progress.

In summary, we performed the experiment to search for the DGTRs in ^{48}Ti . To gain the capability of the observation of the DGTRs, a new heavy-ion double charge exchange reaction probe, $(^{12}\text{C}, ^{12}\text{Be}(0_2^+))$ reaction, was introduced for the first time and was applied on ^{48}Ca in the experiment. The decay timing spectrum demonstrates the feasibility of the $^{12}\text{Be}(0_2^+)$ identification by detecting the γ -rays downstream of the focal plane. Some structures can be seen in the preliminary excitation energy spectrum of ^{48}Ti . Although we can not discuss natures of the structures in detail at present, a comparison with the pion-DCX data indicates that they are possibly the DGTRs.

References

- [1] J. Suhonen and O. Civitarese, *Physics Reports* **300**, 123 (1998).
- [2] For example, F. Avignone, S. Elliott and J. Engel, *Re-*

views of Modern Physics **80**, 481 (2008).

- [3] N. Auerbach, L. Zamick and D.C. Zheng, *Annals of Physics* **192**, 77 (1989).
- [4] J. Blomgren *et al.*, *Phys. Lett. B* **362**, 34 (1995).
- [5] M. Takaki *et al.*, *JPS Conf. Proc.* **6**, 020038 (2015).
- [6] S. Shimoura *et al.*, *Phys. Lett. B* **560**, 31 (2003); *ibid* **654**, 87 (2007).
- [7] M. Kaletka *et al.*, *Phys. Lett. B* **199**, 336 (1987).

Measurement of Deuteron Inelastic Scattering on $^{15,16}\text{O}$ in inverse kinematics using CNS Active Target

H. Tokieda^a, S. Ota^a, M. Dozono^a, M. Itoh^b, C. S. Lee^{a,c}, S. Michimasa^a, M. Kobayashi^a, N. Imai^a, T. Uesaka^c, Y. Kiyokawa^a, Y. Nasu^b, K. Yako^a, J. Zenihiro^c, and E. Takada^d

^aCenter for Nuclear Study, Graduate School of Science, University of Tokyo

^bCyclotron and Radioisotope Center, Tohoku University

^cNishina Center RIKEN (The Institute of Physical and Chemical Research)

^dNational Institute of Radiological Sciences

Alpha clustering is very important for understanding the structure of light nuclei. Several predictions of alpha cluster structures have been reported on $N = 4n$ nuclei such as ^8Be , ^{12}C , ^{16}O , and ^{20}Ne [1–3]. As an example of $N = 4n - 1$ nuclei, the ^{11}B nucleus was reported to have $2\alpha + ^3\text{H}$ cluster structure in excited states [4]. Alpha cluster structure states are characterized by strong isoscalar monopole transitions. In order to clarify alpha cluster structure in excited states, it is important to measure forward inelastic scatterings because of forward peaking nature in $L = 0$ excitations.

We are developing the gaseous active target system called CNS Active Target (CAT) to measure the low-energy recoiled particles corresponding to the forward angle scattering, especially, up to 10 degrees in center-of-mass frame. The CAT consists of a time projection chamber (TPC) and Si detectors surrounding the field cage of TPC. The TPC was operated with 0.4-atm pure deuterium gas. As an electron multiplier of the CAT, 400- μm thick Gas Electron Multipliers are employed.

In 2015, we performed the experiment in Oxygen isotopes $^{15,16}\text{O}$ in Heavy Ion Medical Accelerator in Chiba (HIMAC). In this paper, we report the measurement of the deuteron inelastic scattering (d, d') on $^{15,16}\text{O}$ nuclei at 100 MeV/u in inverse kinematics.

The primary ^{16}O beam at 180 MeV/u bombarded 7-mm thick Be target and the secondary $^{15,16}\text{O}$ beams at 100 MeV/u were selected and decelerated using 7-mm thick Al energy-degrader. Figures 1 and 2 show the experimental setup at F1 and F3 focal plane of SB2 course and photograph of experimental setup around F3 focal plane, respectively, in HIMAC.

Particle identification of the secondary beam was performed on the event-by-event basis by using TOF- ΔE method. The time of flight (TOF) from F1 to F3 focal plane was measured by using two plastic scintillators located at F1 and F3 respectively. The energy loss (ΔE) was measured with a plastic scintillator at F1 focal plane. Figure 3(a) and

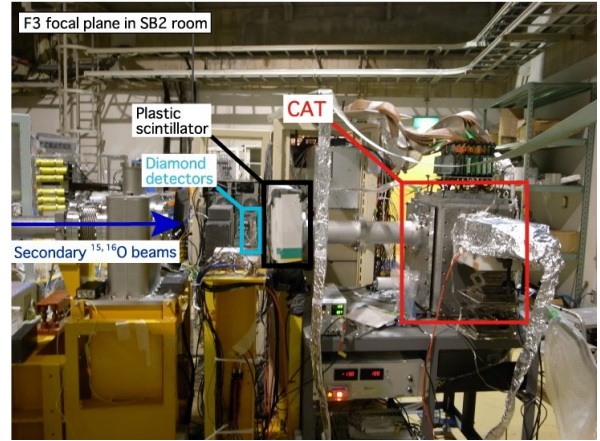


Figure 2: Photograph of experimental setup around F3 focal plane of SB2 course in HIMAC.

(b) display the particle identification plots for ^{15}O and ^{16}O beams, respectively. The size of the secondary beam measured by CAT was less than 20 mm in diameter. The beam intensities of ^{15}O and ^{16}O at F3 focal plane were approximately 580k-ppp and 1.5M-ppp, respectively.

The typical hit pattern in the readout pad is displayed in Fig. 4. Readout pads of CAT are of regular triangular shape with 5-mm and 10-mm side and total number of pads is 400. Color code shows the number of hits, which are determined by rising and falling thresholds of pulse height, in each pad. The hits corresponding to beam particles are found in the region of X position of -20 to 20 mm and the continuous hits in the side region is seen, which seems the trajectory of the recoil particle.

The analysis is in progress.

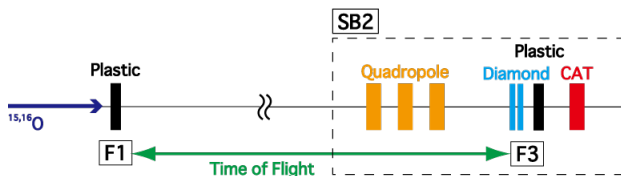


Figure 1: Experimental setup at F1 and F3 focal plane of SB2 course in HIMAC.

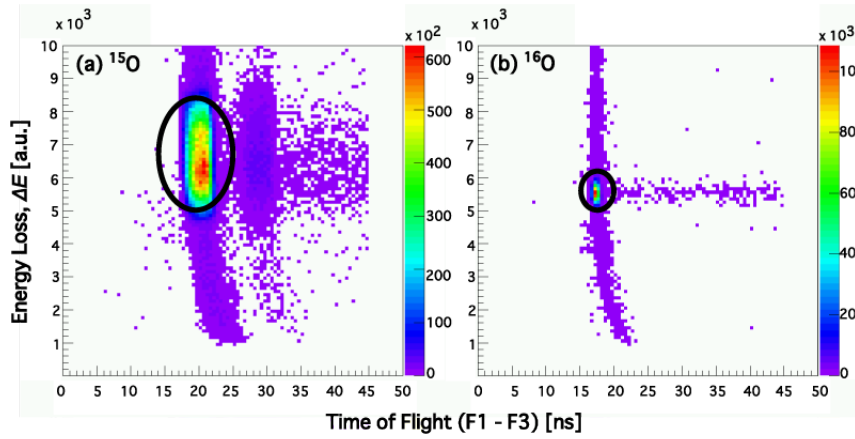


Figure 3: Particle identification plots for the secondary (a) ^{15}O beam and (b) ^{16}O beam.

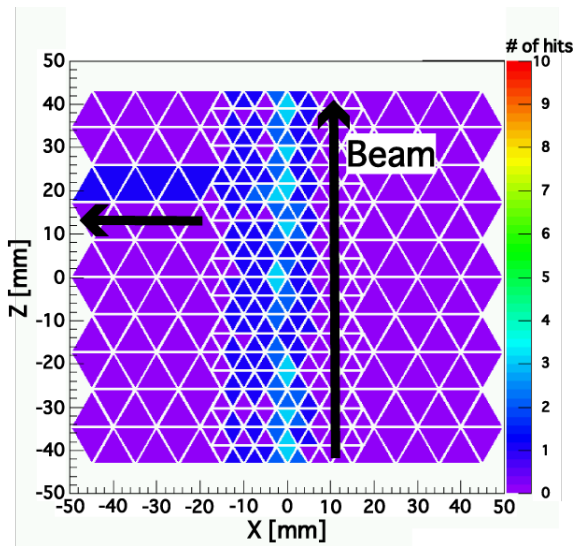


Figure 4: Event display of the hit pattern on TPC.

References

- [1] K. Ikeda et al., Prog. Theor. Phys. Suppl. 68, 1 (1986).
- [2] H. Horiuchi et al., Prog. Theor. Phys. Suppl. 192, 1 (2012).
- [3] M. Freer, Rep. Prog. Phys. 70, 2149 (2007).
- [4] T. Kawabata et al., Phys. Lett. B646 (2007) 6-11

First Determination of the $^{30}\text{S}(\alpha, p)$ Thermonuclear Reaction Rate from Experimental Level Structure of ^{34}Ar

D. Kahl, A. A. Chen^a, S. Kubono, H. Yamaguchi, D. N. Binh, J. Chen^a, S. Cherubini^b, N. N. Duy^c, T. Hashimoto, S. Hayakawa, N. Iwasa^d, H. S. Jung^e, S. Kato^f, Y. K. Kwon^e, S. Michimasa, S. Nishimura^g, S. Ota, K. Setoodehnia^a, T. Teranishi^h, H. Tokieda, T. Yamada^d, C. C. Yun^e, and L. Y. Zhangⁱ

Center for Nuclear Study, Graduate School of Science, University of Tokyo, Japan

^a*Department of Physics & Astronomy, McMaster University, Canada*

^b*Department of Physics, University of Catania & INFN-LNS, Italy*

^c*Institute of Physics, Vietnam*

^d*Department of Physics, Tohoku University, Japan*

^e*Department of Physics, Chung-Ang University, Korea*

^f*Department of Physics, Yamagata University, Japan*

^g*RIKEN (The Institute of Physical and Chemical Research), Japan*

^h*Department of Physics, Kyushu University, Japan*

ⁱ*Institute of Modern Physics, Chinese Academy of Sciences, China*

1. Introduction

Type I x-ray bursts (XRBs) are characterized by the explosive burning of hydrogen and helium on an accreting neutron star in a binary system. Such a neutron star accretes fresh material from a low-mass companion, which builds up as an electron-degenerate envelope on its surface. Thermal instabilities and nuclear reaction rates that depend exponentially on energy eventually lead to a thermonuclear runaway, which is ultimately observed as an increase in photon emission by factors of 10^{1-3} , peaked in the x-ray, for ten to a hundred seconds. These x-ray bursters exhibit periodic behavior, with outbursts separated on typical timescales on the order of hours to days. The nuclear trajectory spans from the proton up to at least neutron-deficient isotopes in the Sn-Sb-Te region, including hundreds of species linked by a large array of reactions, captures, decays, and photodisintegrations. Yet, models show that the burst structure is controlled by a much smaller subset of these, and the $^{30}\text{S}(\alpha, p)$ reaction is identified as contributing significantly to the energy generation [1], timescale [2], and ash composition [3] of x-ray bursts. Unfortunately, very little is known experimentally about the $^{30}\text{S}(\alpha, p)$ cross section nor the compound nucleus ^{34}Ar above the α -threshold,

2. Experimental Method

We performed an experiment measuring ^{30}S alpha resonant elastic scattering at the Center for Nuclear Study low-energy radioactive ion beam separator facility (CRIB) [5]. The ^{30}S beam was produced with a typical purity of 28%, an intensity of 8×10^3 pps, and separated at 4.0 MeV/u [6]. We injected 1.6×10^9 ^{30}S ions during the main measurement over 2 days into an active target system filled with He+CO₂ gas [7]. Succinctly, the experimental setup enabled us to uniquely identify and track incoming ^{30}S ions, as well as the scattering angle, energy loss, and residual energy of scattered alpha particles.

3. Results

We determined the center-of-mass energy event-by-event for scattered alpha particles to produce the $^{30}\text{S}+\alpha$ spectrum. The center-of-mass excitation function is defined as

$$\frac{d\sigma}{d\Omega} = \frac{Y_\alpha S(E_{\text{beam}})}{I_{\text{beam}} n \Delta E \Delta \Omega} \frac{m_\alpha}{m_\alpha + m_{^{30}\text{S}}}, \quad (1)$$

where Y_α is the yield of alpha particles at each energy bin, $S(E_{\text{beam}})$ is the stopping power of He+CO₂ for ^{30}S , I_{beam} is the number of ^{30}S ions injected, n is the number density of ^4He in the active target, ΔE is the energy bin size, $\Delta \Omega$ is the solid angle at a given energy bin, and m_α & $m_{^{30}\text{S}}$ are the mass of ^4He & ^{30}S , respectively.

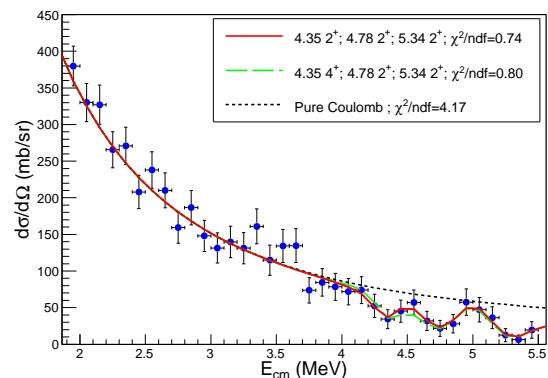


Figure 1: Excitation function for $^{30}\text{S}+\alpha$ elastic scattering, along with R-Matrix fits. The bumps seen near 3.5 MeV correspond to a region of strong background of α particles in the cocktail beam and optically selected by CRIB. Vertical errors are statistical, and horizontal errors are based on the energy resolution.

To extract the resonance energy E_r , spin-parity J^π , alpha partial width Γ_α , and proton partial width Γ_p we performed

Table 1: Resonances found in the present work.

E_r	E_{ex}	ℓ_α	J^π	Γ_α	Γ_p	θ_α^2
(MeV)	(MeV)			(keV)	(keV)	%
4.35	11.09	2, 4	(2 ⁺ , 4 ⁺)	20	25	40
4.78	11.52	2	2 ⁺	100	210	90
5.34	12.08	2	(2 ⁺)	260	340	99

Table 2: Resonance parameters of ^{34}Ar adopted in the calculation of the $^{30}\text{S}(\alpha, p)$ stellar reaction rate calculation. Parameters shown in boldface are based on experimental data. See the text.

E_r (MeV)	J^π	Γ_α (keV)	$\omega\gamma$ (keV)
0.73	0 ⁺	2×10^{-15}	2×10^{-15}
1.14	0 ⁺	2×10^{-9}	2×10^{-9}
1.22	0 ⁺	1×10^{-8}	1×10^{-8}
1.41	0 ⁺	4×10^{-7}	4×10^{-7}
1.56	0 ⁺	4×10^{-6}	4×10^{-6}
1.81	0 ⁺	1×10^{-4}	1×10^{-4}
2.0	0 ⁺	7×10^{-4}	7×10^{-4}
2.15	0 ⁺	3×10^{-3}	3×10^{-3}
2.25	0 ⁺	7×10^{-3}	7×10^{-3}
2.68	0 ⁺	0.1	0.1
3.01	0 ⁺	0.7	0.7
3.58	0 ⁺	7	7
4.07	0 ⁺	30	30
4.35	2⁺	20	100
4.78	2⁺	100	500
5.34	2⁺	260	1300

a multi-channel, multi-level R-Matrix fit with the SAMMY8 code [8]. A particular feature of our fitting routine – which quantified the best fit with the reduced chi-square χ^2_ν – was that we always calculated the channel widths based on the Wigner limit $\Gamma_{w_i} = \frac{2\hbar^2}{\mu_i R_i^2} P_{\ell_i}$ where μ is the channel reduced mass, $R = 1.45(A_1^{1/3} + A_2^{1/3})$ fm is the parameterized channel radius, and P_ℓ is the channel penetrability, respectively, for channel i . Specifically, we calculated and varied the dimensionless reduced partial width $\theta_i^2 = \Gamma_i/\Gamma_{w_i}$ such that the widths could be more reasonably co-varied appropriately with changes in the resonance energies and spin-parities. However, that is not to say that the widths so-determined are model dependent on the precise details of the Wigner limit formulation, but to emphasize that a reasonable range of physically allowed widths could be easily and fully explored from $1\% \leq \theta_i^2 \leq 99\%$, as the allowed widths can drastically increase with low ℓ_α and/or large E_r . The two best fits are shown in Fig. 1, and the resonance parameters are shown in Tab. 1.

To make an evaluation of the stellar reaction rate in XRBs, we should also consider the result of a $^{36}\text{Ar}(p, t)^{34}\text{Ar}$ measurement [4]. However, the results from the RCNP spectroscopic study only provides us with preliminary resonance energies, and some assumptions are required before we may apply them. We naïvely assumed that each state has $J^\pi = 0^+$. As for the partial widths, based on the present

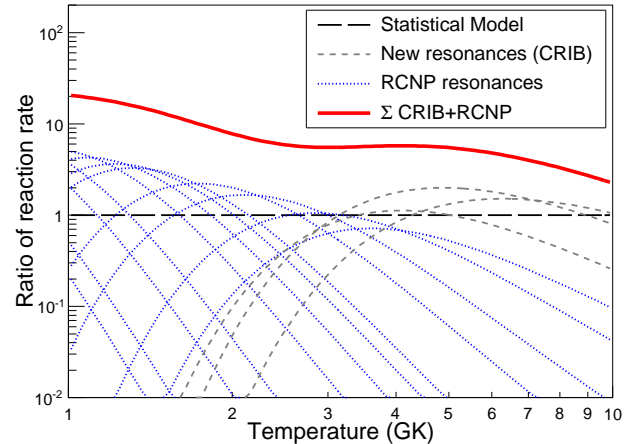


Figure 2: Calculations of the $^{30}\text{S}(\alpha, p)$ stellar reaction rate. The statistical model (SM) rate from NON-SMOKER [9] is shown as the long-dashed black line, to which all the rates are normalized. The dashed grey lines represent our new higher-energy resonances observed at CRIB with our best-fit quantum properties. The dotted (blue) lines represent the thirteen resonances from the $^{36}\text{Ar}(p, t)$ RCNP experiment. The sum of these individual resonant contributions is shown as the thick solid (red) line.

results and the similar level density between the two studies, we set $\Gamma_\alpha = \frac{1}{2}W_{\Gamma_\alpha}$. The resonance parameters adopted in the present work are shown in Tab. 2. A calculation of the $^{30}\text{S}(\alpha, p)$ reaction rate is shown in Fig 2. Further details will be given in Ref. [10].

References

- [1] A. Parikh, J. José, F. Moreno, and C. Iliadis, *Astrophys. J. Supp.* **178** (2008) 110.
- [2] J. L. Fisker, F.-K. Thielemann, and M. Wiescher, *Astrophys. J.* **608** (2004) L61.
- [3] H. Schatz and K. E. Rehm, *Nucl. Phys. A* **777** (2006) 601 (2006).
- [4] S. O'Brien, *et al.*, *AIP Conf. Proc.* **1090** (2009) 288.
- [5] Y. Yanagisawa, *et al.*, *Nucl. Instrum. Methods in Phys. Res., Sect. A* **539** (2005) 74.
- [6] D. Kahl, *et al.*, *AIP Conf. Proc.* **1213** (2010) 208.
- [7] D. Kahl, *et al.*, *AIP Conf. Proc.* **1594** (2014) 163.
- [8] N. Larson, (2000), ORNL/TM-9179/R5 (Unpublished).
- [9] T. Rauscher and F.-K. Thielemann, *Atom. Dat. and Nuc. Dat. Tab.* **79** (2001) 47.
- [10] D. Kahl *et al.*: *Phys. Rev. C* (submitted).

Time-of-flight mass measurements of neutron-rich Ca isotopes beyond $N = 34$

M. Kobayashi, S. Michimasa, Y. Kiyokawa, H. Baba^a, G.P.A. Berg^b, M. Dozono, N. Fukuda^a, T. Furuno^c, E. Ideguchi^d, N. Inabe^a, T. Kawabata^c, S. Kawase, K. Kisamori, K. Kobayashi^e, T. Kubo^a, Y. Kubota, C.S. Lee, M. Matsushita, H. Miya, A. Mizukami^f, H. Nagakura^e, D. Nishimura^f, H. Oikawa^f, S. Ota, H. Sakai^a, S. Shimoura, A. Stolz^g, H. Suzuki^a, M. Takaki, H. Takeda^a, S. Takeuchi^a, H. Tokieda, T. Uesaka^a, K. Yako, Y. Yamaguchi^e, Y. Yanagisawa^a, R. Yokoyama, and K. Yoshida^a

Center for Nuclear Study, Graduate School of Science, University of Tokyo

^aRIKEN Nishina Center

^bJINA and the Department of Physics, University of Notre Dame

^cDepartment of Physics, Kyoto University

^dResearch Center for Nuclear Physics, Osaka University

^eDepartment of Physics, Rikkyo University

^fDepartment of Physics, Tokyo University of Science

^gNational Superconducting Cyclotron Laboratory, Michigan State University

1. Introduction

The mass of the atomic nucleus is one of the crucial quantities in investigating nuclear structure properties such as shell closures and new magic numbers. In particular, the shell evolution in neutron-rich calcium isotopes has attracted much attention, and the new magic numbers of $N = 32$ and 34 have been proposed theoretically [1]. Recently, the subshell closure at $N = 32$ was established by high-precision mass measurements of ^{53}Ca and ^{54}Ca at ISOLDE [2]. Subsequently, the existence of an $N = 34$ subshell closure in ^{54}Ca was suggested by the measurement of the first 2^+ state energy in ^{54}Ca at RIKEN [3]. For establishment of the closed-shell nature of ^{54}Ca , mass data of the Ca isotopes beyond $N = 34$ are essential. The present work aims at studying the nuclear shell evolution at $N = 32$ and 34 by direct mass measurements of neutron-rich nuclei in the vicinity of ^{54}Ca , such as ^{55}Ca and ^{56}Ca .

2. Experiment

We performed the nuclear mass measurement at the RIKEN RI Beam Factory using the SHARAQ spectrometer. Masses were measured directly by the time-of-flight-magnetic-rigidity (TOF- $B\rho$) technique. The TOF- $B\rho$ mass spectrometry can access the short-lived nuclei far from stability owing to its short measurement time, which is on the order of $1 \mu\text{s}$. Furthermore, it has an advantage that masses of a large number of isotopes can be measured at once. In the present experiment, we installed diamond detectors [4] at the focal planes F3 and S2 for the TOF measurement, low-pressure multi-wire drift chambers (LP-MWDCs) [5] at both F3 and S2 to obtain the tracking information, and a parallel plate avalanche counter (PPAC) at the dispersive focus S0, which is the target position of SHARAQ, for the $B\rho$ measurement. The experimental setup is presented in detail in last year's report by Kobayashi *et al.* [6].

3. Analysis

Here, current status of the data analysis is described. We evaluated the timing measurement performance of the diamond detector. Figure 1 shows the time difference between both edges in a strip of the diamond detector for Ca isotopes after the correction for position dependence. The time resolution of the diamond detector including that of the measurement system was estimated to be 11 ps (σ) at an energy deposit of around 100 MeV . The time resolution is dramatically improved from the previous measurement with a 32-MeV α beam [4] because of much higher energy deposit.

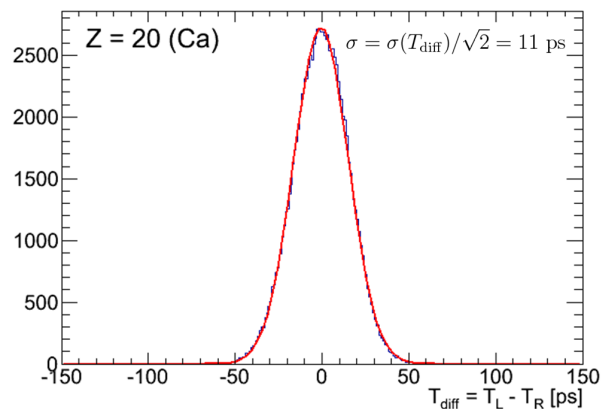


Figure 1: Time difference between both edges in a strip of the diamond detector for Ca isotopes. Position dependence of the time difference has been corrected.

The mass to charge ratio (m/q) is reconstructed by the beam positions and angles at the focal planes F3, S0, and S2 from the beam tracking with up to the fourth-order aberrations. The m/q values are calibrated by using the reference nuclei, $^{53,54}\text{Ca}$, $^{49,51,52}\text{K}$, $^{46,47}\text{Ar}$, $^{43-46}\text{Cl}$, $^{41,42}\text{S}$, $^{39-42}\text{P}$, and ^{38}Si . These reference nuclei have literature mass uncertain-

ties of < 300 keV and have no isomeric states. All of the mass values except for $^{53,54}\text{Ca}$ and ^{52}K are taken from the latest Atomic Mass Evaluation (AME2012) [7], and recent experimental data for $^{53,54}\text{Ca}$ [2] and ^{52}K [8] are also employed. The following polynomial is used as a fitting function:

$$\frac{m}{q} = \sum_{j_0+\dots+j_9 \leq 4} k_j \cdot t^{j_0} x_3^{j_1} a_3^{j_2} y_3^{j_3} b_3^{j_4} x_0^{j_5} x_2^{j_6} a_2^{j_7} y_2^{j_8} b_2^{j_9}, \quad (1)$$

where m/q is the mass-to-charge ratio, t is the TOF value, $x_{3(2)}$, $y_{3(2)}$, $a_{3(2)}$, and $b_{3(2)}$ are the position and angle at F3(S2), x_0 is the position at S0, which is related to the $B\rho$ value, and $k_j \equiv k_{(j_0, \dots, j_9)}$ are the fitting parameters. The fitting parameters are determined by performing the least-square method to the events for the reference nuclei. Using the determined parameters consistent with the calibration, we deduce the mass values of the nuclei of interest.

4. Results

The relative mass resolution of $\sim 1/10000$ (σ) has been achieved for $Z \sim 20$ nuclei. Figure 2 shows the spectrum of the deduced mass-to-charge ratio (A/Q) without any limitation on the proton number Z , and Fig. 3 shows differences of the deduced atomic masses to the literature values for the calibration nuclei. The systematic error σ_{sys} was evaluated to be $\sigma_{\text{sys}} = 110$ keV from the standard deviation of the mass differences for the calibration nuclei. It is noted that even the mass of ^{57}Ca ($A/Z = 2.8$) can be deduced by interpolation because ^{40}Si ($A/Z = 2.857$) is included in the reference nuclei. This allows us to determine the mass of ^{57}Ca more reliably. The total yield of ^{55}Ca , which is one of the target nuclei, is several thousands, and the statistical uncertainty for ^{55}Ca is $\sigma_{\text{stat}} \sim 100$ keV. It is expected that the masses of ^{55}Ca and ^{56}Ca can be deduced with precisions of a few hundred keV. Further analysis is in progress.

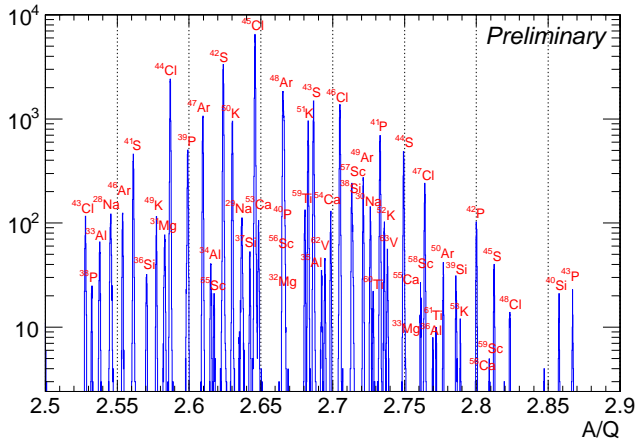


Figure 2: Deduced A/Q spectrum. No gate on the proton number Z is applied in this figure.

References

- [1] T. Otsuka *et al.*, Phys. Rev. Lett. **87**, 082502 (2001).
- [2] F. Wienholtz *et al.*, Nature **498**, 349 (2013).

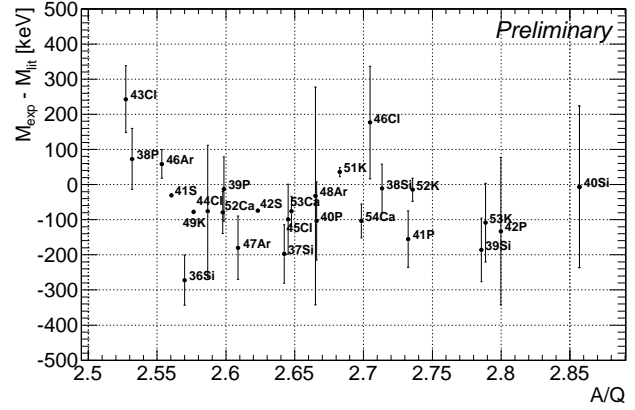


Figure 3: Differences between the masses deduced from the present experiment and the literature values for the reference nuclei used for calibration as a function of A/Q . The error bar denotes the literature uncertainty.

- [3] D. Steppenbeck *et al.*, Nature **502**, 207 (2013).
- [4] S. Michimasa, Nucl. Instr. Meth. B **317**, 305 (2013).
- [5] H. Miya *et al.*, Nucl. Instr. Meth. B **317**, 317 (2013).
- [6] M. Kobayashi *et al.*, CNS-REP-94 13 (2016).
- [7] G. Audi *et al.*, Chinese Physics C **36**, 1287 (2012).
- [8] M. Rosenbusch *et al.*, Phys. Rev. Lett. **114**, 202501 (2015).

Feasibility study of mass production of $^{178m2}\text{Hf}$

N. Kitamura, N. Imai, Y. Yamaguchi, S. Mishimasa, and H. Haba^a

Center for Nuclear Study, Graduate School of Science, University of Tokyo

^aRIKEN Nishina Center

Since the discovery of superdeformation in the nucleus, many superdeformed states have been observed [1]. As further deformed state, hyperdeformation in which the ratio of the long axis to the short axis is 3:1 has been predicted as the extreme quadrupole deformation [2]. However, no such state had been discovered yet. Furthermore, recent theoretical calculation predicts that even deformed torus shape appears at a high spin state [3]. Such deformed state will provide us a stringent test of our understanding on the nuclear physics. The key to produce such states is transferring high angular momentum to the nucleus. If high spin target or high spin beam is available, it would be more probable to populate such an exotic state.

We are developing to make a target of $^{178m2}\text{Hf}$, which has a high spin of 16^+ and a long half-life of 31 years. Among several reactions, the $^{176}\text{Yb}(\alpha,2n)$ reaction is known to have the largest cross section to produce the $^{178m2}\text{Hf}$ [4]. The pioneering work of the mass production of $^{178m2}\text{Hf}$ state was performed at Dubna [5]. The isomeric state was produced by the fusion reaction of $(\alpha,2n)$ with an enriched $^{176}\text{YbO}_2$ target. The cross section was reported to be about 5 mb. The AVF cyclotron at RIBF can provide us 40 MeV α beam of 10 μA , which are enough to make a nano-gram sample of $^{178m2}\text{Hf}$ with a MT of a few days.

Based on the above idea, we performed the feasibility study for production. There are three issues to be checked. First one is measurement of the excitation function of the production cross section of $^{178m2}\text{Hf}$ to optimize the incident beam energy. Second is production cross section of $^{175,172}\text{Hf}$, which will be main contaminant after the irradiation. They have relatively short half-lives, 70 days and 1.87 years, respectively, so that radioactivity of these nuclei will be much larger than that of $^{178m2}\text{Hf}$ when we use the natural Yb target. Production cross section of these nuclei will determine the degree of the enrichment of ^{176}Yb . The third point is the heat damage on the Yb target. The melting point of Yb is about 818 degrees Celsius so that it is not obvious that the target can stand the high intensity α beam.

Experiment was performed at the C03 beam line of the AVF cyclotron. An α beam of 10 MeV/nucleon was directed onto targets. The targets were a stack of ten ^{nat}Yb targets. Thickness of each target was about 20 μm . The target was placed on the water-cooled Ta Faraday Cup, which measured the total beam intensity of the beam. In addition, He gas was flown on the surface of the target to take the heat away. The stack of Yb targets was sandwiched by two 1 μm thick Ti targets to check the energy of α beam by using the monitor reaction $^{nat}\text{Ti}(\alpha,X)^{51}\text{Cr}$. The target was irradiated for eight hours, which was determined by considering the license to handle ^{175}Hf at the AVF cyclotron.

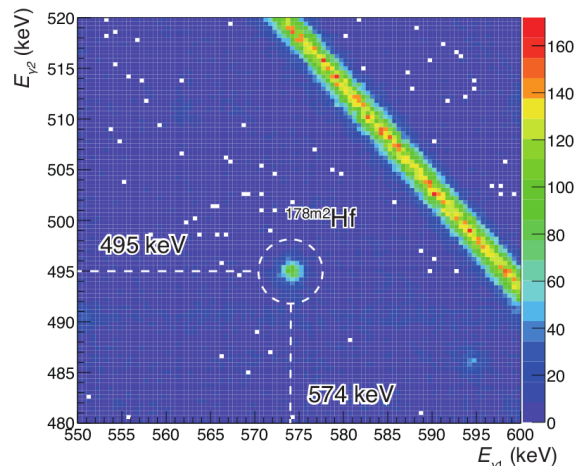


Figure 1: Energy correlation of γ - γ measurement with the ^{nat}Yb target after irradiation of α beam. Two γ rays of 574 and 495 keV were clearly observed as a cascade transition.

When we opened the chamber and checked the target after cooling of 3 days, it turned out that the first nine targets, one Ti and eight Yb were adhered. On the other hand, the last two, one Yb and one Ti, targets could be separated. This indicates that as long as the targets are attached tightly to the water-cooled FC, they can stand the 10 μA beams.

The γ rays from the target were measured with EUroball-RIKEN Cluster Array, EURICA, [6] to determine the radioactivity produced. The γ - γ coincidence measurement clearly demonstrated the 574 and 495 keV γ rays related to $^{178m2}\text{Hf}$ as presented in Fig. 1. Considering the beam dose and the natural abundance of ^{176}Yb , the cross section of $^{176}\text{Yb}(\alpha,2n)^{178m2}\text{Hf}$ was deduced to be 5.1(4) mb at 33.3 MeV. The present value is compared with the result of Ref. [5] as demonstrated by Fig. 2, indicating that the present result is consistent with their values. We evaluated the production cross sections of $^{172,173,175}\text{Hf}$, as well, which are important to determine the enrichment of $^{178m2}\text{Hf}$. The monitor reaction $^{nat}\text{Ti}(\alpha,X)^{51}\text{Cr}$ was confirmed to be consistent with the cross section recommended by IAEA [7]. The production cross sections of $^{172,173,175}\text{Hf}$ were compared with the calculations using a fusion evaporation code PACE4 [8]. All the cross sections were found to be consistent with the calculations.

We also performed the chemical separation of Hf isotope from the Yb target. The procedure is slightly different from the one adopted at Ref. [5], because our production target was Yb and not Yb_2O_3 which was used at Ref. [5]. First of all, the Yb target after irradiation of α beam was dissolved with 3 mL of HCl with a few drops of H_2O_2 . We

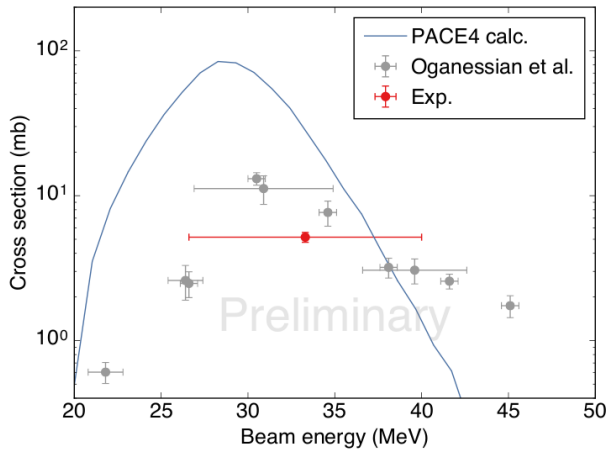


Figure 2: (solid) Excitation function for the $^{176}\text{Yb}(\alpha,2n)^{178m2}\text{Hf}$ reaction.

also added here 4 mg of Hf carrier to get the higher yield. The solution was heated to dryness. Then they were dissolved 25 ml of HCl again and were poured into a column ($l = 54$ mm and $\phi = 6.5$ mm) filled with an ion-exchange resin (Dowex). Hf ions were absorbed on the resin. Finally, the column was washed with 30 mL of 4M HCl so that Hf ions were removed from the resin. The eluent was heated to dryness so that we successfully extracted only Hf from Yb. By repeating the process twice, we achieved 70% chemical yield. In principle, we can achieve 100% by repeating the process. However, because we added 4 mg of Hf carrier, the most of the Hf extracted is the natural Hf not from the reaction product. We're going to measure the efficiency without such a carrier.

In summary, for the future mass production of the $^{178m2}\text{Hf}$ we irradiated ^4He beam of 40 MeV with $10e\mu\text{A}$ on a stack of ^{nat}Yb targets. The $\gamma-\gamma$ analysis on the activated target after chemical separation successfully presented the cascade transition from $^{178m2}\text{Hf}$. We also deduced the production cross section of $^{172,175}\text{Hf}$ from the $^{178m2}\text{Hf}$ and found that they are in good agreement with the theoretical calculations.

References

- [1] X.L. Han and C.L. Wu, At. Data Nucl. Data Table 63, 117 (1996).
- [2] J. Dudek et al., Phys. Lett. B 211, 252 (1988).
- [3] T. Ichikawa et al., Phys. Rev. Lett. 109, 232503 (2012).
- [4] S.A. Karamian, Yad. Fiz. 68 1827 (2005).
- [5] Yu.T. Oganessian et al., J. Phys.G:Nucl. Part. Phys. 18 393 (1992).
- [6] S. Nishimura et al., Prog. Theor. Exp. Phys. Article03C006 (2012).
- [7] <http://www-nds.iaea.org/medical/tia51cr0.html>
- [8] <http://lise.nsl.msui.edu/pace4.html>

Development of a TiD_x target as the test of a Ti^3H_x target

N. Imai, K. Wimmer^a, N. Kitamura, S. Michimasa, and Y. Hatano^b

Center for Nuclear Study, Graduate School of Science, University of Tokyo

^aDepartment of Physics, Univ. of Tokyo

^aHydrogen Isotope Research Center, Toyama Univ.

With the advent of accelerator technology, we can get many short-lived radioactive nuclei which cannot exist in the nature. Basic properties of exotic nuclei have been studied at many facilities all over the world. In particular, in very neutron-rich nuclei, compared to stable nuclei existing in nature, the one neutron separation energy is getting lower. As a result, continuum effects are important and could lead to a new type of collective motion [1]. In addition, recent experimental studies revealed shape co-existence phenomena at low excitation energy in the neutron-rich nuclei [2]. Because both phenomena are associated with the correlation of pairs of neutrons in a nucleus, two-neutron transfer reactions such as the $(^3\text{H}, p)$ reaction are a well-suited tool to investigate such exotic states.

In order to develop a titanium target suitable for the use at RIBF we started a collaboration with the hydrogen isotope research center at Toyama University. The goal of this project is to develop a tritium loaded titanium target (Ti^3H_x with a loading ratio $x \simeq 1.0$) with an active area of $2.5 \times 2.5 \text{ cm}^2$ to fit with the beam spot size of about 2 cm at the OEDO facility for energy degraded beams.

There are three safety issues to be addressed before the tritium target can be manufactured. The first issue is the mechanical stability of fragility of the target. If the loading ratio becomes large, i.e. close to two, the target becomes very brittle and easily breaks. This is a particular concern here because of the large area of the target. A first self supported test target is therefore limited to a loading ratio of $x = 0.24$. Considering the practical upper limit of ^3H at the Hydrogen Isotope Research Center of 5 Ci (185 GBq), this prototype target consists of a $20 \mu\text{m}$ Ti foil loaded with deuterium, $\text{TiD}_{0.24}$. Second issue is that how much ^3H is desorbed from the target at the room temperature. According to Ref. [3], the thermal erosion starts above 200°C . As long as the titanium foil is placed in vacuum at the room temperature, desorption of tritium won't be observed. For instance, the energy deposit in a $20 \mu\text{m}$ titanium foil by a $20 \text{ MeV/nucleon } ^{132}\text{Sn}$ beam with an intensity of 10^6 pps amounts to $44.2 \mu\text{Ws}$. Since the heat diffuses rapidly thanks to the high conductivity of the foil heating of the target by beams with typical intensities for radioactive beam can therefore be neglected. On the other hand, one might suspect that over the course of time tritium in the foil will be exchanged with normal hydrogen from the air. To avoid contamination of the surroundings, the target will be kept either in vacuum or in a dry nitrogen atmosphere for storage. Third point is to establish a way of decommissioning procedure after use with radioactive ion beam at RIBF. In principle, the target can be returned to Toyama University, but only if radioactive activity from other sources than

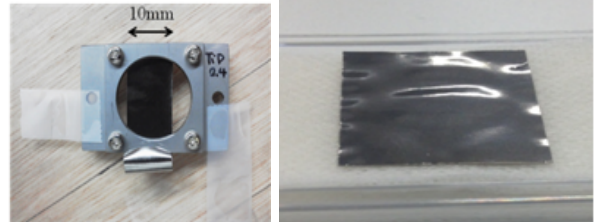


Figure 1: Photos of the rolled $\text{TiD}_{0.24}$ target (left) and the flat $\text{TiD}_{0.10}$ target (right).

^3H cannot be detected. We performed an experiment with a $\text{TiD}_{0.24}$ target to confirm the latter two points with a stable ^{20}Ne beam at an energy of 8.2 MeV/nucleon in July 2016. In this report, we discuss the mechanical stability and report preliminary results from an α source test.

In order to absorb substantial quantities of hydrogen into the titanium foil it is first heated to 600°C inside an evacuated glass tube. Then the desired amount of deuterium gas is inserted and the tube is cooled down to room temperature. Once cold the deuterium remains in the Ti matrix.

Two targets with very different loading ratio of $x = 2.0$ and 0.24 were produced. The $x = 2.0$ target was very brittle and broke upon being taken out of the tube. The second target was self-supporting. However, the target curled upon itself during the cooling down, indicating the change of the physical phase of the hydrogen-titanium matrix. In order to avoid this a third target was produced while the titanium foil was sandwiched between a porous ceramic structure. Both targets can be seen in Fig. 1. In the future, we will attempt to make thinner targets with higher concentrations of deuterium before switching to tritium.

To check the amount of deuterium in the target of $\text{TiD}_{0.24}$, we irradiated α particle from ^{241}Am of 185 kBq to perform an Elastic Recoil Detection Analysis (ERDA) [5]. The ^{241}Am is implanted in the metal plate so that, the energy of α particles were measured to be $3.50 \pm 0.27 \text{ MeV}$, which was lower than typical energy of 5.5 MeV . The target was placed 7 cm away from the source. A double collimator of 1 cm diameter was installed between the target and the source to make a beam of 1 cm diameter. A 1 mm thick Double sided strip silicon detector (DSSD) was placed 5 cm downstream of the target to detect recoil particles at 0° with the respect to the α beam direction. With the target removed, the count rate at the detector was 300α particles/sec. A SRIM [4] calculation predicts the range of α particles in the target to amount $9 \mu\text{m}$. If the α particles hits a deuterium, its recoil energy is 2.6 MeV at 0° . This energy is enough to penetrate the target and be detected in the DSSD.

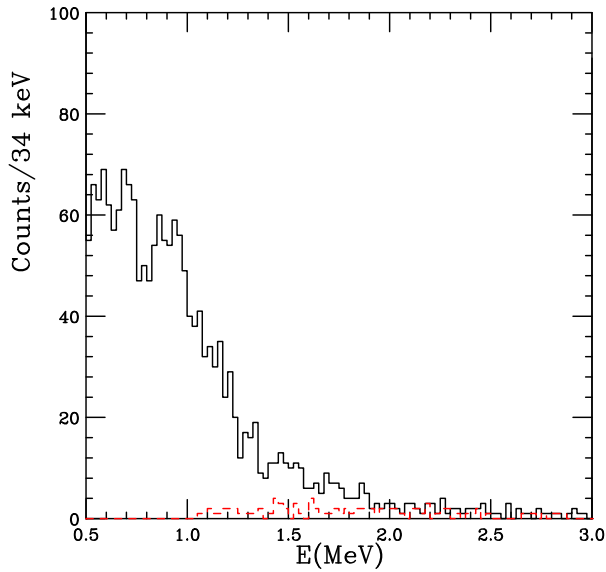


Figure 2: Energy spectra measured with a $\text{TiD}_{0.24}$ target (solid) and a Ti (dashed) target with the α source of 185 kBq.

The measured energy spectrum was presented in Fig. 2. For comparison the measurement was repeated with a pure Ti foil of the same thickness, the resulting energy spectrum is shown by the red dashed line in Fig. 2. The comparison of the spectra measured with Ti and $\text{TiD}_{0.24}$ clearly shows the presence of deuterons in the target. Further analysis and development are on-going.

References

- [1] H. Shinomiya and T. Matsuo, Phys. Rev. C 84, 044317 (2011).
- [2] K. Wimmer et al, Phys. Rev. Lett., 105, 252501(2011).
- [3] H. Chatbi, M. Vergnat and G. Marchal, Applied physics letters 64, 1210 (1994).
- [4] <http://www.srim.org/> .
- [5] W. M. Arnold Bik and F.H.P.M. Habraken, Reports on Progress in Physics 56, 859 (1993).

The ($^{16}\text{O}, ^{16}\text{F}(0^-)$) reaction to study spin-dipole 0^- states

M. Dozono, T. Uesaka^a, K. Fujita^b, N. Fukuda^a, M. Ichimura^a, N. Inabe^a, S. Kawase, K. Kisamori, Y. Kiyokawa, K. Kobayashi^c, M. Kobayashi, T. Kubo^a, Y. Kubota, C. S. Lee, M. Matsushita, S. Michimasa, H. Miya, A. Ohkura^b, S. Ota, H. Sagawa^{a,d}, S. Sakaguchi^b, H. Sakai^a, M. Sasano^a, S. Shimoura, Y. Shindo^b, L. Stuhl^a, H. Suzuki^a, H. Tabata^b, M. Takaki, H. Takeda^a, H. Tokieda, T. Wakasa^b, K. Yako, M. Yamagami^d, Y. Yanagisawa^a, J. Yasuda^b, R. Yokoyama, K. Yoshida^a, and J. Zenihiro^a

Center for Nuclear Study, Graduate School of Science, University of Tokyo

^a*RIKEN Nishina Center*

^b*Department of Physics, Kyushu University*

^c*Rikkyo University*

^d*Center for Mathematics and Physics, University of Aizu*

Spin-dipole (SD) states excited with $\Delta L = 1$, $\Delta S = 1$ and $\Delta J^\pi = 0^-, 1^-, 2^-$ have recently attracted theoretical attention owing to its strong relevance in the tensor correlations in nuclei. For example, self-consistent HF+RPA calculations in Ref. [1] predict that the tensor correlations produce a strong hardening (shifting toward higher excitation energy) effect on the 0^- resonance. It is also predicted that the effect is sensitive to the magnitude of the tensor strength. Thus experimental data of the SD 0^- distribution enable us to examine the tensor correlation effects quantitatively.

On the other hand, experimental identification of 0^- states has been very difficult and, as a consequence of this, experimental data of 0^- states are quite limited at present. The difficulty originates from two features: First, 0^- states are more weakly populated than 1^- and 2^- states, and second, 0^- states are highly fragmented in many cases. One possible approach to overcome this difficulty is to introduce polarization observables that take different values depending on J^π . For example, measurements of tensor analyzing powers in the $^{12}\text{C}(\vec{d}, ^2\text{He})$ reaction [2] and polarization transfer observables in the $^{12}\text{C}(\vec{p}, \vec{n})$ reaction [3] revealed the existence of the 0^- states at $E_x \simeq 9$ MeV in $A = 12$ systems. More recently, the multipole decomposition (MD) technique was applied to the $^{208}\text{Pb}(\vec{p}, \vec{n})$ data [4]. In these analyses, the polarization observables were used to separate different J^π components of the SD excitations. However, for 0^- states, the experimental separation is still difficult and suffer from uncertainties larger than those for 1^- and 2^- states. Thus, a more selective tool is definitely desired for more reliable identification of the 0^- states and for deeper understanding of tensor correlations in nuclei.

We have invented a new experimental probe to investigate the 0^- states, that is the *parity-transfer* ($^{16}\text{O}, ^{16}\text{F}(0^-, \text{g.s.})$) reaction [5]. The parity-transfer reaction uses $0^+ \rightarrow 0^-$ transition in the projectile and transfers a parity to a target nucleus, which results in a unique sensitivity to the transferred spin-parities. Firstly, this reaction populates unnatural-parity states ($J^\pi = 0^-, 1^+, 2^-, \dots$) only and thus the 1^- states can not contaminate in the final spectrum. Secondly, as described below, its angular distribution has different patterns depending on J^π of the ex-

cited unnatural-parity states, which allows a clear discrimination of the 0^- states from other unnatural-parity states. The properties make the parity-transfer reaction quite a selective and efficient probe to the 0^- states. In this paper, we report the results of first application of the parity-transfer ($^{16}\text{O}, ^{16}\text{F}(0^-, \text{g.s.})$) reaction to study of 0^- states in ^{12}B .

The experiment was performed at the RIKEN RI Beam Factory (RIBF) by using the SHARAQ spectrometer and the high-resolution beam line. A schematic layout of the experimental setup can be found in Ref. [6]. A primary ^{16}O beam at 247 MeV/nucleon and 10^7 pps from the superconducting RING cyclotron (SRC) was transported to the S0 target position. The beam line to the spectrometer was set up for dispersion-matched transport. We used a segmented plastic scintillation detector as an active ^{12}C target. This detector consisted of 16 plastic scintillators with a size of $30 \text{ mm} \times 5 \text{ mm} \times 1 \text{ mm}$, and it was used to determine the x -position of the beam on the target. The outgoing $^{15}\text{O} + p$ particles produced by the decay of ^{16}F were measured in coincidence by using a new “separated flow” operating mode of the SHARAQ spectrometer [7]. The ^{15}O particles were detected with two low-pressure MWDCs at the S2 focal plane. On the other hand, the protons were detected with two MWDCs at the S1 focal plane, which has been newly designed at the low-momentum side of the exit of the first dipole magnet.

The preliminary result of the excitation-energy spectrum for the $^{12}\text{C}(^{16}\text{O}, ^{16}\text{F}(0^-))^{12}\text{B}$ reaction at $\theta_{\text{lab}} = 0^\circ - 0.25^\circ$ is shown in Fig. 1. The energy resolution is 2.7 MeV in FWHM. We note that the events at $E_x \sim -10$ MeV are due to the ($^{16}\text{O}, ^{16}\text{F}(0^-)$) reaction on hydrogens in the plastic scintillator used as a reaction target. The obtained distribution is largely different from those previously obtained by other reaction probes such as (n, p) and $(d, ^2\text{He})$ (e.g., see Fig. 1 in Ref. [8]). A distinct difference is that the 1^+ ground-state Gamow-Teller (GT) transition is strongly hindered. Furthermore, an enhancement at $E_x \sim 9$ MeV can be seen, which is due to a known 0^- state at $E_x = 9.3$ MeV [2]. Therefore, the obtained distribution shows high selectivity of the present reaction to 0^- states.

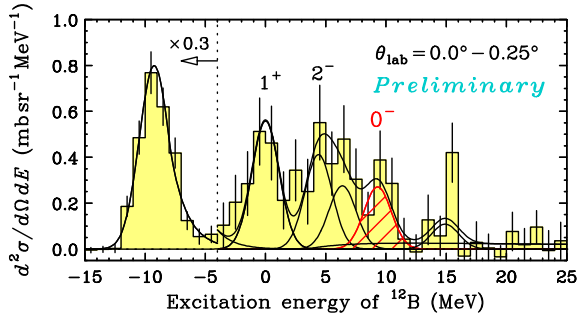


Figure 1: Preliminary result of the excitation-energy spectrum for the $^{12}\text{C}(^{16}\text{O}, ^{16}\text{F}(0^-))^{12}\text{B}$ reaction at $\theta_{\text{lab}} = 0^\circ - 0.25^\circ$.

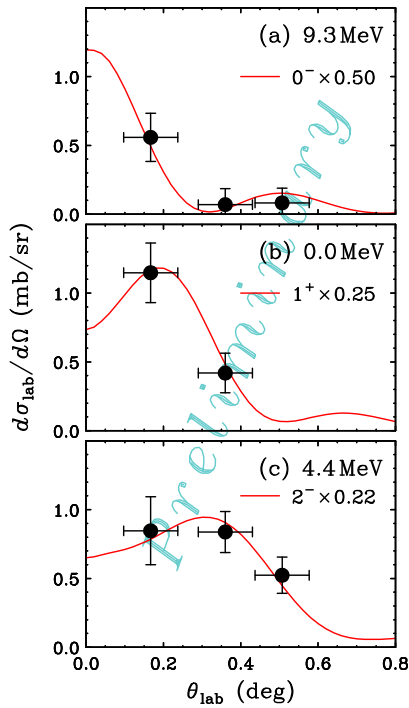


Figure 2: Measured and calculated differential cross sections for $E_x = 9.3$ MeV, 0.0 MeV, and 4.4 MeV states.

In order to extract the yield of the 0^- state, we performed peak fitting, and the results are shown as the solid lines in Fig. 1. Figure 2 shows the angular distribution for the 0^- state at $E_x = 9.3$ MeV together with the results for the 1^+ g.s. and the 2^- state at $E_x = 4.4$ MeV. The solid curves denote the results calculated by the distorted-wave Born approximation (DWBA). The DWBA calculations predict the oscillatory patterns of the cross sections that are different depending on the spin-parity. The 0^- state has the strong forward peaking, while the other states, 1^+ and 2^- , have the first maximum at finite angles. These patterns reproduce the experimental data very well. Thus, the oscillatory pattern of the angular distribution allows a clear spin-parity determination for the unnatural-parity state. Further analysis is underway to finalize experimental results.

From the present analyses, the $(^{16}\text{O}, ^{16}\text{F}(0^-, \text{g.s.}))$ reaction has been established as quite an efficient probe to 0^-

states in nuclei. Our data will provide an important basis to extend this novel method to heavier nuclei where a number of unknown 0^- states are kept to be discovered and to gain valuable information on tensor-interaction effects in nuclear structure.

References

- [1] H. Sagawa and G. Colò, Prog. Part. Nucl. Phys. **76**, (2014) 76.
- [2] H. Okamura *et al.*, Phys. Rev. C **66**, (2002) 054602.
- [3] M. Dozono *et al.*, J. Phys. Soc. Jpn. **77**, (2008) 014201.
- [4] T. Wakasa *et al.*, Phys. Rev. C **85**, (2012) 064606.
- [5] M. Dozono *et al.*, RIKEN Accel. Prog. Rep. **45**, (2012) 10.
- [6] M. Dozono *et al.*, CNS Ann. Rep. **2014**, (2015) 5.
- [7] M. Dozono *et al.*, elsewhere in this report.
- [8] H. Okamura *et al.*, Phys. Lett. B **345**, (1995) 1.

Development of recoil-proton detector for identification multi-neutrons

S. Masuoka, S. Shimoura, R. Yokoyama, S. Michimasa, M. Matsushita, M. Takaki, M. Kobayashi, S. Ota, N. Kitamura, Y. Yamaguchi, and Y. Kunimoto^a,

Center for Nuclear Study, the University of Tokyo
^aDepartment of Physics, Rikkyo University

1. Motivation

Nuclei which consist of only neutrons have been discussed by many physicists since atomic nuclei have been discovered. According to the theoretical model which includes only 2-body nuclear forces, existence of neutron matter is denied. However, a state-of-the-art theory suggests it is allowed by consideration of the 3-body nuclear forces [1]. Then, K. Kisamori *et al.* tried to generate the nucleus which is composed of 4 neutrons (tetra-neutron) at the RIKEN RI Beam Factory (RIBF) using the High-Resolution-Beamline and SHARAQ spectrometer [2]. In this experiment, the ${}^8\text{He}({}^4\text{He}, {}^8\text{Be}){}^4n$ reaction was used as a double charge exchange(DCX) reaction and measured by missing mass spectroscopy. As a result, 4 events were found as candidates of tetra-neutron because its production cross section was too small.

We considered how to make tetra-neutron with a higher cross section than that of the DCX reaction's. Thus, we selected the ${}^8\text{He}(\alpha, p\alpha){}^4n$, a knockout core-nucleus reaction. Is this reaction cross section about 100 times higher than the DCX reaction. However, if we use this reaction, we have to measure 4 neutrons directly. In addition, each neutrons flies straightly (beam like) with an energy almost the same as the beam. It is difficult to detect them at the same time. However, we will be able to measure the invariant mass for tetra-neutron if it is possible.

2. Overview

The our new detector is required to

- Identify multiple neutrons and measure their energies with high energy resolutions respectively.
- Measure the center of mass energy of multiple neutrons.

Figure 1 shows the schmatic view of a reaction inside the usual scintillators. Conventional neutron detectors can not identify multi neutrons at the same time. Thus, we designed the new detector to satisfy the requirements.

The image of this detector is shown in Fig. 3. It is composed 2 types of scintillator units. The first one is called as "Tracker unit", which is an array of 16-strip scintillators for position detection. One scintillator has a size of $100 \times 6 \times 3 \text{ mm}^3$, and put a photon detector, Si-PM (Silicon Photo Multiplier), on each end.

The other unit, called "Timing unit", is for measuring the Time of Flight (ToF). Its size is $100 \times 100 \times 3 \text{ mm}^3$ and each corner is cut out to put Si-PMs there.

This detector is composed like (T,X,T,Y,T,X',T,Y',T,-X,T,-Y,T,-X',T,-Y') $\times 2$ +T (T denotes Timing unit, X means

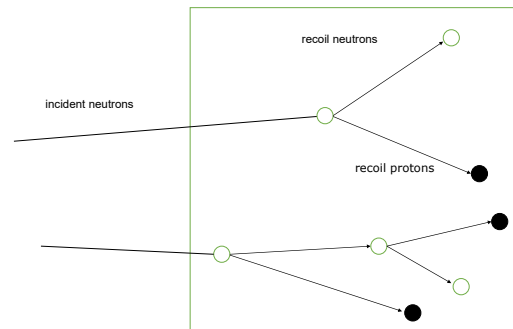


Figure 1: Image of reaction inside usual scintillators. It is difficult to identify each neutron.

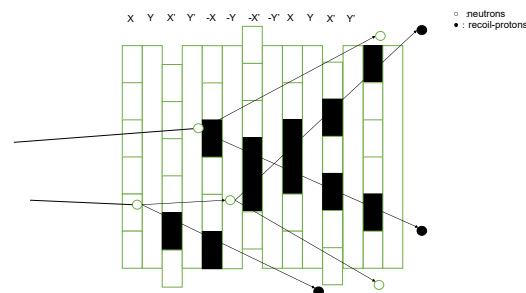


Figure 2: Image of new detector's concept. It can detect track of recoil-proton how scintillator is segmented like Figure this.

Tracking unit, Y means rotation 90 degrees of X, X' means shift 1 cell(6mm) of X, -X means rotation 180 degrees X).

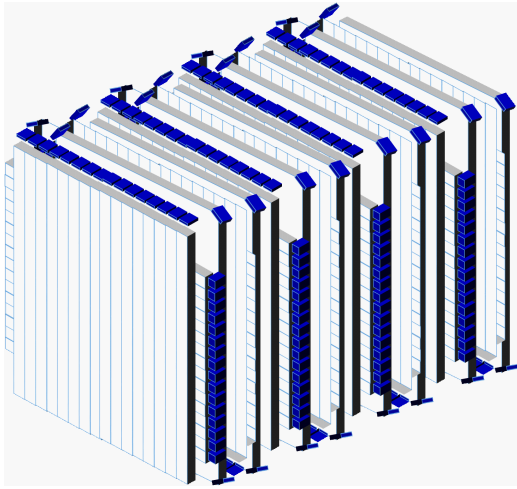


Figure 3: The image of the neutron tracking detector.

2.1. Simulation for Timing Unit

Timing resolution is important for measuring the velocities of neutrons. In order to obtain good timing resolution, detector responses are studied by simulating photon propagation in plastic scintillators. Then, we performed a simulation using Geant4 for Timing Unit to estimate the traveling time for photons which are generated by scintillation. Photons were generated at one point (photon source point) and they traversed along the grid of 1 mm interval. Then, we analyzed the correlation between photon source position and time of photon detection.

2.2. Construction the prototype Tracking unit

Next, we constructed the prototype of Tracker Units. It is composed of 8 segments and 2 planes. We put them like X and Y directions (cross each segment) and measured cosmic rays. We put 2 plastic scintillators, detect by PMT, between the Tracking Units to make a coincidence trigger. The readout system for Tracking Unit use EASIROC NIM Module [3]. It can handle (HV supply, amplifier, shaping, and A/D converter) 64 Si-PMs.

3. Result

3.1. Simulation for Timing Unit

First, the result of simulation for Timing unit is shown in Fig. 4. These plots show the correlations between photon detection time and number of photons where photon source is (-25,-35). According to Fig. 4, it can be concluded

- Number of photons saturate at around 20 ns, which is independent on the position of photon source.
- timing which characterizes the hit position of a recoil-proton corresponds to around the 10th photon.

Then, we found that the optimum threshold was 10 photon equivalent.

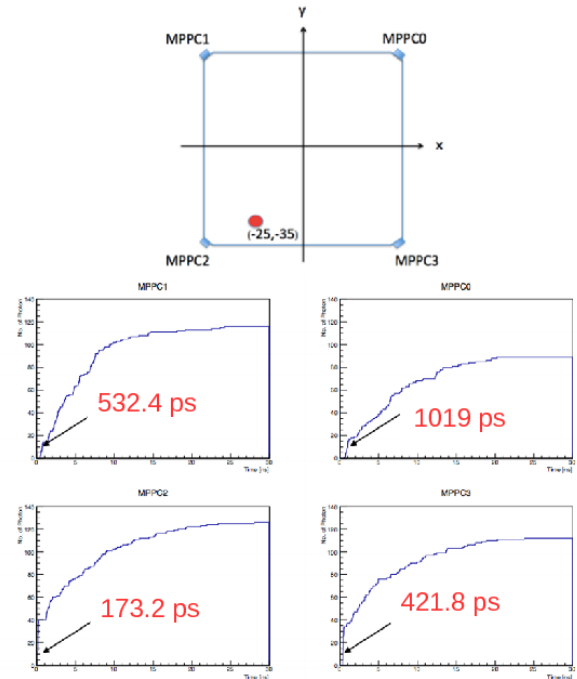


Figure 4: Result of simulation analysis at photon source (-25,-35) and pictures for each Si-PMs. Vertical axes are number of photons and horizontal ones are time of photon capture.

3.2. Test for the prototype of Tracking Unit

Next, we constructed the prototype of Tracking Unit and tested the detector. We succeeded to take data by using EASIROC NIM Module. However, the signals were saturated because of the shaper inside the EASIROC NIM Module. And 2 planes coincidence efficiency was small (less than 10%) Then, optimization the module is required to take data correctly.

Development of this detector is now in progress.

References

- [1] Steven C. Pieper, Phys. Rev. Lett. 90, 252501 (2003)
- [2] K. Kisamori *et al.*, Phys. Rev. Lett. 116, 052501 (2016)
- [3] I. Nakamura *et al.*, Nucl. Inst. Meth. A 787 376-379(2015)

**Experiment Nuclear Physics: PHENIX
Experiment at BNL-RHIC and ALICE
Experiment at CERN-LHC**

Overview of ALICE Results in 2015 and Activities of CNS

T. Gunji, H. Hamagaki, Y. Watanabe, S. Hayashi, Y. Sekiguchi, K. Terasaki, H. Murakami *Center for Nuclear Study, Graduate School of Science, The University of Tokyo, Japan*

1. Introduction

The primary goal of the ALICE experiment is to understand the physics of strongly interacting matter at extreme energy densities, where the formation of a new phase of matter, the quark-gluon plasma is expected [1]. The ALICE detector complex has been built to carry out comprehensive measurements of the hadrons, electrons, muons, and photons created in pp , p -A, and A-A collisions.

There are several upgrades of the ALICE experiment during Long Shutdown of the LHC (2012-2014). The remaining five super modules of the Transition Radiation Detector (TRD), eight modules of new dijet calorimeter (DCal), one module of PHOS, and new ALICE Diffractive detectors (AD) have been installed. ALICE Central Trigger Systems have been upgraded to handle $\times 2$ more trigger classes. The gas mixture of TPC has been changed from Ne(90):CO₂ (10) to Ar(90):CO₂ (10), to provide a more stable operation at high particle fluxes during heavy-ion running.

During the winter shutdown at the end of 2015, new readout module of the Time Projection Chamber (TPC), called Readout Control Unit 2 (RCU2), was installed to improve the readout speed by a factor of 2 in Pb-Pb collisions. The CNS group has been developing FPGA firmware for the data readout and microcontroller system for monitoring the TPC conditions and controlling the TPC front-end cards [3].

2. Start up of Run2 pp and Pb-Pb collisions

The LHC started the operation of Run2 in June 2015 and ALICE started physics taking data in pp collisions at $\sqrt{s} = 13$ TeV. The author, TG, served as the Period Run Coordinator of ALICE in July, which was the time for the LHC to start high-intensity ramp up of pp collisions by increasing the number of colliding bunches from 3 to 1230. TG was responsible for the operation and data taking of the ALICE experiment. ALICE was taking high intensity pp collisions and multiple collisions in one bunch crossing (in-bunch pileup with $\mu = 0.3 - 1.5$) happened frequently, which was far from normal running conditions of ALICE ($\mu \sim 0.01$).

First heavy-ion experiments in Run2 with Pb-Pb collisions at $\sqrt{s_{NN}} = 5.02$ TeV was begun in November 2015. ALICE took minimum bias Pb-Pb events, which were triggered by the coincidence of signals from the scintillator arrays in forward ($2.8 \leq \eta \leq 5.1$) and backward rapidities ($-3.7 \leq \eta \leq -1.7$). Figure 1 shows anisotropy flow parameter ($v_{n=2,3,4}$) as a function of collision centrality at $\sqrt{s_{NN}} = 5.02$ (closed) and 2.76 TeV (open), where small (large) centrality corresponds to central (peripheral) collisions [4]. Slight increase by 3-10% in the anisotropic flow coefficients is observed in 5 TeV Pb-Pb collisions. Solid lines are expectation from hydrodynamical calculations with viscosity/entropy ratio of around 0.2.

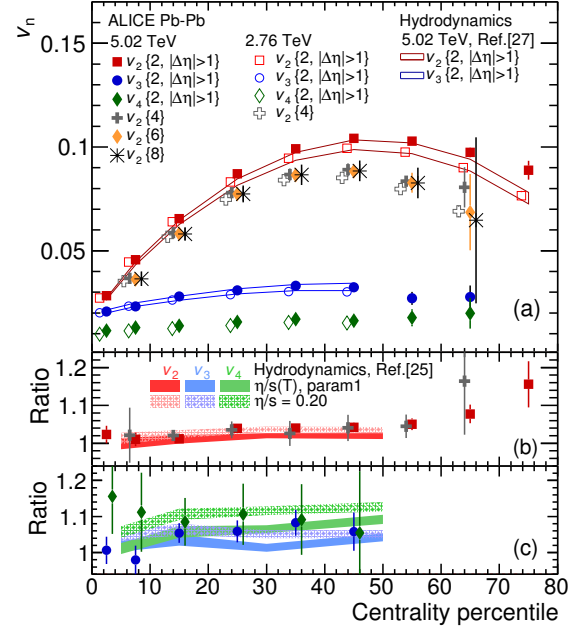


Figure 1: (a) Anisotropy flow v_n as a function of collision centrality for Pb-Pb collisions at $\sqrt{s_{NN}}=5.02$ TeV and 2,76 TeV. (b) Ratio of v_2 between 5.02 and 2.76 TeV. (c) Ratios of $v_{3,4}$

3. Activities of CNS

The CNS group has been participating in the ALICE experiment and has been involving in the operation of the TPC, in the data analyses, and in the TPC upgrade project for Run3 and Run4.

In the FYI 2015, the CNS group has taken a responsible role in mass testing of the new RCU2 modules and developments of the embedding software and applications running on the SoC FPGA.

In recent years, low mass dark photon searches have been performed in the collider experiments. A dark photon is an $U(1)$ gauge boson in the dark matter sector that mixes with an ordinary photon and may be the possible explanation of $g-2$ anomaly and the positron excess observed in the universe by PAMELLA, FERMI, and AMS-2 satellite experiment. The ALICE experiment searches for the signal of dark photon in π^0 Dalitz decay ($\pi^0 \rightarrow e^+e^-\gamma$) samples from Run1 pp (300M minimum bias collisions) and p -Pb collisions (100M minimum bias collisions). Left of Fig. 2 shows e^+e^- invariant mass spectrum below 100 MeV and the fitting with Kroll-Wada + ChebyChev polynomials. Since there is no significant peak in the Dalitz mass spectrum, the 90% confidence level of the upper limit of mixing parameter ϵ^2 as a function of the dark photon mass is extracted by employing the CLs method, a statistical method

widely used for new particle searches in the LHC experiments. Figure 3 shows a mixing parameter e^2 as a function of the dark photon mass, where solid line and two bands represent “ expected level ” of the upper limit without any statistical fluctuation and expected statistical fluctuation of the upper limit at 1σ and 2σ level, respectively. Our ALICE result of the upper limit is within approximately 2σ level.

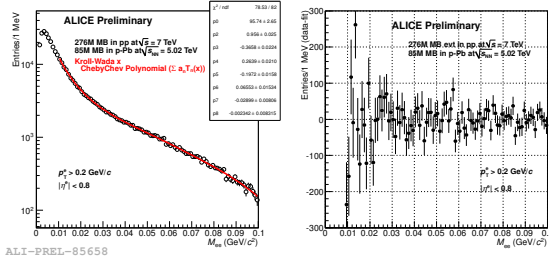


Figure 2: left: Dielectron invariant mass distribution and Knroll-Wada+ChebyChev fitting. Right: Residual between data and fit.

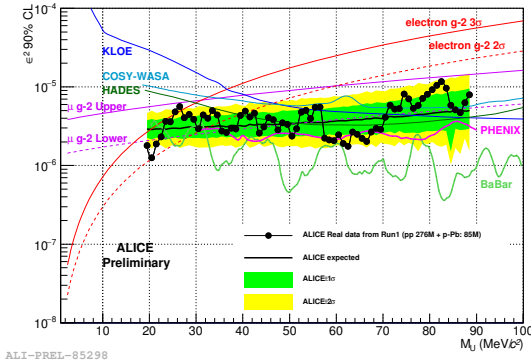


Figure 3: Mixing parameter as a function of dark photon mass.

Space-time evolution and properties of the created medium in Pb-Pb collisions have been extensively studied from the measurements of the transverse momentum spectra and anisotropic flow coefficients of light hadrons (π, K, p, d) and multi-strange baryons (Λ, Ξ, Ω). Correlation of di-quarks in the medium provides further insights of the nature of the medium and space-time evolution of the system. Measurements of heavy-flavor baryons such as Λ_c, Ξ_c are useful for these purposes. The measurements of Λ_c in pp and p -Pb collisions have been performed and invariant cross-section of Λ_c has been newly obtained for semi-leptonic decay channel [5].

One of the recent big findings at the LHC is the observation of collective-like behavior of particle productions in high multiplicity pp and p -Pb collisions. To have a deeper insights of the dynamics of high multiplicity pp and p -Pb collisions, the CNS group has been analyzing the long range particle correlations in rapidity space in p -Pb collisions, quantifying the initial state effects by measuring the di-electron correlations from heavy flavor decays [7], and searching for thermal photons in high multiplicity pp collisions [8].

sions [8].

The CNS group searches for Di-baryons ($p\Omega$) in Pb-Pb collisions, where abundant hadrons are produced and di-baryons can be produced through the coalescence process. Searching for the resonant peaks and correlation functions are being studied [9].

The CNS group has been involving in the TPC upgrade. The TPC will be upgraded to be able to cope with the high luminosity Pb-Pb collisions in Run3 and Run4. Gas Electron Multiplier will be used in the readout chamber to suppress the ionback flow by less than 1% and allow to run TPC continuously without gating grid. The CNS group has conducted R&D of GEM and MicroMegas detectors. In FY2015, the CNS group has started to evaluate the online data processing from the TPC via GPU (Graphical Processing Unit).

4. Summary

The LHC and ALICE started Run2 operation in June 2015 and first full energy Pb-Pb collisions were performed in November 2015. IN FY 2015, the CNS group has involved in the operation of the TPC, data analyses including dark photon searches, heavy baryon measurements, long range correlations, dielectron measurements from heavy flavor decays, thermal photon searches, and di-baryon searches, in Pb-Pb and high multiplicity pp and p -Pb collisions. The CNS group has started some R&D of the online data processing via GPU for the TPC upgrade in Run3 and Run4.

References

- [1] ALICE Collaboration, JINST **3**, (2008), S08002.
- [2] B. Abelev *et al.* (ALICE), Int. J. Mod. Phys. A **29**, (2014) 1430044
- [3] T. Gunji *et al.* (ALICE), Annual Report 2014
- [4] J. Adam *et al.* (ALICE), Phys. Rev. Lett. **116** 132302
- [5] Y. Watanabe *et al.* (ALICE), Annual Report 2015
- [6] Y. Sekiguchi *et al.* (ALICE), Annual Report 2015
- [7] S. Hayashi *et al.* (ALICE), Annual Report 2015
- [8] H. Murakami *et al.* (ALICE), Annual Report 2015
- [9] K. Terasaki *et al.* (ALICE), Annual Report 2015

Charmed baryon measurements with ALICE at the LHC

Y.S. Watanabe for the ALICE collaboration

Center for Nuclear Study, Graduate School of Science, University of Tokyo

1. Introduction

Heavy-flavor quarks, such as charm and bottom quarks, are considered as ideal tools to study the properties of quark-gluon plasma (QGP) created in heavy-ion collisions. These quarks are expected to be produced only at the initial stage of the collisions because the mass of charm and bottom quarks is much larger than the temperature of the QGP. Thus, the information concerning the whole system evolution is imprinted on final heavy-flavor observables, e.g. yields of heavy-flavor hadrons.

So far, experimental measurements of heavy-flavor hadrons are limited to heavy-flavor mesons and little has been studied about heavy-flavor baryons. However, the measurements of heavy-flavor baryons are demanding because such measurements provide unique information about the properties of the QGP, such as the correlation between light quarks, “diquark”. For example, according to Ref. [1], the existence of diquark correlations in the QGP enhances the production of Λ_c^+ by a factor of 4–8 compared to the case without such correlations.

This report presents the measurements of Λ_c^+ and Ξ_c^0 via their semileptonic decays in pp collisions. These results provide the necessary baseline for the measurements in Pb-Pb collisions.

The Λ_c^+ and Ξ_c^0 baryons can also be analyzed with their hadronic decays, such as $\Lambda_c^+ \rightarrow pK_s^0$, $\Lambda_c^+ \rightarrow pK\pi$, etc. The semileptonic-decay measurement has an advantage of less suffering from combinatorial background compared to the hadronic decay modes. This is because, on the one hand, the number of electrons in an event is small, resulting in the smaller number of random combinations, and on the other hand, the branching ratios of the semileptonic decays are comparable to the ones of the hadronic decays.

2. Reconstruction and identification of daughters

The Λ_c^+ and Ξ_c^0 baryons are measured with the $\Lambda_c^+ \rightarrow e^+\Lambda\nu$ and $\Xi_c^0 \rightarrow e^+\Xi^-\nu$ decay modes, respectively. (Charge conjugates are also implied throughout this report.) The decay daughters (electron, Λ , Ξ) are reconstructed by Inner Tracking System (ITS) and Time Projection Chamber (TPC) in the central barrel of the ALICE detector. A detailed description of the ALICE detector can be found in Ref. [2].

Electrons are identified by the dE/dx information of the TPC and by the time-of-flight information of Time-of-Flight detector (TOF). The cuts are tuned such that the hadron contamination is kept to be $\sim 2\%$ up to 5 GeV/c.

The Λ and Ξ baryons decay weakly and have long lifetimes of ~ 5 cm. Therefore, their decay daughters do not originate from the primary collision vertex and can be easily identified using the track impact parameter measurements provided by the ITS and the TPC.

3. Data analysis

The analysis of Λ_c^+ proceeds as follows.

1. Make pairs of electrons and Λ when they satisfy the two following conditions: their opening angle is less than 90 degrees and the invariant mass of e and Λ is less than 2.3 GeV/c.
2. Background subtraction
3. $\Xi_c \rightarrow e\Xi\nu \rightarrow e(\Lambda\pi)\nu$ contribution subtraction
4. Unfold $p_T^{e\Lambda}$ into $p_T^{\Lambda_c^+}$
5. Efficiency correction and event normalization
6. Bottom baryon feeddown correction

The analysis of Ξ_c^0 proceeds almost in the same way as Λ_c^+ , but without step 3. In this section, only background subtraction (step 2) and unfolding (step 4) are described.

Since neutrinos are not measured, the invariant mass spectrum of $e\Lambda$ does not show a peak structure and the usual background subtraction procedure of fitting invariant mass spectra with (gaussian + smooth background function) cannot be used. Here, we can exploit the fact that charmed baryon semileptonic decays are charge asymmetric. For example, in case of Λ_c^+ :

- $\Lambda_c^+ \rightarrow e^+\Lambda\nu$ (Right-sign (RS))
- $\Lambda_c^+ \not\rightarrow e^-\Lambda\nu$ (Wrong-sign (WS))

The WS spectra can be used to estimate background sources, such as combinatorial background pairs, jet correlations between π^0 ($\rightarrow \gamma\gamma \rightarrow ee\gamma$) and Λ , etc. An example of the $e\Lambda$ invariant mass distribution for the RS and WS combinations from real data are shown in Fig. 1. The charmed baryon contribution can be extracted by subtracting the WS spectra from the RS spectra. The excess of the RS spectrum is concentrated in the mass region below 2.3 GeV/c² because the invariant mass of $e\Lambda$ from Λ_c^+ cannot go beyond the mass of Λ_c^+ , ~ 2.3 GeV/c². A similar comparison of the RS and WS spectrum for the Ξ_c^0 analysis is also shown in Fig. 2.

The unfolding procedure (step 4) is necessary again due to the fact that we cannot measure neutrino; what we actually measure is $p_T^{e\Lambda}$ (or $p_T^{e\Xi}$) and not $p_T^{\Lambda_c^+}$ (or $p_T^{\Xi_c^0}$). In this analysis, $p_T^{e\Lambda}$ (or $p_T^{e\Xi}$) is converted into $p_T^{\Lambda_c^+}$ (or $p_T^{\Xi_c^0}$) using the unfolding techniques. This can be justified by the fact that the $p_T^{e\Lambda}$ is strongly correlated with the $p_T^{\Lambda_c^+}$ via the simple decay kinematics of $\Lambda_c \rightarrow e\Lambda\nu$.

The finally obtained p_T distribution of the Λ_c^+ baryon for $|y| < 0.5$, corrected for the efficiency, acceptance, the branching ratio of the decay mode and the Λ_b feeddown,

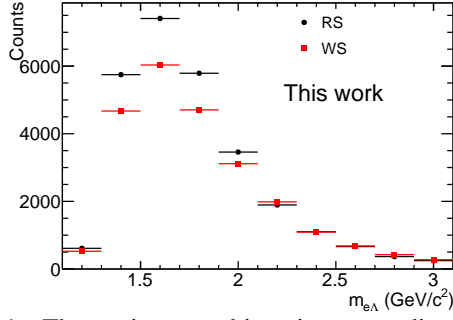


Figure 1: The p_T -integrated invariant mass distribution of $e\Lambda$ pairs. See the text for the definition of RS and WS.

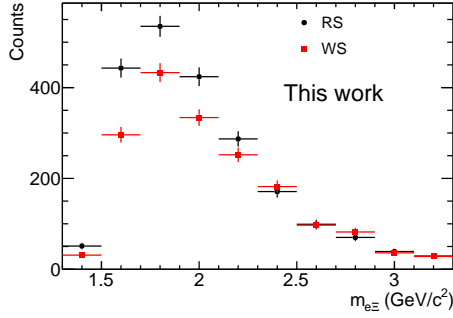


Figure 2: The p_T -integrated invariant mass distribution of $e\Xi$ pairs. See the text for the definition of RS and WS.

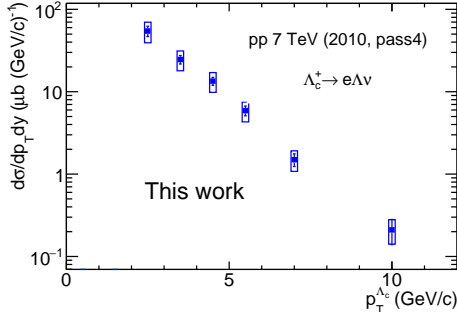


Figure 3: Production cross sections of Λ_c^+ as a function of p_T in pp collisions at $\sqrt{s} = 7$ TeV.

is shown in Fig. 3. Similarly, the p_T distribution of the Ξ_c^0 baryon for $|y| < 0.5$, corrected for the efficiency and acceptance, is shown in Fig. 4. In this case, the spectrum is not corrected for the branching ratio of $\Xi_c^0 \rightarrow e\Xi\nu$ and nor the feeddown from Ξ_b . Statistical and systematic uncertainties on the data points are shown as vertical bars and boxes, respectively. The systematic uncertainties include the uncertainties in track reconstruction, electron identification, Λ (Ξ) selection cuts, background subtraction, $\Xi_c \rightarrow e\Xi\nu \rightarrow e(\Lambda\pi)\nu$ contribution subtraction (only for Λ_c analysis), the unfolding procedure, the bottom baryon feed-down correction, branching ratio and the cross section determination in ALICE.

4. Summary and outlook

The analysis of Λ_c^+ and Ξ_c^0 using their semileptonic decays are presented. Currently, the consistency checks with the analyses using hadronic decay modes are ongoing. Once the analysis with semileptonic decays are validated in

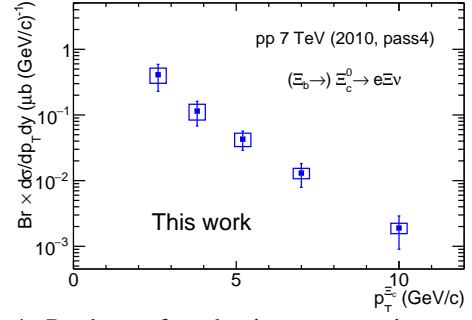


Figure 4: Products of production cross sections and branching ratios as a function of p_T for $\Xi_c^0 \rightarrow e\Xi\nu$ in pp collisions at $\sqrt{s} = 7$ TeV.

pp collisions, the analysis of Pb-Pb data is going to be performed to elucidate the “diquark” structure in the QGP.

References

- [1] S. H. Lee, K. Ohnishi, and S. Yasui, I. Yoo and C. M. Ko, Phys. Rev. Lett. **100** (2008) 222301.
- [2] K. Aamodt *et al.*, JINST **3** (2008) S08002.

Long range two-particle correlations in p -Pb collisions with the ALICE detector

Y. Sekiguchi, H. Hamagaki, and T. Gunji for the ALICE Collaboration

Center for Nuclear Study, Graduate School of Science, The University of Tokyo

1. introduction

Measurement of the correlations in the particle production as a function of the azimuthal angle and rapidity is very useful for investigating particle production in high-energy nucleus-nucleus collisions. The long-range correlations in the rapidity space in near-side angular pairs of dihadrons were firstly observed in Au-Au collisions at $\sqrt{s_{NN}}=200$ GeV at RHIC [1, 2]. The long-range correlations are derived from the collective expansion of the initial geometry fluctuations. Unexpectedly, a similar structure has also been observed in high-multiplicity pp collisions at 7 TeV by the LHC-CMS experiment [3]. The high-density gluon fields in small x (Bjorken x) of nucleus and the collision of two high-density gluon sheets can explain the long-range correlations [4]. This analysis aims to explore the partonic collectivity by measuring two-particle correlations in p -Pb collisions at $\sqrt{s_{NN}}=5.02$ TeV.

2. Analysis

The minimum bias data of p -Pb collisions at $\sqrt{s_{NN}}=5.02$ TeV in 2013 are used (~ 100 M events). The main subsystems in ALICE used in this analysis are the inner tracking system (ITS), time projection chamber (TPC), and VZERO detectors. The ITS consists of 6 layers of silicon detectors for vertex finding and tracking. The TPC is the main tracking detector and is used for particle identification by measuring the specific energy loss. They have a common pseudorapidity acceptance $|\eta| < 0.9$. The VZERO detector is composed of two arrays at $-3.7 < \eta < -1.7$ and $2.8 < \eta < 5.1$, respectively. Each array is segmented in four rings in the radial direction and each ring is divided in eight sections in the azimuthal direction. They are usually used to define centrality and event plane. To define centrality, Zero degree detector which is located in the Pb-going direction ($|\eta| > 8$) is used. The position of the reconstructed vertex along the beam direction is required to be within 10 cm from the detector center. The correlations between trigger particles and associated particles are measured as a function of the azimuthal angle difference $\Delta\phi$ and pseudo-rapidity difference $\Delta\eta$. The trigger particles are unidentified charged hadrons, while VZERO channels are used as associated particles. VZERO detector cannot measure transverse momentum p_T and the multiplicity in each channel is used as the number of tracks in the average ϕ and η of each channel. The correlation function as a function of $\Delta\eta$ and $\Delta\phi$ between two charged particles is defined as:

$$\frac{1}{N_{\text{trig}}} \frac{d^2 N_{\text{asso}}}{d\Delta\eta d\Delta\phi} = \frac{S(\Delta\eta, \Delta\phi)}{B(\Delta\eta, \Delta\phi)} \quad (1)$$

where N_{trig} is the total number of triggered particles in the event class and p_T interval, the signal distribution

$S(\Delta\eta, \Delta\phi) = \frac{1}{N_{\text{trig}}} \frac{d^2 N_{\text{same}} \times w_i}{d\Delta\eta d\Delta\phi}$ is the associated yield per trigger particle from the same event, and the background distribution $B(\Delta\eta, \Delta\phi) = \alpha \frac{d^2 N_{\text{mixed}} \times w_i}{d\Delta\eta d\Delta\phi}$ accounts for pair acceptance and pair efficiency. It is constructed by taking the correlations between trigger particles in one event and associated particles from other events in the same event class. w_i is the multiplicity in each VZERO channel. The α factor is chosen so that it is unity at the maximum bin. This correlation function is studied for different p_T intervals and different event classes.

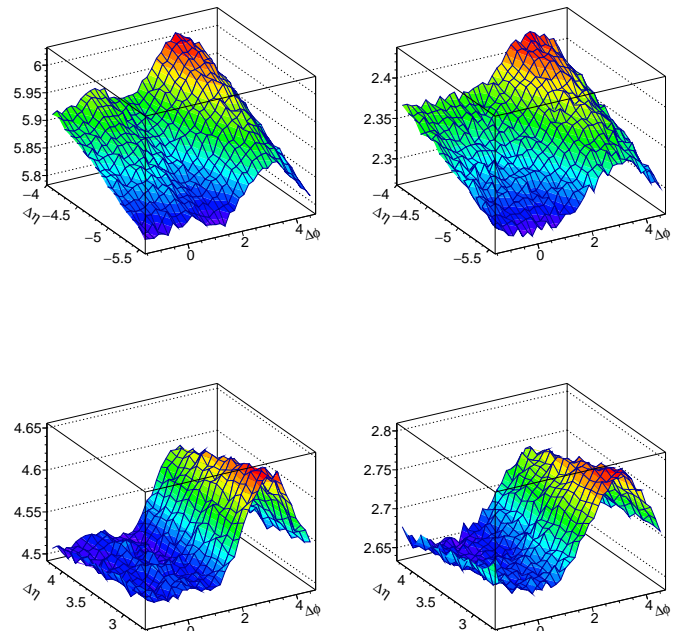


Figure 1: Associated yield per trigger particle for TPC-VZEROA (Ring0) (top) and TPC-VZEROC (Ring0)(bottom) with $1.0 < p_{T,\text{trig}} < 1.5$ GeV for the 0-20%(left) and 60-100%(right) event classes.

The correlation function in the peripheral collisions (60-100%) is subtracted from that in the central collisions (0-20%) to remove the auto-correlations from jets. Figure 2 shows the subtracted TPC-VZERO (Ring0) correlations for $1.0 \leq p_{T,\text{trig}} \leq 1.5$. The projection onto $\Delta\phi$ is shown in Fig. 3. Long range structure on both the near and away side is also observed in TPC-VZEROA and TPC-VZEROC correlations.

The data is described by a fit with Eq. (2) well. The second-order term is the dominant harmonic coefficient. To quantify the azimuthal anisotropy, the Fourier coefficients

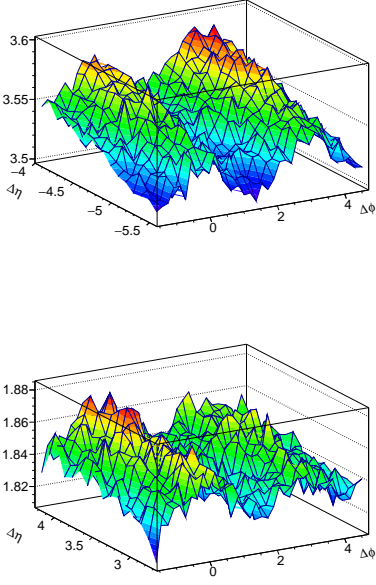


Figure 2: Associated VZEROA and VZEROC yield per trigger particle with $1.0 < p_{T,\text{trig}} < 1.5$ GeV for the 0-20% event class after the subtraction of the 60-100%(left) event class.

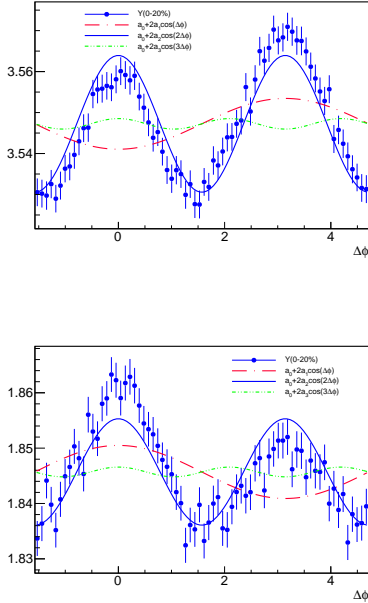


Figure 3: Projection of the subtracted correlation functions of the associated VZEROA(top) and VZEROC (bottom) yield per trigger particle with $1.0 < p_{T,\text{trig}} < 1.5$ GeV.

are extracted by fitting with the following function.

$$\frac{1}{N_{\text{trig}}} \frac{dN_{\text{asso}} \times w_i}{d\Delta\phi} = a_0 + 2a_1 \cos(\Delta\phi) + 2a_2 \cos(2\Delta\phi) + 2a_3 \cos(3\Delta\phi) \quad (2)$$

The $v_{n,n}$ can be obtained as:

$$v_{n,n} = \frac{a_n}{a_0 + b}, v_{n,n} = v_{\text{TPC}} \times v_{\text{V0AorV0C}}, \quad (3)$$

where b is the baseline which is the minimum of the 60-100% event class. Figure 4 shows the extracted $v_{2,2}$ coefficient as a function of p_T of trigger particles. $v_{2,2}$ of TPC-VZEROA is larger than that of TPC-VZEROC. So $v_{2,2}$ of Pb-going is larger than that of p -going.

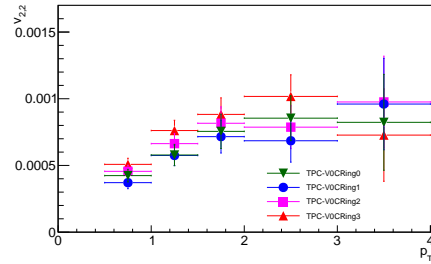
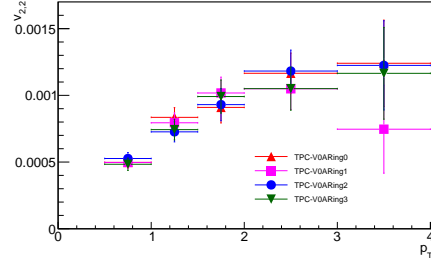


Figure 4: $v_{2,2}$ of TPC-VZEROA and TPC-VZEROC.

3. Summary and Outlook

Two-particle correlations between unidentified charged hadrons and channels of VZERO detectors in p -Pb collisions at $\sqrt{s_{\text{NN}}}=5.02$ TeV are measured. Long range correlations are clearly observed at $-5.6 < \Delta\eta < -2.3$ and $1.15 < \Delta\eta < 4.25$. The measurements of the particle productions with large rapidity gaps and the centrality dependence are important for quantifying the collective expansion. The Measurement of the correlations between V0A and V0C is ongoing.

References

- [1] STAR Collaboration, Phys. Rev. C80 (2009) 064912
- [2] PHOBOS Collaboration, Phys. Rev. Lett. 104 (2010) 062301
- [3] CMS Collaboration, JHEP 09 (2010) 091
- [4] K. Dusling and R. Venugopalan, Phys. Rev. D 87 (2013) 054014
- [5] ALICE Collaboration, Phys. Lett. B, 726 (2013) 164-177

π^0 and η measurement of direct photons via external conversions in high multiplicity pp collisions at 13 TeV

H. Murakami for ALICE collaboration

Center for Nuclear Study, Graduate School of Science, University of Tokyo

1. Introduction

The observations of collective behavior of hadrons in high multiplicity pp and p-Pb collisions at the LHC is one of the most surprising discoveries in recent years [1]. Such collective behavior indicates the formation of thermalized systems such as the new state of matter, quark-gluon plasma (QGP) even in small collision systems [2]. If the QGP is created in high-multiplicity events in small collision systems, the thermal photons are expected to be emitted from the QGP.

A direct photon is an ideal probe to study the properties of QGP, because unlike hadrons, it is an electromagnetic probe and has no final state interaction. To search for the thermal photons, decay photons from π^0 and η decays have to be subtracted from inclusive photons. Therefore, it is necessary to measure π^0 and η spectra in the same collision system,

In this report, current status of π^0 and η measurements in high multiplicity pp collisions at 13 TeV is presented.

2. Direct photon analysis overview

In hadronic collisions, photons are emitted at every stage of the space-time evolution. The emitted photons are categorized into two groups: direct photons and decay photons. The former photons are the thermal radiation and photons produced in elementary hard QCD process such as $q\bar{q} \rightarrow qg$ and $qg \rightarrow q\gamma$. The latter photons are decay photons from $\pi^0 \rightarrow \gamma\gamma$ and $\eta \rightarrow \gamma\gamma$. We first measure the inclusive photon spectrum and then statistically subtract the spectra of decay photons. The invariant yield of direct photons $\gamma_{\text{dir}}(p_T)$ can be expressed in terms of the inclusive photons $\gamma_{\text{inc}}(p_T)$ and that of decay photons $\gamma_{\text{dec}}(p_T)$:

$$\gamma_{\text{dir}}(p_T) = \gamma_{\text{inc}}(p_T) - \gamma_{\text{dec}}(p_T) \quad (1)$$

$$= \left(1 - \frac{\gamma_{\text{dec}}(p_T)}{\gamma_{\text{inc}}(p_T)}\right) \cdot \gamma_{\text{inc}}(p_T) \quad (2)$$

$$= (1 - R_\gamma^{-1}(p_T)) \cdot \gamma_{\text{inc}}(p_T), \quad (3)$$

where $R_\gamma(p_T)$ is the fraction of photons from π^0 and η decays. By using $R_\gamma(p_T)$, the common systematic uncertainties in decay photon and inclusive photon measurements are canceled. In order to obtain decay photons spectrum, π^0 and η which are the major sources of decay photons are measured by various techniques, which includes photon conversion method and calorimeter method. Other sources are estimated by using m_T scaling from measured π^0 and η p_T spectra. Therefore, the determination of the p_T spectra of neutral meson is very important.

3. Data analysis

In the ALICE experiment, photons are detected in two ways: the measurement of their energy deposit in calorime-

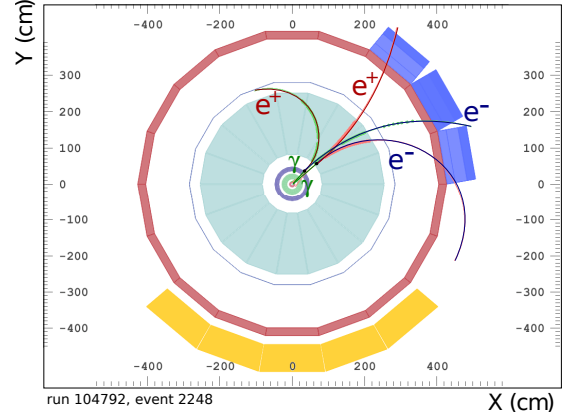


Figure 1: Event display of conversion electrons. Photon conversions occur at ITS and TPC.

ters or the measurement of e^+e^- pairs from photon conversions. The photon conversion method has an advantage of being able to measure photons down to low p_T , where thermal photons dominate.

The main tracking system [3] of the ALICE detector consists of the Inner Tracking System (ITS), the Time Projection Chamber (TPC) and the Time of Flight (TOF). Photons convert into e^+e^- in the material of the ITS and TPC as shown in Fig. 1. The event multiplicity is estimated with V0 detectors, which are made of two arrays of scintillation counters placed on forward and backward of the ALICE interaction point.

In 2015, ALICE successfully collected over 400 M events which correspond to 0.007 pb^{-1} in pp collisions at $\sqrt{s}=13 \text{ TeV}$ with minimum bias (MB) trigger and this data sample is used in this analysis.

The e^+e^- pairs from photon conversions are reconstructed with the V^0 reconstruction method. As shown in Fig. 2, the V^0 reconstruction method finds the secondary vertex for long-lived particles such as $\Lambda^0, \bar{\Lambda}^0, K_s^0, \gamma$. In order to select photons, electron identification cuts, based on the dE/dx in the TPC (Fig. 3) and the time-of-flight from the TOF detector are applied. In order to select pure photon samples from V^0 particles, several cuts such as opening angle between e^+e^- pairs, cut of cosine pointing angle, which is the angle between R and P (Fig. 2), and cut of the Armenteros-Podolanski plot [4] were applied. The Armenteros-Podolanski plot shows transverse momentum of the daughter particle versus longitudinal momentum asymmetry of two charged tracks. Figure 4 shows the two-photon invariant mass spectrum of reconstructed photon candidates. The solid line below data points is the combinatorial background calculated using the event mixing technique. On top of the background, a clear peak can

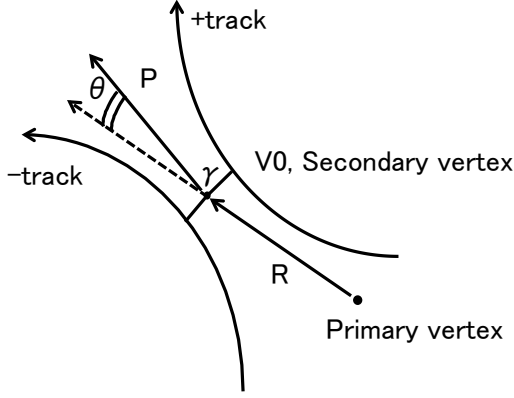


Figure 2: Topology of V^0 decay.

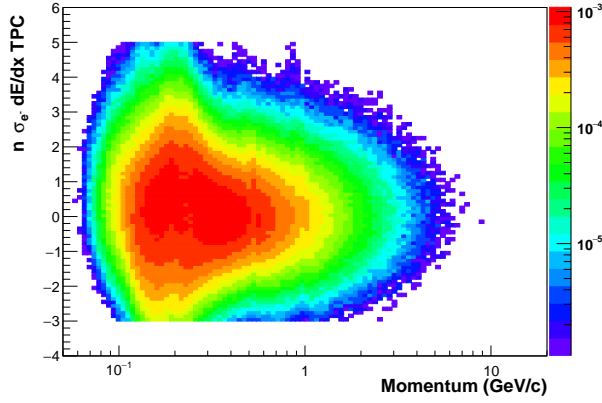


Figure 3: Specific energy loss (dE/dx) vs momentum for TPC tracks from pp collisions at $\sqrt{s}=13$ TeV

be seen at π^0 mass $0.135 \text{ GeV}/c^2$. After subtracting the background contributions, the raw yield of π^0 is extracted by bin-counting for each p_T bins as shown in Fig. 5. The raw yield of η is calculated as well as shown in Fig. 6.

4. Summary and outlook

In this report, the status of neutral meson analysis towards the direct photon are presented. Currently, corrections of the raw yield of π^0 , η , considering acceptance, reconstruction efficiency, event pile up, are begin estimated. Then, we will evaluate the invariant cross section of π^0 and η , and we will carry out an analysis focused on high multiplicity events.

References

- [1] The CMS collaboration, J. High Energy Phys. 09 (2010) 091.
- [2] C.Shen et al, arXiv:nucl-th/1504.07989v1(2015).
- [3] The ALICE Collaboration, JINST 3, S08002 (2008).
- [4] J. Podolansky and R. Armenteros. Phil. Mag. 45(13), 1954.

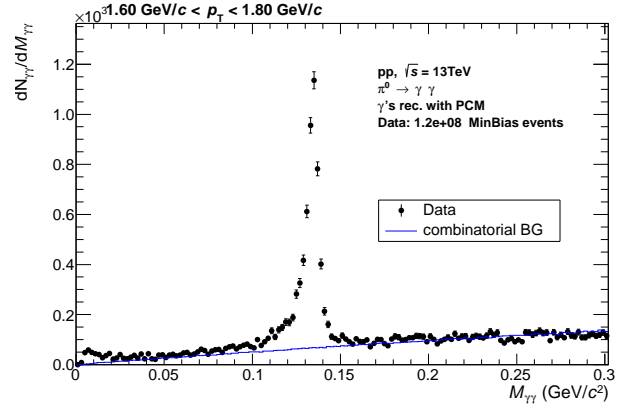


Figure 4: Invariant mass distribution of reconstructed photon pairs $M_{\gamma\gamma}$

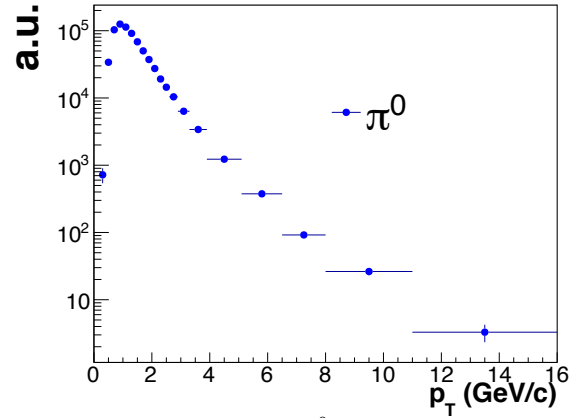


Figure 5: Raw yield of π^0 as a function of p_T

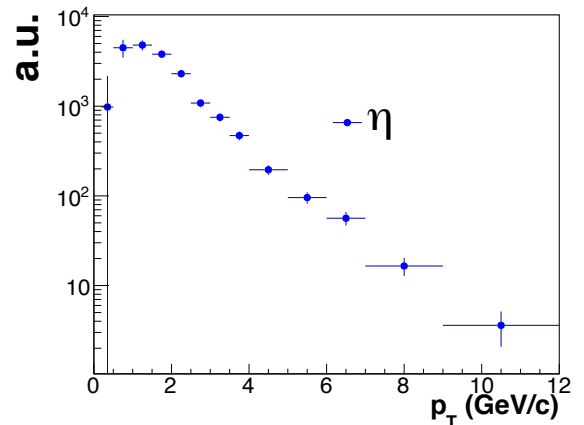


Figure 6: Raw yield of η as a function of p_T

Measurement of dielectrons from charm and bottom quark decays in p-Pb collisions with the ALICE detector

S. Hayashi, H. Hamagaki, and T. Gunji on behalf of ALICE Collaboration

Center for Nuclear Study, Graduate School of Science, University of Tokyo

1. Introduction

Heavy quarks (charm and bottom) are excellent probes for the study of the interactions between quarks and gluons inside the deconfined matter, the quark-gluon plasma (QGP) which is created in heavy ion collisions. In heavy ion collisions, they are produced at the early stage of a collision and pass through the QGP. Therefore they carry the key information on the interaction process in the QGP [1].

Since heavy quarks are produced via gluon fusion, gluon splitting, and flavor excitation at the LHC energy, cold nuclear matter effects such as gluon shadowing, gluon saturation, and Cronin effect cannot be negligible [2]. In order to study the cold nuclear matter effects and decide the initial condition in heavy ion collisions, p -A collisions are suitable. The measurement of electron-muon correlation at PHENIX in d +Au collisions, where the same Bjorken- x can be accessible in the midrapidity at the LHC ($x \sim 10^{-3}$), shows the large suppression of back-to-back correlation [3]. In p -Pb collisions at the LHC, transverse momentum spectra of open heavy flavors doesn't show any modification from the heavy flavor production in pp collisions [4]. However, electron and charged hadron correlation from heavy flavor decays in p -Pb collisions shows the long-range azimuthal correlation which may be due to the gluon saturation or collective expansion of the system [5]. Since electron-positron pairs from semi-leptonic decays of heavy quarks are dominant at $m_{ee} > 1 \text{ GeV}/c^2$ in the dielectron mass spectrum, the dielectron measurements at intermediate and high mass region ($m_{ee} > 1 \text{ GeV}/c^2$) can provide additional information of the heavy flavor production because they can cover wider phase space compared to the single electron analysis and include the correlation of the quark pair creation.

ALICE is one of the main experiments at the LHC and is dedicated for heavy ion collisions [6]. For the dielectron measurements from heavy quark decays, the online electron triggers with the Transition Radiation Detector (TRD) are very useful to enhance electron samples at $p_T > 2 \text{ GeV}/c$. They in particular enable to study the dielectrons from bottom quark pair decays. The integrated luminosity of the TRD triggered data in p -Pb collisions is 1.4 nb^{-1} . It corresponds to 20 times larger statistics than the current minimum bias data (0.067 nb^{-1}). In this report, the extraction of the dielectron spectrum with the TRD triggered data is reported.

2. TRD trigger performance

TRD consists of 6 layers of MWPCs and the radiators (polypropylene fiber mat) for the transition radiation [7]. It can be used for the electron identification at $p_T > 1 \text{ GeV}/c$. During p -Pb runs, two different electron triggers with TRD

were available. One (HSE) is the single electron trigger with an electron identification cut for $p_T > 3 \text{ GeV}/c$. The other is the single electron trigger with tighter online electron identification for $p_T > 2 \text{ GeV}/c$ (HQU). Data taken by both triggers are used in the analysis.

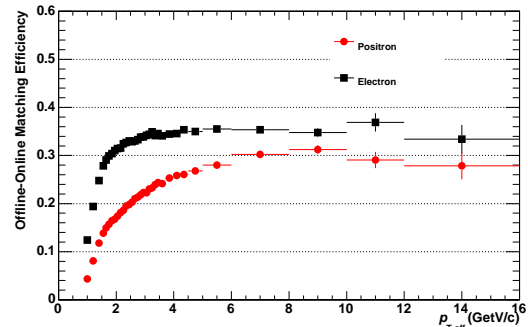


Figure 1: Offline-online track matching efficiency.

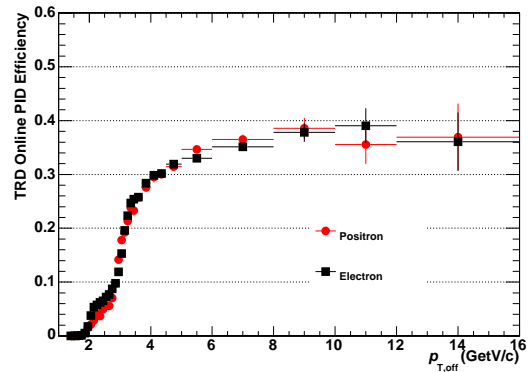


Figure 2: TRD online electron identification efficiency.

The trigger efficiency is evaluated using the minimum bias events.

The clean electron samples from photon conversions inside the detector material can be obtained by the secondary vertex reconstruction [6]. The TRD trigger efficiency can be divided into 2 components. One is the matching efficiency between TRD online tracks and offline (TPC) tracks. The other is TRD online electron identification efficiency. In order to evaluate the matching efficiency, the only triggered tracks which match to the offline tracks are selected. Figure 1 shows offline-online track matching efficiency. The online tracking performance of TRD depends on the charge sign due to the Lorentz angle (the angle of drifting electrons with respect to the electric field lines). Figure 2 shows the TRD online electron identification efficiency. The overall

trigger efficiency of negative and positive tracks including TRD acceptance is about 10% and 7%, respectively.

3. Signal Extraction

The background was estimated using the like-sign pairs in the same events. They contain not only the combinatorial background but also correlated pairs such as cross pairs which are produced from hadron decays with two e^+e^- pairs in the final state, jet contribution, and $B\bar{B}$ oscillation. Due to the acceptance difference between unlike-sign pairs and like-sign pairs, acceptance correction is needed. In this analysis, the acceptance correction factor is obtained as a function of invariant mass and pair p_T using the mixed events as following,

$$R = \frac{N_{+-} + N_{-+}}{2\sqrt{N_{++}N_{--}}_{mixed}}, \quad (1)$$

where N_{+-} and N_{-+} are the numbers of mixed unlike-sign pairs and N_{++} and N_{--} are those of like-sign pairs.

4. Correction

Pair efficiency are evaluated as follows. First, the single electron efficiency is obtained from the full Monte Carlo calculation using GEANT3 simulation. Pair reconstruction efficiency is calculated as the product of the single electron efficiency. Dielectron samples used for pair calculation are generated by hadronic cocktail calculation. Dielectrons from light meson decays ($\pi^0, \eta, \rho, \omega, \eta', \phi$) are generated from EXODUS according to the measured charged pion spectrum in p -Pb collisions and the m_T scaling. For heavy quarks contribution, dielectrons are generated using PYTHIA with the parametrization tuned for the NLO calculation [8]. Momentum smearing is also applied for all leg electrons in order to take into account the effects of the momentum resolution and Bremsstrahlung radiation. Figure 3

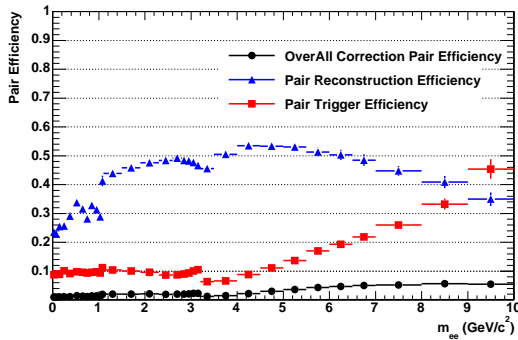


Figure 3: p_T integrated pair efficiency as a function of invariant mass. Triangular and square markers correspond to the pair reconstruction efficiency and TRD trigger efficiency for pairs, respectively.

shows the reconstruction efficiency as a function of invariant mass.

TRD trigger efficiency for pairs is extracted according to Eq 2,

$$\epsilon_{trig}^{pair}(m_{ee}, p_T^{ee}) = 1 - [1 - \epsilon_{trig}^{single}(p_{T1})][1 - \epsilon_{trig}^{single}(p_{T2})]. \quad (2)$$

Figure 4 shows the inclusive invariant yield of dielectrons as a function of invariant mass. There is a large deviation between data and cocktail calculation at higher mass region. This reason is still under investigation.

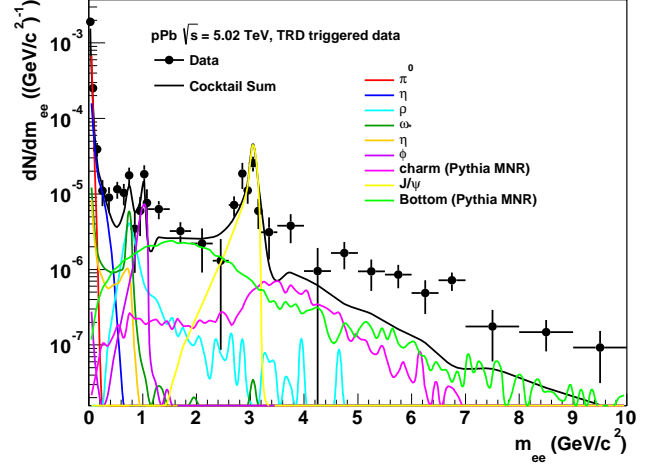


Figure 4: Upper panel: Corrected dielectron yield per inelastic p -Pb collision and the contribution of the hadronic cocktail simulations as a function of invariant mass.

5. Summary and outlook

The corrected yield up to $m_{ee} = 10 \text{ GeV}/c^2$ is obtained with the TRD triggered data. As a next step, the results will be combined with the results of the minimum bias events and $c\bar{c}$ and $b\bar{b}$ cross section will be deduced with the help of theoretical models.

References

- [1] M. Nahrgang *et al*, Phys. Rev. C 90, 024907 (2014), S. Cao *et al*, arXiv: 1505.01869 (2015).
- [2] H. Fuji, K. Watanabe, Nucl. Phys. A 920, 78-93 (2013).
- [3] A. Adare *et al*. (PHENIX Collaboration), Phys. Rev. C 89, 034915, (2014).
- [4] ALICE Collaboration, arXiv:1405.3452 (2014).
- [5] E. Pereira de Oliveira Filho, arXiv:1404.3983v2 (2013).
- [6] ALICE Collaboration, Int. J. Mod. Phys. A 29 1430044 (2014).
- [7] J. Klein, Nucl. Inst. Method. A 706 23-28 (2013).
- [8] M. Mangano, *et al*, Nucl. Phys. B373, 295 (1992).

Accelerator and Instrumentation

Development of polycrystalline CVD diamond detectors

S. Michimasa, M. Kobayashi, A. Stolz^a, M. Takaki, M. Dozono, H. Baba^b, S. Ota, K. Kisamori, H. Miya, H. Tokieda, K. Yako, H. Sakai^b, S. Shimoura, T. Uesaka^b, R.G.T. Zegers^a

Center for Nuclear Study, Graduate School of Science, University of Tokyo

^aNSCL, Michigan State University

^bRIKEN Nishina Center

The diamond is an attractive material for a radiation detector, and has actually a long history in radiation applications. The large displacement energy of the diamond crystal indicates its inherent radiation hardness. The small dielectric constant and the large band gap result in the low detector capacitance and the low leakage current, and thus low-noise level is expected. Its large mobility and saturation velocity of charge carriers enable very good timing resolution of signal responses, combined with a large breakdown field. However, the use of diamond detector was limited owing to the price, the size and the amount of impurity in the natural materials. The chemical vapor deposition (CVD) technique [1–3] has made it possible to create the high-quality diamond material with applicable size, and has provided opportunities as the practical use of diamond radiation detectors [4].

Based on the outstanding properties of the diamond, we have developed a CVD diamond detector as a thin and large-area counter with extremely good timing resolution. The detector development has been performed by the collaboration of CNS and NSCL. We produced a diamond detector with striped cathodes. Its photograph and cathode design are illustrated in Fig. 1. The cathode consists of two layers; 10-nm thick nickel and 100-nm thick gold. The nickel layer is important for the ohmic contact between a diamond and a gold layer. The material is polycrystalline CVD (pCVD) diamond crystal. The area and the thickness are $30 \times 30 \text{ mm}^2$ and 0.2 mm, respectively. The cathode is $28 \times 28 \text{ mm}^2$. The detector has one pad on one side (Side A), and 4 strips the other side (Side B). On the Side A, 4 readout wires are bonded to the corners. On the Side B, 2 readout wires are bonded to the both edges of each strip. The width of the four strips are 9, 5, 5, and 9 mm from the top. The width at the central region is narrower because the more intense beams hit the central part of the detector. Totally a detector has 12 readouts in order to deduce hit position and timing. SMA connectors are used to reduce signal strength loss in a radio frequency region ($\sim 10 \text{ GHz}$). In operation, 200 V was applied to the pad (Side A).

We made two pCVD diamond detectors for time-of-flight measurement with extremely good time resolution, and used the detectors in an experiment of direct mass measurement, which aimed at determining the masses of neutron-rich calcium isotopes [5]. The experimental setup is shown in Fig. 2. In the experiment, nuclear masses are determined by using the following relation:

$$m/q = \frac{B\rho}{c} \sqrt{\left(\frac{ct}{L}\right)^2 - 1}, \quad (1)$$

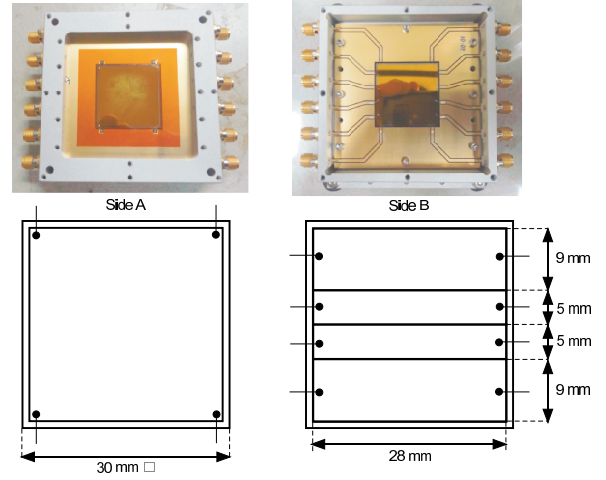


Figure 1: Photographs and cathode pattern of a manufactured diamond detector.

where m , q and c are the nuclear mass, the charge and the light velocity respectively. $B\rho$, t , L show magnetic rigidity, time of flight and flight length of the beam line, respectively. The diamond detectors were used to measure the time of flight, and installed at the BigRIPS F3 and SHARAQ S2 foci, which are 105 meters apart. Here, this report focuses on the performance of the pCVD diamond detector.

To deduce the time resolution of diamond detector, we used time difference between signal pulses from both edges of a strip of diamond detector. The analysis procedure is the same with that in Ref. [6]. The hit-position dependence of the time difference was compensated by using the position information deduced from the tracking detectors installed at each focus. Figure 3 shows the deduced time resolution as a function of the energy deposit in the diamond detector. The data points in the figure show the obtained values from the measurements. The circles were obtained in the present experiment, while a square was already reported in Ref. [6]. The time resolution was well reproduced by a power function of the energy deposit with an offset, which is deduced as $2828.1(\Delta E)^{-1.7525} + 10.00$ by a fitting.

The offset component in the deduced time resolution can be attributed to the intrinsic time resolution of the diamond detector and the time resolution of the data acquisition system. To estimate the time resolution of the data acquisition system, we analyzed the time jitter with changing a transfer fiber length, and the time resolutions of the data acquisition system are shown in Fig. 4. The detail was described in Ref. [6]. In this experimental setup, the signal transfer cable was 158 meters long. Here, we estimated time resolution of the data acquisition system in present experiment

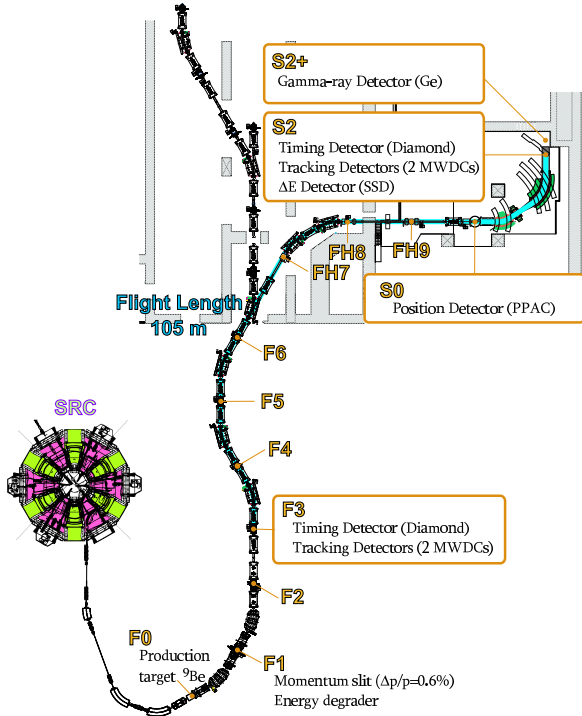


Figure 2: Detector setup for the experiment.

by two different functions, a linear or a square root of the length of the optical fiber. In the linear (square root) case, the resolution of the data acquisition system was estimated to be 10.2 (9.6) ps. This means that the offset of 10.0 ps is dominated by the resolution of the data acquisition system.

The intrinsic time resolution (σ_{int}) can be evaluated by $\sigma_{\text{int}} = \sqrt{\sigma_{\text{meas}}^2 - \sigma_{\text{daq}}^2}$, where σ_{meas} is time resolution in Fig. 3 and σ_{daq} is that in data acquisition (σ_{daq}), respectively. In cases of $\sigma_{\text{daq}} = 9.6\text{--}10.2$ [ps], the intrinsic time resolution of the diamond detector also shows in Fig. 3. Therefore, the intrinsic time resolution of the diamond detector is as good as 8 ps (σ) for 50-MeV deposit and 5 ps (σ) for 100-MeV deposit.

We studied the basic properties of pCVD diamond detectors. We also made a system to achieve the time resolution of 10 ps, which is enough to determine the mass with 200 keV resolution. Analysis of the mass measurement is in progress.

References

- [1] W.G. Eversole, U.S. Patent Nos. 3030187 and 3030188 (1958).
- [2] J.C. Angus, H.A. Will and W.S. Stanko, J. Appl. Phys. **39** (1968) 2915.
- [3] B.V. Deryaguin *et al.*, J. Cryst. Growth **2** (1968) 380.
- [4] The RD42 Collaboration, Nucl. Instr. and Meth. A **435** (1999) 194.
- [5] M. Kobayashi *et al.*, *elsewhere in this report*.
- [6] S. Michimasa *et al.*, Nucl. Instr. and Meth. B **317** (2013) 710.

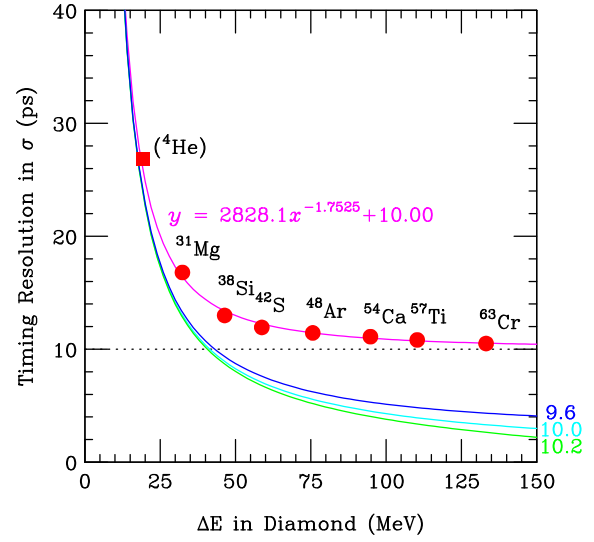


Figure 3: Time resolution of the CVD diamond detector as a function of the energy loss. The circle (square) points show the obtained values for isotopes in the present (previous [6]) experiment. The red curve is obtained by fitting to the data. The lower three curves show intrinsic time resolution of a diamond detector when the time resolutions of the optical fiber are 9.6, 10.0 and 10.2 ps(σ), respectively.

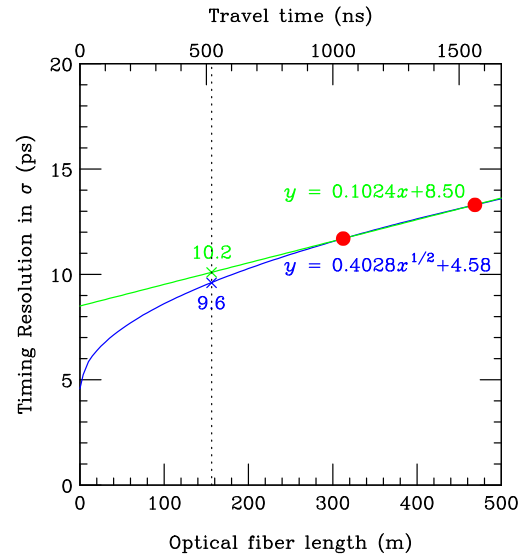


Figure 4: Timing resolution of the data acquisition system as a function of the optical fiber length or the travel time. Solid curves show estimations by two different functions.

Development of particle identification method using fast response detectors

S. Ota, J. Zenihiro^a, H. Takeda^a, S. Michimasa, M. Dozono, M. Matsushita, K. Kisamori, M. Kobayashi, Y.N. Watanabe^b, Y. Kiyokawa, Y. Yamaguchi, S. Masuoka, S. Shimoura, K. Yako, N. Imai, H. Baba^a, T. Kubo^a, K. Yoshida^a, N. Inabe^a, N. Fukuda^a, H. Suzuki^a, D.S. Ahn^a, D. Murai^a, H. Sato^a, Y. Sato^a, H. Otsu^a, and T. Uesaka^a

Center for Nuclear Study, Graduate School of Science, University of Tokyo

^aRIKEN Nishina Center for Accelerator-based Science

^b Department of Physics, Faculty of Science, University of Tokyo

Recent development of accelerators enables us to utilize high-intensity primary beams and resultant high-intensity secondary beams at RIBF. Available intensity of the secondary beam becomes more than 10^5 cps at BigRIPS. However, when we apply the standard particle identification method of TOF- $B\rho$ - ΔE for such high-intensity beams, in particular around $Z=50$ beams, three problems arise.

One serious problem is that the resolution of ΔE becomes worse due to the pile up of the slow signal from the ionization chamber, thereby reducing the resolution of atomic number. The other problem is the radiation damage to plastic scintillators that are used to measure the TOF. In addition to these problems, the PPAC had a larger discharge probability with the high-intensity beams than that with the low-intensity beams. In this paper, we report a new particle identification method using detectors with the high radiation hardness and the fast time response at BigRIPS, in order to resolve these problems and to identify the high-intensity secondary beams.

We propose the new particle identification method of TOF- $B\rho$ - $B\rho$, where ΔE is not measured directly. An energy degrader is placed at the dispersive second focus (F5) and the energy loss at the degrader is indirectly used for determining atomic number. Assuming that mass number and charge do not change at the degrader, the energy loss at F5 is expressed by $\Delta E = (\gamma_{35} - 1)Am_u - (\gamma_{57} - 1)Am_u = cZ(\frac{B\rho_{35}}{\beta_{35}} - \frac{B\rho_{57}}{\beta_{57}})$, where β and γ is the ratio of velocity to the speed of light and the Lorentz factor, respectively. The subscription 35 (57) indicates the value is the one between two foci F3(F5) and F5(F7). Combining this expression with the Bethe-Bloch formula for the energy loss, $\Delta E \sim d\frac{Z^2}{\beta_{35}^2}$, where d is the thickness of the degrader, and assuming that the ion is fully stripped, namely $Q = Z$, the atomic number can be obtained as,

$$Z = C\left(\frac{B\rho_{35}}{\beta_{35}} - \frac{B\rho_{57}}{\beta_{57}}\right)\frac{\beta_{35}^2}{d}. \quad (1)$$

In order to overcome the difficulty of radiation damage and discharge, plastic scintillators and PPACs are replaced with diamond detectors [1] and low-pressure multi-wire drift chambers [2] (LP-MWDC), respectively.

The test experiment was performed using a ^{132}Sn beam at incident energies of 100 and 200 MeV/u. The typical intensity was 1×10^6 cps and the maximum intensity was 3.4×10^6 cps. Figure 1 shows the correlation between the atomic numbers deduced using the new method and the

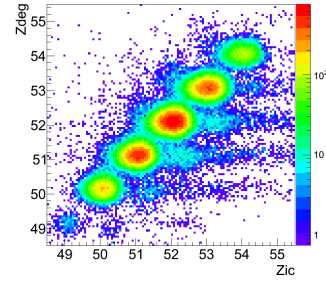


Figure 1: Correlation between the atomic numbers deduced using the new method (Zdeg) and the standard method (Zic).

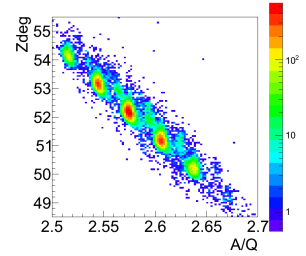


Figure 2: Intensity dependence of the correlation between the atomic number and the mass-to-charge ratio in the new method for 10^4 cps (left) and 10^6 cps (right).

standard method, which are shown by the horizontal and vertical axes, respectively. There is a clear correspondence of two values, which validates that the new method extracts the correct atomic number. Figure 2(a) shows the plot for particle identification with a low-intensity beam (less than 10^3 cps). Vertical and horizontal axes show the atomic number and mass-to-charge ratio, respectively. Figure 2(b) shows the same plot with the high-intensity beams (about 10^6 cps). Efficiency seems worse for the high-intensity beams, which may be caused by wrong position deduction of LP-MWDC, which will be recovered by further analysis.

References

- [1] S. Michimasa *et al.*, Nucl. Instrum. Meth. **B317** (2013) 710.
- [2] H. Miya *et al.*, Nucl. Instrum. Meth. **B317** (2013) 701.

Development of the gamma-ray interaction point calculation algorithm using the GRAPE Ge detector

Y. Yamamoto, N. Aoi, Y. Fang, E. Ideguchi, S. Noji, and T. Yamamoto

Research Center for Nuclear Physics, Osaka University, Ibaraki, Osaka 567-0047, Japan

We have been developing an algorithm to obtain gamma-ray interaction points in a Ge detector from the signal pulse shape. The determination of three-dimensional positions of gamma-ray interaction points is an essential technology for the gamma-ray tracking technique, which is the most advanced gamma-ray detection method [1] to enable us Compton suppression without additional Compton shields. The capability of an accurate position determination is also useful for Doppler-shift correction for the energy of gamma-rays emitted from fast moving sources. In this report, we present the development of the calculation method of signal shapes using the CNS GRAPE Ge detector [2].

When a gamma ray interacts with an electron in the Ge crystal, the recoiled electron, which has received part of or all of the gamma-ray energy, creates electron-hole pairs along its trajectory. These electrons and holes move towards the anode and cathode, respectively, being swept by the electric fields applied between these electrodes. The motion of the electrons and holes causes the induced signal on the electrodes. Depending on the gamma-ray interaction points, the trajectory of the electrons and holes are different, and therefore the induced signal shape depends on the gamma-ray interaction point. By utilizing this feature, gamma-ray interaction point can be determined from the shape of the signals. For this purpose, we develop a calculation method of the signal shape as a function of gamma-ray interaction points.

The calculation consists of three steps; 1) construction of the electric field in the crystal, 2) calculation of the motion of electrons and holes created at the gamma-ray interaction points, and 3) calculation of the induced signal.

We use the CNS GRAPE module [2], which consists of two disc-shaped planar Ge detectors with dimensions; 70 mm in diameter and 20 mm in thickness. An anode and cathode of each detector are of circular shape with 60 mm diameter. The cathode is divided in 3×3 segments. The outer most rings with 5 mm width surrounding the anode and cathodes are used as a guard ring. High voltage of +2500 V is applied to the anode while the cathode is grounded. The Ge crystal is of p-type with impurity concentration of $0.75 \times 10^{10} / \text{cm}^3$. With these conditions electric field is calculated by the finite element method using the OPERA code [3]. The motion of electrons and holes created at a given position is calculated using the Runge-Kutta method based on the electric field calculated above. Finally, we calculate induced charge at each position of electrons and holes using the weighting potential method [4]. By these methods, we are able to calculate the induced signals of each segment as a function of time for a given gamma-ray interaction point. Figure 1 shows calculated net signals

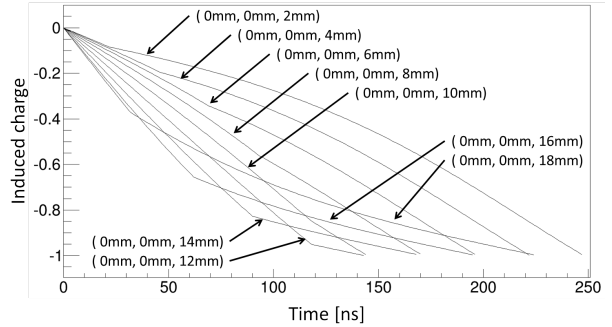


Figure 1: Calculated net signals for several different interaction points indicated by (x,y,z) . See the text for the definition of the coordinates.

for events with several gamma-ray interaction points along Z direction. The coordinate is defined so that the center of the anode is the origin. The anode is defined as the XY plane and the cylindrical axis is defined as the Z direction. Each pulse shape is dependent on the interaction point.

The result of the calculation has been evaluated by comparing with the signal shape experimentally measured. Figure 2 shows the experimental setup used in this work to observe the pulse shape for a scattering event at a given position. The Ge crystal is irradiated with gamma rays from

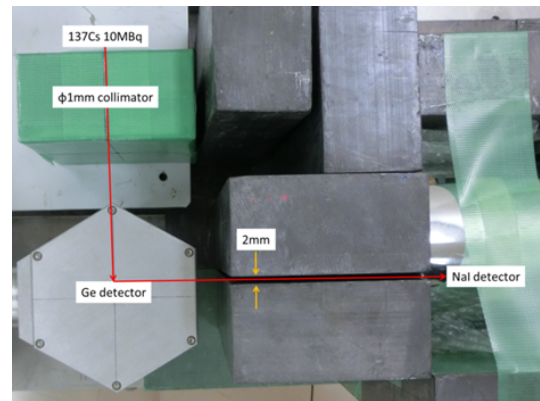


Figure 2: Experimental setup for the measurement of the signal shape.

a 10 MBq ^{137}Cs source through a collimator of a 50 mm-thick Pb block with a hole of a 1 mm diameter. The gamma rays scattered by the Ge crystal are measured by a $5'' \times 3''$ NaI(Tl) detector through a slit placed at 90 degrees with respect to the gamma-ray incident axis. The slit is a 100 mm-thick Pb block with a 2 mm gap. The signals from the Ge detector and the NaI(Tl) detector were read out by the GRETINA digitizer [5] with 14 bits ADC operating at 100 MHz sampling. The multiply scattered events were eliminated by requiring the energy deposits in Ge and NaI(Tl) to be 373 ± 1 keV and 290 ± 90 , respectively. By these con-

ditions, the gamma-ray scattering position is limited to the intersection between the collimator and the slit within 1.5 mm accuracy. In this setup, we obtained 2 events a day. The signal shape for the selected events are shown in Fig. 3. Black curve is the measured waveform. Blue curves show

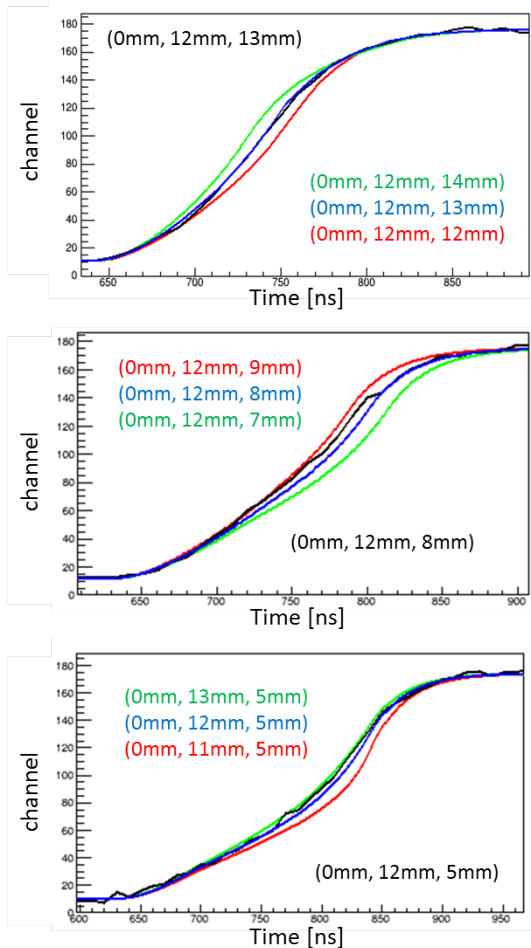


Figure 3: Comparison of measured and calculated signals. Black curves show the measured signal. Blue, red, and green curves are the calculations.

the result of the calculation for the event at the center of the irradiated region, while the red and green curves show those for the positions deviated from the center by ± 1 mm. Acquired signals are distorted due to finite time response of the preamplifier. Calculated signals are corrected for according to the integration time constant of $\tau = 28$ ns so that the measured signal shape is reproduced. One can see that the calculation reproduces the observed signal shape very well.

To summarize, we have calculated the induced signals for the events at given interaction points. We have also measured the signal shapes for given gamma-ray interaction points. From the comparison of measured and calculated net signals, we confirmed that a calculated net signal reproduces a measurement signal. For the next step, we will take signals from all the electrodes including the neighboring ones, with which the position in X and Y direction will be determined.

References

- [1] M. A. Deleplanque, Nucl. Instr. Meth. Phys. Res. A 430 (1999) 292.
- [2] S. Shimoura, Nucl. Instr. Meth. Phys. Res. A 525 (2004) 188.
- [3] <http://www.cobham.com/>
- [4] Zhong He, Nucl. Instr. Meth. Phys. Res. A 463 (2001) 250.
- [5] J. T. Anderson, IEEE Nuclear Science Symposium Conference Record (2007) N25-6.

Performance Evaluation of CAT in $^{132}\text{Xe}(\text{d}, \text{d}')\text{ Measurement}$

C. S. Lee^{a,b}, S. Ota^a, H. Tokieda^a, T. Uesaka^b

^aCenter for Nuclear Study, Graduate School of Science, The University of Tokyo

^bNishina Center for Accelerator-based Science, RIKEN

A low-pressure gaseous active target, CNS Active Target (CAT), has been developed for a deuteron inelastic scattering off unstable nuclei [1]. The CAT consists of a GEM-TPC and Si detectors. Three dual gain THGEMs (400 μm -thick), where the electrodes of the beam region ($\pm 10\text{ mm}$ from the centre axis) and the recoil region (rest of the active area, left and right sides) are separated individually, are employed as an amplification apparatus of the GEM-TPC to control the magnitude of gas gain at each region, independently. Properties of a triple and a double THGEM configurations in a low-pressure deuterium were well-studied by corresponding authors [2, 3] in a test chamber. In this article, evaluations of the gas gain, the charge resolution, and the attachment coefficient of the CAT in $^{132}\text{Xe}(\text{d}, \text{d}')\text{ measurement}$ are reported.

Figure 1 shows a schematic view of the setup of the CAT. An alpha source is employed to evaluate the gas gain and the charge resolution. Considering the previous study for gain [3], expected gain for the recoil region is between 2000 and 3000 at this gas pressure, 40.4 kPa D_2 . A typical charge

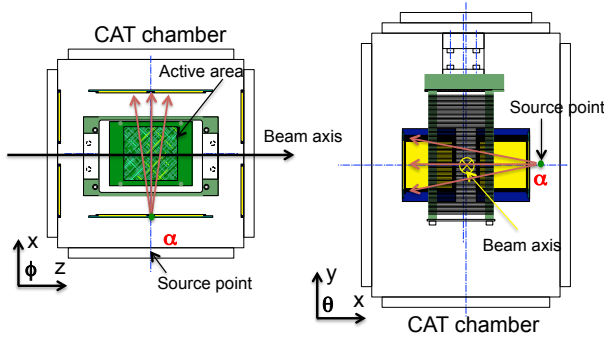


Figure 1: A schematic view of the setup of the CAT.

distribution at a single readout pad contributed by alpha particles from the source is shown in the Fig. 2 (left). From

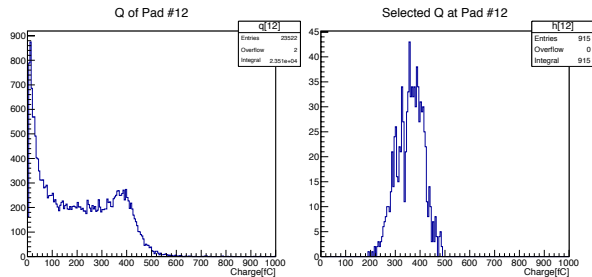


Figure 2: A typical charge distribution at a single readout pad ID 12, contributed by alpha particles from the source (left) and a selected charge distribution at a single readout pad contributed by alpha particles whose path is well defined (right).

this charge distribution, an appropriate value of the charge

for the evaluation of the gas gain should be selected. Since the position of the alpha source is well-defined in the CAT chamber, it is feasible to manually draw a straight line from the source point to a specific readout pad on the xz -plane as a path of α -particle by assuming the incidence angle for xy -plane $\theta \simeq 0$. In fact, it is probable to select such an event like the manually drawn line by restricting the hit pattern of the readout pad and the difference of the drift time (arrival time of electrons from the trigger timing) between hit pads. By following this procedure to choose the event whose the length of the path is well-known, the calculation of the energy loss ΔE and the initial charge Q_i can be unambiguously done. Figure 2 (right) shows the selected charge distribution at the pad ID 12 for instance. By making use of a Gaussian fitting to Fig. 2 (right), $Q_{\text{pad}}(\theta \simeq 0)$ can be derived for the evaluation of the gas gain. Q_i is derived from energy loss calculation. Because of an insufficient gain (under 100) on the beam region, the number of selectable events of α -particles on the beam region is too small to fit with a Gaussian, therefore, the evaluation of gain only for the recoil region has been carried out for this report. Figure 3 shows the obtained results of evaluation of the effective gas gain G_{eff} at 40.4 kPa deuterium. The mean value of G_{eff} was 2505 and the standard deviation was 269.8.

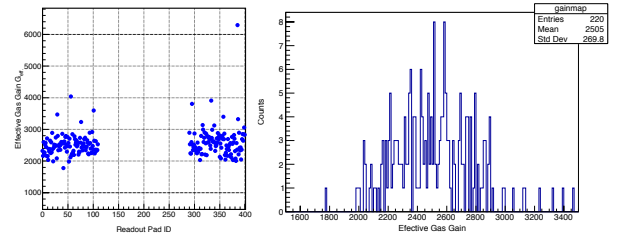


Figure 3: Correlation between gain and each readout pad ID on the recoil region (left) and the distribution of gain (right).

Together with G_{eff} , the charge resolution should be also properly evaluated. An approach by comparing the charges of neighbouring pads to a certain chosen pad is attempted to evaluate the charge resolution. In order to determine the initial charge correctly, specific events where the solid angle for the α -particle detection from the source is almost zero is selected by restricting the hit pattern and the drift time of the event, as usual. To ensure that the energy loss of the alpha particle on each pad to be evaluated, a pair of two neighbouring pads is considered. Each amount of summed-charge for the pair is expressed as Q_1, Q_2 and Q_3 . Assuming that the path length, i.e. the energy loss, is almost constant for each pair of readout pads.

Concentrating on the pair in the middle which is denoted as Q_2 , the residual from the mean of neighbouring charges ε is defined as $\varepsilon = Q_2 - (Q_1 + Q_3)/2$. Assuming the charge



Figure 4: A schematic view of the path of particles and pairs of the readout pads for the evaluation of the charge resolution.

resolution $\delta Q = \delta Q_1 = \delta Q_2 = \delta Q_3$, then δQ is described as $\delta Q = \delta \varepsilon \times \sqrt{2/3}$. Following this procedure, the charge resolution δQ can be deduced from Fig 5.

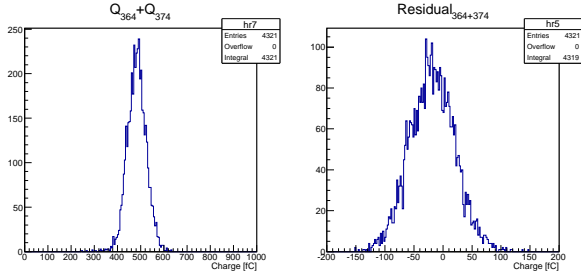


Figure 5: A selected charge distribution for a pair of pad ID 364 and 374 as Q_2 (left) where the location is on the centre of readout pads on the right side of the beam, and the distribution of the residual ε (right).

By make fitting of the charge distribution and residual above, $\delta Q/Q$ is 15.14 % (FWHM) for this example.

In the case of our apparatus, the CAT, the main reason for the electron attachment is a contamination of the air influx into the CAT chamber and other gas line pipes. Because the attachment of initial electrons during drift toward the amplification stage affects significantly to the evaluation of the initial charge Q'_i right before the amplification by GEMs, the attachment coefficient η , as defined below, should be accurately determined. When N_0 electrons are formed initially by an α -particle and, as a result of attachment, N electrons are left at a distance x from the point of formation. The number dN attached in a distance x is described as $dN = -\eta N c dx$, where η is the electron attachment coefficient expressed as the probability of attachment per cm, of travel in the field direction and c is unit concentration, in parts per million, of the attaching gas in the non-attaching carrier. Q'_i is represented by $Q'_i = Q_i e^{-\eta \cdot L_{\text{drift}}}$, where Q_i indicates the initial charge at the point of formation and L_{drift} is the total drift length of electrons. An estimation of η is given by the charge ratio between two selected events where the drift lengths are different each other but ΔE and, naturally, Q_i are identical. Here, following assumptions are made: the effective gas gain G_{eff} of GEMs is constant in a certain properties of the gas; and the drift velocity v_{drift} of electrons is well estimated by MAGBOLTZ simulation. The second term of the assumption about the drift velocity is practically tested by our collaborators for the inside of the CAT by using an alpha source with a slitted silicon detector, and it turned out that the difference between the measured and simulated values of the drift velocity is almost negligible. If the events of alpha particles, where the drift length L_{drift} is almost zero at the most distant point of

the readout pad from the source point, are chosen, Q'_i and Q_i become the same in principle. After the incident angle of such alpha particles ($L_{\text{drift}} \simeq 0$) are calculated as θ_0 and relevant events are chosen, the events which have the incident angle toward the exactly opposite direction $-\theta_0$ can be also chosen. Those two events have the same energy loss and initial charge Q_i^0 but different Q'_i (Q'_i will be used for a distinguishing). By taking the ratio of the collected charge $Q_{\text{pad}}(\theta, L_{\text{drift}})$ at the same readout pad for these two cases, following relation is obtained.

$$\eta = \frac{1}{L_{\text{drift}}} \ln \left(\frac{Q_{\text{pad}}(\theta_0, L_{\text{drift}} \simeq 0)}{Q_{\text{pad}}(-\theta_0, L_{\text{drift}} \neq 0)} \right) \quad (1)$$

Hence, η can be estimated by using this relation and a typical value of η was around 0.02 cm^{-1} . According to the MAGBOLTZ simulation for η , it is proportional to the density of oxygen in percent (see Fig. 6), therefore, the oxygen density can be also estimated by the correlation between η and O_2 density. It turned out that the oxygen density in the CAT during the measurement was near 0.01 %.

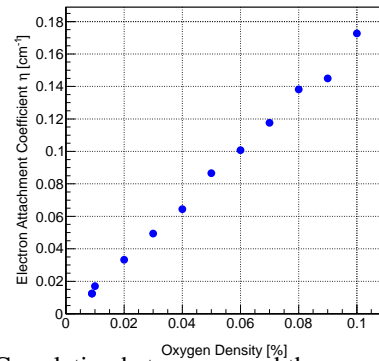


Figure 6: Correlation between η and the oxygen density in %. Each value is obtained from the MAGBOLTZ simulation at 40 kPa deuterium gas for a static electric field of $\simeq 1 \text{ kV/cm/atm}$.

References

- [1] S. Ota *et al.*, CNS Annual Report **2011** CNS-REP-90(2013) 70-71.
- [2] C.S. Lee *et al.*, CNS Annual Report **2014** CNS-REP-94(2016) 55-56.
- [3] C.S. Lee *et al.*, JINST **9** (2014) C05014.

Development of Data Acquisition System for Ge Detectors Array for Multi Gamma-Ray with DSP

Y. Yamaguchi, S. Shimoura, K. Wimmer, N. Imai, N. Kitamura

Center for Nuclear Study, Graduate School of Science, University of Tokyo

1. Introduction

In-beam γ -spectroscopy is a powerful tool for investigating nuclear structure. We have been developing data acquisition and coincidence analysis system for CNS-GRAPe(Gamma-Ray detectors-array with Position and Energy sensitivity) [1]. CNS-GRAPe consists of 18 Ge detectors, and each detector has two Ge crystals each of which is segmented into 9. Therefore, 18 channels have to be read in one Ge detector, which results in a difficulty of using CNS-GRAPe as a detectors-array because of many read-out circuits that have to be controlled.

For the reasons above, we have developed APV7110 which is a digital signal processor (DSP) for γ -ray spectroscopy with Techno-AP. APV7110 is capable of converting 18ch analog signals into digital ones at the same time (Thus, it can be used for one Ge detector) and data transportation by using ethernet, so there needs to be a software to extract data from APV7110. What is more, two or more DSPs should be synchronized by using time stamps when CNS-GRAPe is used as a detectors-array. Therefore, when data from CNS-GRAPe is to be analyzed, the data should be sorted by using time stamps that each event contains, and there needs to be a software that can do that.

In this article, data-acquisition system and data-sorting system that we have developed are introduced.

2. Data Acquisition System and Coincidence Analysis

A circuit diagram in APV7110 is shown in Fig. 1. Advantages of APV7110 are:

1. One CPU can be applied to one Ge detector, so that CPU cannot be a bottleneck.
2. It provides high energy resolution thanks to the trapezoidal filter.
3. It sends data with a size of 1 KB/event (containing pulse shape data) under a rate of 9kHz thanks to SiTCP read-out.

First, we have developed a data acquisition system for one Ge detector. Functions of the data acquisition system are :

1. Controlling registers(gain, threshold, etc..) in APV7110.
2. Acquiring data from APV7110 via ethernet, and store them in HDD.
3. Decoding data to analyzable ones according to data-structure of APV7110.

Spectra obtained by using the data acquisition system are shown in Fig. 2. It clearly shows the system is working properly.

Secondly, we developed data acquisition system for multi Ge detectors. In order to test the system, we used 3 Ge detectors, and 3 APV7110. All APV7110 are synchronized

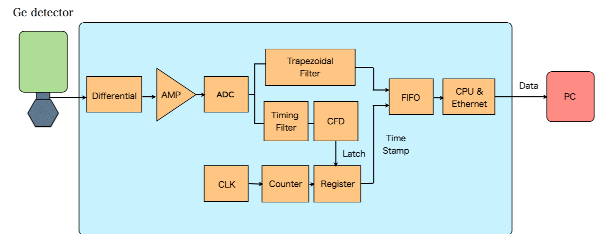


Figure 1: A circuit diagram in APV7110. Once analog signals are sent, they are converted into digital signals, and go through two different kinds of filter, one of which is a trapezoidal pulse shaping filter, and the other is a timing filter. After that, data is sent to a computer via ethernet.

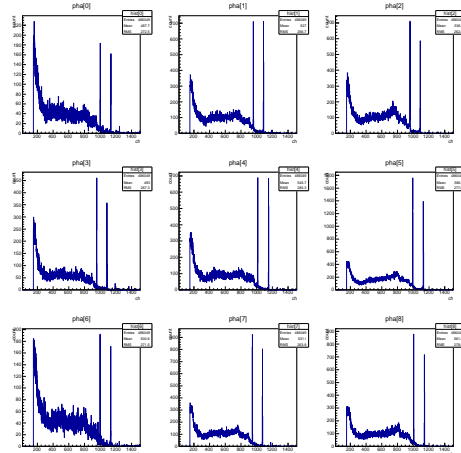


Figure 2: Spectra obtained by using the data acquisition system for one Ge detector (not calibrated). The data was taken with ^{60}Co , and the spectra is from one crystal of the Ge detector, so 9 spectra are shown.

by using clock signals. In order to do the coincidence analysis, we developed an event-builder "Fruit Juice" for CNS-GRAPe. Event-building procedure is:

1. Each of APV7110 sends data from a Ge detector to the computer.
2. Fruit Juice searches all data that have been taken, and sort events according to time stamps and event-build window that users can define.
3. Time-sorted events are packed into one event, and the data is ready to be analyzed.

The data were taken successfully, and Fig. 3 is the plot of events in which γ -ray scattered from one crystal to the other one in the same detector. It shows that Compton scattering events are obtained with Fruit Juice. Thus we succeeded in event-building with 2 different crystals in one detector. However, we could not obtain the evidence that γ -ray scattered from one "detector" to another. Probably it is because that among APV7110s, time-stamps are not synchronized

correctly because of an offset of starting time of data acquisition of each APV7110.

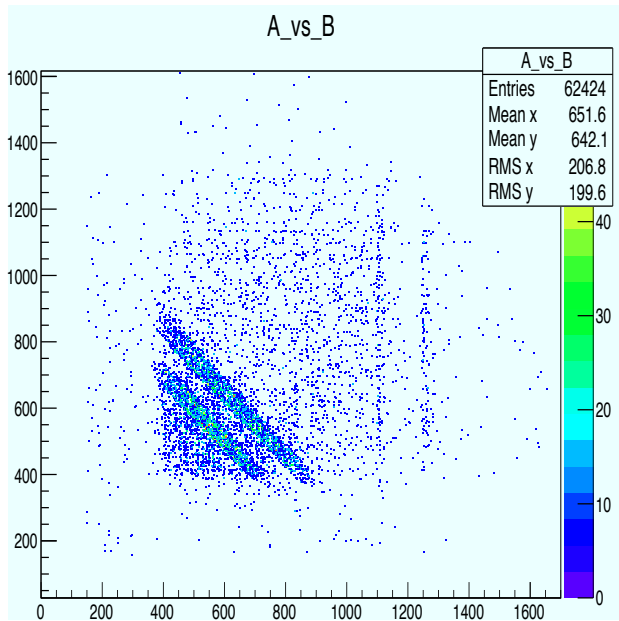


Figure 3: A spectrum obtained with an event-builder "Fruit Juice" for CNS GRAPE (Both X and Y axis are ch, Not Calibrated). A source used for this measurement was ^{60}Co . Two diagonal lines show that γ -ray compton-scattered from one crystal(A) to the other one(B) in each detectors. γ -ray is photo-absorbed in the crystal B.

3. Summary and Future Plan

As a summary, we have succeeded in developing a data acquisition system for CNS GRAPE with DSP "APV7110". We have developed an event-builder "Fruit Juice" for CNS GRAPE, and succeeded in event-building of data obtained from multi Ge detectors. We have successfully obtained the evidence of γ -rays that compton-scattered from one crystal to the other one in the same detector, but have not seen events in which γ -rays scattered in one detector to another. We think this is because time-stamp offset due to the data acquisition starting time difference among APV7110s, so this problem is to be solved soon. Here is our future plan:

- 1.The dead-time of APV7110 needs to be measured.
- 2.Four or more APV7110 operation should be tested because we think that we had better apply one computer to three APV7110 due to data transportation traffic, so for example, if we want to use six APV7110, we need two computers operating at the same time.
- 3.Pulse shape analysis needs to be done in order to be able to correct the doppler-shift in energy spectrum for in-beam experiments.

References

- [1] S. Shimoura, Nucl. Instr. and Meth. A **525** (2004) 188.

Pulse-height defect in single crystal CVD diamond detectors

O. Beliuskina, A.O. Strelakovsky^a, A.A. Aleksandrov^a, I.A. Aleksandrova^a, H.M. Devaraja^b,
 C. Heinz^c, S. Heinz^{c,d}, S. Hofmann^d, S. Ilich^a, N. Imai, D.V. Kamanin^a, M. Kis^d,
 G.N. Knyazheva^a, C. Kozhuharov^d, E.A. Kuznetsova^a, J. Maurer^d, G.V. Mishinsky^a,
 M. Pomorski^e, Yu.V. Pyatkov^a, O.V. Strelakovsky^a, M. Träger^d and V.E. Zhuchko^a

Center for Nuclear Study, Graduate School of Science, University of Tokyo

^a*Flerov Laboratory of Nuclear Reactions, JINR*

^b*Manipal Centre for Natural Sciences, Manipal University*

^c*Justus-Liebig-Universität Gießen, II. Physikalisches Institut*

^d*GSI Helmholtzzentrum für Schwerionenforschung GmbH*

^e*CEA, LIST, Diamond Sensor Laboratory, CEA/Saclay*

It has long been known that the response of semiconductor detectors to heavy ions is complicated by the presence of a pulse-height defect (PHD), such that heavy ions produce a smaller pulse height than lighter ions of the same kinetic energy [1–4]. The pulse height defect ΔE is the difference between the true energy E_t of an ion incident on a detector and its apparent energy E_a as given by the response curve for light ions such as protons and alpha particles.

The energy-response characteristics for heavy ions are charge and mass dependent, thus requiring special calibration techniques for their energy determinations. The most widely used technique has been proposed by Schmitt *et al.* [1]. Experimental data on PHD in surface-barrier silicon detectors show that the response of those detectors to ions in the mass and energy range of fission fragments is linear and mass-dependent. The calibration method of Schmitt was based on combined measurements of the response of silicon semiconductor detectors to the single ^{252}Cf spontaneous fission fragments with ions of bromine and iodine, and was expressed by the following equation:

$$E(x, A) = (a + a'A)x + b + b'A, \quad (1)$$

where E is the calibrated energy, A is the ion mass, x is the channel number and a , a' , b , b' are parameters.

Table 1: Parameters of eq. (1) (in MeV) for fission fragments of ^{252}Cf and ^{235}U .

Parameter	^{252}Cf	^{235}U
a	$\frac{24.0203}{X_l - X_h}$	$\frac{30.9734}{X_l - X_h}$
a'	$\frac{0.03574}{X_l - X_h}$	$\frac{0.04596}{X_l - X_h}$
b	$89.6083 - a \cdot X_l$	$87.8626 - a \cdot X_l$
b'	$0.1370 - a' \cdot X_l$	$0.1345 - a' \cdot X_l$

The channel numbers of the peak positions for the average light (LF) and heavy (HF) fission fragment groups, X_l and X_h respectively, were then related to the four parameters in eq. (1) which are presented in table 1, so that a measurement of one of the standard fission spectra sufficed to determine these parameters. Although eq. (1) has been used

successfully in the fission fragment range of masses and energies, its originators warned that this calibration method may not be valid outside of this range.

Most wide studies of the PHD were performed for Si detectors. Nevertheless, another promising detector material, CVD diamond [5, 6], appears to extend the possible applications for heavily-ionizing particles. Diamond detectors reveal fast timing properties and large radiation hardness while the energy resolution achieved with single crystal CVD (scCVD) diamonds for ~ 5 MeV α particles ($\Delta E/E \sim 0.3\%$) is comparable to the one of Si detectors [5].

The investigation of diamond detectors with low-energetic heavy ions is still at its very beginning. There are only few publications about the PHD in scCVD diamond detectors [7–9]. Authors in [9] have studied scCVD diamonds as fission fragment detectors. They concluded that all their scCVD diamond detectors show inadequate energy resolution and suffer from an extensive PHD. The detected pulse height never exceeds about 30% of what is expected for fission fragments.

We investigated the PHD in scCVD diamond detector for fission fragments of ^{252}Cf at four different field settings between (0.7 – 2.5) V/ μm .

The energy calibration was performed with α particles from a ^{226}Ra source which has energies of 4.772, 5.490, 6.002, and 7.682 MeV. The calibration of the electronics up to the highest energy of 100 MeV was performed with a precision pulser. Assuming no PHD for α particles, this calibration method for the signals of fission fragments stopped in scCVD is a direct measurement of the energy of the ions converted into an electric signal. The difference to the kinetic energies of LF and HF results in the PHD. Kinetic energies of LF and HF of ^{252}Cf are the mean values for the two groups of fission fragments taken from the literature.

Table 2 shows the energies of fission fragments of ^{252}Cf measured in the present work with the scCVD diamond detector at different electric field values. At 0.7 V/ μm the PHD is about 70 % for HF and LF, and about 59 % at 2.5 V/ μm . With increasing electric field from 0.7 V/ μm to 2.5 V/ μm the charge collection was improved by $\sim 10\%$.

As mentioned above, the response of surface-barrier silicon detectors to ions in the mass and energy range of fission fragments ($A \approx (80 - 150)$ a.m.u, $E \approx (35 - 120)$ MeV)

Table 2: Energy E_{dia} measured with the scCVD diamond detector and corresponding PHD (in %) for HF and LF fission fragments of ^{252}Cf at different electric fields.

Electric field / (V/ μm)	$\Delta E(\text{HF})$ / MeV	$\Delta E(\text{LF})$ / MeV
0.7	23.6	30.9
PHD in %	70 %	70 %
1.0	26.8	34.8
PHD in %	66 %	66 %
2.0	31.1	40.2
PHD in %	60 %	61 %
2.5	32.1	41.6
PHD in %	59 %	59 %

Table 3: Reconstructed energies of LF and HF of ^{252}Cf , measured with the scCVD diamond detector and comparison with literature values from measurements with Si detectors. The energy calibration was performed with the method of Schmitt *et al.* The LF and HF energies correspond to fission fragments with mass $M_l=106$ and $M_h=142$, respectively, which are located at the maxima of the fission fragment peaks.

Ion	HF	LF
present work	79.9 MeV	104.1 MeV
[1]	79.4 MeV	103.8 MeV
[10]	78.9 MeV	103.0 MeV

is linear and mass-dependent. The method suggested by Schmitt *et al.* [1] enables the channel-energy-calibration for ions in this range by measuring a standard fission fragment energy spectrum. We were going to check this method for diamond detectors. The Schmitt calibration requires to determine the parameters a, a', b, b' in eq. (1). For this, we measured fission spectra of ^{252}Cf and determined the respective channel numbers, X_l and X_h , which correspond to the maxima of the light and heavy fission fragment groups, respectively. Then, taking into account the equations in Table 1 we determined a, a', b, b' . Finally, we considered that the maxima correspond to fission fragments with light $M_l=106$ and heavy $M_h=142$ mass, respectively (typical mass numbers for fission fragment groups of ^{252}Cf), and calibrated their energy according to eq. (1). The obtained energy values of LF and HF are shown in table 3 and compared with literature values [1, 10]. The reconstructed energies are very close to the values of the same fission fragments measured with Si detectors in [1, 10].

It has to be mentioned that for the best fit, the constants in the equations in Table 1 have to be adjusted for the given detector (as described in [10]) otherwise the calibrated energies might be over- or underestimated. We can conclude that the reconstructed energies of HF and LF fission fragments of ^{252}Cf are in good agreement with the literature values. The calibration method of Schmitt *et al.* works in

fission fragment mass and energy regions for diamond detectors as well as for Si detectors.

We studied experimentally the pulse-height defect (PHD) in single crystal CVD diamond detectors for fission fragments of ^{252}Cf at different electric fields and found it to be significant. We adapted and applied the method of Schmitt *et al.* and concluded that this calibration method works in the fission fragment mass and energy range for diamond detectors as good as for Si detectors. However, constants have to be adjusted for diamond material, otherwise the reconstructed energies might be slightly over- or underestimated.

While the studies of PHD in Si detectors have a long history and many experimental data are available, the investigation of the PHD in CVD diamond detectors for low-energetic ions is only at its very beginning and more experimental data are needed before drawing final conclusions.

References

- [1] H. W. Schmitt, W. E. Kiker, and C. W. Williams, Phys. Rev. **137** (1965) B837.
- [2] B.D. Wilkins *et al.*, Nucl. Instr. and Meth. **92** (1971) 381.
- [3] S.B. Kaufman *et al.*, Nucl. Instr. and Meth. **115** (1974) 47.
- [4] E.C. Finch, M. Ashgar and M. Forte, Nucl. Instr. and Meth. **163** (1979) 467.
- [5] M. Pomorski *et al.*, Phys. Stat. Sol. (a) **202** (2005) 2199.
- [6] M. Pomorski *et al.*, Phys. Stat. Sol. (a) **203** (2006) 3152.
- [7] Y. Sato *et al.*, Euro. Phys. Let. **104** (2013) 22003.
- [8] Y. Sato and H. Murakami, Jpn. J. Appl. Phys. **54** (2015) 096401.
- [9] M.O. Fregeau *et al.*, Nucl. Instr. and Meth. A **791** (2015) 58.
- [10] G.N. Knyazheva *et al.*, Nucl. Instr. and Meth. B **248** (2006) 7.

Beam transport analysis of RIKEN AVF Cyclotron injection line using pepper-pot emittance monitor

Y. Kotaka, Y. Ohshiro, H. Yamaguchi, N. Imai, T. Nagatomo^a
M. Kase^a, K. Hatanaka^b, H. Mutoh^c and S. Shimoura

Center for Nuclear Study, Graduate School of Sciences, University of Tokyo

^aRiken Nishina Center

^bResearch Center for Nuclear Physics, Osaka University

^cCenter of General Education, Tokyo University of Science, Suwa

1. Introduction

The transmission efficiency from ECRIS to the center of AVF Cyclotron is 19%. This means that 81% of ion beams are lost in the beam injection line. In order to improve this transmission efficiency and to increase beam intensity, the beam transport system of the injection line has to be optimized. For the optimization, we need to investigate the beam orbit using measured beam emittance. Since the horizontal (x) and vertical (y) beam elements are coupled by solenoid coils or Glaser coils in this injection beam line, the four-dimensional emittance is necessary. For this reason, we have developed a pepper-pot emittance monitor [2].

2. The beam injection line of AVF Cyclotron

Figure 1 shows the side view of the beam injection line of AVF Cyclotron. The ion beam extracted by Hyper ECRIS is separated into the desired ion species by Analyzing Magnet. Leaving the Analyzing Magnet, the ion beam goes straight to the Vertical Bending Magnet (DMI23). On this straight line, a profile monitor (PF_IH10), a pepper-pot emittance monitor (PEM_IH10) and a viewer plate (I23viewer) are set in order as diagnostics and first solenoid coil (SOIH11) is set as a focusing element behind the PEM_IH10.

When the ion beam arrives at DMI23, it is bent downward by DMI23 and goes straight to the inflector which is positioned at the center of AVF Cyclotron. On this downward line, a pepper-pot emittance monitor (PEM_I30) and a profile monitor (PF_I30) are set in order as diagnostics. Below PF_I30, second solenoid coil (SOI30), four quadrupole magnets and third solenoid coil (SOI36) are set in order as focusing elements. Below SOI36, a two-dimensional emittance monitor (EM_I36) is set as diagnostic. Below EM_I36, two Glaser coils are set as focusing elements.

We reported the beam transport calculation from PEM_IH10 to I23viewer [3].and insisted that using the calculated magnet field and the real solenoid model [4] for the beam transport of SOIH11 is effective.

Currently, we are promoting the beam transport calculation up to the position of EM_I36. At first, we faced problems that the standard Edge Focus of DMI23 and the standard Hard Edge model of quadrupole magnet are not effective for beam transport calculation.

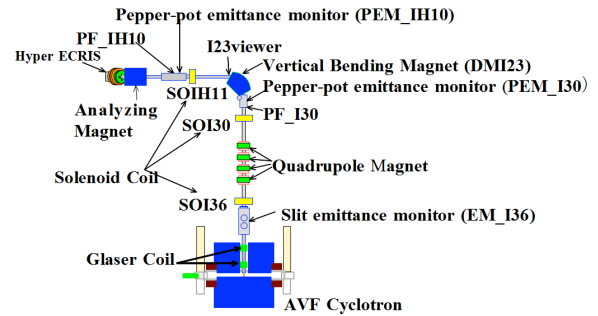


Figure 1 The side view of the injection line of AVF Cyclotron.

3. Beam transport model of the edge focus

The Edge Focus works when the pole-face of bending magnet is rotated with respect to the beam direction. This effect doesn't shift a beam position but a beam angle. DMI23 is rotated by 30 degree.

TRANSPORT [5] indicates that the calculation for Edge Focus needs a correction corresponding to the type of fringing field boundary. Therefore, we calculated Edge Focus with the correction, which is called "Square-edged Magnet".

In order to evaluate the correction, we transported the four-dimensional emittance of ${}^4\text{He}^{2+}$ 20keV ion beam measured by PEM_IH10 to the position of PEM_I30 and make x-y distribution (the right image of Figure 2). Compared with the beam image on the x-y plane measured by PEM_I30 (the left image of Figure 2), the shape of the right image of Figure 2 is similar. We think the correction for edge focus is effective.

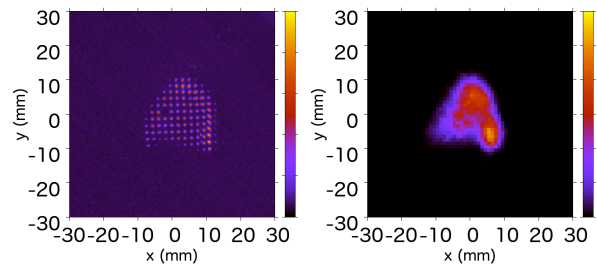


Figure 2: The right image is obtained by PEM_IH10. The left image is measured by PEM_I30

4. Beam transport model of quadrupole magnet

The Hard Edge model of quadrupole magnet is an

approximate uniform distribution of the magnetic field gradient. It is usually used for the beam transport. However, the Hard Edge model does not fit for our case.

As the calculated magnetic field is useful for the case of solenoid coil, we tried to use the calculated magnetic field gradient of quadrupole magnet. In order to see the effect, we transported the four-dimensional emittance of ${}^4\text{He}^{2+}$ 20keV ion beam measured by PEM_I30 to the position of EM_I36 and make two-dimensional emittance distribution (The right column of Figure 3). The coordinate system (u, w) is rotated 45 degree with respect to the coordinate system (x, y). The upper and lower images show (u, u') distributions and (w, w') distributions, respectively in the Figure 3. Compared with the two-dimensional emittance measured by EM_I36 (the left column of Figure 3), both shapes are similar. Therefore, we decided to use the calculated magnetic field.

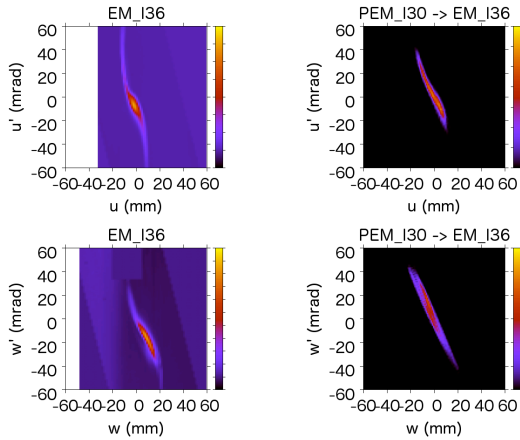


Figure 3: The images of the right column are two-dimensional emittance measured by EM_I36. The images of the left column are two-dimensional emittance calculated using the measured result of PEM_I30. The upper and lower row indicate (u, u') distribution and (w, w') distribution, respectively.

5. Beam transport from PEM_IH10 to EM_I36

We solved the beam transport model of the focusing element. Therefore, we transported the four-dimensional emittance of ${}^4\text{He}^{2+}$ 25.42keV ion beam with the intensity of $5\mu\text{A}$ measured by PEM_IH10 to the position of EM_I36 directly and made two-dimensional emittance distribution (The right column of Figure 4). In case of this beam intensity, we consider that the space charge effect is negligible. The format of the upper and lower image of Figure 4 is same as Figure 3. Compared with the two-dimensional emittance measured by EM_I36 (the left column of Figure 4), the shape of the right column of Figure 4 is found to be similar.

Next, we must investigate the beam transport calculation against the high intensity beam because our purpose is increasing beam intensity. Therefore, using ${}^4\text{He}^{2+}$ 25.42keV ion beam with the intensity of $240\mu\text{A}$, we performed the same experiment as the case of low intensity beam. Figure 5 shows the result. The format of images of the Figure 5 is same as Figure 4. We find that

(w, w') distribution in the right column of Figure 5 is particularly different from that in the left column of Figure 5. We think the reason is that our beam transport calculation excludes space charge effect. We will include the space charge effect for the beam transport calculation.

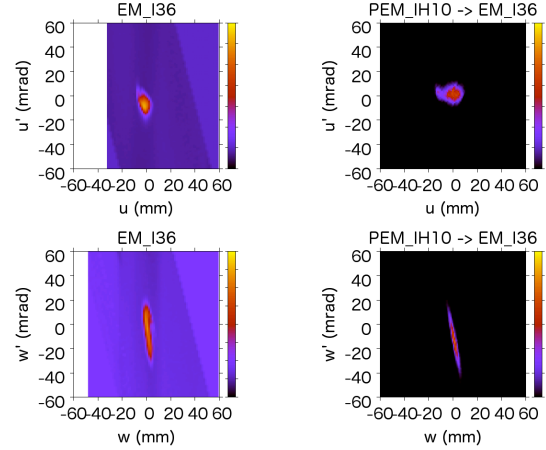


Figure 4: The images of the right column are two-dimensional emittance measured by EM_I36. The images of the left column are two-dimensional emittance calculated using the measured result of PEM_IH10. The upper and lower row indicate (u, u') distribution and (w, w') distribution, respectively.

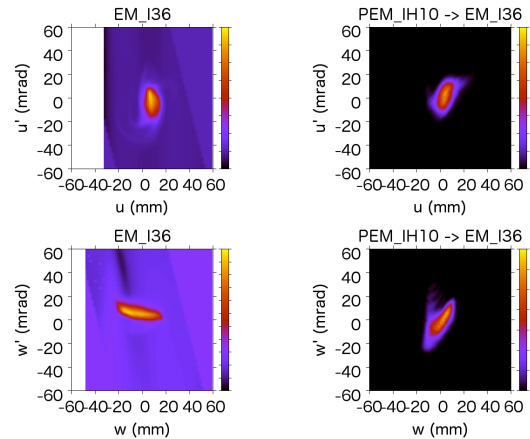


Figure 5: The images of the right column are two-dimensional emittance measured by EM_I36. The images of the left column are two-dimensional emittance calculated using the measured result of PEM_IH10. The upper and lower row indicate (u, u') distribution and (w, w') distribution, respectively.

References

- [1] Y.Yanagisawa et al., Nucl. Instr. and Meth. Phys. Res., **A539** (2005) 74.
- [2] T.Hoffmann et al., Proc. 9th BIW 2000, Cambridge, USA, PP.432-439.
- [3] Y.Kotaka et al., CNS Ann. Rep. 2014 (2016) 61
- [4] H. Wiedemann, Particle Accelerator Physics, 3rd ed., Berlin, Springer, 2007.
- [5] D.C. Carey et al., FERMILAB-Pub-98/310

Beam emittance of fixed plasma boundary in Hyper ECR ion source

Y. Ohshiro, Y. Kotaka, S. Watanabe, H. Muto^a, H. Yamaguchi, N. Imai and S. Shimoura

Center for Nuclear Study, Graduate School of Sciences, University of Tokyo

^aCenter of General Education, Tokyo University of Science, Suwa

1. Introduction

At the RIKEN AVF cyclotron, we have been improving beam transmission efficiency from the Hyper ECR ion source [1,2], called the Hyper ECR, to the cyclotron. Recently, users request light ion beams with high intensity. However, supply beam intensity is currently 50 to 60% of required that, since transmission efficiency from the Hyper ECR to the cyclotron exit is 3% or less.

This year, variation of beam emittance to a shape of plasma boundary in the Hyper ECR was investigated. A plasma boundary of a beam extraction system was fixed in the spherical shape of convex, concave and parallel, and the beam emittance was measured, respectively. The emittance of the parallel boundary was the most improved. We are trying to construct the beam extraction system obtained the low beam emittance in order to improve the transmission efficiency.

In this paper, the fixed plasma boundary and its beam emittance are described.

2. Emittance measurement of plasma boundary

Figure 1 shows a plasma electrode attached a mesh in the Hyper ECR. An electrode hole is 12 mm in diameter, the tungsten mesh is 30 meshes and the wire diameter is 0.03 mm. Plasma left the hole is limited by the mesh with the spherical shape of convex, concave and parallel, respectively. In this way, fluctuation of the plasma boundary caused by the balance between the plasma pressure and the extraction electric field strength is prevented.

Beam emittance was measured by a mixed beam measurement method developed last year [2]. A device consists of a 0.25 mm wide slit (E1) moving in a vertical plane of 308 mm from the plasma electrode, a beam shutter (E2) moving in a vertical plane of 830 mm from the slit, and an analyzing magnet (see Fig. 1). The mixed beam divided by the E1 was gradually shut off at the E2, and analyzed. The beam emittance was obtained from the attenuation rate of the analyzed beam intensity to the position of E1. In the method, we were able to measure the beam emittance closer to the plasma electrode.

3. Beam emittance diagram

Some example of the beam emittance diagrams are shown in Fig. 2. These are in the case of the mesh type of convex, concave and parallel, and the 95% emittance to total beam current is 210, 177, 159 π mm * mrad, respectively. The total beam current was obtained by extrapolation from the correlation between several

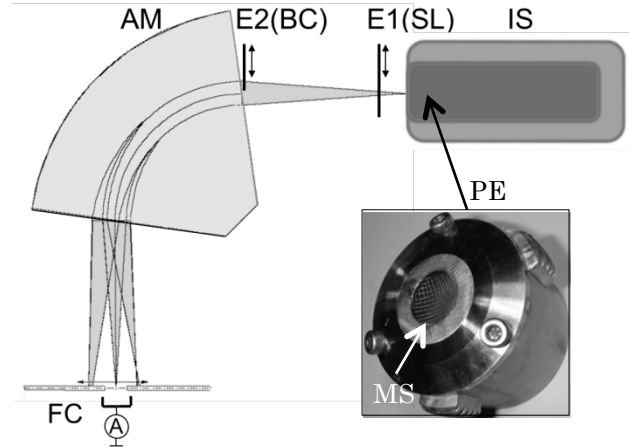


Fig. 1: A schematic view of an emittance measurement system and a photo of a plasma electrode attached a tungsten mesh. A plasma boundary was fixed with the mesh and the emittance at E1 was measured. IS: Hyper ECR E1: Beam slit E2: Beam shutter AM: Analyzer FC: Faraday cup PE: Plasma electrode MS: Mesh

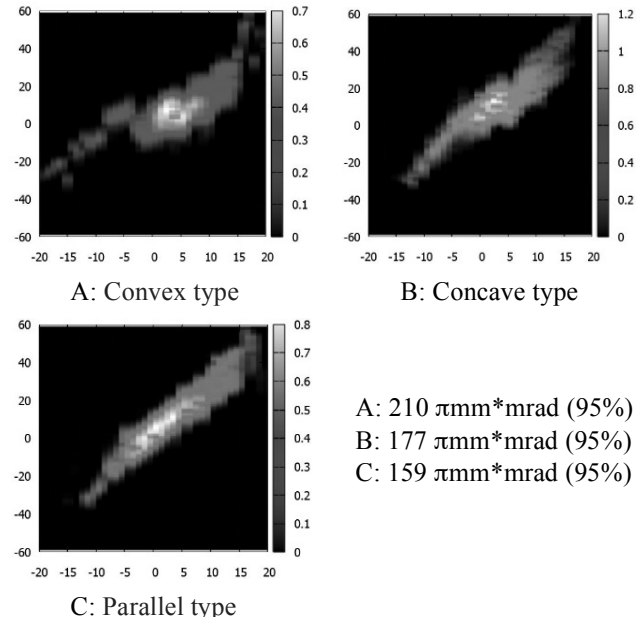


Fig. 2: Examples of emittance diagrams for alpha ion beam production. These are in the case of the mesh type of convex, concave and parallel to the beam extraction. The beam extraction voltage and intensity are constant at 11.14 kV and 320 μ A, respectively

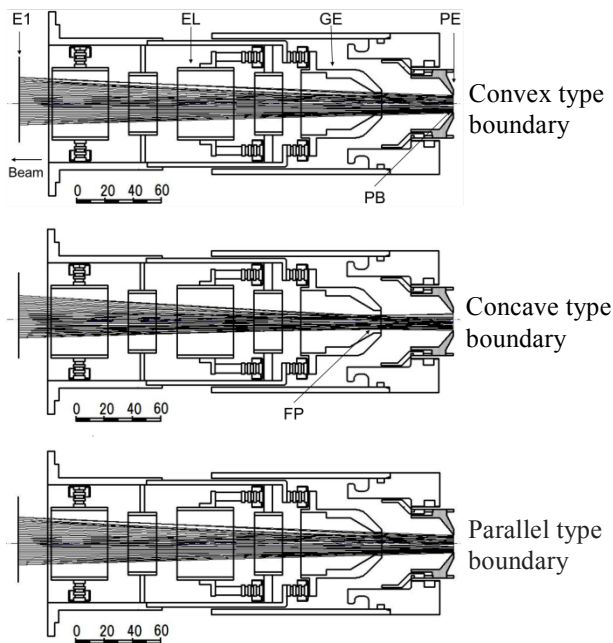


Fig. 3: Schematic view of the extraction system of the Hyper ECR ion source that contains the beam ray trace. PE: Plasma electrode GE: Ground electrode EL: Einzel lens E1: Beam slit PB: Plasma boundary FP: Focus point of the beam

measured currents and their emittance, because it was difficult to measure due to measurement accuracy and variations of minute currents. As a result, the emittance of the parallel boundary was the smallest.

4. Estimation of plasma boundary

Figure 3 shows the beam extraction system [3] with a beam trajectory in the Hyper ECR. The beam is extracted by the electric field between the plasma electrode and a ground electrode, and converged by an einzel lens. The beam trajectories were drawn by extending a line from X and X' of the 95% emittance measured at 308 mm from the plasma electrode, respectively. The trajectories are shown in the type of plasma boundary of a convex, concave and parallel in order from the top to the bottom. From these trajectories, a change in the shape of the beam starting surface is assumed.

The beam trajectory diagrams show the characteristics of the plasma boundary as follows.

- 1) In the case of the convex type and the parallel type, the beam trajectory is divergent with virtual object point in the plasma, and in the concave case trajectory is convergence with real object point near the ground electrode.
- 2) The linear density in the vicinity of the axis is low for convex type, and the concave type and parallel type are relatively uniform. The former and the latter tend to be hollow beams and parallel beams, respectively.

These suggest choosing the extraction system that always forms a plasma boundary (PB) of a concave or parallel spherical surface. In order to enhance the light

ion beams by improving the transmission efficiency to the cyclotron, we are constructing an extraction system that constantly obtains low beam emittance.

5. Summary

We fixed the plasma boundary and measured the beam emittance. Emittance was found to change with the shape of plasma boundary. We are currently constructing a beam extraction system that can obtain low beam emittance.

References

- [1] Y. Ohshiro, S. Yamaka, S. Watanabe, K. Kobayashi, Y. Kotaka *et al.*, *Rev. Sci. Instrum.* **85** (2014) 02A912.
- [2] Y. Ohshiro, S. Yamaka *et al.*, *RIKEN Accel. Prog. Rep.* **39** (2005) 231.
- [3] Y. Ohshiro, Y. Kotaka *et al.*, *CNS Annual Report 2015* (2014) 59
- [4] Y. Ohshiro, S. Watanabe *et al.*, *CNS Annual Report 2004* (2003) 71.

Theoretical Nuclear Physics

Stochastic estimation of nuclear level density in large-scale shell-model calculations

N. Shimizu^a, Y. Utsuno^{b,a}, Y. Futamura^c, T. Sakurai^{c,d}, T. Mizusaki^e, and T. Otsuka^{f,a,g,h}

^aCenter for Nuclear Study, Graduate School of Science, the University of Tokyo

^bAdvanced Science Research Center, Japan Atomic Energy Agency

^cFaculty of Engineering, Information and Systems, University of Tsukuba

^dCREST, Japan Science and Technology Agency

^eInstitute of Natural Sciences, Department of Physics, Senshu University

^fDepartment of Physics, Graduate School of Science, the University of Tokyo

^gNational Superconducting Cyclotron Laboratory, Michigan State University, East Lansing, MI 48824, USA

^hInstituut voor Kern- en Stralingsfysica, Katholieke Universiteit Leuven, B-3001 Leuven, Belgium

Nuclear level density is one of the key quantities to connect nuclear structure and nuclear reactions. While nuclear level density is known to well follow phenomenological formulas, investigating microscopic theories of nuclear level density is still important for the understanding of nuclear structure and reactions. The large-scale shell-model calculation provides, in principle, quite reliable level density (e.g. [1]) because it takes many-body correlations into account, thus well describing level structures. However, the amount of the computation is quite heavy in large-scale shell model calculations of medium-heavy nuclei. Especially for obtaining level density, we need to compute highly excited eigenenergies which require enormous computational resources in the conventional Lanczos method. A lot of efforts have been paid to overcome this difficulty [2–4]. In this report, we propose to adopt a stochastic estimation of eigenvalue count based on a shifted Krylov-subspace method [5]. By utilizing this method, we succeeded in reproducing the observed equilibrium of $J^\pi = 2^+$ and 2^- states in ^{58}Ni microscopically. This report is condensed from Refs. [6, 7].

Here we describe an efficient method for stochastically estimating eigenvalue distribution of large sparse matrix [5]. In large-scale shell model calculations, a nuclear wave function is described as a linear combination of a huge amount of many-body configurations, which are called the M -scheme basis states. The shell-model energy is obtained as an eigenvalue of the M -scheme shell-model Hamiltonian matrix, H . Hence, the nuclear level density is obtained by estimating the number of eigenvalues of the Hamiltonian matrix in a specified eigenvalue region. The number of eigenvalues μ_k in a certain range $E^{(k-1)} < E < E^{(k)}$ is obtained by the contour integral Γ_k on the complex plane in Fig.1 as

$$\begin{aligned} \mu_k &= \frac{1}{2\pi i} \oint_{\Gamma_k} dz \operatorname{tr}((z-H)^{-1}) \\ &\simeq \sum_j w_j \operatorname{tr}((z_j^{(k)} - H)^{-1}). \end{aligned} \quad (1)$$

The contour integral on Γ_k is numerically obtained by discretizing the contour line with mesh points $z_j^{(k)}$ (blue crosses of Fig.1) and their weights w_j .

The trace of the inverse of matrix in Eq.(1) is stochastically estimated by sampling dozens of random vectors from

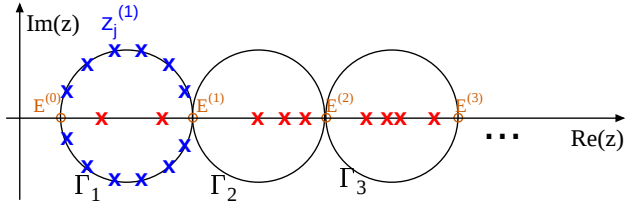


Figure 1: (Color Online) Schematic view of the contour integral to count the eigenvalues (red crosses). Blue crosses denote the discretized mesh points $z_j^{(1)}$ along the integral contour Γ_1 . $E^{(k-1)}$ and $E^{(k)}$ are the intersections of Γ_k and the real axis. Taken from Ref. [6].

the whole Hilbert space. An unbiased estimation is given by

$$\operatorname{tr}((z-H)^{-1}) \simeq \frac{1}{N_s} \sum_s \mathbf{v}_s^T (z-H)^{-1} \mathbf{v}_s \quad (2)$$

where \mathbf{v}_s are vectors whose elements take 1 or -1 with equal probability randomly and N_s is the number of \mathbf{v}_s . This stochastic method is called Hutchinson's estimator [9].

The remaining task is to obtain $\mathbf{v}_s^T (z_j^{(k)} - H)^{-1} \mathbf{v}_s$ numerically. Since the dimension of the matrix H is often quite huge and reaches $O(10^{10})$, the inverse of the matrix cannot be computed directly. However, since H is quite sparse, we can efficiently obtain the $H^{-1} \mathbf{v}_s$ by solving the linear equations $\mathbf{v}_s = H \mathbf{x}$ utilizing the Krylov-subspace method. In practice, we adopt the block bilinear form of the blocked complex orthogonal conjugate gradient (BCOFG) method [10] combined with the shifted algorithm [11] for efficient computation. Further details of this algorithm and its feasibility are discussed in [6, 7].

By applying this stochastic estimation to large-scale shell-model calculations, we evaluate the spin-parity dependent level densities of ^{58}Ni . The 2^+ and 2^- level densities of ^{58}Ni were observed experimentally and show close values to each other. Although this equilibration between the positive and negative parity level densities is assumed often by phenomenological formulas, the preceding microscopic calculations failed in reproducing it [8].

In this work, in order to describe both parity states of nuclei around ^{58}Ni with the shell model, we take the $0\hbar\omega$ and $1\hbar\omega$ states in the full $sd+pf+sdg$ valence shell for natural- and unnatural-parity states, respectively. The realistic ef-

fective interaction for this model space is constructed in the same way as the SDPF-MU interaction [12]. The single-particle energies of the sdg orbits are determined to reproduce the experimental spectroscopic information of nuclei around ^{58}Ni and ^{90}Zr . The large-scale shell model calculations utilizing this realistic interaction reproduce the experimental data of low-lying excited energies and spectroscopic factors of natural- and unnatural-parity states of ^{57}Co , ^{57}Ni , ^{59}Cu and ^{59}Ni successfully (see Ref. [6] for details). The M -scheme dimension for the 2^- levels of ^{58}Ni reaches 1.5×10^{10} . For the conventional Lanczos diagonalization method, this dimension is nearly the current limit to obtain a few low-lying states, and is far beyond the current limit to obtain a few thousand eigenvalues to evaluate the level density. In the present work, the contamination of spurious center-of-mass excitation is clearly removed by the Lawson method [7].

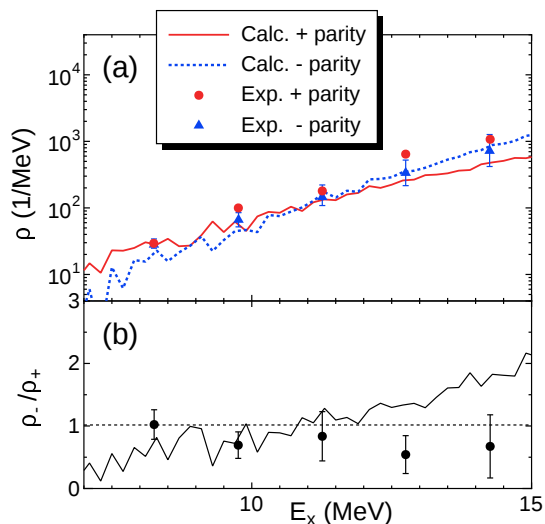


Figure 2: Level densities of 2^+ and 2^- states of ^{58}Ni against the excitation energy. (a) The theoretical results are shown by solid ($J^\pi = 2^+$) and dotted (2^-) lines, while the experimental values are shown by circles (2^+) and triangles (2^-) [8]. (b) The theoretical (experimental) ratio of the 2^- and 2^+ level densities is shown as a line (symbols with error bars). Redrawn from Fig. 4 in [6].

Figure 2 (a) represents the present shell-model results of the level densities of 2^+ and 2^- states of ^{58}Ni and the experimental ones. These densities show good agreement with the experimental results. Figure 2 (b) shows the ratio of the 2^- and 2^+ level densities. The experimental ratio is close to 1 and shows the equilibration between the positive and negative parity states even in a low-energy region at $E_x \simeq 8$ MeV.

In summary, we introduced a stochastic estimation of the level density in nuclear shell-model calculations. This method enables us to estimate the level density of medium-heavy nuclei utilizing the realistic effective interaction, which successfully describes low-lying levels and their spectroscopic factors around ^{58}Ni including those of the unnatural parity states. With this realistic interaction and

the stochastic method, we obtained the level densities of $J^\pi = 2^+$ and $J^\pi = 2^-$ in ^{58}Ni . These densities are in excellent agreement with the experimental results and show the equilibration at $E_x \geq 8$ MeV, whereas the preceding microscopic calculations showed strong parity dependence. The present framework bridges the low-lying spectroscopy and microscopic understanding in statistical region; thus, further studies in this direction should be quite promising.

This work has been supported by the HPCI Strategic Program from MEXT, CREST from JST, the CNS-RIKEN joint project for large-scale nuclear structure calculations, and KAKENHI grants (25870168, 23244049, 15K05094) from JSPS, Japan. The numerical calculations were performed on K computer at RIKEN AICS (hp140210, hp150224) and COMA supercomputer at the University of Tsukuba.

References

- [1] B. A. Brown and A. C. Larsen, Phys. Rev. Lett. **113**, 252502 (2014).
- [2] Y. Alhassid, G.F. Bertsch, S. Liu and H. Nakada, Phys. Rev. Lett. **84**, 4313 (2000); H. Nakada, and Y. Alhassid, Phys. Rev. Lett. **79**, 2939 (1997).
- [3] R. A. Sen'kov and V. Zelevinsky, Phys. Rev. C **93**, 064304 (2016); R. A. Sen'kov and M. Horoi, Phys. Rev. C **82**, 024304 (2010).
- [4] B. Strohmaier, S. M. Grimes, and S. D. Bloom, Phys. Rev. C **32** 1397 (1985); S. M. Grimes, S. D. Bloom, R. F. Hausman Jr., and B. J. Dalton, Phys. Rev. C **19**, 2378 (1979).
- [5] Y. Futamura, H. Tadano and T. Sakurai, JSIAM Lett. **2**, 127 (2010).
- [6] N. Shimizu, Y. Utsuno, Y. Futamura, T. Sakurai, T. Mizusaki and T. Otsuka, Phys. Lett. B **753**, 13 (2016).
- [7] N. Shimizu, Y. Utsuno, Y. Futamura, T. Sakurai, and T. Otsuka, EPJ Web of Conf. **122**, 02003 (2016).
- [8] Y. Kalmykov, C. Ozen, K. Langanke, G. Martinez-Pinedo, P. von Neumann-Cosel and A. Richter, Phys. Rev. Lett. **99**, 202502 (2007).
- [9] M. F. Hutchinson, Commun. Stat., Sim. Comput. **19**, 433 (1990).
- [10] L. Du, Y. Futamura, and T. Sakurai, Comput. Math. Appl. **66**, 12 (2014).
- [11] S. Yamamoto, T. Sogabe, T. Hoshi, S.-L. Zhang, and T. Fujiwara, J. Phys. Soc. Jpn. **77**, 114713 (2008).
- [12] Y. Utsuno, T. Otsuka, B. A. Brown, M. Honma, T. Mizusaki, and N. Shimizu, Phys. Rev. C **86**, 051301(R) (2012).

New aspect of island of inversion shed by microscopic theory and large-scale calculation

N. Tsunoda, T. Otsuka^{a,b}, N. Shimizu^a

Center for Nuclear Study, Graduate School of Science, University of Tokyo

^aDepartment of Physics, University of Tokyo

^bNational Superconducting Cyclotron Laboratory, Michigan State University

Unbalanced numbers of neutrons (N) and protons (Z) result in rich features of nuclei. Among them in this report, we report a new aspect of neutron-rich nuclei particularly in the region so-called “island of inversion” by the large-scale shell-model (SM) calculation and the microscopic theory based on nuclear force.

Theoretical researches on this region have been quite fruitful in which the experimental findings are explained by vanishing $N = 20$ major gap of neutrons. In these works, at least two-major shell degrees of freedom had to be taken into account, which was a breakthrough on the understanding of neutron-rich nuclei [1–3]. However, works in this line have been limited to those with the empirical effective interactions. Although many-body perturbation theory (MBPT) is one of the most reliable theory to derive the effective interaction starting from the nuclear force, this theory has not been utilized for the case of two major shell [4]. The major reason is the long-standing problem of the MBPT, that is, one meets inevitable divergence on perturbation procedures when applied to non-degenerate model space [5].

In this work, on the other hands, we overcome this problem by a newly developed theory, so-called Extended Kuo-Krenciglowa (EKK) theory, which enables us to derive the effective interaction in two-major shells [5]. Then, we construct the effective interaction starting from microscopic interaction as follows,

$$H_{\text{eff}} = H_{\text{BH}}(\xi) + \sum_{k=1}^{\infty} \frac{1}{k!} \frac{d^k \hat{Q}(\xi)}{d\xi^k} \{H_{\text{eff}} - \xi\}^k, \quad (1)$$

where H_{BH} and \hat{Q} are the Bloch-Horowitz Hamiltonian and the so-called \hat{Q} -box [5], respectively. The latter contains all possible valence linked and irreducible diagrams up to third order, whose examples are shown in Fig. 1. The quantity ξ

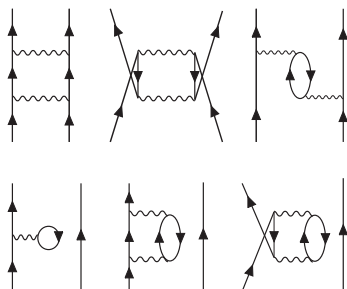


Figure 1: Diagrams included in \hat{Q} -box of the second order in perturbation.

is a parameter, and the poles of $\hat{Q}(\xi)$ can be avoided with its

appropriate value. We renormalize the $\chi\text{N}^3\text{LO}$ interaction using the so-called $V_{\text{low}k}$ approach with a cutoff 2.0 fm^{-1} . We solve Eq. (1) with a harmonic oscillator basis with the oscillator parameter $\hbar\omega = 45A^{-1/3} - 25A^{-2/3} \text{ MeV} = 12.10 \text{ MeV}$ where $A = 28$ ($A = Z + N$). Three-nucleon forces are included through the Fujita-Miyazawa term with its strength given by a standard $\pi\text{-}N\text{-}\Delta$ coupling. This term is transformed into a medium-dependent two-body interaction [6]. We name this interaction as EEdf1, derived from EFT-based $\chi\text{N}^3\text{LO}$ iteration with EKK theory, in the model space of full $sdpf$ -shell.

We calculated Ne($Z=10$), Mg($Z=12$) and Si($Z=14$) isotopes with neutron number $10 \leq N \leq 22$. All the calculations are performed with Lanczos diagonalization in $sdpf$ -shell. At most $8\hbar\omega$ excitation from the normal configuration of each nuclei is taken into account, confirming the convergent results. The largest dimension of the Lanczos diagonalization is 7.53×10^{10} .

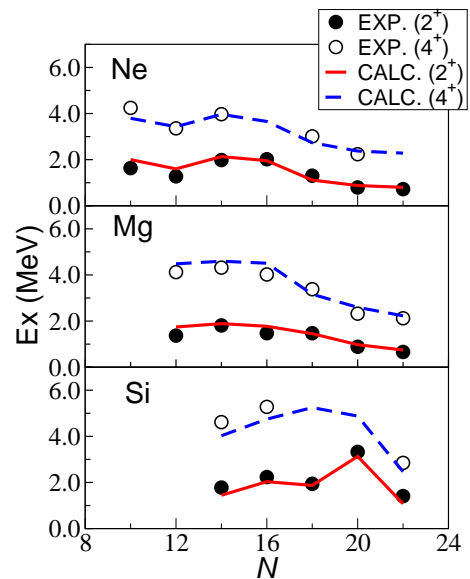


Figure 2: Energy of first excited 2^+ and 4^+ states of Ne, Mg and Si isotopes.

Figure 2 shows excitation energy of 2^+ and 4^+ states. All the calculations are well reproduced experimental trends. Most importantly, ^{30}Ne and ^{32}Mg have low-lying 2^+ states but ^{34}Si has high-lying 2^+ state. This clearly shows that EEdf1 interaction correctly reproduces the experimental size of $N=20$ shell gap and the mixing of sd -to- pf -shell, which is the physics in so-called island of inversion. The sd -to- pf excitation is weakened for Si case. As the onset of island of inversion, from $N=16$ to $N = 18$, the energies of

4^+ states are changed differently. For example, in Mg isotope 4^+ energy drops down where 2^+ stays almost constant. This indicates not only the degrees of deformation but also the shape itself is changing.

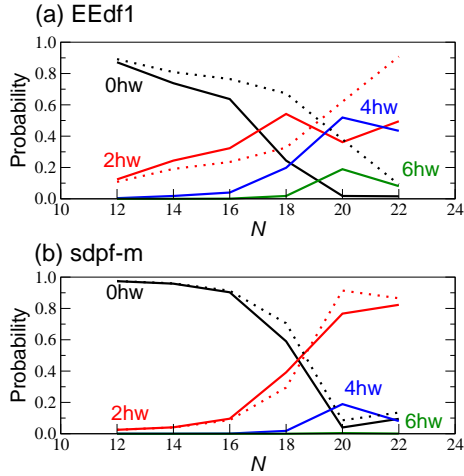


Figure 3: Probability amplitude of $0\hbar\omega$, $2\hbar\omega$, $4\hbar\omega$ and $6\hbar\omega$ excitation from normal configuration for Mg isotopes. Solid line shows the calculation in full space, and dashed line shows the truncated space, which include only $0\hbar\omega$ and $2\hbar\omega$ excitations.

Let us next examine the wave functions. In Fig. 3 the probability amplitude of $0\hbar\omega$, $2\hbar\omega$, $4\hbar\omega$ and $6\hbar\omega$ excitation from normal configuration of Mg isotopes (ground states) are shown. Figure. 3 (a,b) show the case with EEdf1 and sdpf-m [1], respectively. Solid lines represent the calculations in full space and dashed lines represent those of truncated space, that is, $0\hbar\omega$ and $2\hbar\omega$ space. Both iterations have almost no probabilities of the $0\hbar\omega$ configuration in $N=20, 22$ cases. The considerable difference is the large fraction of $4\hbar\omega$ configuration in EEdf1 interaction. In fact, the full and truncated calculations are quite different for EEdf1, while they are almost identical for sdpf-m interaction. In particular, the dominant component of ^{32}Mg is $4\hbar\omega$ configuration in EEdf1 iteration. In addition, sizable contribution of $2\hbar\omega$ configurations in $N=12, 14, 16$ isotopes in EEdf1 is also different from sdpf-m. This can be interpreted as follows: the sd -shell part of sdpf-m interaction is constructed by corrections of USD interaction, which include the virtual excitation from sd -to- pf shell. EEdf1 interaction, on the other hand, handle those excitations explicitly, results in larger fraction of sd -to- pf excitations. The large fraction of $4\hbar\omega$ excitation can be then interpreted intuitively as 2-particle-2-hole excitation from already excited states.

This difference of EEdf1 from previously known interaction become conspicuous in the transitional region. Figure 4 shows the level schemes of ^{31}Mg of experimental data and various theoretical calculations. To describe the nearly degenerate positive and negative states as ground and low-lying states, the mixing of sd - and pf -shells is essential. Among four different theoretical calculations, only EEdf1 and AMD+GCM calculations can reproduce the correct ordering of four low-lying states. For sdpf-U-mix calcula-

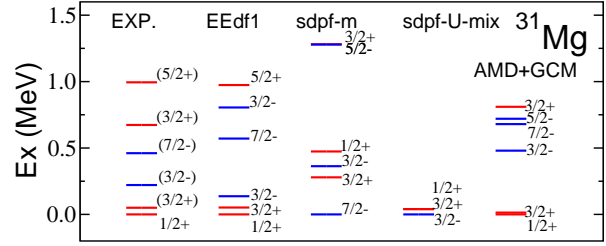


Figure 4: the level schemes of ^{31}Mg of experimental data and various theoretical calculations.

tion, they did not try fine-tuning of the interaction. This is understandable since the number of fitting parameters are significantly larger than that of the experimental data. In our approach, on the other hand, we are free from this kind of difficulty, because we derive the interaction starting from nuclear force and microscopic theory.

In summary, we constructed the effective interaction for the shell model in $sdpf$ -shell space, named EEdf1 interaction. Among $10 \leq N \leq 22$ nuclei, levels of Ne, Mg and Si isotopes were calculated and experimental excitation energies of 2^+ and 4^+ states are well reproduced. A large fraction of many-particle-many-hole excitations is found for this interaction in island of inversion, which is quite different from previous studies on nuclei in this region. This is a new aspect of island of inversion and the intuitive interpretation of this is given with the natural relation with previous theories. Also we demonstrated the importance of many-particle-many-hole excitation by showing that levels in ^{31}Mg are well described with calculations with EEdf1 interaction.

The Lanczos shell-model calculation is performed with the code "KSHELL" [7]. This work was supported in part by Grants-in-Aid for Scientific Research (23244049,15K05090). It was supported in part by HPCI Strategic Program (hp140210, hp150224, hp160221), in part by MEXT and JICFuS as a priority issue (Elucidation of the fundamental laws and evolution of the universe) to be tackled by using Post 'K' Computer, and also by CNS-RIKEN joint project for large-scale nuclear structure calculations.

References

- [1] Y. Utsuno, T. Otsuka, T. Mizusaki, and M. Honma, Phys. Rev.C **60**, 054315 (1999).
- [2] E. Caurier, F. Nowacki, and A. Poves, Phys. Rev. C **90**, 014302 (2014).
- [3] M. Kimura, Phys. Rev. C **75**, 041302 (2007).
- [4] T. Kuo, E. Osnes, Lecture Notes in Physics, **364**, 1 170 (1990).
- [5] N. Tsunoda, K. Takayanagi, M. Hjorth-Jensen, T. Otsuka, Phys. Rev. C **89**, 024313 (2014).
- [6] T. Otsuka, T. Suzuki, J. D. Holt, A. Schwenk, and Y. Akaishi, Phys. Rev. Lett. **105**, 032501 (2010).
- [7] N. Shimizu, arXiv:1310.5431v1 [nucl-th] (2013)

$E1$ strength function in Monte Carlo shell model

T. Togashi^a, T. Otsuka^{a,b}, N. Shimizu^a, and Y. Utsuno^{a,c}

^aCenter for Nuclear Study, University of Tokyo

^bDepartment of Physics, University of Tokyo

^cJapan Atomic Energy Agency

Monte Carlo shell model (MCSM) is a powerful method to describe low-lying spectra of medium-heavy nuclei [1]. However, collective excitation such as giant dipole resonance (GDR) is difficult to be described even by the MCSM directly, since the level density is rather high and an enormous number of eigenstates are needed to be obtained. This work presents a new extension of the MCSM framework to describe the strength function without obtaining these eigenstates exactly. In this extension, we generate the MCSM basis states by using $E1$ operators as $|\phi^{E1}\rangle = \exp(i\varepsilon \cdot E1)|\phi_0\rangle$, where $|\phi_0\rangle$ is the MCSM basis state, and additional variational procedure. The exact strength function is approximated by the strength function obtained by the subspace spanned by these MCSM basis states. The detail of this method is explained below.

We adopt the first step of Lanczos strength function method [2] where the excited states by $E1$ transitions are generated by acting an $E1$ operator on the basis states of the ground state. Since the basis states in the MCSM are represented by Slater determinants, we introduce an exponential of one-body operators which transforms one Slater determinant into another following Eqs. (30)-(35) in [3]. Here, considering that an $E1$ operator is proportional to a single-particle coordinate \vec{r}_i , we introduce the exponential operator of $E1$ as follows:

$$\exp(i\varepsilon \cdot E1) \equiv \exp\left(i\varepsilon \cdot \sum_{i=1}^{N_f} e_{E1} (x_i + y_i + z_i)\right), \quad (1)$$

where ε is an arbitrary real value, N_f is the number of fermions, and e_{E1} is $N/(N+Z)$ for a proton or $-Z/(N+Z)$ for a neutron to remove the spurious center-of-mass motion by $E1$ excitation. The basis state to describe the states in $E1$ spectrum is generated from the N_0 basis states of the ground state $\{|\phi_n^{g.s.}\rangle\}$ ($n = 1, \dots, N_0$) as

$$|\phi_n^{E1}\rangle \equiv \exp(i\varepsilon \cdot E1)|\phi_n^{g.s.}\rangle. \quad (2)$$

The above basis states are projected out onto the spin-parity of the final states of $E1$ transitions from the ground state. The norm and Hamiltonian matrices represented by the basis states $\{|\phi_1^{E1}\rangle, \dots, |\phi_{N_0}^{E1}\rangle\}$ are diagonalized to describe $E1$ spectrum. ε is determined by maximizing the sum of $B(E1)$ strength.

One exponential operator $\exp(i\varepsilon \cdot E1)$ is too naive to describe physical spectrum because its $E1$ strength distribution is concentrated around one peak whose $E1$ strength exhausts almost all of $B(E1)$ sum rule. To solve this problem, we decompose an $E1$ operator for the purpose to separate peaks corresponding to individual single-particle transitions due to different orbital combinations. The $E1$ operator can be represented as $\sum T_{j_b, j_a} [c_{j_b}^\dagger \otimes c_{j_a}]^{J=1}$ where T_{j_b, j_a}

is proportional to the reduced matrix $\langle j_b || rY^{(1)} || j_a \rangle$ between the orbits j_a and j_b . The decomposed $E1$ operator that treats the excitation from the orbit j_a to j_b is defined as $E1(j_a \rightarrow j_b) \equiv T_{j_b, j_a} [c_{j_b}^\dagger \otimes c_{j_a}]^{J=1}$. We adopt the basis states generated by the decomposed $E1$ operator $E1(j_a \rightarrow j_b)$ to obtain the states in $E1$ spectrum:

$$|\phi_n^{E1(j_a \rightarrow j_b)}\rangle \equiv \exp(i\varepsilon \cdot E1(j_a \rightarrow j_b))|\phi_n^{g.s.}\rangle. \quad (3)$$

In the case of N_T orbital combinations, $E1$ spectrum is obtained by $N_0 \times N_T$ basis states.

For description of fine strength distribution in $E1$ spectrum, we generate additional new basis states by the variation of the set of the basis states. Here, the basis states are optimized by lowering the average of eigenvalues: $\sum \mathcal{E}_m$, where \mathcal{E}_m is the eigenvalue of the state with the excitation energy ≤ 25 MeV within the energy region of GDR. In the above variation, we vary one basis state at a time by conjugate gradient method mentioned in [1]. This variation to lower the energy average corresponds to a variational shift for the set of basis states. The variational shifts are iterated in several cycles to generate different several sets of basis states. When we perform the variational shifts in N_V cycles for the set of $N_0 \times N_T$ basis states, we obtain the $N_0 \times N_T \times N_V$ additional new basis states.

In the present work, we apply the new extension of MCSM to calculate photoabsorption cross sections by describing $E1$ spectrum. Photoabsorption cross sections are essential to describe (γ, n) reaction which is understood as a part of particle emissions via photoabsorption process. The (γ, n) reaction is important as photodisintegration in silicon burning and $\gamma(p)$ -process in astrophysical phenomena. Furthermore, this reaction is a candidate for nuclear transmutation of long-lived fission products (LLFPs) in radioactive waste in nuclear engineering.

We calculate $E1$ spectrum and photoabsorption cross sections of ^{88}Sr ($Z = 38, N = 50$) and ^{90}Sr ($Z = 38, N = 52$). The model space of the present work is composed of pf - sdg shells, $0h_{11/2}$, $1f_{7/2}$, and $2p_{3/2}$ orbits with a ^{40}Ca inert core. The effective Hamiltonian is constructed by the combination of existing ones. GXPF1A [4] is used for pf -shell orbits. JUN45 [5] is used for $1p_{3/2,1/2}$, $0f_{5/2}$ and $0g_{9/2}$ orbits. SNBG3 [6] is used for the $T = 1$ interaction for $0g_{7/2}$, $1d_{5/2,3/2}$, $2s_{1/2}$ and $0h_{11/2}$. V_{MU} [7, 8] is used for the other part. The central force in the above interactions is scaled by 0.55 and 0.5 for V_{MU} and the orbits for pf shell and $0g_{9/2}$, respectively. The single-particle energies are determined by reproducing the effective single-particle energies [9] in ^{90}Zr ($Z = 40, N = 50$). We add the term to remove the spurious center-of-mass motion proposed by

Gloeckner and Lawson [10] to the present Hamiltonian. Note that, for the present model space and the Hamiltonian, the conventional shell-model calculation is not feasible because the M -scheme dimension of the Hamiltonian matrix is over 10^{36} for these nuclei studied while the current limit of dimension is $\sim 10^{10}$.

The 0_1^+ ground states are represented by 20 basis states $|\phi_n^{g.s.}\rangle$ of the MCSM in the present work ($N_0 = 20$). The 18 orbital combinations $E1(j_a \rightarrow j_b)$ can be considered in the present model space ($N_T = 18$). Following Eq. (3), the basis states $|\phi_n^{E1(j_a \rightarrow j_b)}\rangle$ to describe the $E1$ spectrum of 1^- states are generated by $N_0 \times N_T = 20 \times 18 = 360$ basis states. For computational efficiency, we choose 15 basis states in the ground states ($N_0 = 15$) and 10 orbital combinations ($N_T = 10$) so as not to affect the calculated spectrum. And then, we perform variational shifts twice ($N_V = 2$) and obtain $N_0 \times N_T \times N_V = 15 \times 10 \times 2 = 300$ additional basis states. The low-lying 1^- states are independently solved by 100 basis states in the normal framework of MCSM [1]. Finally, we add these 100 basis states to $360 + 300$ basis states generated by the above method.

Figure 1 presents the theoretical results of photoabsorption cross sections in comparison with the experimental (γ, n) and (γ, γ') data of ^{88}Sr [11–13]. The photoabsorption cross sections are calculated from $B(E1)$ strength smeared by Lorentz functions as mentioned in [14]. The width of Lorentz function is taken as 2 MeV. Figure 1 shows that the experimental cross section in ^{88}Sr is well reproduced by the present calculation.

The present MCSM calculation succeeds in solving the states in $E1$ spectrum around the region of GDR in these nuclei studied as shown above. As well as GDR, this result reproduces apparent pygmy dipole resonance (PDR) around the excitation energy 9 MeV indicated by the $^{88}\text{Sr}(\gamma, \gamma')$ reaction in [13]. For ^{90}Sr , one of the LLFPs without available data of photoabsorption cross section, the existence of PDR around the excitation energy 9 MeV as well as ^{88}Sr is predicted in the present work. As the distinction between ^{88}Sr and ^{90}Sr , the PDR of ^{88}Sr exists below one neutron threshold energy S_n , whereas that of ^{90}Sr is predicted over its S_n . With regard to prediction of PDR, it depends on effective Hamiltonian whether PDR is described theoretically or not. We find that the PDR in these Sr isotopes fails to be described when the effective Hamiltonian composed of only V_{MU} is applied. Hence, we are proceeding to discuss the effective Hamiltonian in the nuclei of this mass region.

This work was supported in part by HPCI Strategic Program (Project ID: hp140210, hp150224), in part by MEXT and JICFuS, and by CNS-RIKEN joint project for large-scale nuclear structure calculations.

References

- [1] N. Shimizu *et al.*, Prog. Theor. Exp. Phys. **2012**, 01A205 (2012).
- [2] R. R. Whitehead, *Moment Methods in Many-Fermion Systems*, p.235 (1980).
- [3] T. Otsuka *et al.*, Prog. Part. Nucl. Phys. **47**, 319 (2001).

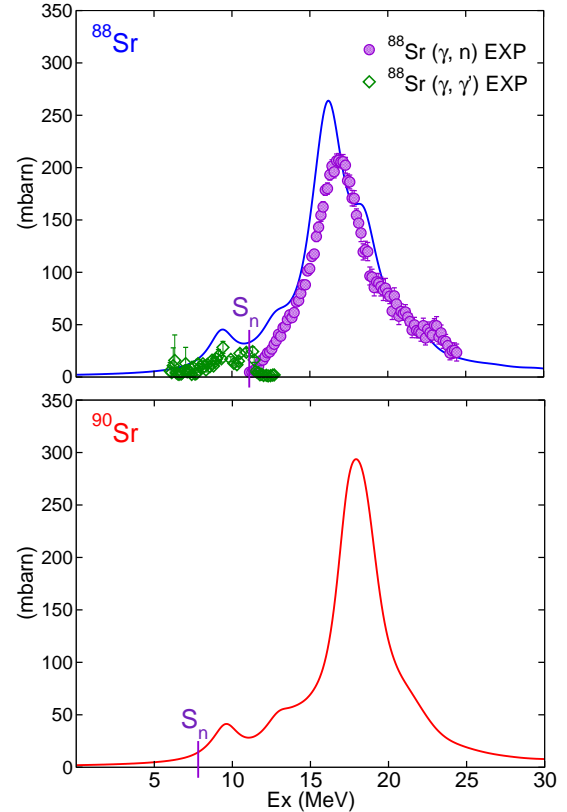


Figure 1: Theoretical results of photoabsorption cross sections for ^{88}Sr and ^{90}Sr . The result of ^{88}Sr is compared with the experimental (EXP) data taken from [11–13]. S_n represents one neutron threshold energy taken from [15].

- [4] M. Honma *et al.*, Eur. Phys. J. A **25**, 499 (2005).
- [5] M. Honma *et al.*, Phys. Rev. C **80**, 064323 (2009).
- [6] M. Honma *et al.*, RIKEN Accel. Prog. Rep. **45**, 35 (2012).
- [7] T. Otsuka *et al.*, Phys. Rev. Lett. **104**, 012501 (2010).
- [8] Y. Utsuno *et al.*, Phys. Rev. C **86**, 051301(R) (2012).
- [9] M. H. Storm *et al.*, J. Phys. G: Nucl. Phys. **9**, L165 (1983).
- [10] D. H. Gloeckner and R. D. Lawson, Phys. Lett. **53B**, 313 (1974).
- [11] A. M. Goryachev and G. N. Zalesnyy, Vopr. Teor. Yad. Fiz. **8**, 121 (1982).
- [12] Data extracted using the Centre for Photonuclear Experiments Data (CDFE) World Wide Web site from the Chart of Giant Dipole Resonance Main Parameters database.
- [13] R. Schwengner *et al.*, Phys. Rev. C **76**, 034321 (2007).
- [14] H. Sagawa and T. Suzuki, Phys. Rev. C **59**, 3116 (1999).
- [15] NuDat 2.6, <http://www.nndc.bnl.gov/nudat2/>.

Structure of Be isotopes

T. Yoshida^a, N. Shimizu^a, T. Abe^b and T. Otsuka^{a, b, c, d}

^a Center for Nuclear Study, Graduate School of Science, University of Tokyo

^b Department of Physics, University of Tokyo

^c National Superconducting Cyclotron Laboratory, Michigan State University
, East Lansing, Michigan, USA

^d Instituut voor Kern- en Stralingsfysica, Katholieke Universiteit Leuven

The states which have developed α cluster are suggested in Be isotopes around the α break-up threshold by cluster model [1]. The appearance of molecular orbit for valence neutrons around the two α 's is also suggested with phenomenological approach [2]. Recently, applications of the ab-initio calculations [3] are also focus on these nuclei. The existence of rotational bands in these nuclei are also discussed in the shell model framework with no-core full configuration interaction (NCFC [4]).

The Monte Carlo shell model (MCSM) approach is one of such method. We expect that the MCSM describe not only the single particle excitations but also many particle-hole excitations which create the α cluster relative motion. For theoretical calculations, the breaking of the $N = 8$ magicity is one of the important problem [5,6]. Because the phenomena is related both to the description of α clusters relative motion in the two α cores part and the single particle motion on the molecular orbits around the core. In the previous report, we showed that the α cluster structure can be treated in our model by using the intrinsic density of the MCSM wave function [7, 8]. The model space is truncated by the maximum number of the major shell (N_{shell}) in which the nucleon can be occupied.

In the present study, we see whether the wave function of MCSM reproduce the overall low-lying energies and $B(E2)$'s of even-even Be isotopes. We use the model space with the harmonic oscillator parameter $\hbar\omega = 15$ MeV as an empirical one. The calculation procedure is the same one as before. The interaction is JISP16 [9] and the center of mass motion is treated by the Lawson's method [10]. The numerical calculation was performed on the K computer (RIKEN AICS) and FX10 (the University of Tokyo). The extrapolation method using energy variance [11] is applied not only for the total energy but also for the $B(E2)$ when we estimate the exact value for the given N_{shell} .

In Fig. 1, the energy spectra are shown with the experimental values. There are some deviations from the experimental values especially for the 0_2^+ states. Even though, the overall values are in the reasonable range compared with the experiments. For ^{10}Be , we check the intrinsic shape of the π molecular orbit for the valence neutrons. The excited state have the σ orbit in the intrinsic shape. Due to the effect of the σ orbit, two α inter clusters distance increases compare to the ground state. This effect is not taken into account for the small model space ($N_{\text{shell}} = 4$). By increasing the model space to $N_{\text{shell}} = 6$, the relative two α motion (~ 1 fm) is taken into account. However, the larger 0_2^+ energy of MCSM may indicate that the present model space

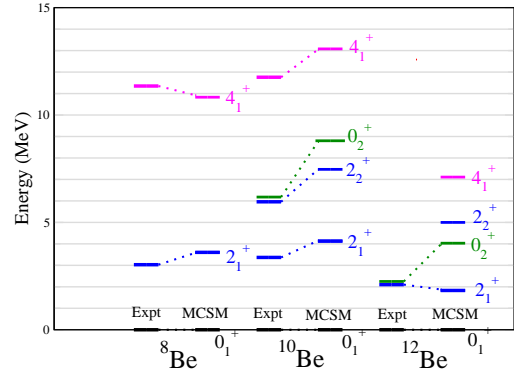


Figure 1: The 2_1^+ energies for experiments (left bars) and MCSM (right bars) for $^{8,10,12}\text{Be}$. The 0^+ , 2^+ , 4^+ states are shown with different colors.

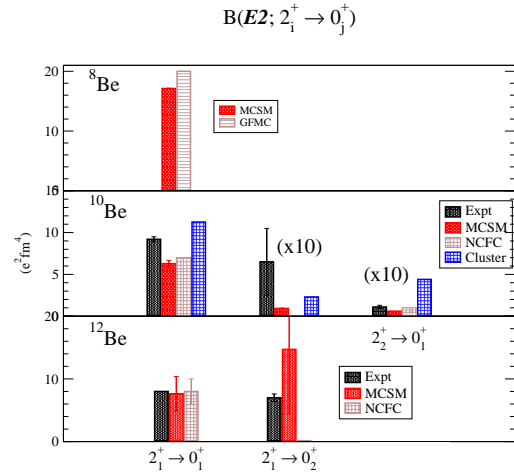


Figure 2: The $B(E2)$ values for Be isotopes. The black, red bars show the experimental, MCSM results, respectively. The brown, blue bars show the other microscopic, cluster model results, respectively.

is not enough for the quantitative analysis for these specific states. The breaking of the $N = 8$ magicity affects directly to the decrease of the 2_1^+ energy. As shown in the figure, the MCSM result has this decrease. From the theoretical studies, the mixing of the π and σ orbits are important to understand the breaking of the $N = 8$ magicity. This effect is also understood as an appearance of relatively large occupation number of neutron sd orbits. The numbers are 1.3, 1.0, and 1.9 for $0_{1,2}^+$ and 2_1^+ , respectively. This indicates the breaking of $N = 8$ magicity for these states. On the other hand, the experimental $0_1^+, 2_1^+, 4_1^+$ band structure are well reproduced with MCSM.

In Fig. 2, the $B(E2)$ values have been calculated. We notice that during the calculation, the bare charges are used. The MCSM results show the reasonable agreement with the experiments and other calculations. The ^8Be $B(E2)$ value for the MCSM shows the reasonable agreement with the Green's function Monte Carlo (GFMC) results. For the GFMC result, Argonne v_{18} two-nucleon and Illinois7 three-nucleon potential is applied. For $^{10,12}\text{Be}$, the $B(E2; 2_1 \rightarrow 0_1^+)$ values show good agreement with the others. The $B(E2; 2_1 \rightarrow 0_2^+)$ and $B(E2; 2_2 \rightarrow 0_1^+)$ value for ^{10}Be are also shown. The values are smaller than the experimental and cluster model calculations.

If we assume that the effective single particle energy for the neutron $0p_{1/2}$ orbit is much lower than that for the sd orbit, the mixing effect of sd orbit ($\sim \sigma$ orbits) is small for the 0_1^+ and 2_1^+ states. In such a case, the orbit of the 0_2^+ state should be completely different from the 2_1^+ state. As a result, the $B(E2; 2_1^+ \rightarrow 0_2^+)$ value should be small. The calculated large $B(E2)$ indicates the existence of the mixing effect. Although there are some uncertainty when we estimate the error bars of the extrapolation method, this MCSM results show large value as experimental values show.

In the future studies, quantitative study of observables as a function of N_{shell} and $\hbar\omega$ are needed. We will also extend this study to the nuclei which contain many α configurations such as carbon isotopes. The nuclei show the breaking of the axial symmetry of the intrinsic state. We have developed the method to extract such structure from the summation of Slater determinants. For the test calculation, three α like configurations are seen for $^{12,13,14}\text{C}$. This work has been supported by the SPIRE Field 5 from MEXT, and the CNS-RIKEN joint project for large-scale nuclear structure calculations.

References

- [1] M. Ito, N. Itagaki, H. Sakurai and K. Ikeda, *Phys. Rev. Lett.* **100**, 182502 (2008).
- [2] N. Itagaki and S. Okabe, *Phys. Rev. C* **61**, 044306 (2000).
- [3] R. B. Wiringa, S. C. Pieper, J. Carlson and V. R. Pandharipande, *Phys. Rev. C* **62**, 014001 (2000).
- [4] P. Maris, J.P. Vary, A.M. Shirokov, *Phys. Rev. C* **79**, 014308 (2009); P. Maris, A.M. Shirokov, and J.P. Vary, *ibid.* **81**, 021301(R) (2010).
- [5] A. Navin, et al., *Phys. Rev. Lett.* **85**, 266 (2000).
- [6] S. Shimoura, et al. *Phys. Lett. B* **654** 87 (2007).

- [7] L. Liu, T. Otsuka, N. Shimizu, Y. Utsuno, and R. Roth *Phys. Rev. C* **86**, 014302 (2012).
- [8] N. Shimizu, T. Abe, Y. Tsunoda, Y. Utsuno, T. Yoshida, T. Mizusaki, M. Honma and T. Otsuka, *Prog. Theor. Exp. Phys.* **2012**, 01A205 (2012).
- [9] A.M. Shirokov, J.P. Vary, A.I. Mazur, S.A. Zaytsev, and T.A. Weber, *Phys. Lett. B* **621**, 96 (2005).
- [10] D. Gloeckner and R. Lawson, *Phys. Lett. B* **53**, 313 (1974).
- [11] N. Shimizu, Y. Utsuno, T. Mizusaki, T. Otsuka, T. Abe, and M. Honma, *Phys. Rev. C* **82**, 061305(R) (2010).

Monte Carlo shell model calculations for structure of nuclei around $Z=28$

Y. Tsunoda^a, T. Otsuka^{b,a,c,d}, N. Shimizu^a, M. Honma^e, and Y. Utsuno^f

^aCenter for Nuclear Study, the University of Tokyo

^bDepartment of Physics, the University of Tokyo

^cNational Superconducting Cyclotron Laboratory, Michigan State University, USA

^dInstituut voor Kern- en Stralingsfysica, KU Leuven, Belgium

^eCenter for Mathematical Sciences, University of Aizu

^fAdvanced Science Research Center, Japan Atomic Energy Agency

Nuclear shape is one of the most important property of nuclear collectivity. We discuss the property of the shape of the 0^+ states of Ni isotopes ($Z = 28$) from ^{64}Ni ($N = 36$) to ^{76}Ni ($N = 48$) in this report. We have investigated Ni isotopes by using the Monte Carlo shell model (MCSM) calculations [1,2] and our calculations can describe the properties known from experiments. Some of our calculational results of Ni isotopes were published in Refs. [3–7].

The model space used in our calculations is the full pf shell, the $0g_{9/2}$ and $1d_{5/2}$ orbits for both protons and neutrons. We use the effective interaction used in Ref. [3]. We performed MCSM calculations so that the calculation in the large model space is available. In the MCSM, the wave function $|\Psi\rangle$ is represented as the superposition of the projected Slater determinants (MCSM basis vectors) as

$$|\Psi\rangle = \sum_{n,K} f_{n,K} P_{MK}^{J\pi} |\phi_n\rangle,$$

where $P_{MK}^{J\pi}$ is the angular-momentum and parity projector and $|\phi_n\rangle$ is a Slater determinant. We can analyze the nuclear intrinsic shape by using the MCSM basis vector before projection, $|\phi_n\rangle$. This method has been used in the study of Ni isotopes [3,5,6]. In this method, we use the figure (referred to as T-plot) of the potential energy surface (PES) with circles indicating the shape of the MCSM basis vector. An example of T-plot is shown in Fig. 1. The PES is calculated by constrained Hartree-Fock method using the shell-model effective interaction. We calculate the quadrupole moments, Q_0 and Q_2 , of the MCSM basis vector before projection and locate a circle at the corresponding place in the PES. The area of the circle is proportional to the overlap probability between the MCSM basis vector $P_{MK}^{J\pi} |\phi_n\rangle$ and the wave function $|\Psi\rangle$. Thus, the distribution pattern of the circles indicates the nuclear intrinsic shape of the eigenstate. Although the $J = 0$ wave function is isotropic, we can analyze intrinsic shape of the 0^+ state because we use the MCSM basis vector before the angular-momentum projection.

We calculated three or four 0^+ states for $^{64-76}\text{Ni}$ even-even nuclei. The shape of each calculated level was determined by using T-plot. There are states with spherical, oblate and prolate shapes and shape coexistence in this region is predicted by our calculations. Figure 2 shows calculated excitation energies of the 0^+ states and the yrast 2^+ state. The energy of the oblate state is lower than that of the prolate state for $N \leq 40$. The order is interchanged for $N \geq 42$. The energy of the deformed states is lower for $N \sim 42$.

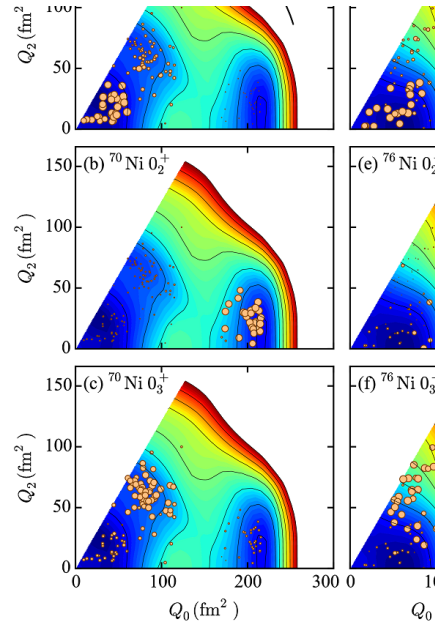


Figure 1: T-plots of the 0^+ states of ^{70}Ni and ^{76}Ni . Details are explained in the text.

Shape coexistence in this region can be explained by considering type II shell evolution [3, 7]. Type I shell evolution is the change of the nuclear shell structure in different isotopes or isotones. This is caused by the change of the proton or neutron number. On the other hand, type II shell evolution is the change of the shell structure in the same nuclide with different configuration. The shell structure can be changed by the particle-hole excitation. The $Z = 28$ shell gap between the proton $0f_{7/2}$ and $0f_{5/2}$ orbits and the $N = 40$ gap between the neutron $0f_{5/2}$ and $0g_{9/2}$ orbits are related to type II shell evolution in neutron-rich Ni isotopes. Both neutrons in the $0g_{9/2}$ orbit and neutron holes in the $0f_{5/2}$ orbit reduce the proton $0f_{7/2}$ - $0f_{5/2}$ gap due to general property of the tensor force. When neutron particle-hole excitation occurs, the proton gap becomes small and the nucleus can gain deformation energy easily. Thus, deformed state can appear in low excitation energy. When few neutrons are excited and the proton gap remains large, the spherical state can exist in low energy. These states of different shapes with different configurations can coexist due

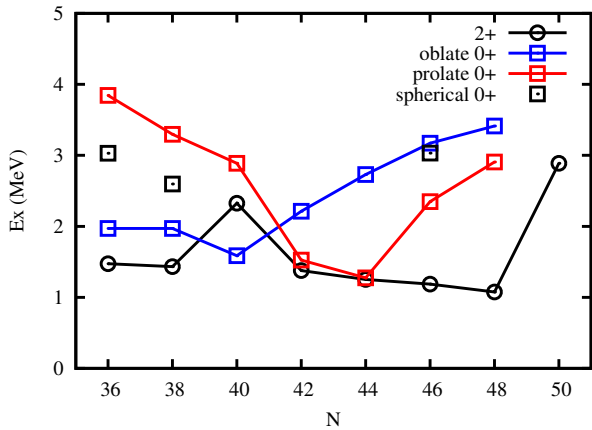


Figure 2: Calculated excitation energies of the 0^+ and yrast 2^+ states in Ni isotopes. The 0^+ and 2^+ states are shown by square and circle, respectively. The prolate and oblate 0^+ states are shown in red and blue, respectively. The ground state is spherical 0^+ and the excited spherical 0^+ state is shown by black square.

to type II shell evolution. The effect of type II shell evolution is large when many particles can excite across the shell gap, and the deformed state is expected to have low excitation energy near $N = 40$.

We can study nuclear shape by using the local minimum of the PES. Figures 1 (a)-(c) show T-plots of three 0^+ states of ^{70}Ni and circles are distributed around the different local minimum of the PES. T-plots of three 0^+ states of ^{76}Ni in Figs. 1 (d)-(f) also show different nuclear shapes, but circles are not necessarily located around the local minimum. Thus, T-plot can give us more information which cannot be obtained by using the PES only.

This work has been supported in part by the HPCI Strategic Program Field 5 and the RIKEN-CNS joint research project on large-scale nuclear-structure calculations. The MCSM calculations were performed on the K computer at the RIKEN AICS (Project ID: hp150224).

References

- [1] T. Otsuka, M. Honma, T. Mizusaki, N. Shimizu, and Y. Utsuno, *Prog. Part. Nucl. Phys.* **47**, 319 (2001).
- [2] N. Shimizu, T. Abe, Y. Tsunoda, Y. Utsuno, T. Yoshida, T. Mizusaki, M. Honma, and T. Otsuka, *Prog. Theor. Exp. Phys.* **2012**, 01A205 (2012).
- [3] Y. Tsunoda, T. Otsuka, N. Shimizu, M. Honma, and Y. Utsuno, *Phys. Rev. C* **89**, 031301(R) (2014).
- [4] S. Suchyta *et al.*, *Phys. Rev. C* **89**, 021301(R) (2014).
- [5] F. Flavigny *et al.*, *Phys. Rev. C* **91**, 034310 (2015).
- [6] C. J. Chiara *et al.*, *Phys. Rev. C* **91**, 044309 (2015).
- [7] T. Otsuka, and Y. Tsunoda, *J. Phys. G: Nucl. Part. Phys.* **43**, 024009 (2016).

Other Activities

The 14th CNS International Summer School (CNSSS15)

K. Yako^a, S. Shimoura^a, T. Gunji^a, H. Hamagaki^a, E. Hiyama^b, N. Imai^a, Y. Iwata^a,
S. Michimasa^a, T. Nakatsukasa^c, S. Ota^a, T. Otsuka^{a,d}, H. Sakai^b, H. Sakurai^{b,d}, N. Shimizu^a,
T. Uesaka^b, Y. Utsuno^{a,e}, and H. Utsunomiya^{a,f}

^aCenter for Nuclear Study, Graduate School of Science, University of Tokyo

^bRIKEN Nishina Center

^cDepartment of Physics, University of Tsukuba

^dDepartment of Physics, Graduate School of Science, University of Tokyo

^eJapan Atomic Energy Agency (JAEA)

^fDepartment of Physics, Konan University

The 14th CNS International Summer School (CNSSS15) was hosted jointly by Center for Nuclear Study (CNS), the University of Tokyo in the period of August 26–September 1, 2015. The venues were the Nishina hall in the Wako campus of RIKEN (Aug26-28, Aug30-Sep1) and Koshiba hall in the Hongo campus of University of Tokyo (Aug29).

This summer school was the fourteenth one in the series which aimed at providing graduate students and postdocs with basic knowledge and perspectives of nuclear physics. It consisted of lectures by leading scientists in the fields of both experimental and theoretical nuclear physics. Each lecture started with an introductory talk from the fundamental point of view and ended with up-to-date topics in the relevant field.

The list of lecturers and the title of lectures are shown below.

Robert Janssens (Argonne National Laboratory, USA)

“Physics at the extremes with large gamma-ray arrays”

Wilton Catford (University of Surrey, UK)

“What we can learn from nucleon transfer reactions using radioactive beams”

Javier Menéndez (University of Tokyo, Japan)

“Ab-initio framework to study nuclear structure and fundamental symmetries”

Naoyuki Itagaki (Yukawa Institute for Theoretical Physics, Kyoto Univ., Japan)

“Exotic clustering in neutron-rich nuclei and connection to the shell structure”

Haozhao Liang (RIKEN Nishina Center, Japan)

“Covariant density functional theory and nuclear spin-isospin excitations”

Hiroyuki Takahashi (University of Tokyo, Japan)

“Current trends in radiation measurements”

Hiroyuki Oigawa (Japan Atomic Energy Agency, Japan)

“Transmutation technology for long-lived nuclear wastes”

Yuichi Ichikawa (RIKEN Nishina Center, Japan)

“Spin orientation in RI beam”

This year, 8 lecturers and 97 participants attended from 7 countries. Two lecturers and 24 participants were from foreign institutes. Participants communicated with each

other in the free discussion time between the lectures and in the welcome and farewell parties in a relaxed atmosphere.

There were 4 sessions of “Young Scientist’s Session”. Here, 26 talks and 19 posters were presented by graduate students and postdocs.

All the information concerning the summer school is open for access at the following URL:

<http://www.cns.s.u-tokyo.ac.jp/summerschool/cnsss15>

The organizers appreciate Graduate School of Science, University of Tokyo for the use of Koshiba Hall and RIKEN Nishina Center for providing the venue as well as the accommodations. We are grateful to supports from HPCI Strategic Program Field 5, and Asian Nuclear Physics Association (ANPhA). We thank administration staffs of the CNS for their helpful supports. We also thank graduate students and postdocs in the CNS for their dedicated efforts. Finally, we acknowledge all the lecturers and participants for their contributions to this summer school.

Laboratory Exercise for Undergraduate Students

S. Ota, M. Niikura^a, N. Kitamura, T. Saito^a, K. Yako, H. Sakurai^{a,b} and S. Shimoura

Center for Nuclear Study, Graduate School of Science, University of Tokyo

^a*Department of Physics, University of Tokyo*

^b*RIKEN Nishina Center*

Nuclear scattering experiments were performed as a laboratory exercise for undergraduate students of the University of Tokyo. This program was aiming at providing undergraduate students with an opportunity to learn how to study subatomic physics by using an ion beam from an accelerator. In 2015, 31 students attended this program.

The four beam times were scheduled in the second semester for third-year students, and 8 students participated in each beam time. The experiments were performed at the RIBF using a 26-MeV alpha beam accelerated by the AVF cyclotron. The alpha beam extracted from the AVF cyclotron was transported to the E7B beam line in the E7 experimental hall. The scattering chamber has two separate target ports which enable us to perform two independent experiments without opening the chamber during the beam time. In each beam time, the students were divided into two groups and took one of the following two subjects:

1. Measurement of elastic scattering of incident alpha particle with ^{197}Au , to learn how to determine nuclear size.
2. Measurement of gamma rays emitted from the cascade decay of highly excited ^{154}Gd and ^{184}Os , to learn the nuclear deformation.

Before the experiment, the students took a course on the basic handling of the semiconductor detectors and electronic circuits at the Hongo campus, and attended a radiation safety lecture at RIKEN. They also joined a tour to the RI beam factory at RIKEN.

In the $\alpha+^{197}\text{Au}$ measurement, α particles scattered with the Au target with a thickness of $1\ \mu\text{m}$ were detected using a silicon PIN-diode located 15-cm away from the target. A collimator with a diameter of 6 mm was attached on the silicon detector. The energy spectrum of the scattered α particles was recorded by a multi-channel analyzer (MCA) system. The beam was stopped by a Faraday cup located downstream of the scattering chamber. The cross section for the alpha elastic scattering was measured in the angular range of $\theta_{\text{lab}} = 20-150^\circ$.

The measured cross section was compared with the calculated cross section of the Rutherford scattering. The cross section was also analyzed by the potential model calculation, and the radius of the ^{197}Au nucleus was discussed. Some students obtained the radius of $\sim 10\ \text{fm}$ by using a classical model where the trajectory of the α particle in the nuclear potential is obtained using the Runge-Kutta method. Others tried to understand the scattering process by calculating the angular distribution using the distorted wave Born approximation method with a Coulomb wave function and

a realistic nuclear potential.

In the measurement of gamma rays, excited states in ^{154}Gd and ^{184}Os nuclei were populated by the $^{152}\text{Sm}(\alpha,2n)$ and $^{182}\text{W}(\alpha,2n)$ reactions, respectively. The gamma rays emitted from the cascade decay of the rotational bands were measured by a high-purity germanium detector located 30-cm away from the target. The energy of the gamma ray were recorded by the MCA system. The gain and the efficiency of the detector system had been calibrated using standard gamma-ray sources of ^{22}Na , ^{60}Co , ^{133}Ba , and ^{137}Cs . The gamma rays from the 10^+ and 8^+ states in ^{154}Gd and ^{184}Os , respectively, were successfully identified. Based on the energies of the gamma rays, the moment of inertia and the deformation parameters of the excited states were discussed by using a classical rigid rotor model and a irrotational fluid model. The students found that the reality lies between the two extreme models. The initial population among the levels in the rotational band was also discussed by taking the effect of the internal conversion into account.

It was the first time for most of the students to use large experimental equipments. They learned basic things about the experimental nuclear physics and how to extract physics from the data. We believe this program was very impressive for the students. The authors would like to thank Dr. Y. Uwamino, the CNS accelerator group, and the RIBF cyclotron crew for their helpful effort in the present program.

Appendices

**Symposium, Workshop, Seminar, PAC and
External Review**

CNS Reports

Publication List

Talks and Presentations

Personnel

Symposium, Workshop, Seminar, Colloquium, and PAC

A. Symposium and Workshop

1. OEDO-SHARAQ International Collaboration Workshop <http://indico.cns.s.u-tokyo.ac.jp/conferenceDisplay.py?confId=244>, Sept. 8-9, 2015, Center for Nuclear Study, the University of Tokyo, RIKEN
2. 第12回 AVF サイクロトロン合同打ち合わせ:
Oct. 1-2, 2015, RIKEN

B. CNS Seminar

1. Haozhao Liang (RNC): “Nuclear spin and isospin physics in collective excitations and single-particle spectra” Jun. 23, 2015, Hongo, The University of Tokyo
2. Prof. Takaharu OTSUKA (UT, CNS): “Structure evolutions in exotic nuclei and nuclear forces”, Jul. 2-3, 2015, RIBF NP Seminar 203 / RIBF+CNS Nuclear Physics Seminar 2-Slot Series Plus, RIKEN
3. Andrea Vitturi (U. Padova/INFN): “Pair transfer reactions as a structure spectroscopic tool for the study of pairing interactions”, Jul. 14, 2015, Hongo, The University of Tokyo
4. Andrea Vitturi (U. Padova/INFN): “Excitation of low-lying (PDR) and high-lying (GDR) dipole modes in neutron-rich nuclei by nuclear and electromagnetic fields”, Jul. 16, 2015, Hongo, The University of Tokyo
5. Prof. Olga BELIUSKINA (CNS): “On the synthesis of neutron-rich isotopes along the N=126 shell in multinucleon transfer reactions”, “Diamond dE-E-ToF telescope for heavy ion reactions at low energies” Jul. 16, 2015, RIKEN
6. Anatoli Afanasjev (Mississippi State U.): “The extremes of nuclear landscape in density functional theory”, Jul. 21, 2015, Hongo, The University of Tokyo
7. Dr. Philipp SCHROCK (CNS): “The Electric Dipole Response of ^{132}Sn ” Dec. 17, 2015, RIBF NP Seminar 212, RIKEN
8. Prof. Koichi HAGINO (Tohoku Univ.): “Heavy-ion subbarrier fusion: a sensitive tool to probe nuclear structure” Feb. 22, 2016, Center for Nuclear Study, the University of Tokyo

C. Program Advisory Committee for Nuclear-Physics Experiments at RI Beam Factory

1. The 16th NP-PAC meeting
Date: December 3-5, 2015
Place: RIBF Conference Hall on the 2nd floor of the RIBF Building

CNS Reports

#94 “CNS Annual Report 2014”

Edited by T. Gunji, and Y. Kushi February, 2016

Publication List

A. Original Papers

1. A. Pakou, N. Keeley, D. Pierrousakou, M. Mazzocco, L. Acosta, X. Aslanoglou, A. Boiano, C. Boiano, D. Carbone, M. Cavallaro, J. Grebosz, M. La Commara, C. Manea, G. Marquinez-Duran, I. Martel, C. Parascandolo, K. Rusek, A.M. Sanchez-Benitez, O. Sgouros, C. Signorini, F. Soramel, V. Soukeras, E. Stiliaris, E. Strano, D. Torresi, A. Trzcinska, Y.X. Watanabe, and H. Yamaguchi: “Total reaction cross sections for $^8\text{Li}+^{90}\text{Zr}$ at near barrier energies”, *Eur. Phys. J. A* **51** 55 (2015).
2. S. Cherubini, M. Gulino, C. Spitaleri, G. G. Rapisarda, M. La Cognata, L. Lamia, R. G. Pizzone, S. Romano, S. Kubono, H. Yamaguchi, S. Hayakawa, Y. Wakabayashi, N. Iwasa, S. Kato, T. Komatsubara, T. Teranishi, A. Coc, N. de Séréville, F. Hammache, G. Kiss, S. Bishop, D. N. Binh: “First application of the trojan horse method with a radioactive ion beam: Study of the $^{18}\text{F}(p, \alpha)^{15}\text{O}$ reaction at astrophysical energies”, *Phys. Rev. C* **92** 015805 (2015).
3. A. Kim, N.H. Lee, M. H. Han, J.S. Yoo, K.I. Hahn, H. Yamaguchi, D. N. Binh, T. Hashimoto, S. Hayakawa, D. Kahl, T. Kawabata, Y. Kurihara, Y. Wakabayashi, S. Kubono, S. Choi, Y. K. Kwon, J. Y. Moon, H. S. Jung, C.S. Lee, T. Teranishi, S. Kato, T. Komatsubara, B. Guo, W. P. Liu, B. Wang, and Y. Wang: “Measurement of the $^{14}\text{O}(p, p')^{17}\text{F}$ cross section at $E_{\text{c.m.}} = 2.1\text{--}5.3$ MeV” *Phys. Rev. C* **92** 035801 (2015).
4. H. Utsunomiya, S. Katayama, I. Gheorghe, S. Imai, H. Yamaguchi, D. Kahl, Y. Sakaguchi, T. Shima, K. Takahisa, and S. Miyamoto: “Photodisintegration of ^9Be through the $1/2+$ state and cluster dipole resonance”, *Phys. Rev. C* **92** 064323 (2015).
5. A. Adare *et al.* [PHENIX Collaboration], “Inclusive cross section and double-helicity asymmetry for π^0 production at midrapidity in $p+p$ collisions at $\sqrt{s} = 510$ GeV,” *Phys. Rev. D* **93**, no. 1, 011501 (2016)
6. J. Adam *et al.* [ALICE Collaboration], “Pseudorapidity and transverse-momentum distributions of charged particles in proton-proton collisions at $\sqrt{s} = 13$ TeV,” *Phys. Lett. B* **753**, 319 (2016)
7. J. Adam *et al.* [ALICE Collaboration], “Inclusive quarkonium production at forward rapidity in pp collisions at $\sqrt{s} = 8$ TeV,” *Eur. Phys. J. C* **76**, no. 4, 184 (2016)
8. J. Adam *et al.* [ALICE Collaboration], “Measurement of electrons from heavy-flavour hadron decays in p-Pb collisions at $\sqrt{s_{\text{NN}}} = 5.02$ TeV,” *Phys. Lett. B* **754**, 81 (2016)
9. J. Adam *et al.* [ALICE Collaboration], “Azimuthal anisotropy of charged jet production in $\sqrt{s_{\text{NN}}} = 2.76$ TeV Pb-Pb collisions,” *Phys. Lett. B* **753**, 511 (2016)
10. J. Adam *et al.* [ALICE Collaboration], “Direct photon production in Pb-Pb collisions at $\sqrt{s_{\text{NN}}} = 2.76$ TeV,” *Phys. Lett. B* **754**, 235 (2016)
11. J. Adam *et al.* [ALICE Collaboration], “Centrality evolution of the charged-particle pseudorapidity density over a broad pseudorapidity range in Pb-Pb collisions at $\sqrt{s_{\text{NN}}} = 2.76$ TeV,” *Phys. Lett. B* **754**, 373 (2016)
12. J. Adam *et al.* [ALICE Collaboration], “Measurement of D_s^+ production and nuclear modification factor in Pb-Pb collisions at $\sqrt{s_{\text{NN}}} = 2.76$ TeV,” *JHEP* **1603**, 082 (2016)
13. J. Adam *et al.* [ALICE Collaboration], “Multiplicity and transverse momentum evolution of charge-dependent correlations in pp, p-Pb, and Pb-Pb collisions at the LHC,” *Eur. Phys. J. C* **76**, no. 2, 86 (2016)
14. J. Adam *et al.* [ALICE Collaboration], “Transverse momentum dependence of D-meson production in Pb-Pb collisions at $\sqrt{s_{\text{NN}}} = 2.76$ TeV,” *JHEP* **1603**, 081 (2016)
15. A. Adare *et al.* [PHENIX Collaboration], “Scaling properties of fractional momentum loss of high- p_T hadrons in nucleus-nucleus collisions at $\sqrt{s_{\text{NN}}}$ from 62.4 GeV to 2.76 TeV,” *Phys. Rev. C* **93**, no. 2, 024911 (2016)
16. A. Adare *et al.* [PHENIX Collaboration], “Transverse energy production and charged-particle multiplicity at midrapidity in various systems from $\sqrt{s_{\text{NN}}} = 7.7$ to 200 GeV,” *Phys. Rev. C* **93**, no. 2, 024901 (2016)

17. A. Adare *et al.* [PHENIX Collaboration], “ ϕ meson production in the forward/backward rapidity region in Cu+Au collisions at $\sqrt{s_{NN}} = 200$ GeV,” *Phys. Rev. C* **93**, no. 2, 024904 (2016)
18. A. Adare *et al.* [PHENIX Collaboration], “Forward J/ψ production in U+U collisions at $\sqrt{s_{NN}}=193$ GeV,” *Phys. Rev. C* **93**, no. 3, 034903 (2016)
19. A. Adare *et al.* [PHENIX Collaboration], “Dielectron production in Au+Au collisions at $\sqrt{s_{NN}}=200$ GeV,” *Phys. Rev. C* **93**, no. 1, 014904 (2016)
20. A. Adare *et al.*, “Single electron yields from semileptonic charm and bottom hadron decays in Au+Au collisions at $\sqrt{s_{NN}} = 200$ GeV,” *Phys. Rev. C* **93**, no. 3, 034904 (2016)
21. A. Adare *et al.* [PHENIX Collaboration], “Centrality-dependent modification of jet-production rates in deuteron-gold collisions at $\sqrt{s_{NN}}=200$ GeV,” *Phys. Rev. Lett.* **116**, no. 12, 122301 (2016)
22. J. Adam *et al.* [ALICE Collaboration], “Coherent $\psi(2S)$ photo-production in ultra-peripheral Pb Pb collisions at $\sqrt{s_{NN}} = 2.76$ TeV,” *Phys. Lett. B* **751**, 358 (2015)
23. J. Adam *et al.* [ALICE Collaboration], “Precision measurement of the mass difference between light nuclei and anti-nuclei,” *Nature Phys.* **11**, no. 10, 811 (2015)
24. J. Adam *et al.* [ALICE Collaboration], “Study of cosmic ray events with high muon multiplicity using the ALICE detector at the CERN Large Hadron Collider,” *JCAP* **1601**, no. 01, 032 (2016)
25. J. Adam *et al.* [ALICE Collaboration], “Centrality dependence of pion freeze-out radii in Pb-Pb collisions at $\sqrt{s_{NN}} = 2.76$ TeV,” *Phys. Rev. C* **93**, no. 2, 024905 (2016)
26. A. Adare *et al.* [PHENIX Collaboration], “Measurements of elliptic and triangular flow in high-multiplicity $^3\text{He}+\text{Au}$ collisions at $\sqrt{s_{NN}} = 200$ GeV,” *Phys. Rev. Lett.* **115**, no. 14, 142301 (2015)
27. J. Adam *et al.* [ALICE Collaboration], “Event shape engineering for inclusive spectra and elliptic flow in Pb-Pb collisions at $\sqrt{s_{NN}} = 2.76$ TeV,” *Phys. Rev. C* **93**, no. 3, 034916 (2016)
28. J. Adam *et al.* [ALICE Collaboration], “Elliptic flow of muons from heavy-flavour hadron decays at forward rapidity in Pb Pb collisions at $\sqrt{s_{NN}} = 2.76$ TeV,” *Phys. Lett. B* **753**, 41 (2016)
29. J. Adam *et al.* [ALICE Collaboration], “Production of light nuclei and anti-nuclei in pp and Pb-Pb collisions at energies available at the CERN Large Hadron Collider,” *Phys. Rev. C* **93**, no. 2, 024917 (2016)
30. J. Adam *et al.* [ALICE Collaboration], “Centrality dependence of inclusive J/ψ production in p-Pb collisions at $\sqrt{s_{NN}} = 5.02$ TeV,” *JHEP* **1511**, 127 (2015)
31. J. Adam *et al.* [ALICE Collaboration], “ $^3_\Lambda\text{H}$ and $^3_\Lambda\bar{\text{H}}$ production in Pb-Pb collisions at $\sqrt{s_{NN}} = 2.76$ TeV,” *Phys. Lett. B* **754**, 360 (2016)
32. A. Adare *et al.* [PHENIX Collaboration], “ ϕ meson production in $d+\text{Au}$ collisions at $\sqrt{s_{NN}} = 200$ GeV,” *Phys. Rev. C* **92**, no. 4, 044909 (2015)
33. J. Adam *et al.* [ALICE Collaboration], “Forward-central two-particle correlations in p-Pb collisions at $\sqrt{s_{NN}} = 5.02$ TeV,” *Phys. Lett. B* **753**, 126 (2016)
34. J. Adam *et al.* [ALICE Collaboration], “One-dimensional pion, kaon, and proton femtoscopy in Pb-Pb collisions at $\sqrt{s_{NN}} = 2.76$ TeV,” *Phys. Rev. C* **92**, no. 5, 054908 (2015)
35. A. Adare *et al.* [PHENIX Collaboration], “Measurement of higher cumulants of net-charge multiplicity distributions in Au+Au collisions at $\sqrt{s_{NN}} = 7.7 - 200$ GeV,” *Phys. Rev. C* **93**, no. 1, 011901 (2016)
36. J. Adam *et al.* [ALICE Collaboration], “Search for weakly decaying $\bar{\Lambda}n$ and $\Lambda\Lambda$ exotic bound states in central Pb-Pb collisions at $\sqrt{s_{NN}} = 2.76$ TeV,” *Phys. Lett. B* **752**, 267 (2016)
37. J. Adam *et al.* [ALICE Collaboration], “Centrality dependence of the nuclear modification factor of charged pions, kaons, and protons in Pb-Pb collisions at $\sqrt{s_{NN}} = 2.76$ TeV,” *Phys. Rev. C* **93**, no. 3, 034913 (2016)

38. J. Adam *et al.* [ALICE Collaboration], “Centrality dependence of high- p_T D meson suppression in Pb-Pb collisions at $\sqrt{s_{NN}} = 2.76$ TeV,” JHEP **1511**, 205 (2015)
39. J. Adam *et al.* [ALICE Collaboration], “Measurement of jet quenching with semi-inclusive hadron-jet distributions in central Pb-Pb collisions at $\sqrt{s_{NN}} = 2.76$ TeV,” JHEP **1509**, 170 (2015)
40. J. Adam *et al.* [ALICE Collaboration], “Measurement of charm and beauty production at central rapidity versus charged-particle multiplicity in proton-proton collisions at $\sqrt{s} = 7$ TeV,” JHEP **1509**, 148 (2015)
41. A. Adare *et al.* [PHENIX Collaboration], “Measurement of parity-violating spin asymmetries in W^\pm production at midrapidity in longitudinally polarized $p+p$ collisions,” Phys. Rev. D **93**, no. 5, 051103 (2016)
42. J. Adam *et al.* [ALICE Collaboration], “Inclusive, prompt and non-prompt J/ψ production at mid-rapidity in Pb-Pb collisions at $\sqrt{s_{NN}} = 2.76$ TeV,” JHEP **1507**, 051 (2015)
43. A. Adare *et al.* [PHENIX Collaboration], “Systematic study of charged-pion and kaon femtoscopia in Au + Au collisions at $\sqrt{s_{NN}}=200$ GeV,” Phys. Rev. C **92**, no. 3, 034914 (2015)
44. J. Adam *et al.* [ALICE Collaboration], “Measurement of pion, kaon and proton production in proton proton collisions at $\sqrt{s} = 7$ TeV,” Eur. Phys. J. C **75**, no. 5, 226 (2015)
45. J. Adam *et al.* [ALICE Collaboration], “Coherent ρ^0 photoproduction in ultra-peripheral Pb-Pb collisions at $\sqrt{s_{NN}} = 2.76$ TeV,” JHEP **1509**, 095 (2015)
46. J. Adam *et al.* [ALICE Collaboration], “Rapidity and transverse-momentum dependence of the inclusive J/ψ nuclear modification factor in p-Pb collisions at $\sqrt{s_{NN}} = 5.02$ TeV,” JHEP **1506**, 055 (2015)
47. J. Adam *et al.* [ALICE Collaboration], “Measurement of dijet k_T in p Pb collisions at $\sqrt{s_{NN}}=5.02$ TeV,” Phys. Lett. B **746**, 385 (2015)
48. J. Adam *et al.* [ALICE Collaboration], “Measurement of charged jet production cross sections and nuclear modification in p-Pb collisions at $\sqrt{s_{NN}} = 5.02$ TeV,” Phys. Lett. B **749**, 68 (2015)
49. J. Adam *et al.* [ALICE Collaboration], “Measurement of jet suppression in central Pb-Pb collisions at $\sqrt{s_{NN}} = 2.76$ TeV,” Phys. Lett. B **746**, 1 (2015)
50. J. Adam *et al.* [ALICE Collaboration], “Two-pion femtoscopia in p-Pb collisions at $\sqrt{s_{NN}} = 5.02$ TeV,” Phys. Rev. C **91**, 034906 (2015)
51. J. Adam *et al.* [ALICE Collaboration], “Forward-backward multiplicity correlations in pp collisions at $\sqrt{s} = 0.9, 2.76$ and 7 TeV,” JHEP **1505**, 097 (2015)
52. J. Adam *et al.* [ALICE Collaboration], “Centrality dependence of particle production in p-Pb collisions at $\sqrt{s_{NN}}=5.02$ TeV,” Phys. Rev. C **91**, no. 6, 064905 (2015)
53. A. Adare *et al.* [PHENIX Collaboration], “Systematic Study of Azimuthal Anisotropy in Cu+Cu and Au+Au Collisions at $\sqrt{s_{NN}} = 62.4$ and 200 GeV,” Phys. Rev. C **92**, no. 3, 034913 (2015)
54. B. B. Abelev *et al.* [ALICE Collaboration], “Inclusive photon production at forward rapidities in proton-proton collisions at $\sqrt{s} = 0.9, 2.76$ and 7 TeV,” Eur. Phys. J. C **75**, no. 4, 146 (2015)
55. B. B. Abelev *et al.* [ALICE Collaboration], “Charged jet cross sections and properties in proton-proton collisions at $\sqrt{s} = 7$ TeV,” Phys. Rev. D **91**, no. 11, 112012 (2015)
56. B. B. Abelev *et al.* [ALICE Collaboration], “Production of inclusive $\Upsilon(1S)$ and $\Upsilon(2S)$ in p-Pb collisions at $\sqrt{s_{NN}} = 5.02$ TeV,” Phys. Lett. B **740**, 105 (2015)
57. A. Adare *et al.* [PHENIX Collaboration], “Charged-pion cross sections and double-helicity asymmetries in polarized p+p collisions at $\sqrt{s}=200$ GeV,” Phys. Rev. D **91**, no. 3, 032001 (2015)
58. A. Adare *et al.* [PHENIX Collaboration], “Search for dark photons from neutral meson decays in $p + p$ and $d + Au$ collisions at $\sqrt{s_{NN}} = 200$ GeV,” Phys. Rev. C **91**, no. 3, 031901 (2015)
59. B. B. Abelev *et al.* [ALICE Collaboration], “Multiplicity dependence of jet-like two-particle correlation structures in p Pb collisions at $\sqrt{s_{NN}}=5.02$ TeV,” Phys. Lett. B **741**, 38 (2015)

60. B. B. Abelev *et al.* [ALICE Collaboration], “Production of $\Sigma(1385)^\pm$ and $\Xi(1530)^0$ in proton-proton collisions at $\sqrt{s} = 7$ TeV,” *Eur. Phys. J. C* **75**, no. 1, 1 (2015)
61. B. B. Abelev *et al.* [ALICE Collaboration], “Elliptic flow of identified hadrons in Pb-Pb collisions at $\sqrt{s_{NN}} = 2.76$ TeV,” *JHEP* **1506**, 190 (2015)
62. B. B. Abelev *et al.* [ALICE Collaboration], “Measurement of electrons from semileptonic heavy-flavor hadron decays in pp collisions at $\sqrt{s} = 2.76$ TeV,” *Phys. Rev. D* **91**, no. 1, 012001 (2015)
63. A. Adare *et al.* [PHENIX Collaboration], “Cross section for $b\bar{b}$ production via dielectrons in $d+Au$ collisions at $\sqrt{s_{NN}} = 200$ GeV,” *Phys. Rev. C* **91**, no. 1, 014907 (2015)
64. A. Adare *et al.* [PHENIX Collaboration], “Centrality dependence of low-momentum direct-photon production in $Au+Au$ collisions at $\sqrt{s_{NN}} = 200$ GeV,” *Phys. Rev. C* **91**, no. 6, 064904 (2015)
65. A. Adare *et al.* [PHENIX Collaboration], “Heavy-quark production and elliptic flow in $Au+Au$ collisions at $\sqrt{s_{NN}} = 62.4$ GeV,” *Phys. Rev. C* **91**, no. 4, 044907 (2015)
66. A. Adare *et al.* [PHENIX Collaboration], “Measurement of long-range angular correlation and quadrupole anisotropy of pions and (anti)protons in central $d+Au$ collisions at $\sqrt{s_{NN}}=200$ GeV,” *Phys. Rev. Lett.* **114**, no. 19, 192301 (2015)
67. A. Adare *et al.* [PHENIX Collaboration], “Measurement of $Y(1S + 2S + 3S)$ production in $p + p$ and $Au+Au$ collisions at $\sqrt{s_{NN}} = 200$ GeV,” *Phys. Rev. C* **91**, no. 2, 024913 (2015)
68. B. B. Abelev *et al.* [ALICE Collaboration], “ $K^*(892)^0$ and (1020) production in Pb-Pb collisions at $\sqrt{s_{NN}} = 2.76$ TeV,” *Phys. Rev. C* **91**, 024609 (2015)
69. Y.G. Ma, D.Q. Fang, X.Y. Sun, P. Zhou, Y. Togano, N. Aoi, H. Baba, X.Z. Cai, X.G. Cao, J.G. Chen, Y. Fu, W. Guo, Y. Hara, T. Honda, Z.G. Hu, K. Ieki, Y. Ishibashi, Y. Ito, N. Iwasa, S. Kanno, T. Kawabata, H. Kimura, Y. Kondo, K. Kurita, M. Kurokawa, T. Moriguchi, H. Murakami, H. Ooishi, K. Okada, S. Ota, A. Ozawa, H. Sakurai, S. Shimoura, R. Shioda, E. Takeshita, S. Takeuchi, W.D. Tian, H.W. Wang, J.S. Wang, M. Wang, K. Yamada, Y. Yamada, Y. Yasuda, K. Yoneda, G.Q. Zhang, T. Motobayashi: “Different mechanism of two-proton emission from proton-rich nuclei ^{23}Al and ^{22}Mg ”, *Phys. Lett. B* **743**, 306–309 (2015)
70. K. Kisamori, S. Shimoura, H. Miya, S. Michimasa, S. Ota, M. Assie, H. Baba, T. Baba, D. Beaumel, M. Dozono, T. Fujii, N. Fukuda, S. Go, F. Hammache, E. Ideguchi, N. Inabe, M. Itoh, D. Kameda, S. Kawase, T. Kawabata, M. Kobayashi, Y. Kondo, T. Kubo, Y. Kubota, M. Kurata-Nishimura, C.S. Lee, Y. Maeda, H. Matsubara, K. Miki, T. Nishi, S. Noji, S. Sakaguchi, H. Sakai, Y. Sasamoto, M. Sasano, H. Sato, Y. Shimizu, A. Stolz, H. Suzuki, M. Takaki, H. Takeda, S. Takeuchi, A. Tamii, L. Tang, H. Tokieda, M. Tsumura, T. Uesaka, K. Yako, Y. Yanagisawa, R. Yokoyama, K. Yoshida: “Candidate Resonant Tetraneutron State Populated by the $^4He(^8He, ^8Be)$ Reaction”, *Phys. Rev. Lett.* **116**, 052501 (2016)
71. D. Steppenbeck, S. Takeuchi, N. Aoi, P. Doornenbal, M. Matsushita, H. Wang, Y. Utsuno, H. Baba, S. Go, J. Lee, K. Matsui, S. Michimasa, T. Motobayashi, D. Nishimura, T. Otsuka, H. Sakurai, Y. Shiga, N. Shimizu, P.-A. Söderström, T. Sumikama, R. Taniuchi, J.J. Valiente-Dobón, and K. Yoneda: “Low-Lying Structure of ^{50}Ar and the $N = 32$ Subshell Closure”, *Phys. Rev. Lett.* **114**, 252501 (2015)
72. D. Suzuki, H. Iwasaki, D. Beaumel, M. Assié, H. Baba, Y. Blumenfeld, F. de Oliveira Santos, N. de Séréville, A. Drouart, S. Franchoo, J. Gibelin, A. Gillibert, S. Giron, S. Grévy, J. Guillot, M. Hackstein, F. Hammache, N. Keeley, V. Lapoux, F. Maréchal, A. Matta, S. Michimasa, L. Nalpas, F. Naqvi, H. Okamura, H. Otsu, J. Pancin, D.Y. Pang, L. Perrot, C.M. Petrache, E. Pollacco, A. Ramus, W. Rother, P. Roussel-Chomaz, H. Sakurai, J.-A. Scarpaci, O. Sorlin, P.C. Srivastava, I. Stefan, C. Stodel, Y. Tanimura, S. Terashima: “Second 0^+ state of unbound ^{12}O : Scaling of mirror asymmetry”, *Phys. Rev. C* **93**, 024316 (2016)
73. Z. Patela, Zs. Podolyák, P.M. Walker, P.H. Regan, P.-A. Söderström, H. Watanabe, E. Ideguchi, G.S. Simpson, S. Nishimura, F. Browne, P. Doornenbal, G. Lorusso, S. Rice, L. Sinclair, T. Sumikama, J. Wu, Z.Y. Xu, N. Aoi, H. Baba, F.L. Bello Garrote, G. Benzoni, R. Daido, Zs. Dombrádi, Y. Fang, N. Fukuda, G. Gey, S. Go, A. Gottardo, N. Inabe, T. Isobe, D. Kameda, K. Kobayashi, M. Kobayashi, T. Komatsubara, I. Kojouharov, T. Kubo, N. Kurz, I. Kuti, Z. Li, H.L. Liu, M. Matsushita, S. Michimasa, C.-B. Moon, H. Nishibata, I. Nishizuka, A. Odahara, E. Şahin, H. Sakurai, H. Schaffner, H. Suzuki, H. Takeda, M. Tanaka, J. Taprogge, Zs. Vajta, F.R. Xu, A. Yagi, R. Yokoyama: “Decay spectroscopy of ^{160}Sm : The lightest four-quasiparticle K isomer”, *Phys. Lett. B* **753**, 182–186 (2016)

74. C. Santamaria, C. Louchart, A. Obertelli, V. Werner, P. Doornenbal, F. Nowacki, G. Authelet, H. Baba, D. Calvet, F. Chateau, A. Corsi, A. Delbart, J.-M. Gheller, d A. Gillibert, T. Isobe, V. Lapoux, M. Matsushita, S. Momiyama, T. Motobayashi, M. Niikura, H. Otsu, C. Peron, A. Peyaud, E.C. Pollacco, J.-Y. Rousse, H. Sakurai, M Sasano, Y. Shiga, S. Takeuchi, R. Taniuchi, T. Uesaka, H. Wang, K. Yoneda, F. Browne, L.X. Chung, . Zs. Dombradi, S. Franchoo, F. Giacoppo, A. Gottardo, K. Hadynska-Klek, Z. Korkulu, S. Koyama, Y. Kubota, J Lee, M. Lettmann, R. Lozeva, K. Matsui, T. Miyazaki, S. Nishimura, L. Olivier, S. Ota, Z. Patel, N. Pietralla, E. Sahin, C. Shand, P.-A. Soderstrom, I. Stefan, D. Steppenbeck, T. Sumikama, D. Suzuki, Zs. Vajta, J. Wu, Z. Xu: “Extension of the N=40 Island of Inversion towards N=50: Spectroscopy of ^{66}Cr , ^{70}Fe , ^{72}Fe ”, *Phys. Rev. Lett.* **115**, 192501 (2016)
75. A. Corsi, S. Boissinot, A. Obertelli, P. Doornenbal, M. Dupuis, F. Lechaftois, M. Matsushita, S. Peru, S. Takeuchi, H. Wang, N. Aoi, H. Baba, P. Bednarczyk, M. Ciemala, A. Gillibert, T. Isobe, A. Jungclauss, V. Lapoux, J. Lee, M. Martini, K. Matsui, T. Motobayashi, D. Nishimura, S. Ota, E. Pollacco, H. Sakurai, C. Santamaria, Y. Shiga, D. Sohler, D. Steppenbeck, R. Taniuchi, “Neutron-driven collectivity in light tin isotopes: Proton inelastic scattering from ^{104}Sn ”, *Phys. Lett. B* **743**, 451-455 (2016)
76. D.A. Finl, T.E. Cocolios, A.N. Andreyev, S. Antalic, A.E. Bazarkh, B. Bastin, D.V. Fedorov, V.N. Fedosseev, K.T. Flanagan, L.Ghys, A. Gottberg, M. Huyse, N. Imai, T. Kron, N. Lecesne, K. M. Lynch, B.A. Marsh, D. Pauwels, E. Rapisarda, S.D. Richter, R.E. Rossel, S. Rothe, M.D. Seliverstov, A.M. Sjordin, C. Van Beveren, P. Van Duppen, K.D.A. Wendt: “In-Source Laser Spectroscopy with the Laser Ion Source and Trap: First Direct Study of the Ground-State Properties of $^{217,219}\text{Po}$ ”, *Phys. Rev. X* **5**, 011018 (2015).
77. A. Matta, D. Beaumel, H. Otsu, V. Lapoux, N.K. Timofeyuk, N. Aoi, N. Assie, H. Baba, S. Boissinot, R.J. Chen, F. Delaunay, N. de Sereville, S. Franchoo, P. Gangnant, J. Gibelin, F. Hammache, Ch. Houarner, N. Imai, N. Kobayashi, T. Kubo, Y. Kondo, Y. Kawada, L.H. Khiem, M. Kurata-Nishimura, E.A. Kuzmin, J. Lee, J.F. Libin, T. Motobayashi, T. Nakamura, L. Nalpas, E.Yu. Nikoskii, A. Obertelli, E.C. Pollacco, E. Rindel, Ph. Rosier, F. Saillant, T. Sako, H. Sakurai, A.M. Sanchez-Benitez, J-A. Scarpaci, I. Stefan, D. Suuki, K. Takahashi, M. Takechi, H. Wang, R. Wolski, and K. Yoneda: “New findings on structure and production of ^{10}He from ^{11}Li with the (d , ^3He) reaction”, *Phys.Rev. C* **92**, 041302 (2015), *Pub.Note Phys.Rev. C* **92**, 044903 (2015)
78. Y.X. Watanabe, Y. H. Kim, S.C. Jeong, Y. Hirayama, N. Imai, H. Ishiyama, H.S. Jung, H. Miyatake, S. Choi, J.S. Song, E. Clement, G. de France, A. Navin, M. Rejmund, C. Shmitt, G. Pollarolo, L. Corradi, E. Fioretto, D. Montanari, M. Niikura,, D. Suzuki, H. Nishibata, J. Takatsu, “Pathway for the Production of Neutron-Rich Isotopes around the N=126 Shell Closure”, *Phys.Rev.Lett.* **115**, 172503 (2015).
79. T. Miyagi, T. Abe, R. Okamoto, and T. Otsuka: “Ground-state energies and charge radii of ^4He , ^{16}O , ^{40}Ca , and ^{56}Ni in the unitary-model-operator approach”, *Prog. Theor. Exp. Phys.* **2015**, no. 4, 041D01 (2015).
80. Y. Iwata: “Energy-dependent existence of soliton in the synthesis of chemical elements”, *Mod. Phys. Lett. A* **30**, No. 16, 155008 (2015).
81. D. Steppenbeck, S. Takeuchi, N. Aoi, P. Doornenbal, M. Matsushita, H. Wang, Y. Utsuno, H. Baba, S. Go, J. Lee, K. Matsui, S. Michimasa, T. Motobayashi, D. Nishimura, T. Otsuka, H. Sakurai, Y. Shiga, N. Shimizu, P.-A. Soderstrom, T. Sumikama, R. Taniuchi, J.J. Valiente-Dobon, and K. Yoneda: “Low-Lying Structure of ^{50}Ar and the $N = 32$ Subshell Closure”, *Phys. Rev. Lett.* **114** 252501 (2015).
82. Y. Iwata, T. Ichikawa, N. Itagaki, J.A. Maruhn, and T. Otsuka: “Examination of the stability of a rod-shaped structure in ^{24}Mg ”, *Phys. Rev. C* **92** 011303(R) (2015).
83. K. Steiger, S. Nishimura, Z. Li, R. Gernhauser, Y. Utsuno, R. Chen, T. Faestermann, C. Hinke, R. Krucken, M. Kurata-Nishimura, G. Lorusso, Y. Miyashita, N. Shimizu, K. Sugimoto, T. Sumikama, H. Watanabe, and K. Yoshinaga: “Nuclear structure of $^{37,38}\text{Si}$ investigated by decay spectroscopy of $^{37,38}\text{Al}$ ”, *Eur. Phys. J. A* **51** 117 (2015).
84. N. Shimizu, Y. Utsuno, Y. Futamura, T. Sakurai, T. Mizusaki, and T. Otsuka: “Stochastic estimation of nuclear level density in the nuclear shell model: An application to parity-dependent level density in ^{58}Ni ”, *Phys. Lett. B* **753** 13-17 (2016).
85. T. Otsuka, and Y. Tsunoda: “The role of shell evolution in shape coexistence”, *J. Phys. G: Nucl. Part. Phys.* **43** 024009 (2016).
86. T. Suzuki, T. Otsuka, C. Yuan, and N. Alfari: “Two-neutron “ halo ” from the low-energy limit of neutron-neutron interaction: Applications to drip-line nuclei ^{22}C and ^{24}O ”, *Phys. Lett. B* **753** 199-203 (2016).

87. Y. Shiga, K. Yoneda, D. Steppenbeck, N. Aoi, P. Doornenbal, M. Matsushita, S. Takeuchi, H. Wang, H. Baba, P. Bednarczyk, Zs. Dombradi, Zs. Fulop, S. Go, T. Hashimoto, M. Honma, E. Ideguchi, K. Ieki, K. Kobayashi, Y. Kondo, R. Minakata, T. Motobayashi, D. Nishimura, T. Otsuka, H. Otsu, H. Sakurai, N. Shimizu, D. Sohler, Y. Sun, A. Tamii, R. Tanaka, Z. Tian, Y. Tsunoda, Zs. Vajta, T. Yamamoto, X. Yang, Z. Yang, Y. Ye, R. Yokoyama, and J. Zenihiro: “Investigating nuclear structure in the vicinity of ^{78}Ni : Low-lying excited states in the neutron-rich isotopes $^{80,82}\text{Zn}$ ”, *Phys. Rev. C* **93** 024320 (2016).
88. A. Gade, J.A. Tostevin, V. Bader, T. Baugher, D. Bazin, J.S. Berryman, B.A. Brown, D.J. Hartley, E. Lunderberg, F. Recchia, S.R. Stroberg, Y. Utsuno, D. Weisshaar, and K. Wimmer: “One-neutron pickup into ^{49}Ca : Bound neutron $g_{9/2}$ spectroscopic strength at $N = 29$ ”, *Phys. Rev. C* **93** 031601 (2016).
89. Y. Iwata, N. Shimizu, T. Otsuka, Y. Utsuno, J. Menendez, M. Honma, and T. Abe: “Large-scale shell-model analysis of the neutrinoless $\beta\beta$ decay of ^{48}Ca ”, *Phys. Rev. Lett.* **116** 112502 (2016).

B. Proceedings

1. S. Sanfilippo, S. Cherubini, S. Hayakawa, A. Di Pietro, P. Figuera, M. Gulino, M. La Cognata, M. Lattuada, C. Spitaleri, H. Yamaguchi, D. Kahl, T. Nakao, S. Kubono, Y. Wakabayashi, T. Hashimoto, N. Iwasa, Y. Okoda, K. Ushio, T. Teranishi, M. Mazzocco, C. Signorini, D. Torresi, J.Y. Moon, T. Komatsubara, P.S. Lee, K.Y. Chae, M.S. Gwak: “ β delayed α decay of ^{16}N and the $^{12}\text{C}(\alpha, \gamma)^{16}\text{O}$ cross section at astrophysical energies: A new experimental approach”, *American Institute of Physics Conference Series* **1645** 387–391 (2015).
2. Pilsoo Lee, Chun Sik Lee, Jun Young Moon, Kyung Yuk Chae, Soo Mi Cha, Hidetoshi Yamaguchi, Taro Nakao, David M. Kahl, Shigeru Kubono, Silvio Cherubini, Seiya Hayakawa, Cosimo Signorini: “Development and performance test of the analysis software for the CRIB active target”, *Journal of the Korean Physical Society* **66** 459–464 (2015).
3. H. Yamaguchi, D. Kahl, S. Hayakawa, Y. Sakaguchi, T. Nakao, Y. Wakabayashi, T. Hashimoto, T. Teranishi, S. Kubono, S. Cherubini, M. Mazzocco, C. Signorini, M. Gulino, A. Di Pietro, P. Figuera, M. La Cognata, M. Lattuada, C. Spitaleri, D. Torresi, P.S. Lee, C.S. Lee, T. Komatsubara, N. Iwasa, Y. Okoda, D. Pierrousakou, C. Parascondolo, M. La Commara, E. Strano, C. Boiano, A. Boiano, C. Manea, A.M. Sanchez-Benitez, H. Miyatake, Y.X. Watanabe, H. Ishiyama, S.C. Jeong, N. Imai, Y. Hirayama, S. Kimura, M. Mukai, Y.H. Kim, C.J. Lin, H.M. Jia, L. Yan, Y.Y. Yang, T. Kawabata, Y.K. Kwon, D.N. Binh, L.H. Khiem, and N.N. Duy: “Studies on Nuclear Astrophysics and Exotic Structure at the Low-Energy RI Beam Facility CRIB”, *The Physical Society of Japan Conference Proceedings* **6** 010011 (2015).
4. K. Roed, T. Gunji *et al.* [ALICE TPC Collaboration], “Upgrade of the ALICE TPC FEE online radiation monitoring system,” *JINST* **10**, no. 12, P12019 (2015).
5. Shoichiro Kawase, Tsz Leung Tang, Tomohiro Uesaka, Didier Beaumel, Masanori Dozono, Toshihiko Fujii, Taku Fukunaga, Naoki Fukuda, Alfredo Galindo-Uribarri, SangHoon Hwang, Naohito Inabe, Daisuke Kameda, Tomomi Kawahara, Wooyoung Kim, Keiichi Kisamori, Motoki Kobayashi, Toshiyuki Kubo, Yuki Kubota, Kensuke Kusaka, CheongSoo Lee, Yukie Maeda, Hiroaki Matsubara, Shin 'ichiro Michimasa, Hiroyuki Miya, Tetsuo Noro, Alexandre Obertelli, Shinsuke Ota, Elizabeth Padilla-Rodal, Satoshi Sakaguchi, Hideyuki Sakai, Masaki Sasano, Susumu Shimoura, Samvel Stepanyan, Hiroshi Suzuki, Motonobu Takaki, Hiroyuki Takeda, Hiroshi Tokieda, Tomotsugu Wakasa, Takashi Wakui, Kentaro Yako, Yoshiyuki Yanagisawa, Jumpei Yasuda, Rin Yokoyama, Koichi Yoshida, Juzo Zenihiro: “Spectroscopy of Single-Particle States in Oxygen Isotopes via $(\bar{p}, 2p)$ Reaction”, *Proceedings of the Conference on Advances in Radioactive Isotope Science (ARIS2014)*, *JPS Conf. Proc.* **6**, 020003 (2015)
6. Motonobu Takaki, Hiroaki Matsubara, Tomohiro Uesaka, Nori Aoi, Masanori Dozono, Takashi Hashimoto, Takahiro Kawabata, Shoichiro Kawase, Keiichi Kisamori, Yuki Kubota, Cheng Soo Lee, Jenny Lee, Yukie Maeda, Shin 'ichiro Michimasa, Kenjiro Miki, Shinsuke Ota, Masaki Sasano, Susumu Shimoura, Tomokazu Suzuki, Keiji Takahisa, Tsz Leung Tang, Atsushi Tamii, Hiroshi Tokieda, Kentaro Yako, Rin Yokoyama, Juzo Zenihiro: “Heavy-Ion Double-Charge Exchange Study via a $^{12}\text{C}(^{18}\text{O}, ^{18}\text{Ne})^{12}\text{Be}$ Reaction”, *Proceedings of the Conference on Advances in Radioactive Isotope Science (ARIS2014)*, *JPS Conf. Proc.* **6**, 020038 (2015)
7. Yasuhiro Togano, Yusuke Yamada, Naohito Iwasa, Kazunari Yamada, Tohru Motobayashi, Nori Aoi, Hidetada Baba, Shawn Bishop, Xiangzhou Cai, Pieter Doornenbal, Deqing Fang, Takeshi Furukawa, Kazuo Ieki,

- Takahiro Kawabata, Shoko Kanno, Nobuyuki Kobayashi, Yosuke Kondo, Takamasa Kuboki, Naoto Kume, Kazuyoshi Kurita, Meiko Kurokawa, Yu-Gang Ma, Yukari Matsuo, Hiroshi Murakami, Masafumi Matsushita, Takashi Nakamura, Kensuke Okada, Shinsuke Ota, Yoshiteru Satou, Susumu Shimoura, Ryota Shioda, Kana Tanaka, Satoshi Takeuchi, Wendong Tian, Hongwei Wang, Jiansong Wang, Ken-ichiro Yoneda: “Hindered Proton Collectivity in the Proton-Rich Nucleus ^{28}S : Possible Magic Number $Z = 16$ at Proton-Rich Side”, Proceedings of the Conference on Advances in Radioactive Isotope Science (ARIS2014), JPS Conf. Proc. 6, 030002 (2015)
8. Shintaro Go, Eiji Ideguchi, Rin Yokoyama, Motoki Kobayashi, Keiichi Kisamori, Motonobu Takaki, Hiroyuki Miya, Shinsuke Ota, Shinichiro Michimasa, Susumu Shimoura, Megumi Niikura, Takeshi Koike, Takeshi Yamamoto, Yosuke Ito, Jun Takatsu, Ayumi Yagi, Hiroki Nishibata, Tomokazu Suzuki, Kotaro Shirotori, Yutaka Watanabe, Yoshikazu Hirayama, Masahiko Sugawara, Mitsuo Koizumi, Yosuke Toh, Toshiyuki Shizuma, Atsushi Kimura, Hideo Harada, Kazuyoshi Furutaka, Shoji Nakamura, Fumito Kitatani, Yuichi Hatsukawa, Masumi Oshima, Iolanda Matea, Daisuke Suzuki, David Verney, Faïçal Azaiez: “Superdeformation in ^{35}S ”, Proceedings of the Conference on Advances in Radioactive Isotope Science (ARIS2014), JPS Conf. Proc. 6, 030005 (2015)
 9. Yoshiteru Satou, Jongwon Hwang, Sunji Kim, Kyoungsoo Tshoo, Seonho Choi, Takashi Nakamura, Takashi Sugimoto, Yosuke Kondo, Nobuyuki Matsui, Yoshiko Hashimoto, Takumi Nakabayashi, Toshifumi Okumura, Mayuko Shinohara, Naoki Fukuda, Toru Motobayashi, Yoshiyuki Yanagisawa, Nori Aoi, Satoshi Takeuchi, Tomoko Gomi, Hiroyoshi Sakurai, Hideaki Otsu, Masayasu Ishihara, Yasuhiro Togano, Shoko Kawai, Hooi Ong, Takeo Onishi, Susumu Shimoura, Mitsuru Tamaki, Toshio Kobayashi, Yohei Matsuda, Natsumi Endo, Mitsuhisa Kitayama: “Hole States in ^{16}C Observed via One-Neutron Knockout of ^{17}C ”, Proceedings of the Conference on Advances in Radioactive Isotope Science (ARIS2014), JPS Conf. Proc. 6, 030029 (2015)
 10. Keiichi Kisamori, Susumu Shimoura, Hiroyuki Miya, Marlene Assie, Hidetada Baba, Tatsuo Baba, Didier Beaumel, Masanori Dozono, Toshihiko Fujii, Naoki Fukuda, Shintaro Go, Fariouz Hammache, Eiji Ideguchi, Naohiro Inabe, Masatoshi Itoh, Daisuke Kameda, Shoichiro Kawase, Takahiro Kawabata, Motoki Kobayashi, Yosuke Kondo, Toshiyuki Kubo, Yuki Kubota, Mizuki Kurata-Nishimura, CheongSoo Lee, Yukie Maeda, Hiroaki Matsubara, Shin 'ichiro Michimasa, Kenjiro Miki, Takahiro Nishi, Shumpei Noji, Shinsuke Ota, Satoshi Sakaguchi, Hideyuki Sakai, Yoshiko Sasamoto, Masaki Sasano, Hiromi Sato, Yohei Shimizu, Andreas Stolz, Hiroshi Suzuki, Motonobu Takaki, Hiroyuki Takeda, Satoshi Takeuchi, Atsushi Tamii, Leung Tang, Hiroshi Tokieda, Miho Tsumura, Tomohiro Uesaka, Kentaro Yako, Yoshiyuki Yanagisawa, Rin Yokoyama: “Missing-Mass Spectroscopy of the 4-Neutron System by Exothermic Double-Charge Exchange Reaction $^4\text{He}(^8\text{He}, ^8\text{Be})4n$ ”, Proceedings of the Conference on Advances in Radioactive Isotope Science (ARIS2014), JPS Conf. Proc. 6, 030075 (2015)
 11. Tsz Leung Tang, Shoichiro Kawase, Tomohiro Uesaka, Didier Beaumel, Masanori Dozono, Naoki Fukuda, Taku Fukunaga, Toshihiko Fujii, Alfredo Galindo-uribarrí, SangHoon Hwang, Daisuke Kameda, Tomomi Kawahara, Wooyoung Kim, Keiichi Kisamori, Motoki Kobayashi, Yuki Kubota, Kensuke Kusaka, CheongSoo Lee, Yukie Maeda, Hiroaki Matsubara, Shin 'ichiro Michimasa, Hiroyuki Miya, Tetsuo Noro, Alexandre Obertelli, Shinsuke Ota, Elizabeth Padilla-Rodal, Satoshi Sakaguchi, Masaki Sasano, Susumu Shimoura, Samvel Stepanyan, Hiroshi Suzuki, Motonobu Takaki, Hiroyuki Takeda, Hiroshi Tokieda, Tomotsugu Wakasa, Takashi Wakui, Kentaro Yako, Jumpei Yasuda, Rin Yokoyama, Juzo Zenihiro: “Proton Single-Particle Energy of ^{23}F by Quasi-Free ($\bar{p}, 2p$) Scattering and Operation of Polarized Proton Target”, Proceedings of the Conference on Advances in Radioactive Isotope Science (ARIS2014), JPS Conf. Proc. 6, 030077 (2015)
 12. Motoki Kobayashi, Kentaro Yako, Susumu Shimoura, Masanori Dozono, Naoki Fukuda, Naohito Inabe, Daisuke Kameda, Shoichiro Kawase, Keiichi Kisamori, Toshiyuki Kubo, Yuki Kubota, CheongSoo Lee, Shin 'ichiro Michimasa, Hiroyuki Miya, Shinsuke Ota, Hideyuki Sakai, Masaki Sasano, Hiroshi Suzuki, Motonobu Takaki, Hiroyuki Takeda, Yoshiyuki Yanagisawa: “Spin-Isospin Response of the Neutron-Rich Nucleus ^8He via the (p, n) Reaction in Inverse Kinematics”, Proceedings of the Conference on Advances in Radioactive Isotope Science (ARIS2014), JPS Conf. Proc. 6, 030089 (2015)
 13. Shin 'ichiro Michimasa, Yoshiyuki Yanagisawa, Kiyohiko Inafuku, Nori Aoi, Zoltón Elekes, Zsolt Fülöp, Yuichi Ichikawa, Naohito Iwasa, Kazuyoshi Kurita, Meiko Kurokawa, Tomohiro Machida, Tohru Motobayashi, Takashi Nakamura, Takumi Nakabayashi, Masahiro Notani, Hooi Jin Ong, Takeo Onishi, Hideaki Otsu, Hiroyoshi Sakurai, Mayuko Shinohara, Toshiyuki Sumikama, Satoshi Takeuchi, Kanenobu Tanaka, Yasuhiro Togano, Kazunari Yamada, Mitsutaka Yamaguchi, Ken-ichiro Yoneda: “Proton Inelastic Scattering on Island-of-Inversion

Nuclei”, Proceedings of the Conference on Advances in Radioactive Isotope Science (ARIS2014), JPS Conf. Proc. 6, 020007 (2015)

14. David Steppenbeck, Satoshi Takeuchi, Nori Aoi, Pieter Doornenbal, Masafumi Matsushita, He Wang, Hidetada Baba, Naoki Fukuda, Shintaro Go, Michio Honma, Jenny Lee, Keishi Matsui, Shin 'ichiro Michimasa, Tohru Motobayashi, Daiki Nishimura, Takaharu Otsuka, Hiroyoshi Sakurai, Yoshiaki Shiga, Noritaka Shimizu, Pär-Anders Söderström, Toshiyuki Sumikama, Hiroshi Suzuki, Ryo Taniuchi, Yutaka Utsuno, Jose Javier Valiente-Dobn, Ken 'ichiro Yoneda: “In-Beam γ -Ray Spectroscopy of Very Neutron-Rich $N = 32$ and 34 Nuclei”, Proceedings of the Conference on Advances in Radioactive Isotope Science (ARIS2014), JPS Conf. Proc. 6, 020019 (2015)
15. H. Liu, J. Lee, P. Doornenbal, H. Scheit, S. Takeuchi, N. Aoi, K. Li, M. Matsushita, D. Steppenbeck, H. Wang, H. Baba, E. Ideguchi, N. Kobayashi, Y. Kondo, G. Lee, S. Michimasa, T. Motobayashi, H. Sakurai, M. Takechi, Y. Togano, J.A. Tostevin, Y. Utsuno: “Single-Neutron Knockout Reaction from ^{30}Ne ”, Proceedings of the Conference on Advances in Radioactive Isotope Science (ARIS2014), JPS Conf. Proc. 6, 030003 (2015)
16. Rin Yokoyama, Eiji Ideguchi, Gary Simpson, Mana Tanaka, Shunji Nishimura, Pieter Doornnbal, Pär-Anders Söderström, Giuseppe Lorusso, Zhengyu Xu, Jin Wu, Toshiyuki Sumikama, Nori Aoi, Hidetada Baba, Frank Bello, Frank Browne, Rie Daido, Yifan Fang, Naoki Fukuda, Guillaume Gey, Shintaro Go, Naohiro Inabe, Tadaaki Isobe, Daisuke Kameda, Kazuma Kobayashi, Motoki Kobayashi, Tetsuro Komatsubara, Toshiyuki Kubo, Istvan Kuti, Zhihuan Li, Masafumi Matsushita, Shin 'ichiro Michimasa, Chang-Bum Moon, Hiroki Nishibata, Ipei Nishizuka, Atsuko Odahara, Zena Patel, Simon Rice, Eda Sahin, Laura Sinclair, Hiroshi Suzuki, Hiroyuki Takeda, Jan Taprogge, Zsolt Vajta, Hiroshi Watanabe, Ayumi Yagi: “Isomers of Pm Isotopes on the Neutron-Rich Frontier of the Deformed $Z = 60$ Region”, Proceedings of the Conference on Advances in Radioactive Isotope Science (ARIS2014), JPS Conf. Proc. 6, 030021 (2015)
17. Shinsuke Ota, H. Tokieda, C.S. Lee, R. Kojima, Y.N. Watanabe, A. Corsi, M. Dozono, J. Gibelin, T. Hashimoto, T. Kawabata, S. Kawase, S. Kubono, Y. Kubota, Y. Maeda, H. Matsubara, Y. Matsuda, S. Michimasa, T. Nakao, T. Nishi, A. Obertelli, H. Otsu, C. Santamaria, M. Sasano, M. Takaki, Y. Tanaka, T. Leung, T. Uesaka, K. Yako, H. Yamaguchi, J. Zenihiro, E. Takada: “Development of CNS Active Target for Deuteron Induced Reactions with High Intensity Exotic Beam”, Proceedings of the Conference on Advances in Radioactive Isotope Science (ARIS2014), JPS Conf. Proc. 6, 030117 (2015)
18. Yuki Kubota, Masaki Sasano, Tomohiro Uesaka, Masanori Dozono, Masatoshi Itoh, Shoichiro Kawase, Motoki Kobayashi, CheongSoo Lee, Hiroaki Matsubara, Kenjiro Miki, Hiroyuki Miya, Shinsuke Ota, Kimiko Sekiguchi, Tatsushi Shima, Takahiro Taguchi, Atsushi Tamii, Tsz Leung Tang, Hiroshi Tokieda, Tomot-sugu Wakasa, Takashi Wakui, Jumpei Yasuda, Juzo Zenihiro: “A Segmented Neutron Detector with a High Position Resolution for the (p, pn) Reactions”, Proceedings of the Conference on Advances in Radioactive Isotope Science (ARIS2014), JPS Conf. Proc. 6, 030118 (2015)
19. Clementine Santamaria, Alexandre Obertelli, Shinsuke Ota, Masaki Sasano, Eichi Takada, Laurent Audirac, Hidetada Baba, Denis Calvet, Frédéric Château, Anna Corsi, Alain Delbart, Pieter Doornenbal, Arnaud Giganon, Alain Gillibert, Yosuke Kondo, Yuki Kubota, Caroline Lahonde-Hamdoun, Valérie Lapoux, Cheong Soo Lee, Hideaki Otsu, Alan Peyaud, Emanuel C. Pollacco, Hiroshi Tokieda, Tomohiro Uesaka, Juzo Zenihiro: “In-Beam Performances of the MINOS TPC for the Spectroscopy of Very Exotic Nuclei”, Proceedings of the Conference on Advances in Radioactive Isotope Science (ARIS2014), JPS Conf. Proc. 6, 030130 (2015)
20. CheongSoo Lee, Shinsuke Ota, Hiroshi Tokieda, Reiko Kojima, Yuni Watanabe, Raphael Saiseau, Tomohiro Uesaka: “Property of THGEM in Low-Pressure Deuterium for a Low-Pressure Gaseous Active Target”, Proceedings of the Conference on Advances in Radioactive Isotope Science (ARIS2014), JPS Conf. Proc. 6, 030140 (2015)
21. G. Benzoni, H. Watanabe, A.I. Morales, S. Nishimura, R. Avigo, H. Baba, F.L. Bello Garrote, N. Blasi, A. Bracco, F. Browne, S. Ceruti, F.C.L. Crespi, R. Daido, G. de Angelis, M.C. Delattre, Zs. Dombradi, P. Doornenbal, Y. Fang, A. Gottardo, T. Isobe, I. Kuti, G. Lorusso, K. Matsui, B. Melon, D. Mengoni, T. Miyazaki, V. Modamio-Hoybjor, S. Momiyama, D.R. Napoli, M. Niikura, R. Orlandi, Z. Patel, S. Rice, E. Sahin, H. Sakurai, L. Sinclair, P. A. Söderström, D. Sohler, T. Sumikama, R. Taniuchi, J. Taprogge, Zs. Vajta, J. J. Valiente-Dobón, O. Wieland, J. Wu, Z.Y. Xu, A. Yagi, M. Yalcinkaya, R. Yokoyama: “ β -Decay Measurements in the Vicinity of ^{78}Ni with the EURICA Setup”, Proceedings of the Conference on Advances in Radioactive Isotope Science (ARIS2014), JPS Conf. Proc. 6, 020021 (2015)

22. Yoshiaki Shiga, Ken-ichiro Yoneda, David Steppenbeck, Nori Aoi, Pieter Doornenbal, Jenny Lee, Hongna Liu, Masafumi Matsushita, Satoshi Takeuchi, He Wang, Hidetada Baba, Piotr Bednarczyk, Zsolt Dombradi, Zsolt Fulop, Shintaro Go, Takashi Hashimoto, Eiji Ideguchi, Kazuo Ieki, Kota Kobayashi, Yosuke Kondo, Ryogo Minakata, Tohru Motobayashi, Daiki Nisimura, Hideaki Otsu, Hiroyoshi Sakurai, Dora Sohler, Yelei Sun, Atsushi Tamii, Ryuki Tanaka, Zhengyang Tian, Zsolt Vajta, Tetsuya Yamamoto, Xiaofei Yang, Zaihong Yang, Yanlin Ye, Rin Yokoyama, Juzo Zenihiro: “Persistence of $N = 50$ Shell Closure in the Vicinity of ^{78}Ni Studied by In-Beam γ -Ray Spectroscopy”, Proceedings of the Conference on Advances in Radioactive Isotope Science (ARIS2014), JPS Conf. Proc. 6, 030008 (2015)
23. He Wang, Nori Aoi, Satoshi Takeuchi, Masafumi Matsushita, Pieter Doornenbal, Tohru Motobayashi, David Steppenbeck, Kenichiro Yoneda, Hidetada Baba, Lucia Cáceres, Zsolt Dombradi, Yosuke Kondo, Jenny Lee, Kuang Li, Hong-Na Liu, Ryogo Minakata, Daiki Nishimura, Hideaki Otsu, Satoshi Sakaguchi, Hiroyoshi Sakurai, Heiko Scheit, Dora Sohler, Ye-Lei Sun, Zheng-Yang Tian, Ryuki Tanaka, Yasuhiro Togano, Zsolt Vajta, Zaihong Yang, Tetsuya Yamamoto, Yan-Lin Ye, Rin Yokoyama: “Collectivity in the Neutron-Rich Pd Isotopes Towards $N = 82$ ”, Proceedings of the Conference on Advances in Radioactive Isotope Science (ARIS2014), JPS Conf. Proc. 6, 030010 (2015)
24. A. Yagi, A. Odahara, R. Daido, Y. Fang, H. Nishibata, R. Lozeva, C.-B. Moon, S. Nishimura, P. Doornenbal, G. Lorusso, P.A. Söderström, T. Sumikama, H. Watanabe, T. Isobe, H. Baba, H. Sakurai, F. Browne, Z. Patel, S. Rice, L. Sinclair, J. Wu, Z.Y. Xu, R. Yokoyama, T. Kubo, N. Inabe, H. Suzuki, N. Fukuda, D. Kameda, H. Takeda, D.S. Ahn, D. Murai, F.L. Bello Garrote, J.M. Daugas, F. Didierjean, E. Ideguchi, T. Ishigaki, H.S. Jung, T. Komatsubara, Y. K. Kwon, C.S. Lee, P.S. Lee, S. Morimoto, M. Niikura, I. Nishizuka, T. Shimoda, K. Tshoo: “New Isomers in Neutron-Rich Cs Isotopes”, Proceedings of the Conference on Advances in Radioactive Isotope Science (ARIS2014), JPS Conf. Proc. 6, 030019 (2015)
25. J. Wu, S. Nishimura, G. Lorusso, Z.Y. Xu, E. Ideguchi, G. S. Simpson, H. Baba, F. Browne, R. Daido, P. Doornenbal, Y. F. Fang, T. Isobe, Z. Li, Z. Patel, S. Rice, L. Sinclair, P.-A. Söderström, T. Sumikama, H. Watanabe, A. Yagi, R. Yokoyama, N. Aoi, F.L. Bello Garrote, G. Benzoni, G. Gey, A. Gottardo, H. Nishibata, A. Odahara, H. Sakurai, M. Tanaka, J. Taprogge, T. Yamamoto, and the EURICA collaboration: “ β -Decay of Neutron-Rich Nuclei around ^{158}Nd and the Origin of Rare-Earth Elements”, Proceedings of the Conference on Advances in Radioactive Isotope Science (ARIS2014), JPS Conf. Proc. 6, 030064 (2015)
26. K. Sekiguchi, Y. Wada, J. Miyazaki, T. Taguchi, U. Gebauer, M. Dozono, S. Kawase, Y. Kubota, C.S. Lee, Y. Maeda, T. Mashiko, K. Miki, H. Okamura, S. Sakaguchi, H. Sakai, N. Sakamoto, M. Sasano, Y. Shimizu, K. Takahashi, T.L. Tang, T. Uesaka, T. Wakasa, K. Yako: “Complete Set of Deuteron Analyzing Powers for dp Elastic Scattering at Intermediate Energies and Three Nucleon Forces”, Proceedings of the Conference on Advances in Radioactive Isotope Science (ARIS2014), JPS Conf. Proc. 6, 030087 (2015)
27. H. Yamaguchi, D. Kahl, S. Hayakawa, Y. Sakaguchi, T. Nakao, Y. Wakabayashi, T. Hashimoto, T. Teranishi, S. Kubono, S. Cherubini, M. Mazzocco, C. Signorini, M. Gulino, A. Di Pietro, P. Figuera, M. La Cognata, M. Latuada, C. Spitaleri, D. Torresi, P.S. Lee, C.S. Lee, T. Komatsubara, N. Iwasa, Y. Okoda, D. Pierroutsakou, C. Parascondolo, M. La Commara, E. Strano, C. Boiano, A. Boiano, C. Manea, A. M. Sánchez-Bentez, H. Miyatake, Y.X. Watanabe, H. Ishiyama, S. C. Jeong, N. Imai, Y. Hirayama, S. Kimura, M. Mukai, Y.H. Kim, C. J. Lin, H.M. Jia, L. Yan, Y.Y. Yang, T. Kawabata, Y.K. Kwon, D.N. Binh, L.H. Khiem, N.N. Duy: “Studies on Nuclear Astrophysics and Exotic Structure at the Low-Energy RI Beam Facility CRIB”, Proceedings of the Conference on Advances in Radioactive Isotope Science (ARIS2014), JPS Conf. Proc. 6, 010011 (2015)
28. N. Imai, M. Mukai, J. Cederkäll, H. Aghai, P. Golubev, H. T. Johansson, D. Kahl, T. Teranishi, Y.X. Watanabe: “Quenched Spectroscopic Factors for Low-Lying Positive Parity States in ^{31}Mg ”, Proceedings of the Conference on Advances in Radioactive Isotope Science (ARIS2014), JPS Conf. Proc. 6, 020005 (2015)
29. A. Matta, D. Beaumel, H. Otsu, V. Lapoux, N.K. Timofeyuk, N. Aoi, M. Assie, H. Baba, S. Boissinot, R. Chen, F. Delaunay, N. de Sereville, S. Franchoo, P. Gangnant, J. Gibelin, F. Hammache, C. Houarner, N. Imai, N. Kobayashi, T. Kubo, Y. Kondo, Y. Kawada, L.H. Khiem, M. Kurata-Nishimura, E.A. Kuzmin, J. Lee, J.F. Libin, T. Motobayashi, T. Nakamura, L. Nalpas, E. Yu. Nikolskii, A. Obertelli, E.C. Pollacco, E. Rindel, Ph. Rosier, F. Saillant, T. Sako, H. Sakurai, A. Sanchez-Benitez, J.-A. Scarpaci, I. Stefan, D. Suzuki, K. Takahashi, M. Takechi, S. Takeuchi, H. Wang, R. Wolski, K. Yoneda “Missing Mass Spectroscopy of ^8He and ^{10}He by $(d, ^3\text{He})$ Reaction” Proceedings of the Conference on Advances in Radioactive Isotope Science (ARIS2014), JPS Conf. Proc. 6, 030026 (2015)

30. Y. Hirayama, Y.X. Watanabe, N. Imai, H. Ishiyama, S.C. Jeong, H. Miyatake, M. Oyaizu, M. Mukai, S. Kimura, Y. H. Kim, T. Sonoda, M. Wada, M. Huyse, Yu. Kudryavtsev, P. Van Duppen: “Beta-Decay Spectroscopy of r-Process Nuclei with $N = 126$ at KEK Isotope Separation System”, Proceedings of the Conference on Advances in Radioactive Isotope Science (ARIS2014), JPS Conf. Proc. 6, 030125 (2015)
31. M. Mukai, Y. Hirayama, N. Imai, H. Ishiyama, S.C. Jeong, H. Miyatake, M. Oyaizu, Y.X. Watanabe, Y.H. Kim, S. Kimura: “Search for Efficient Laser Resonance Ionization Schemes of Refractory Elements for KISS”, Proceedings of the Conference on Advances in Radioactive Isotope Science (ARIS2014), JPS Conf. Proc. 6, 030127 (2015)
32. T. Sumikama, D.S. Ahn, N. Fukuda, N. Inabe, T. Kubo, Y. Shimizu, H. Suzuki, H. Takeda, N. Aoi, D. Beaumel, K. Hasegawa, E. Ideguchi, N. Imai, T. Kobayashi, M. Matsushita, S. Michimasa, H. Otsu, S. Shimoura, T. Teranishi: “First test experiment to produce the slowed-down RI beam with the momentum-compression mode at RIBF” Proceedings of 17th International Conference on Electromagnetic Isotope Separators and Related Topics (EMIS2015), Nucl. Instr. Meth. Phys. Res. B (2016), in press
33. J. Yasuda, M. Sasano, R.G.T. Zegers, H. Baba, W. Chao, M. Dozono, N. Fukuda, N. Inabe, T. Isobe, G. Jhang, D. Kameda, T. Kubo, M. Kurata-Nishimura, E. Milman, T. Motobayashi, H. Otsu, V. Panin, W. Powell, H. Sakai, M. Sako, H. Sato, Y. Shimizu, L. Stuhl, H. Suzuki, S. Tangwanchaoen, H. Takeda, T. Uesaka, K. Yoneda, J. Zenihiro, T. Kobayashi, T. Sumikama, T. Tako, T. Nakamura, Y. Kondo, Y. Togano, M. Shikata, J. Tsubota, K. Yako, S. Shimouraf, S. Otaf, S. Kawasef, Y. Kubotaf, M. Takakif, S. Michimasaf, K. Kisamorif, C.S. Leef, H. Tokieda, M. Kobayashi, S. Koyama, N. Kobayashi, T. Wakasa, S. Sakaguchi, A. Krasznahorkay, T. Murakami, N. Nakatsuka, M. Kaneko, Y. Matsuda, D. Mucher, S. Reichert, D. Bazin, J.W. Lee: “Inverse kinematics (p, n) reactions studies using the WINDS slow neutron detector and the SAMURAI spectrometer”, Proceedings of 17th International Conference on Electromagnetic Isotope Separators and Related Topics (EMIS2015), Nucl. Instr. Meth. Phys. Res. B (2016), in press
34. M. Sasano, J. Yasuda, R.G.T. Zegers, H. Baba, W. Chao, M. Dozono, N. Fukuda, N. Inabe, T. Isobe, G. Jhang, D. Kameda, T. Kubo, M. Kurata-Nishimura, E. Milman, T. Motobayashi, H. Otsu, V. Panin, W. Powell, H. Sakai, M. Sako, H. Sato, Y. Shimizu, L. Stuhl, H. Suzuki, S. Tangwanchaoen, H. Takeda, T. Uesaka, K. Yoneda, J. Zenihiro, T. Kobayashi, T. Sumikama, T. Tako, T. Nakamura, Y. Kondo, Y. Togano, M. Shikata, J. Tsubota, K. Yako, S. Shimoura, S. Ota, S. Kawase, Y. Kubota, M. Takaki, S. Michimasa, K. Kisamori, C.S. Lee, H. Tokieda, M. Kobayashi, S. Koyama, N. Kobayashi, T. Wakasa, S. Sakaguchi, A. Krasznahorkay, T. Murakami, N. Nakatsuka, M. Kaneko, Y. Matsuda, D. Mucher, S. Reichert, D. Bazin J.W. Lee: “Study of Gamow-Teller transitions from ^{132}Sn via the (p, n) reaction at 220 MeV/u in inverse kinematics”, Proceedings of International Conference on Nuclear Structure and Related Topics (NSRT15), EPJ Web of Conferences, 107 (2016) 06003
35. Hideshi Mutoa, Yukimitsu Ohshiro, Shoichi Yamaka, Shin-ichi Watanabe, Michihiro Oyaizu, Shigeru Kubono, Hidetoshi Yamaguchi, Masayuki Kase, Toshiyuki Hattori, Susumu Shimoura: “Status of Plasma Spectroscopy Method for CNS Hyper-ECR Ion Source at RIKEN”, Proceedings of 23rd International Conference on the Application of Accelerators in Research and Industry (CAARI 2014), Physics Procedia, **66**, 140–147 (2015)
36. Y. Kotaka, Y. Ohshiro, S. Watanabe, H. Yamaguchi, N. Imai, S. Shimoura, M. Kase, S. Kubono, K. Hatanaka, A. Goto, H. Muto: “Development of low-energy heavy-ion beams by the Riken AVF cyclotron and Hyper ECR ion source of CNS”, Proceedings of the 13th International Conference on Heavy Ion Accelerator Technology, 58–61 (2016)
37. H. Muto, Y. Oshiro, Y. Kotaka, S. Yamaka, S. Watanabe, H. Yamaguchi, S. Shimoura, M. Kase, S. Kubono, K. Kobayashi, M. Nishimura, M. Oyaizu, T. Hattori: “Observation of sublimation effect of Mg and Ti ions at the Hyper-electron cyclotron resonance ion source”, Proceedings of the 13th International Conference on Heavy Ion Accelerator Technology, 262–264 (2016)
38. S. Ota, H. Tokieda, C.S. Lee, Y.N. Watanabe: “CNS active target (CAT) for missing mass spectroscopy with intense beams”, Proceedings of the 27th world conference of the international nuclear target, J. Radioanalytical and Nuclear Chemistry,
39. Y. Utsuno, T. Otsuka, Y. Tsunoda, N. Shimizu, M. Honma, T. Togashi, T. Mizusaki, “Recent Advances in Shell Evolution with Shell-Model Calculations”, JPS Conf. Proc. **6** 010007 (2015).
40. N. Shimizu, T. Abe, M. Honma, T. Otsuka, Y. Tsunoda, Y. Utsuno, and T. Yoshida: “Frontier of nuclear shell-model calculations and high performance computing”, JPS Conf. Proc. **6** 010021 (2015).

41. T. Yoshida, N. Shimizu, T. Abe, T. Otsuka: “Cluster structure of Be isotopes based on Monte Carlo shell model”, JPS Conf. Proc. **6** 030028 (2015).
42. T. Miyagi, T. Abe, R. Okamoto and T. Otsuka: “Many-Body Calculations for Medium-Mass Nuclei by the Unitary Transformation Method”, JPS Conf. Proc. **6** 030037 (2015).
43. T. Togashi, N. Shimizu, Y. Utsuno, T. Otsuka, M. Honma: “Shell-Model Calculation of High-Spin States in Neutron-Rich Cr and Fe Isotopes”, JPS Conf. Proc. **6** 030046 (2015).
44. Y. Iwata, N. Shimizu, Y. Utsuno, M. Honma, T. Abe, T. Otsuka: “Ingredients of nuclear matrix element for two-neutrino double-beta decay of ^{48}Ca ”, JPS Conf. Proc. **6** 030057 (2015).

C. Theses

1. R. Yokoyama: “Shape evolution in neutron-rich midshell nuclei studied by γ -ray spectroscopy”, PhD Thesis, the University of Tokyo, March 2015.

D. Other Publications

1. 大塚孝治、阿部喬: “原子核物理における大規模数値計算の進展” パリティ Vol.30 (2015年6月号) p.24-28(丸善出版社).

Talks and Presentations

A. Conferences

1. H. Yamaguchi for the CRIB collaboration (oral, invited): “Nuclear astrophysics projects with low-energy RI beams at CRIB”: Pioneering Symposium: “Nuclear physics at the RIB facilities” in Korean Physical Society Meeting, Apr 22–24, 2015, Daejeon Convention Center, Daejeon, Korea.
2. H. Yamaguchi (oral, invited): “Studying astrophysical reactions with low-energy RI beams at CRIB” H. Yamaguchi, D. Kahl, S. Hayakawa, Y. Sakaguchi, Y. Wakabayashi, T. Hashimoto, S. Kubono, S. Cherubini, M. Gulino, C. Spitaleri, G.G. Rapisarda, M. La Cognata, L. Lamia, R.G. Pizzone, M.L. Sergi, S. Romano, N. Iwasa, T. Teranishi, T. Kawabata, Y.K. Kwon, D.N. Binh, L.H. Khiem, N.N. Duy, S. Kato, T. Komatsubara, A. Coc, N. de Sereville, F. Hammache, G. Kiss, and S. Bishop The 12th International Conference on Nucleus-Nucleus Collisions (NN2015), June 21–26 2015, Department of Physics and Astronomy, Catania University.
3. 坂口裕司 (oral): “CRIB による ^{14}C の linear-chain cluster states の探索”, RCNP 研究会「アイソスカラー型単極遷移で探る原子核の励起状態とクラスター構造」, 2015 年 7 月 16–17 日, 阪大 RCNP
4. S. Ota (invited): “アクティブ標的を用いた錫 ^{132}Sn 近傍原子核の巨大単極共鳴測定”, RCNP 研究会「アイソスカラー型単極遷移で探る原子核の励起状態とクラスター構造」, 2015 年 7 月 16–17 日, 阪大 RCNP
5. H. Yamaguchi (oral): “Recent activities at the low-energy RI beam separator CRIB”, RIBF Users Meeting 2015, Sep. 10–11, 2015, RIKEN Nishina Center, Wako, Saitama, Japan.
6. 早川勢也 (oral): 「CRIB における Trojan horse method の応用による Big Bang 元素合成反応の測定計画」, 宇宙核物理連絡協議会研究会 2016 年 2 月 22–24 日, 国立天文台 三鷹キャンパス
7. H. Yamaguchi (oral): “Experimental study on astrophysical reactions with low-energy RI beams”, The 13th Russbach School on Nuclear Astrophysics, Mar. 6–11, 2016, Russbach am Pass Gschutt, Austria.
8. S. Hayakawa (oral): “Trojan horse method at CRIB for RI+n reactions”, The 8th Japan-Italy symposium, Mar. 7–10 2016, RIKEN, Saitama, Japan.
9. T. Gunji for the ALICE Collaboration (oral): “Overview of Recent ALICE Results”, XXV International Conference on Ultrarelativistic Nucleus-Nucleus Collisions (QM2015), Sept. 19 - Oct. 3, 2015, Kobe, Japan
10. T. Gunji (oral, invited): “Quarkonia and heavy flavour production in heavy-ion collisions - an experimental overview”, 6th Asian Triangle Heavy-Ion Conference, Feb. 15–19, India International Center, New Delhi, India
11. T. Gunji (oral, invited): “Dark photon search in heavy ion experiments at RHIC and LHC”, International workshop on Light Dark Matter at Accelerator, June 24 - 26, 2015, Camogli, Italy
12. Y. Watanabe (oral, invited): “Experimental overview on EM observables”, XXV International Conference on Ultrarelativistic Nucleus-Nucleus Collisions (QM2015), Sept. 19 - Oct. 3, 2015, Kobe, Japan
13. Y. Watanabe (oral, invited): “Dilepton production in heavy ion collisions”, 6th Asian Triangle Heavy-Ion Conference, Feb. 15–19, India International Center, New Delhi, India
14. Y. Watanabe for the PHENIX Collaboration (oral): “Dielectron measurements by PHENIX”, ECT* workshop on New perspectives on Photons and Dileptons in Ultrarelativistic Heavy-Ion Collisions at RHIC and LHC, Nov. 30 - Dec. 11, Trento, Italy
15. Y. Watanabe (oral, invited): “Charmed and exotic hadron measurements with ALICE at the LHC”, ExHIC2016 workshop, Mar. 24, 2016, Kyoto, Japan
16. S. Hayashi on behalf of the ALICE Collaboration (oral): “Dielectron measurement in pp, p-Pb, and Pb-Pb collisions with the ALICE detector”, Hard Probes 2015, June 29 -July 3, 2015, McGill University, Montreal, Canada
17. S. Hayashi on behalf of the ALICE Collaboration (poster): “Dielectron measurement from charm and bottom quark decays in p-Pb collisions with the ALICE detector”, XXV International Conference on Ultrarelativistic Nucleus-Nucleus Collisions (QM2015), Sept. 27 - Oct. 3, Kobe, Japan

18. Y.Sekiguchi for the ALICE collaboration (oral): “Two particle correlations in p -Pb collisions at $\sqrt{s_{NN}}=5.02$ TeV with the ALICE detector”, 6th Asian Triangle Heavy-Ion Conference, Feb. 15-19, India International Center, New Delhi, India
19. T. Gunji (invited), “高エネルギー重イオン衝突実験の面白さと今後の課題”, QCD Club, Dec. 18, 2015, the University of Tokyo, Hongo, Japan
20. T. Gunji (invited), “高エネルギー重イオン衝突実験の今後の展望”, 高密度核物質に挑む実験の将来 - 施設装置の観点から, Dec. 5, 2015, RIKEN, Japan
21. K. Terasaki, T. Gunji, H. Hamagaki (oral): “LHC-ALICE 実験 TPC 高度化の為の研究開発と量産準備状況”, 第 12 回 MPDG 研究会, Dec.4-5, Hiroshima University, Higashi-hiroshima, Japan
22. M. Matsushita (Oral): “New energy-degrading scheme for low-energy reaction measurements of rare isotope beams”, Advances in Nuclear Structure at Extreme Conditions, Feb. 19–22, 2014, Bormio, Italy.
23. S. Shimoura (invited): “Nucleon-nucleon correlation in neutron-rich nuclei”, International Workshop & the 12th RIBF Discussion on Neutron-Proton Correlations, July 6–9, 2015, Hong Kong.
24. S. Ota (invited): “On pn-pair transfer/pick-up reactions”, International Workshop & the 12th RIBF Discussion on Neutron-Proton Correlations, July 6–9, 2015, Hong Kong.
25. S. Ota (invited): “Using TPC to study ISGMR/ISGDR”, Science with SpRIT TPC Workshop, June, 5–6, 2015, RIKEN, Japan.
26. S. Ota (invited): “Active Target Development in Japan”, Workshop on Active Targets and Time Projection Chambers for Nuclear Physics Experiments, May 18–20, 2015, MSU
27. S. Michimasa (Oral): “Construction of OEDO beamline”, OEDO-SHARAQ International Collaboration Workshop, September 8–9, 2015, CNS Wako, Saitama, Japan
28. M. Matsushita (Oral): “Simulation of OEDO beam line”, OEDO-SHARAQ International Collaboration Workshop, September 8–9, 2015, CNS Wako, Saitama, Japan
29. S. Shimoura (Oral): “Present status of GRAPE”, OEDO-SHARAQ International Collaboration Workshop, September 8–9, 2015, CNS Wako, Saitama, Japan
30. K. Yako (Oral): “Spin-isospin studies at SHARAQ”, OEDO-SHARAQ International Collaboration Workshop, September 8–9, 2015, CNS Wako, Saitama, Japan
31. M. Kobayashi (Oral): “Direct mass measurements of neutron-rich Ca isotopes beyond $N = 34$ ”, OEDO-SHARAQ International Collaboration Workshop, September 8–9, 2015, CNS Wako, Saitama, Japan
32. M. Dozono (Oral): “The parity-transfer ($^{16}\text{O}, ^{16}\text{F}$) reaction for studies of the spin-dipole 0^- mode”, OEDO-SHARAQ International Collaboration Workshop, September 8–9, 2015, CNS Wako, Saitama, Japan
33. M. Takaki (Oral): “Investigation of Double Gamow-Teller Giant Resonances via heavy-ion double charge exchange reactions”, OEDO-SHARAQ International Collaboration Workshop, September 8–9, 2015, CNS Wako, Saitama, Japan
34. S. Ota (Oral): “Transfer Reaction and Active Target”, OEDO-SHARAQ International Collaboration Workshop, September 8–9, 2015, CNS Wako, Saitama, Japan
35. N. Imai (Oral): “Two experimental proposals using the energy-degraded beams”, OEDO-SHARAQ International Collaboration Workshop, September 8–9, 2015, CNS Wako, Saitama, Japan
36. M. Dozono (Oral): “Parity-transfer reaction for study of spin-dipole 0^- mode”, 5th International Conference on Collective Motion in Nuclei under Extreme Conditions (COMEX5), September 14–18, 2015, Kraków, Poland
37. S. Ota (Oral): “Towards the first observation of isoscalar giant monopole resonance in unstable Tin isotopes with CNS active target”, 5th International Conference on Collective Motion in Nuclei under Extreme Conditions (COMEX5), September 14–18, 2015, Kraków, Poland

38. M. Takaki (Oral): “Search for double Gamow-Teller resonance via heavy-ion double charge exchange reaction”, 5th International Conference on Collective Motion in Nuclei under Extreme Conditions (COMEX5), September 14–18, 2015, Kraków, Poland
39. R. Yokoyama (Oral): “Investigation of the octupole correlation of neutron-rich Z 56 isotopes by beta-gamma spectroscopy”, 5th International Conference on Collective Motion in Nuclei under Extreme Conditions (COMEX5), September 14–18, 2015, Kraków, Poland
40. S. Shimoura (invited): “OEDO project – New energy degraded beam line at RIBF”, International symposium on the Frontier of γ -ray spectroscopy (Gamma15), October 1–3, 2015, Osaka University, Japan
41. R. Yokoyama (Oral): “Investigation of the octupole correlation of neutron-rich Z \sim 56 isotopes by beta-gamma spectroscopy”, International symposium on the Frontier of γ -ray spectroscopy (Gamma15), October 1–3, 2015, Osaka University, Japan
42. S. Michimasa (invited): “Dispersion-matching of RI-beams and its applications to nuclear structure studies”, HRS-Workshop on high-resolution magnetic spectrometers and experiments with them, November 4–6, 2015, GSI, Darmstadt, Germany.
43. S. Shimoura (invited): “OEDO Project: EXTENDED dispersion-matching technique for production of low-energy RI beams”, HRS-Workshop on high-resolution magnetic spectrometers and experiments with them, November 4–6, 2015, GSI, Darmstadt, Germany.
44. M. Takaki (invited): “Challenges with heavy-ion double charge exchange reactions at RCNP and RIBF”, NUMEN2015 workshop, December 1–2, 2015, Catania, Italy
45. M. Dozono (poster): “The parity-transfer ($^{16}\text{O}, ^{16}\text{F}$) reaction for studies of the spin-dipole 0^- mode”, International symposium on Physics with Fragment Separators – 25th Anniversary of RIKEN-Projectile Fragment Separator (RIPS25), December 6–7, 2015, Hayama, Kanagawa, Japan
46. M. Kobayashi (poster): “Time-of-flight mass measurements of neutron-rich Ca isotopes beyond N = 34”, International symposium on Physics with Fragment Separators – 25th Anniversary of RIKEN-Projectile Fragment Separator (RIPS25), December 6–7, 2015, Hayama, Kanagawa, Japan
47. S. Michimasa (poster): “OEDO beamline for high-quality slow-down RI beams”, International symposium on Physics with Fragment Separators – 25th Anniversary of RIKEN-Projectile Fragment Separator (RIPS25), December 6–7, 2015, Hayama, Kanagawa, Japan
48. S. Shimoura (invited): “Tetraneutron at SHARAQ” International Workshop on Critical Stability in Few-Body Systems, Date: Feb. 1–5 2016, RIKEN, Wako, Japan
49. M. Takaki (invited): “Recent Activities with Heavy-Ion Double Charge Exchange Reactions at RCNP and RIBF”, 8th Japan-Italy symposium on Nuclear Physics, March 7–10, 2016, RIKEN, Japan
50. Y. Kotaka, Y. Ohshiro, S. Watanabe, H. Yamaguchi, N. Imai, S. Shimoura, M. Kase, S. Kubono, K. Hatanaka, A. Goto, H. Muto (poster): “Development of low-energy heavy-ion beams by the Riken AVF cyclotron and Hyper ECR ion source of CNS”, 13th International Conference on Heavy Ion Accelerator Technology (HIAT2015), September 7-11, 2015, Yokohama, Japan
51. H. Muto, Y. Oshiro, Y. Kotaka, S. Yamaka, S. Watanabe, H. Yamaguchi, S. Shimoura, M. Kase, S. Kubono, K. Kobayashi, M. Nishimura, M. Oyaizu, T. Hattori (poster): “Observation of sublimation effect of Mg and Ti ions at the Hyper-electron cyclotron resonance ion source”, 13th International Conference on Heavy Ion Accelerator Technology (HIAT2015), September 7-11, 2015, Yokohama, Japan
52. S. Ota (invited): “GMR で探る状態方程式”, 宇宙核物理連絡協議会研究会, February 22–24, 2016, Mitaka campus, National Astronomical Observatory of Japan.
53. Y. Utsuno(Oral, Invited): “Shell and shape evolution in exotic nuclei”, Korean Physical Society (KPS) Spring Meeting 2015, Apr. 22-24, 2015, Daejeon, Korea.
54. Y. Utsuno(Oral, Invited), T. Otsuka, N. Shimizu, and T. Togashi: “Probing shell evolution with large-scale shell-model calculation ”, International Collaborations in Nuclear Theory: Theory for open-shell nuclei near the limits of stability, May 11-29, 2015, East Lansing, Michigan, USA.

55. N. Tsunoda: “Neutron-rich nuclei from the nuclear force”, International Collaborations in Nuclear Theory (ICNT) workshop, May 24-30, 2015, Michigan State University, Michigan, USA.
56. 岩田順敬: “ニュートリノレス二重ベータ崩壊の核行列要素の大規模殻模型計算”, 新学術領域「宇宙の歴史をひもとく地下素粒子原子核研究」2015年領域研究会、2015年5月15日、神戸大学百年記念館、神戸市.
57. Y. Tsunoda(Oral, Invited): “Structure of Exotic Ni and Neighboring Nuclei”, The 2015 Gordon Research Conference on Nuclear Chemistry, June 2, 2015, Colby-Sawyer College, New Hampshire, USA.
58. N. Tsunoda(Poster): “Neutron-rich nuclei from the nuclear force”, Gordon Research Conference, May 31- June 5, 2015, Colby-Sawyer college, NH, USA.
59. Y. Iwata, N. Shimizu, T. Otsuka, Y. Utsuno, J. Menendez, M. Honma, and T. Abe: “ Large-scale shell model calculation project for neutrinoless double-beta decay of Ca48”, June 1-5, 2015, Neutrons and Dark Matter in Nuclear Physics 2015 (NDM15), Jyväskylä, Finland.
60. T. Otsuka: “Dual quantum liquid picture of nuclei and its implication to reflection asymmetry”, “Reflections on the atomic nucleus”, July 30, 2015, University of Liverpool, U.K.
61. Y. Iwata: “TDDFTによる超重核合成反応の計算”, 2015年8月, SI研究会, 近畿大学, 大阪.
62. Y. Tsunoda: “Large-scale shell model calculations for structure of nuclei around Z=28”, The 14th CNS International Summer School (CNSSS15), Aug. 28, 2015, RIKEN, Wako, Saitama, Japan.
63. N. Tsunoda: “Construction of Effective interaction for shell model calculation and its application to island of inversion”, The 14th CNS International Summer School (CNSSS15), Aug. 26- Sep. 1, 2015, RIKEN, Wako, Saitama, Japan.
64. T. Otsuka: “Shell-model perspectives for quantities of astrophysical interests in medium and heavy nuclei”, Numazu Workshop 2015: “Challenges of modeling supernovae with nuclear data”, Sep. 2, 2015, Mishima, Numazu, Japan.
65. N. Shimizu(Oral, Invited): “Large-scale shell model calculations on E1 spectra in medium-heavy nuclei”, The 5th international conference on “Collective Motion in Nuclei under Extreme Conditions (COMEX5)”, Sep. 15, 2015, Krakow, Poland.
66. Y. Tsunoda(Oral, Invited): “Monte Carlo shell model calculations for structure of Ni isotope”, the international symposium on the “Frontier of γ -ray spectroscopy” (Gamma15), Oct. 1, 2015, Osaka University, Toyonaka campus, Osaka, Japan.
67. T. Otsuka(Oral, Invited): “Dual quantum liquid picture of atomic nuclei”, the international symposium on the “Frontier of γ -ray spectroscopy” (Gamma15), Oct. 1-3, 2015, Osaka University, Toyonaka campus, Osaka, Japan.
68. T. Otsuka: “Quantum chaos and symmetry”, YIPQS Long-term workshop Computational Advances in Nuclear and Hadron Physics (CANHP 2015), Sep. 30, 2015, Yukawa Institute, Kyoto University, Kyoto, Japan.
69. N. Shimizu: “Shell model study of nuclei around N=80”, YIPQS Long-term workshop Computational Advances in Nuclear and Hadron Physics (CANHP 2015), Oct. 2, 2015, Yukawa Institute, Kyoto University, Kyoto, Japan.
70. Y. Tsunoda: “Monte Carlo shell model calculations for structure of nuclei around Z=28”, YIPQS Long-term and Nishinomiya-Yukawa Memorial International workshop Computational Advances in Nuclear and Hadron Physics (CANHP 2015), Sep. 29, 2015, Kyoto, Japan.
71. T. Togashi, N. Shimizu, Y. Utsuno, T. Otsuka, and M. Honma: “Electric dipole transitions in medium-heavy nuclei described with Monte Carlo shell model”, YIPQS Long-term and Nishinomiya-Yukawa Memorial International workshop Computational Advances in Nuclear and Hadron Physics (CANHP 2015), Oct. 2, 2015, Kyoto, Japan.
72. Y. Utsuno, N. Shimizu, T. Otsuka, M. Honma, S. Yoshida, and S. Ebata: “Shell-model study of strength function in the sd-pf shell region”, YIPQS Long-term and Nishinomiya-Yukawa Memorial International workshop Computational Advances in Nuclear and Hadron Physics (CANHP 2015), Sep. 28-Oct. 2, 2015, Kyoto, Japan.
73. Y. Iwata: “Two-neutrino and neutrinoless double beta decay of Ca48”, YIPQS Long-term and Nishinomiya-Yukawa Memorial International workshop Computational Advances in Nuclear and Hadron Physics (CANHP 2015), Sep. 28-Oct. 2, 2015, Kyoto, Japan.

74. Y. Iwata: “Heavy Neutrino-Exchange Potential for the Large-Scale Shell Model Calculations of Double-Beta Decay”, YIPQS Long-term and Nishinomiya-Yukawa Memorial International workshop Computational Advances in Nuclear and Hadron Physics (CANHP 2015), Sep. 28-Oct. 2, 2015, Kyoto, Japan.
75. T. Yoshida, N. Shimizu, T. Abe, and T. Otsuka: “Study of shell and cluster configurations of ^{12}Be based on Monte Carlo shell model”, YIPQS Long-term and Nishinomiya-Yukawa Memorial International workshop Computational Advances in Nuclear and Hadron Physics (CANHP 2015), Sep. 28-Oct. 2, 2015, Kyoto, Japan.
76. N. Tsunoda: “Construction of Effective interaction for shell model calculation and its application to island of inversion”, YIPQS Long-term and Nishinomiya-Yukawa Memorial International workshop Computational Advances in Nuclear and Hadron Physics (CANHP 2015), Sep. 21-Oct. 30, 2015, Kyoto, Japan.
77. T. Otsuka, K. Tsukiyama and R. Fujimoto: “Feshbach’s doorway-state resonances, heavy-ion induced nucleon transfer reactions and exotic nuclei” YIPQS Long-term workshop Computational Advances in Nuclear and Hadron Physics (CANHP 2015), Oct. 28, 2015, Yukawa Institute, Kyoto University, Kyoto, Japan.
78. Y. Utsuno(Oral, Invited), N. Shimizu, and T. Otsuka: “Current frontiers and perspectives in large-scale shell-model study”, RIBF Users Meeting 2015, Sep. 10-11, 2015, Wako, Japan.
79. T. Togashi(Oral, Invited), N. Shimizu, Y. Utsuno, T. Otsuka, and M. Honma: “Photoabsorption cross sections in medium-heavy nuclei calculated with Monte Carlo shell model”, The 5th International Workshop on Compound-Nuclear Reactions and Related Topics (CNR*15), Oct. 19, 2015, Tokyo, Japan.
80. N. Shimizu: “Stochastic estimation of level density in nuclear shell-model calculations”, The 5th International Workshop on Compound-Nuclear Reactions and Related Topics (CNR*15), Oct. 20, 2015, Tokyo Institute of Technology, Ookayama, Tokyo, Japan.
81. Y. Utsuno(Poster), N. Shimizu, and T. Otsuka: “Large-scale shell-model calculation for β -ray strength function”, The 5th International Workshop on Compound-Nuclear Reactions and Related Topics, Oct. 19-23, 2015, Tokyo, Japan.
82. 岩田順敬: “ニュートリノレス二重ベータ崩壊の核行列要素の成分分析”, 第7回「学際計算科学による新たな知の発見・統合・創出」シンポジウム, 筑波大学, つくば市 2015年10月.
83. T. Otsuka: “Report on Large-scale Quantum Many-body Calculation on Nuclear Properties and its Applications”, International symposium on “Quarks to Universe in Computational Science (QUCS 2015)”, Nov. 4, 2015, Nara Kasugano International Forum IRAKA, Nara, Japan.
84. N. Tsunoda(Oral, Invited): “Nuclear force to Neutron-rich nuclei”, “Quark to Universe in Computational Science 2015 (QUCS2015)”, Nov. 4-8, 2015, Nara Kasugano International Forum IRAKA, Nara, Japan.
85. N. Shimizu(Oral, Invited): “Nuclear structure and excitations clarified by Monte Carlo Shell Model calculation on K computer”, International symposium on “Quarks to Universe in Computational Science (QUCS 2015)”, Nov. 4-8, 2015, Nara Kasugano International Forum IRAKA, Nara, Japan.
86. Y. Tsunoda: “Monte Carlo shell model calculations for structure of nuclei around $Z=28$ ”, International symposium on “Quarks to Universe in Computational Science (QUCS 2015)”, Nov. 4-8, 2015, Nara Kasugano International Forum IRAKA, Nara, Japan.
87. T. Togashi, N. Shimizu, Y. Utsuno, T. Otsuka, and M. Honma: “Monte Carlo shell model for electric dipole strength distribution in medium-heavy nuclei”, Nov. 5, 2015, Symposium on Quarks to Universe in Computational Science (QUCS 2015), Nara, Japan.
88. Y. Iwata: “The nuclear matrix element of double beta decay”, Nov. 4-8, 2015. Symposium on Quarks to Universe in Computational Science (QUCS 2015), Nara, Japan. T. Yoshida(Poster), N. Shimizu, T. Abe, and T. Otsuka: “Alpha-cluster structure for Be isotopes appeared in the wave function of Monte Carlo shell model”, Nov. 4-8, 2015, Symposium on Quarks to Universe in Computational Science (QUCS 2015), Nara, Japan.
89. Y. Utsuno(Oral, Invited), N. Shimizu, T. Otsuka, M. Honma, S. Ebata, T. Mizusaki, Y. Futamura, and T. Sakurai: “Large-scale shell-model study of E1 strength function and level density”, Nov. 16-19, 2015, “ High-resolution Spectroscopy and Tensor interactions ” (HST15), Osaka, Japan.

90. Y. Tsunoda: “「モンテカルロ殻模型計算による Z=28 近傍の核構造の研究」”, KEK 理論センター研究会「原子核・ハドロン物理の課題と将来」, 2015 年 11 月 25 日、高エネルギー加速器研究機構研究本館、つくば市.
91. Y. Utsuno(Oral, Invited), S. Yoshida, N. Shimizu, and T. Otsuka: “Shell model calculations for Gamow-Teller strength function in the neutron-rich sd-pf shell region”, Dec. 1-2, 2015, 27th ASRC International Workshop “Nuclear Fission and Exotic Nuclei”, Tokai, Japan.

B. JPS Meetings

1. Y. Watanabe for the ALICE Collaboration, “LHC-ALICE 実験におけるチャームバリオン生成の測定”, 71th JPS annual meeting, Mar.19-22, Tohoku Gakuin University, Sendai, Japan
2. Y. Sekiguchi for the ALICE collaboration, “Long-range correlations in p -Pb collisions at $\sqrt{s_{NN}}=5.02$ TeV with the ALICE detector”, 71th JPS annual meeting, Mar.19-22, Tohoku Gakuin University, Sendai, Japan
3. K. Terasaki for the ALICE Collaboration, “Search for exotic strange dibaryon at LHC-ALICE”, 71th JPS annual meeting, Mar.19-22, Tohoku Gakuin University, Sendai, Japan
4. H. Murakami for the ALICE collaboration, “Status of direct photon measurements via external conversions in high multiplicity pp collisions at 13 TeV with ALICE”, 71th JPS annual meeting, Mar.19-22, Tohoku Gakuin University, Sendai, Japan
5. S. Shimoura (invited): “Experimental studies of the tetra-neutron system by using RI-beam”, 「ドリップライン近傍のハイパー核と不安定核」シンポジウム, JPS Fall meeting, September 25–28, 2015, Osaka City University, Osaka, Japan
6. K. Yako (invited): “荷電交換反応による新モード探索” 「スピン・アイソスピン応答研究の新たな地平」シンポジウム, JPS Fall meeting, September 25–28, 2015, Osaka City University, Osaka, Japan
7. S. Ota *et al.*: “理研 RIBF BigRIPS における大強度不安定核ビームの粒子識別の開発”, JPS Fall meeting, September 25–28, 2015, Osaka City University, Osaka, Japan
8. M. Takaki *et al.*: “重イオン二重荷電交換反応による ^{48}Ti の二重ガモフテラー共鳴探索”, JPS Fall meeting, September 25–28, 2015, Osaka City University, Osaka, Japan
9. R. Yokoyama *et al.*: “ $\beta - \gamma$ 核分光を用いた中性子過剰 La 同位体の変形”, JPS Fall meeting, September 25–28, 2015, Osaka City University, Osaka, Japan
10. M. Kobayashi *et al.*: “中性子数 34 近傍カルシウム同位体の直接質量測定”, JPS Fall meeting, September 25–28, 2015, Osaka City University, Osaka, Japan
11. Y. Kiyokawa *et al.*: “SHARAQ におけるアイソマー同定システムの開発”, JPS Fall meeting, September 25–28, 2015, Osaka City University, Osaka, Japan
12. M. Dozono *et al.*: “パリティ移行核反応による原子核の 0^- 状態の研究 II”, JPS Fall meeting, September 25–28, 2015, Osaka City University, Osaka, Japan
13. S. Michimasa, M. Kobayashi, Y. Kiyokawa, M. Takaki, M. Dozono, S. Go, H. Baba, E. Ideguchi, K. Kisamori, T. Matsubara, M. Matsushita, H. Miya, S. Ota, H. Sakai, S. Shimoura, A. Stolz, T.L. Tang, H. Tokieda, T. Uesaka, R.G.T. Zegers: “多結晶ダイヤモンド検出器の開発”, JPS Spring meeting, March 19–22, 2016, Tohoku Gakuin University, Sendai, Japan
14. Y. Kubota *et al.*: “ポロミオン核 (p,pn) 反応を用いた二中性子運動量相関の研究”, JPS Spring meeting, March 19–22, 2016, Tohoku Gakuin University, Sendai, Japan
15. Y. Kiyokawa *et al.*: “SHARAQ における中性子過剰 Sc 近傍核の核異性体 γ 線分光”, JPS Spring meeting, March 19–22, 2016, Tohoku Gakuin University, Sendai, Japan
16. S. Masuoka, S. Shimoura, K. Kobayashi, Y. Kunimoto: “複数中性子識別のための反跳陽子飛跡検出器の開発”, JPS Spring meeting, March 19–22, 2016, Tohoku Gakuin University, Sendai, Japan

17. Y. Yamaguchi, S. Shimoura, N. Imai, K. Wimmer, T. Kitamura: “DSP を用いた多重ガンマ線検出用 Ge 検出器アレイのためのデータ収集系の開発”, JPS Spring meeting, March 19–22, 2016, Tohoku Gakuin University, Sendai, Japan
18. T. Kitamura, N. Imai, Y. Yamaguchi, H. Haba: “高スピンアイソマー $^{178m2}\text{Hf}$ 標的開発のためのアイソマー生成および純化手法の検討”, JPS Spring meeting, March 19–22, 2016, Tohoku Gakuin University, Sendai, Japan
19. Y. Iwata(Oral, Invited): “TDHF で見た fission”, the JPS Autumn Meeting, Sep. 25-28, 2015, Osaka City University, Osaka, Japan.
20. N. Shimizu, Y. Futamura, T. Sakurai, T. Mizusaki, Y. Utsuno, and T. Otsuka: “殻模型計算における確率論的な準位密度計算法”, the JPS Autumn Meeting, Sep. 27, 2015, Osaka City University, Osaka, Japan.
21. Y. Utsuno, N. Shimizu, T. Togashi, T. Otsuka, T. Suzuki, and M. Honma: “第一禁止ベータ崩壊データによる中性子過剰カルシウム同位体の殻進化の解析”, the JPS Autumn Meeting, Sep. 25-28, 2015, Osaka City University, Osaka, Japan.
22. Y. Iwata, N. Shimizu, T. Otsuka, Y. Utsuno, J. Menendez, M. Honma, and T. Abe: “48Ca の二重ベータ崩壊の殻模型計算による記述 III”, the JPS Autumn Meeting, Sep. 25-28, 2015, Osaka City University, Osaka, Japan.
23. T. Togashi, T. Otsuka, N. Shimizu, and Y. Utsuno: “モンテカルロ殻模型によるセレン 79 の光吸収断面積の計算”, the JPS Autumn Meeting, Sep. 25-28, 2015, Osaka City University, Osaka, Japan.
24. T. Yoshida, N. Shimizu, T. Abe, and T. Otsuka: “12Be における殻構造と クラスター構造のモンテカルロ殻模型による研究”, the JPS Autumn Meeting, Sep. 26, 2015, Osaka City University, Osaka, Japan.
25. N. Tsunoda: “核力に基づいた中性子過剰 Ca 同位体の構造”, the JPS Autumn Meeting, Sep. 25-28, 2015, Osaka City University, Osaka, Japan.
26. Y. Tsunoda: “大規模殻模型計算による Z=28 近傍の核構造の研究”, the JPS Autumn Meeting, Sep. 27, 2015, Osaka City University, Osaka, Japan.
27. Y. Utsuno(Oral, Invited): “中性子過剰な原子核の物理”, the JPS Spring Meeting, Mar. 19-22, 2016, Tohoku Gakuin University, Sendai, Japan.
28. Y. Tsunoda: “大規模殻模型計算による Z=28 近傍の核構造の研究”, the JPS Spring Meeting, Mar. 22, 2016, Tohoku Gakuin University, Sendai, Japan.
29. T. Yoshida, N. Shimizu, T. Abe, and T. Otsuka: “Be 同位体における intrinsic 状態の研究”, the JPS Spring Meeting, Mar. 19, 2016, Tohoku Gakuin University, Sendai, Japan.
30. T. Togashi, T. Otsuka, N. Shimizu, and Y. Utsuno: “モンテカルロ殻模型による 79Se, 90Sr, 93Zr の光吸収断面積の計算”, the JPS Spring Meeting, Mar. 22, 2016, Tohoku Gakuin University, Sendai, Japan.
31. Y. Iwata, N. Shimizu, T. Otsuka, J. Menendez, Y. Utsuno, M. Honma, and T. Abe: “Ca48 のニュートリノレス二重ベータ崩壊に対するステライル・ニュートリノの影響”, the JPS Spring Meeting, Mar. 19-22, 2016, Tohoku Gakuin University, Sendai, Japan.
32. N. Tsunoda: “核力に基づいた pf-shell 原子核の構造”, the JPS Spring Meeting, Mar. 19-22, 2016, Tohoku Gakuin University, Sendai, Japan.

C. Lectures

1. S. Shimoura: “RI ビームによる核反応と核応答”, 第 4 回中性子核物質ウィンタースクール, February 24–26, 国立天文台
2. T. Otsuka: “Structure evolutions in exotic nuclei and nuclear forces”, Nuclear Physics Seminar 2-SlotSeries Plus!, July 1-2 2015, RIKEN, Tokyo, Japan.

D. Seminars

1. Y. Watanabe, “Low-mass dielectron measurement at RHIC-PHENIX with Hadron Blind Detector”, University of Tsukuba, Feb. 29, 2016
2. S. Shimoura: “Experimental studies of the tetra-neutron system by using RI-beam”, December 18, 2015, JAEA, Tokai, Japan
3. 岩田順敬: “TDDFT による元素の合成・分裂過程の計算”, 近畿大学 2015 年 10 月 5 日.

Personnel

Director

OTSUKA, Takaharu *Professor, Department of Physics,
Graduate School of Science*

Scientific Staff

SHIMOURA, Susumu *Professor*
HAMAGAKI, Hideki *Professor*
YAKO, Kentaro *Associate Professor*
IMAI, Nobuaki *Associate Professor*
SHIMIZU, Noritaka *Project Associate Professor*
YAMAGUCHI, Hidetoshi *Lecturer*
WIMMER, Kathrin *Lecturer*
MICHIMASA, Shin'ichiro *Assistant Professor*
GUNJI, Taku *Assistant Professor*
OTA, Shinsuke *Assistant Professor*

Guest Professors

UTSUNOMIYA, Hiroaki *Konan University*
UTSUNO, Yutaka *JAEA*

Technical Staff

KOTAKA, Yasuteru

Technical Assistants

OHSHIRO, Yukimitsu
YOSHIMURA, Kazuyuki
YAMANAKA, Yukio

YAMAKA, Shoichi
KATAYANAGI, Mamoru

Post Doctoral Associates

IWATA, Yoritaka
MATSUSHITA, Masafumi
HAYAKAWA, Seiya
TSUNOAD, Naofumi
DOZONO, Masanori

YOSHIDA, Tooru
WATANABE, Yosuke
TOGASHI, Tomoaki
TSUNODA, Yusuke
SCHROCK Philipp

Graduate Students

KAHL, David
KAWASE, Shoichiro
TAKAKI, Motonobu
KOBAYASHI, Motoki
MASUOKA, Soichiro
SEKIGUCHI, Yuko
KUBOTA, Yuki
KIYOKAWA, Yu
KAWATA, Keita
ABE, Keijiro

MIYA, Hiroyuki
TOKIEDA, Hiroshi
YOKOYAMA, Rin
YAMAGUCHI, Yuki
HAYASHI, ShinIchi
TERASAKI, Kohei
LEE, CheongSoo
KITAMURA, Noritaka
SAKAGUCHI, Yuji

Administration Staff

YOSHIMURA, Hiroshi (-2015.6)
YAMAMOTO, Ikuko
ENDO, Takako
DOI, Sachiko

OKI, Mikio (2015.7-)
KISHI, Yukino
SOMA, Yuko

Committees

Steering Committee

FUKUDA, Hiroo	<i>Department of Biological Science, Graduate School of Science, UT</i>
YAMANOUCHI, Kaoru	<i>Department of Chemistry, Graduate School of Science, UT</i>
SANO, Masaki	<i>Department of Physics, Graduate School of Science, UT</i>
OTSUKA, Takaharu	<i>Department of Physics, Graduate School of Science, UT</i>
SAKURAI, Hiroyoshi	<i>Department of Physics, Graduate School of Science, UT</i>
SHIMOURA, Susumu	<i>Center for Nuclear Study, Graduate School of Science, UT</i>
HAMAGAKI, Hideki	<i>Center for Nuclear Study, Graduate School of Science, UT</i>
MORI, Toshinori	<i>International Center for Elementary Particle Physics, UT</i>
TAKAHASHI, Hiroyuki	<i>Department of Nuclear Engineering and Management, Graduate School of Engineering, UT</i>
NAGAMIYA, Shoji	<i>RIKEN</i>

